
THE UNIVERSITY *of* EDINBURGH

# Purely elastic shear flow instabilities: linear stability, coherent states and direct numerical simulations


*Toby William Searle*

A thesis submitted in fulfilment of the requirements
for the degree of Doctor of Philosophy
to the
University of Edinburgh
March 2017

# Lay Summary

Liquids can contain many different components, from individual atoms to small molecules and up to large crystals. We are interested in gooey fluids (known as viscoelastic fluids), which contain long string-like molecules made up of hundreds or thousands of atoms. There are many examples of these fluids in our lives, including cosmetic products, oil, blood, mucus and semen. These viscoelastic fluids flow smoothly at low speeds, but at high speeds the flow becomes less smooth and more difficult to predict. We would like to understand the conditions that lead to this unsteady flow, so that we can design better devices for the chemical industry and medical science (for example, better creams and medicines, and more effective surgery).

In this thesis, we use computers to model the flow of viscoelastic fluids. We examine channel flow — the flow between two parallel plates — and try to work out the flow speed for different kinds of fluid that leads to unsteady, unpredictable flow.

Specifically, we consider four different kinds of flow in a channel. The first is a simple fluid flow between two plates driven by a constant pressure at the inlet. We look for a way to explain the unsteadiness that sets in when the fluid is particularly gooey or the pressure at the inlet is high. Unfortunately, we are unable to explain the transition to unsteady flow using our results. In the second flow we consider what happens when the velocity changes sharply in a layer halfway between the plates. In simple fluids, this channel flow becomes unsteady at high flow velocities. In viscoelastic fluids containing many long molecules, we show that this channel flow can become unsteady in a different way at much lower flow velocities. Thirdly, we look at a flow where an oscillating piston pushes fluid forwards and backwards along a channel. This flow is similar to the pumping flows found in blood circulation, oil recovery, and filtration. Experiments using viscoelastic fluids show that this flow is not smooth, and that some fluid during the pumping cycle moves in the opposite direction to the piston. Using computer simulations we show why this happens and predict the frequency and amplitude of the piston which will trigger this flow. Finally, we look at a channel flow where the top and bottom walls of the channel are moving in opposite directions. We find a possible explanation for the unsteadiness of this flow when the fluid is viscoelastic and walls are

moving slowly.

# Abstract

Recently, a new kind of turbulence has been discovered in the flow of concentrated polymer melts and solutions. These flows, known as purely elastic flows, become unstable when the elastic forces are stronger than the viscous forces. This contrasts with Newtonian turbulence, a more familiar regime where the fluid inertia dominates. While there is little understanding of purely elastic turbulence, there is a well-established dynamical systems approach to the transition from laminar flow to Newtonian turbulence. In this project, I apply this approach to purely elastic flows.

Laminar flows are characterised by ordered, locally-parallel streamlines of fluid, with only diffusive mixing perpendicular to the flow direction. In contrast, turbulent flows are in a state of continuous instability: tiny differences in the location of fluid elements upstream make a large difference to their later locations downstream. The emerging understanding of the transition from a laminar to turbulent flow is in terms of exact coherent structures (ECS) — patterns of the flow that occur near to the transition to turbulence.

The problem I address in this thesis is how to predict when a purely elastic flow will become unstable and when it will transition to turbulence. I consider a variety of flows and examine the purely elastic instabilities that arise. This prepares the ground for the identification of a three-dimensional steady state solution to the equations, corresponding to an exact coherent structure.

I have organised my research primarily around obtaining a purely elastic exact coherent structure, however, solving this problem requires a very accurate prediction of the exact solution to the equations of motion. In Chapter 2 I start from a Newtonian ECS (travelling wave solutions in two-dimensional flow) and attempt to connect it to the purely elastic regime. Although I found no such connection, the results corroborate other evidence on the effect of elasticity on travelling waves in Poiseuille flow.

The Newtonian plane Couette ECS is sustained by the Kelvin-Helmholtz instability. I discover a purely elastic counterpart of this mechanism in Chapter 3, and explore the non-linear evolution of this instability in Chapter 4. In Chapter 5 I turn to a slightly different problem, a (previously unexplained) instability in a purely elastic oscillatory

shear flow. My numerical analysis supports the experimental evidence for instability of this flow, and relates it to the instability described in Chapter 3. In Chapter 6 I discover a self-sustaining flow, and discuss how it may lead to a purely elastic 3D exact coherent structure.

# Declaration

Except where otherwise stated, the research undertaken in this thesis was the unaided work of the author. Where the work was done in collaboration with others, a significant contribution was made by the author.

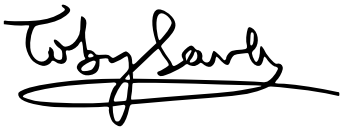

*T. W. Searle*
March 2017

# Acknowledgements

I would like to thank all those who helped me in the course of this project.

I thank my supervisor Alexander Morozov for his enthusiastic guidance, patient support and an out-of-date cream egg.

I thank my office comrade Andrew Tadrowski for useful and not-so-useful conversations, and my other friends for being good company and keeping things interesting.

I would also like to thank both my parents and my step-father for their unwavering support.

This work was supported by the CM-CDT[1], SUPA[2] and EPSRC[3].

[1]The Scottish Centre for Doctoral Training in Condensed Matter Physics
[2]The Scottish Universities Physics Alliance
[3]Engineering and Physical Sciences Research Council

# Contents

# List of Figures

# List of Tables

# Chapter 1

# Introduction

The jet of water from an open tap at high flow rates is turbulent. At lower flow rates, the jet appears smoother, and the flow more ordered. We say that the ordered case is laminar, because it consists of layers of fluid travelling with the same velocity. The differences in behaviour of these two regimes is large: turbulent flows dissipate energy into recirculating regions, and increase the drag at the boundaries. Unlike water, many fluids also contain long structures, such as macromolecules or polymers, which can have a large influence on the flow. The stretching of these macromolecules can cause a different kind of turbulence, affecting biological flows, the processing of polymers for industry, and flows in the Earth's mantle [1]. We shall refer to the first kind of turbulence as *Newtonian* and the second as *purely elastic* throughout this thesis. We explore purely elastic turbulence and attempt to predict its onset for some simple flows using non-laminar solutions to the equations of motion, known as Exact Coherent Structures.

To understand purely elastic turbulence it will be necessary to use results and methods from two different research areas: viscoelasticity, and the dynamical systems approach to the transition to turbulence. In the first part of this introduction, we will consider viscoelastic fluids: both the basic phenomenology and the continuum equations for their behaviour. Then we will explore the transition to turbulence in Newtonian fluids, examining the kinds of transition available and the theoretical techniques used. Later, we will explore the notion of Exact Coherent Structures in more detail, including a literature review of the first calculations of these structures for Newtonian fluids and the current state of the art. Finally, we shall consider the research programme used in this thesis to search for purely elastic exact coherent structures.

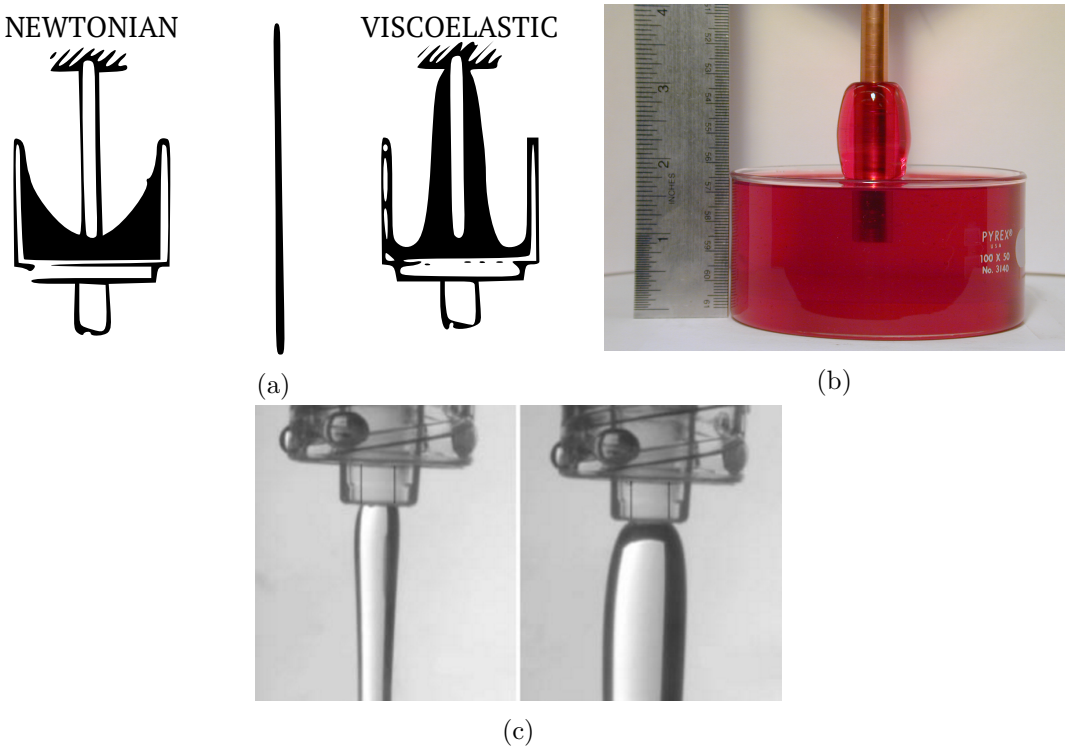


Figure 1.1: a) The rod climbing or Weissenberg effect. A rotating rod is immersed in a viscoelastic fluid. For a Newtonian fluid (left hand side) the laminar flow is concave. For high enough rotation speeds and an elastic enough fluid the fluid climbs the rod (the right hand side). Image reproduced with permission from [2]. b) Image of the experiment, reproduced with permission from the McKinley group website [3]. c) The die swell or Barus effect. A jet of viscoelastic fluid forced out of a narrow opening will swell to a diameter much larger than the diameter of the opening. Image reproduced with permission from [3].

## 1.1 Viscoelasticity

Viscoelastic fluids respond both elastically and viscously to stress. On short time scales they behave like a solid, with an elastic response to deformation. On larger timescales they flow like Newtonian fluids. Molten polymers, polymer solutions, blood, mucus and cosmetic products like shampoo are all examples of this kind of fluid. In this section we will explore some of the phenomenology of these fluids due to viscoelastic effects, the models used for their flow and review the literature on some of these flows. Then we will examine the evidence for purely elastic turbulence.

### 1.1.1 Basic phenomenology

Consider a cylindrical vessel partially filled with a fluid, and with a rod inserted into the centre of the cylinder. For a Newtonian fluid, steady rotation of the rod will cause fluid to move to the walls of the cylinder, producing a concave, laminar flow. However, a viscoelastic fluid will climb the rotating rod (Fig. 1.1a) [2]. Fig. 1.1b shows a viscoelastic flow caused by what is known as the rod-climbing or Weissenberg effect. Another example of uniquely viscoelastic behaviour is known as the Barus, or die-swell effect. In this experiment, polymer solution is squeezed through a nozzle. Immediately following the outlet, the jet of fluid suddenly expands (see Fig. 1.1c). By contrast, a laminar Newtonian jet remains narrow.

Viscoelasticity can affect turbulent, as well as laminar flows through a process called drag reduction. Turbulent flows create recirculation of fluid, which dissipates energy. The addition of a small concentration of polymers introduces extra stresses which contribute to the stability of the flow, allowing for faster flow rates. This has already been used in Alaskan oil pipe lines, is proposed for use in large scale heating and cooling systems, and for ship hydrodynamics to increase efficiency [4].

None of these experiments can be explained using Newtonian fluid mechanics — as we shall see, extra stresses from the elongated macromolecular constituents of the fluid are responsible for this interesting flow behaviour.

### 1.1.2 Modelling viscoelastic fluids

At this point we will outline the fundamentals of viscoelastic fluid mechanics, beginning with a brief review of the Navier-Stokes and continuity equations for incompressible fluids. Then we will will explore some of the numerous models used to extend the Navier-Stokes equation to apply to viscoelastic fluids. This discussion will closely follow the discussion by Morozov and Spagnolie [5], however, comprehensive introductions to Newtonian fluid mechanics [6] and viscoelasticity [7] can be found elsewhere.

#### Newtonian flows and Cauchy stress

Hydrodynamicists use a continuum approximation in order to produce a field theory for fluids. First, we break the flow up into small pieces, known as fluid parcels. We assume each parcel is large enough to be at thermodynamic equilibrium, with a constant pressure, density and temperature. We then assume that each parcel is small enough so that variations in the relevant variables between parcels are continuous. This allows us to average over the molecular degrees of freedom in each parcel and consider the velocity, density, and stress for each parcel in the flow. To generate equations for the flow of Newtonian and Non-Newtonian fluids, we start from conservation laws, like

the conservation of mass and momentum, and generate differential equations for the motion of the parcels.

The conservation of mass implies that the integral over any arbitrary volume in the fluid,

$$\frac{\mathrm{d}}{\mathrm{d}t}\int \rho(\mathbf{x},t)\,\mathrm{d}V = 0\,, \tag{1.1}$$

where $\mathrm{d}V$ is a volume element, $\mathbf{x}$ is the position vector, and $\rho$ is the density. This is the equation for the density of a fluid particle. To make it an equation for the density at a point in the coordinate system of the experiment, we take a detour and introduce the Lagrangian and Eulerian descriptions. The Lagrangian description relates a parcel of fluid at an initial point $\mathbf{a}$, to its position later, $\mathbf{x} = \chi(\mathbf{a}, t)$. The Lagrangian coordinate system is the coordinate system which is deformed with the fluid, such that the fluid particle always has position vector $\mathbf{a}$. The Eulerian description, however, is a fixed frame of the coordinate system of the experimenter. We can see that the total derivative in the Eulerian description must takes account of the change from the Lagrangian frame,

$$\frac{\mathrm{d}}{\mathrm{d}t}f(\mathbf{x}(\mathbf{a},t),t) = \frac{\partial f}{\partial t} + \frac{\partial f}{\partial x_i}\frac{\partial x_i}{\partial t} = \left[\frac{\partial}{\partial t} + \mathbf{v}\cdot\nabla\right] f\,, \tag{1.2}$$

where $f$ is some scalar function, $\mathbf{v}$ is the velocity, and we use Einstein summation notation. The operator on the right hand side is known as the material derivative, $\frac{D}{Dt}$. To calculate the time derivative of the volume element $\mathrm{d}V$ used in the integral form of the continuity equation we introduce the deformation gradient tensor, $F = \frac{\partial \mathbf{x}}{\partial \mathbf{a}}$. This is a Jacobian matrix of the mapping $\chi(\mathbf{a}, t)$, so that a small volume element in the Eulerian frame is related to the Lagrangian frame by $\mathrm{d}V_x = \det(F)\mathrm{d}V_a$ and the time derivative of the Jacobian $J = \det(F)$ is given by,

$$\frac{\mathrm{d}J}{\mathrm{d}t} = (\nabla\cdot\mathbf{v})\,J\,. \tag{1.3}$$

For an incompressible fluid, the volume is conserved under the mapping $\chi$ and so $J = 1$ and

$$\nabla\cdot\mathbf{v} = 0\,. \tag{1.4}$$

This is the continuity equation. We also find that $\frac{\partial}{\partial t}\mathrm{d}V_x = \frac{\partial J}{\partial t}\mathrm{d}V_a = 0$. Now we express the conservation of mass in the Lagrangian frame, apply the derivative and return to

the Eulerian frame,

$$0 = \frac{\mathrm{d}}{\mathrm{d}t}\int \rho(\mathbf{x},t)\,\mathrm{d}V = \int \frac{\mathrm{D}}{\mathrm{D}t}\rho(\mathbf{x},t)\,\mathrm{d}V\,. \tag{1.5}$$

Making the control volume infinitesimal (whilst keeping it larger than the parcel diameter) we find,

$$\frac{\mathrm{D}}{\mathrm{D}t}\rho(\mathbf{x},t) = 0\,. \tag{1.6}$$

So, starting by assuming $J = 1$ (the fluid is incompressible) we find that density is constant in time, demonstrating the link between the continuity equation and the conservation of mass.

To produce an equation for the velocity, we consider the conservation of momentum via Newton's second law for a control volume moving through the fluid. This gives,

$$\frac{\mathrm{d}}{\mathrm{d}t}\int \rho\mathbf{v}(\mathbf{x},t)\,\mathrm{d}V = \int \mathbf{f}\,\mathrm{d}V + \int \mathbf{t}\,\mathrm{d}S\,, \tag{1.7}$$

where $\mathrm{d}V$ is a volume element and $\mathrm{d}S$ is the surface element. Here the external forces are given by $\mathbf{f}$ and the vector of surface tractions on the volume by $\mathbf{t}$. Writing the surface tractions in terms of the Cauchy stress tensor, $\mathbf{t} = \boldsymbol{\sigma}\cdot\mathbf{n}$, using the divergence theorem, and following the same process of switching to the Lagrangian description and back again, we can obtain the conservation of momentum equation,

$$\rho\frac{\mathrm{D}\mathbf{v}}{\mathrm{D}t} = \mathbf{f} + \nabla\cdot\boldsymbol{\sigma}\,. \tag{1.8}$$

The Cauchy stress tensor contains information on the total stresses between fluid parcels. The traction on the surface with normal $\mathbf{e}_1$, for example, is given by $\mathbf{t} = \boldsymbol{\sigma}\cdot\mathbf{e}_1 = \sigma_{11}\mathbf{e}_1 + \sigma_{12}\mathbf{e}_2 + \sigma_{13}\mathbf{e}_3$, so that the diagonal elements of $\sigma$ give the pressure on each face of a fluid parcel and the other components give the traction from shearing the parcel walls. For all that follows we assume that $\sigma$ is symmetric, so that there are no torques on a parcel. This is due to the conservation of angular momentum on a parcel [5].

The deviatoric stress tensor, $\boldsymbol{\tau}$, gives the stress without a contribution from the isotropic pressure field, $p$,

$$\boldsymbol{\sigma} = -p\mathbb{I} + \boldsymbol{\tau}\,. \tag{1.9}$$

For a Newtonian fluid $\boldsymbol{\tau}$ is traceless, however we shall see that viscoelastic fluids can introduce stresses on the diagonal of $\boldsymbol{\tau}$.

Relations between $\boldsymbol{\tau}$ and $\mathbf{v}$ are known as constitutive equations. All the constitutive equations we consider start from the local strain rate in the fluid. To approximate this local strain rate we Taylor expand the velocity, $\mathbf{v}(\mathbf{x}, t)$, about its current position,

$$\mathbf{v}(\mathbf{x} + \mathrm{d}\mathbf{x}, t) = \mathbf{v}(\mathbf{x}, t) + \mathrm{d}\mathbf{x} \cdot \nabla\mathbf{v}(\mathbf{x}, t) + \mathcal{O}(|\mathrm{d}\mathbf{x}|^2)\,, \tag{1.10}$$

where $\nabla\mathbf{v} = \frac{\partial u_j}{\partial x_i}$. We are only interested in the symmetric part of this tensor, since the antisymmetric part is only responsible for rigid body rotations, so it cannot generate any stresses. The symmetric part of $\nabla\mathbf{v}$ is known as the rate of strain tensor,

$$\dot{\boldsymbol{\gamma}} = \left(\nabla\mathbf{v} + \nabla\mathbf{v}^T\right)\,, \tag{1.11}$$

where the $T$ indicates the transpose. A Newtonian fluid is defined as a fluid which is both isotropic and has a linear relationship between the deviatoric stress and the rate of strain tensor. For an incompressible fluid this gives $\boldsymbol{\tau} = \eta\dot{\boldsymbol{\gamma}}$ so that,

$$\boldsymbol{\sigma} = -p\mathbb{I} + \eta\dot{\boldsymbol{\gamma}}\,, \tag{1.12}$$

where $\eta$ is the viscosity of the fluid. Substitution of (1.12) into (1.8) gives the Navier-Stokes equations for an incompressible fluid,

$$\begin{aligned} \rho\frac{\mathrm{D}\mathbf{v}}{\mathrm{D}t} &= -\nabla p + \eta\nabla^2\mathbf{v} + \mathbf{f} \\ \nabla\cdot\mathbf{v} &= 0\,. \end{aligned} \tag{1.13}$$

If we define some length ($L$), time ($T$) and velocity ($U = L/T$) scales, we can non-dimensionalise the equations. We define the dimensionless variables:

$$\begin{aligned} \tilde{\mathbf{x}} = \mathbf{x}/L\,, \quad \tilde{\mathbf{v}} = \mathbf{v}/U\,, \quad \tilde{t} = t/T\,, \\ \tilde{p} = p\frac{L}{\eta U}\,, \quad \tilde{\mathbf{f}} = \mathbf{f}\frac{L^2}{\eta U}\,. \end{aligned} \tag{1.14}$$

This allows us to form the dimensionless incompressible Navier-Stokes equations,

$$\begin{aligned} Re\frac{\mathrm{D}\mathbf{v}}{\mathrm{D}t} &= -\nabla p + \nabla^2\mathbf{v} + \mathbf{f} \\ \nabla\cdot\mathbf{v} &= 0\,, \end{aligned} \tag{1.15}$$

where we have dropped the $\tilde{\cdot}$ notation for the dimensionless variables for clarity. Provided we choose our scales appropriately, this dimensional analysis allows us to

compare flows with similar geometry using only the Reynolds number $Re$,

$$Re = \frac{\rho U L}{\eta} . \tag{1.16}$$

Fluids which obey (1.15) are known as incompressible Newtonian fluids, and are successful for explaining many flow phenomena. However, the viscoelastic effects responsible for viscoelastic instabilities and purely elastic turbulence cannot be described with Newtonian fluid mechanics. These fluids have a complex microstructure and a complex relationship between stress and deformation. There are three main effects of this microstructure: shear thinning/thickening, stress memory and stress anisotropy. Shear thinning/thickening refers flows where the shear rate either reduces or increases the apparent viscosity of the solution. These effects are key for non-Newtonian flows, however they are not directly responsible for purely elastic turbulence, so are not of great importance to this project. Stress anisotropy refers to the tendency for a flow to align elongated macromolecules. This introduces differences between the stress perpendicular to the direction of alignment and the stress parallel to it. Stress memory refers to the finite stress relaxation time of the constituents of the flow. This effect means that the stress can be partly due to stresses applied to the fluid earlier, rather than being instantaneously due to the rate of strain as in Newtonian fluids. To account for all of these effects, we need to introduce a differential equation for the stress, known as a constitutive equation.

### Constitutive equations

Before considering constitutive equations for the stress, we return to the basic properties of a viscoelastic fluid. The goal is to motivate the form of constitutive equations and to hopefully construct some equations which will include memory and anisotropy of the stress.

Picture a simple box of material, with the upper surface and lower surface displaced such that the box is under shear (see Fig. 1.2a). What is the stress on the box as it resists this shear? Recall that viscoelastic fluids have an elastic and a viscous response to stress, so an intuitive model would involve a combination of these effects. We can visualise this combination with a spring and dashpot (a dashpot is the device used in doors to stop them slamming). The spring represents a solid like response, where displacements will introduce restoring forces to bring the box back to its original configuration. The dashpot represents the viscous response, where the material will resist, but adapt to its new configuration. Fig. 1.2b shows a schematic picture of the stresses in a solid-like liquid. As time passes, the dashpot will adjust to adapt to the applied strain, and

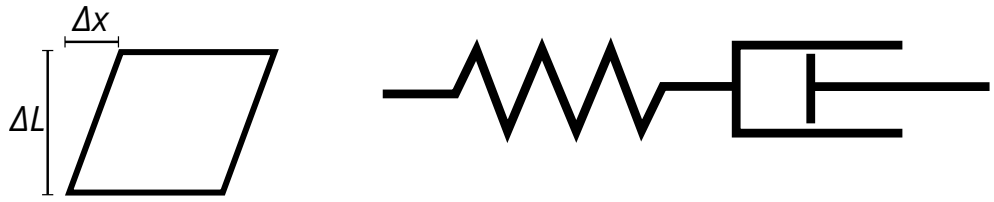


(a)

(b)

Figure 1.2: a) A diagram of a box of material under shear. b) A schematic for the response to stress of a viscoelastic solid-like liquid. A spring and dashpot are connected in series, so that on short timescales the spring response dominates but on longer timescales the dashpot relaxes away the stress.

the material flows. The viscous response of this material can be modelled just like a Newtonian fluid,

$$\Sigma_d = \eta \dot{\Gamma}_d \,, \tag{1.17}$$

where $\Sigma_d$ is the viscous stress and $\dot{\Gamma} = \frac{\partial}{\partial t}\frac{\Delta x(t)}{\Delta l}$ is the rate of strain on the box. By Hookes law a spring response would be,

$$\Sigma_s = G\Gamma_s \,, \tag{1.18}$$

where $G$ is the elastic modulus of the material. Connecting these two in series (as in Fig. 1.2b) we arrive at the total strain in the material, $\Gamma = \Gamma_s + \Gamma_d$, and a total stress of $\Sigma = \Sigma_s = \Sigma_d$. Therefore the stress on the box is given by,

$$\Sigma + \frac{\eta}{G}\dot{\Sigma} = \eta\dot{\Gamma} \,. \tag{1.19}$$

This equation is known as the linear Maxwell model. At the moment, it gives only the shear stress given the shear strain for a box of viscoelastic material. We would like to turn this into a partial differential equation with the power of the Navier-Stokes equation, (1.13). However there is a problem: the time derivatives used in the linear Maxwell model are not frame invariant. Just as we saw when calculating the conservation of momentum, we need to take account of the fact that the fluid at a coordinate in the experimenters frame is changing with the flow. In the conservation of momentum equation we did this using the material derivative. In this equation we are

dealing with a rank 2 tensor, and so we need the corresponding frame invariant time derivative for this case. The time derivatives due to the co- and contra-variant stress tensors are given by,

$$\overset{\triangledown}{\boldsymbol{\sigma}} = \frac{\partial \boldsymbol{\sigma}}{\partial t} + \mathbf{v} \cdot \boldsymbol{\sigma} - (\nabla \mathbf{v})^T \cdot \boldsymbol{\sigma} - \boldsymbol{\sigma} \cdot \nabla \mathbf{v} \tag{1.20}$$

$$\overset{\triangle}{\boldsymbol{\sigma}} = \frac{\partial \boldsymbol{\sigma}}{\partial t} + \mathbf{v} \cdot \boldsymbol{\sigma} + \nabla \mathbf{v} \cdot \boldsymbol{\sigma} + \boldsymbol{\sigma} \cdot (\nabla \mathbf{v})^T , \tag{1.21}$$

where $\overset{\triangledown}{\boldsymbol{\sigma}}$ is the upper-convected derivative of $\boldsymbol{\sigma}$ and $\overset{\triangle}{\boldsymbol{\sigma}}$ is the lower-convected derivative. These derivatives are the most popular ones for the formation of constitutive equations and are used for all the models we will consider.

Now we have two frame invariant derivatives of the stress tensor, we can form a physically plausible constitutive equation. Returning to the linear Maxwell model (1.19), if we use the upper-convected derivative for the stress tensor we obtain the upper-convected Maxwell model (the UCM model),

$$\boldsymbol{\tau}_p + \lambda \overset{\triangledown}{\boldsymbol{\tau}}_p = \eta_p \dot{\boldsymbol{\gamma}} , \tag{1.22}$$

where $\lambda = \eta_p / G$ is the Maxwell or polymer relaxation time, $\eta_p$ is the polymer viscosity, and $G$ is the elastic modulus. The corresponding model using the lower-convected derivative does not fit with experimental observations and so is not usually used. If we add a Newtonian solvent to the UCM model we obtain the Oldroyd-B model with the Cauchy stress given by $\boldsymbol{\sigma} = -p\mathbb{I} + \eta_s \dot{\boldsymbol{\gamma}} + \boldsymbol{\tau}_p$. The Newtonian component can be thought of as the solvent for a polymer solution. The Oldroyd-B model in full is then,

$$\begin{aligned}
&\rho \left[ \frac{\partial \mathbf{v}}{\partial t} + \mathbf{v} \cdot \nabla \mathbf{v} \right] = -\nabla p + \eta_s \nabla^2 \mathbf{v} + \nabla \cdot \boldsymbol{\tau} \\
&\nabla \cdot \mathbf{v} = 0 \\
&\boldsymbol{\tau} + \lambda \left[ \frac{\partial \boldsymbol{\tau}}{\partial t} + \mathbf{v} \cdot \nabla \boldsymbol{\tau} - (\nabla \mathbf{v})^T \cdot \boldsymbol{\tau} - \boldsymbol{\tau} \cdot (\nabla \mathbf{v}) \right] = \eta_p \left( (\nabla \mathbf{v})^T + \nabla \mathbf{v} \right) .
\end{aligned} \tag{1.23}$$

There are other possible viscoelastic models, such as the Gisekus and Phan-Thien-Tanner models which involve adding extra terms nonlinear in $\boldsymbol{\tau}_p$ to the UCM equation (1.22). However we are primarily concerned with the Oldroyd-B model, and the FENE-P model, which we will motivate shortly.

There is another approach to constructing constitutive models using the microscopic dynamics of their constituents. The UCM model can be obtained from considerations of small dumbbells suspended in a fluid, with a spring between the ends. This approach leads to the same equations and provides an intuition for the sources of the some the

terms. A derivation of this approach can be found in [5, 7]. The dumbbell model is a way of representing on the microscale the behaviour of a viscoelastic fluids, similar to the sense in which phonons represent vibrations on a lattice. In fact, the microscale may look nothing at all like dumbbells. All that we can show is that the average behaviour of a continuum of polymers is like the average behaviour of many dumbbells.

A benefit of this way of thinking is that it allows us to see the connections between various viscoelastic models. As we will now see, simple changes to the spring force between the dumbbells lead to a more realistic model. $\mathbf{R}$ is the end-to-end vector along the dumbbell. We can write a dumbbell model in terms of a dimensionless form of $\langle \mathbf{RR} \rangle$ (the thermodynamic average of the outer product of $\mathbf{R}$ with itself), known as the conformation tensor, $\mathbf{C}$,

$$\boldsymbol{\tau}_p + \left[ \frac{\partial \mathbf{C}}{\partial t} + \mathbf{v} \cdot \nabla \mathbf{C} - (\nabla \mathbf{v})^T \cdot \mathbf{C} - \mathbf{C} \cdot (\nabla \mathbf{v}) \right] = 0 \,. \tag{1.24}$$

The relationship between the stress and $\mathbf{C}$ can be adjusted independently of the conformation equation, this is similar to changing the spring force between the dumbbells. For the UCM model this is,

$$\boldsymbol{\tau}_p = \frac{1}{\lambda} \left( \mathbf{C} - \mathbb{I} \right) \,. \tag{1.25}$$

One of the limitations of the UCM and Oldroyd-B models is that Hookean springs have infinite length, and so generate very large forces for large separations. In reality, the polymeric fluid gets stiffer as it is extended further until the macromolecules in the fluid reach their maximum extension. From the definition of the conformation tensor we know that the eigenvalues of $\mathbf{C}$ are the squares of the lengths of the principal axes, $R_1^2, R_2^2, R_3^2$. Therefore, the square of the length of the dumbbell is given by $\mathrm{Tr}(\mathbf{C})$. A spring force which saturates at the maximum length of a dumbbell generates a Finite Extensibility Non-linearly Elastic (FENE) model. For example the FENE-P model is given by,

$$\boldsymbol{\tau}_p = \frac{1}{\lambda} \frac{\mathbf{C} - \mathbb{I}}{1 - \frac{Tr(\mathbf{C})}{\ell^2}} \,, \tag{1.26}$$

where $L^2$ is a measure of the maximum extension length of a polymer molecule in the fluid. The stress in the FENE-P model fluid is reduced for large shear rates, therefore it also includes the effects of shear-thinning as well as stress memory and anisotropy. This makes it a useful model to measure the importance of shear thinning relative to elastic effects.

The conformation tensor also allows us to appreciate a related issue in the analysis

of these equations. We know that the eigenvalues of $\mathbf{C}$ give the squared length in the principal directions. Therefore negative eigenvalues of $\mathbf{C}$ must be unphysical, since this corresponds to imaginary end-to-end vectors $\mathbf{R}$. This is equivalent to requiring that the conformation tensor is positive semi-definite at all times. For many models (including the Oldroyd-B) it has been shown that if the equations start with an initial positive semi-definite state, the state will not evolve to become unphysical. In this thesis we deal with numerical methods and their associated errors, which can lead to a simulation becoming unphysical. To prevent this, we check all numerical results to ensure that they are positive semi-definite.

Finally we non-dimensionalise the Oldroyd-B model, just as we did with the Navier-Stokes equations. To do this, we identify some dimensionless groups for the stress and an extra dimensionless number, the Weissenberg number, which is the shear rate times the relaxation time of the polymers,

$$Wi = \lambda \frac{U}{L}\,, \tag{1.27}$$

and the Reynolds number now contains the total viscosity, $Re = \frac{\rho LU}{\eta_p+\eta_s}$. We use equations similar to (1.14) with $U = L/T$ for some length and time scales $L$ and $T$:

$$\begin{aligned}
&\tilde{\mathbf{x}} = \mathbf{x}/L\,, \quad \tilde{\mathbf{u}} = \mathbf{u}/U\,, \quad \tilde{t} = t/T\,,\\
&\tilde{p} = p\frac{L}{(\eta_p+\eta_s)U}\,, \quad \tilde{\mathbf{f}} = \mathbf{f}\frac{L^2}{(\eta_p+\eta_s)U}\,, \quad \tilde{\boldsymbol{\tau}}_p = \frac{L}{\eta_p U}\boldsymbol{\tau}_p\,,\\
&\beta = \eta_s/(\eta_s+\eta_p)\,.
\end{aligned} \tag{1.28}$$

When substituted into the Oldroyd-B equations (1.23), we obtain,

$$\begin{aligned}
&Re\left[\frac{\partial \mathbf{v}}{\partial t} + \mathbf{v}\cdot\nabla\mathbf{v}\right] = -\nabla p + \beta\nabla^2\mathbf{v} + (1-\beta)\nabla\cdot\boldsymbol{\tau} + \mathbf{f}\\
&\nabla\cdot\mathbf{v} = 0\\
&\boldsymbol{\tau} + Wi\left[\frac{\partial \boldsymbol{\tau}}{\partial t} + \mathbf{v}\cdot\nabla\boldsymbol{\tau} - (\nabla\mathbf{v})^T\cdot\boldsymbol{\tau} - \boldsymbol{\tau}\cdot(\nabla\mathbf{v})\right] = (\nabla\mathbf{v})^T + \nabla\mathbf{v}\,.
\end{aligned} \tag{1.29}$$

### 1.1.3 Elastically driven instabilities

Now we return to the interesting effects that have been observed in viscoelastic fluids at low Reynolds number in section 1.1.1. First, we consider the Weissenberg effect of Fig. 1.1b, and try to understand why the fluid climbs the rotating rod. Then we consider how this mechanism causes instability in other flows with curved streamlines,

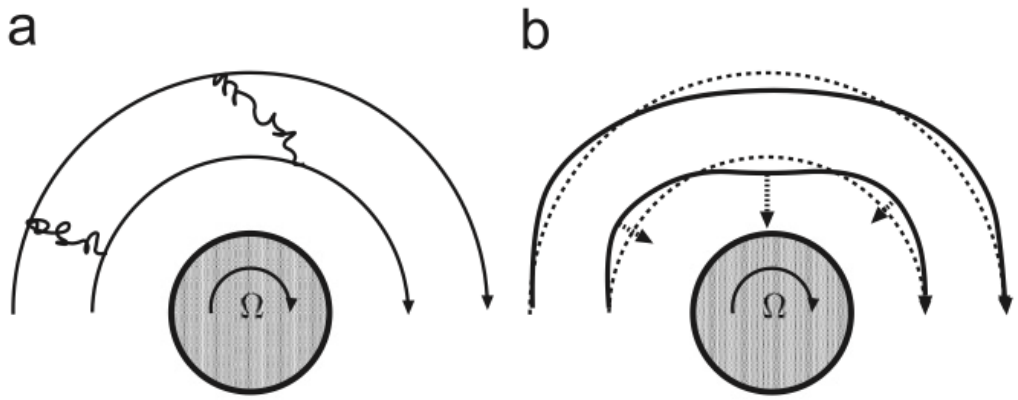


Figure 1.3: Sketch of the Weissenberg or normal stress effect and instability, produced with permission from [8]. a) The differences in velocity cause the polymer on the left to be reoriented to look more like the polymer on the right. This leads to a hoop stress along the streamlines, around the rod. These hoop stresses pull the fluid inwards towards the rod. b) fluid further from the rod experiences a smaller hoop stress and is drawn towards the rod more weakly than fluid closer to the rod. A small perturbation to the streamlines will be amplified and so the flow is unstable.

before examining the other types of instability possible in purely elastic flows.

### Flows with curved streamlines

Imagine a dumbbell in the flow around a rotating rod (Fig. 1.3). Shear rotates and stretches the dumbbell such that it lies along a streamline. This creates an anisotropic stress, with more polymeric stress along a streamline than perpendicular to it. In the Weissenberg effect both the streamlines and therefore the stretched dumbbells, encircle the rod. The stresses from the dumbbells lead to stresses along the streamlines (known as hoop stresses), which act to pull fluid inwards strangling the rod. If there is no solid upper boundary the flow inwards climbs the rod.

A similar mechanism to the one that causes the rod-climbing can cause an instability. First, recall that the shear rate closer to the rod is larger and the hoop stresses are stronger. Consider a small, wavy displacement of the streamlines — fluid moves either closer or further from the rod relative to the laminar flow. The fluid closer to the rod experiences greater shear and a stronger hoop stress pulling it even closer to the rod, however, the fluid furthest from the rod feels a weaker hoop stress. The relative magnitude of the hoop stresses is shown by the arrows in Fig. 1.3. We can see that a wavy displacement will become more wavy, the perturbation to the streamlines will be magnified, and so flow is unstable. The appropriate measure for the strength of

the Weissenberg effect is the first normal stress difference: the difference between the streamwise and wall normal stresses. In this case we use a cylindrical coordinate system centred on the rod and so the first normal stress difference is given by $N_1 = \tau_{\theta\theta} - \tau_{rr}$.

Many other curved streamline flows can exhibit the same instability. For example the flow between two counter-rotating cylinders, Taylor-Couette flow, is also unstable at low Reynolds number and high Weissenberg number. This has been shown both experimentally and numerically [1, 9]. This instability is subcritical, meaning there is a sudden transition from the laminar flow to a new, more complex flow state [10]. This new state consists of a stack of vortices between the cylinders. Numerical studies predict that the vortices are wavy in the azimuthal direction [11–13], while experiments usually find axisymmetric ones close to the instability [1, 10]. However this discrepancy is thought to be due to viscous heating of the polymer solutions in the experiments [10]. Two more examples of purely elastic instability can be seen in cone-plate [14] and plate-plate [15] flows. For this experimental setup, a lower disk is held stationary while an upper coaxial disk (or cone) rotates at a constant speed. This provides a shear across the elastic fluid lying between the two plates. Byars et al. [16] discovered spiral patterns in the flow of a viscoelastic fluid between two plates. Öztekin and Brown [17] used the Oldroyd-B model to do a linear stability analysis on this system and found that these flow patterns bifurcate from the laminar state. All three of these instabilities, plate-plate, cone-plate and Taylor-Couette, can be predicted using the Oldroyd-B model and seen experimentally with a fluid that is not shear-thinning. This suggests that they are all caused by the normal stress mechanism.

Pakdel and McKinley have suggested a measure for the linear stability of curved flows due to the normal stress mechanism [18], $M$. This number takes into account both the streamline curvature and the elasticity of the polymers in a single condition. Morozov and van Saarloos [8] re-expressed this number as

$$M = \frac{\lambda U}{R} \frac{N_1}{\tau_{p,shear}}, \tag{1.30}$$

where $\lambda U$ is the lengthscale for the relaxation of the polymers in a flow with velocity scale $U$. $\tau_{p,shear}$ is the relevant component of the polymer stress which gives the shear rate - in the Weissenberg effect this would be $\tau_{r\theta}$. $R$ is the total curvature so that $1/R = a/L + b/H$ where $L$ and $H$ are length scales of the flow and $a$ and $b$ are unknown constants. Although the constants $a$ and $b$ are fitting parameters, this conditions shows that there is simple relationship between streamline curvature, normal stress and stability. For all of the above scenarios, the flow is unstable when $M > 4 - 6$ [18]. This Pakdel-McKinley condition for instability captures the normal stress effect in any flow with curved streamlines. However, as we shall see, other viscoelastic flows can also

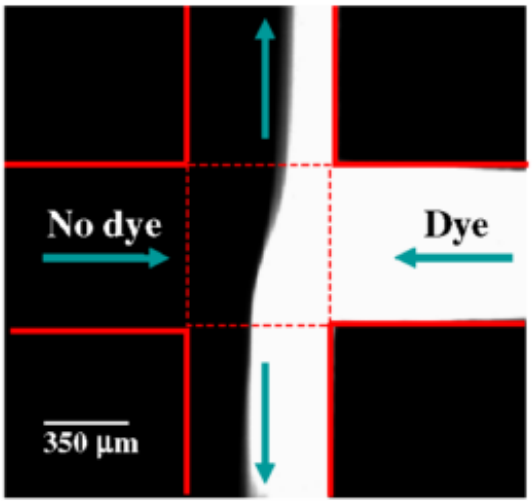


Figure 1.4: An experimental realisation of the extensional instability in a cross-slot device at high Weissenberg number. Fluid enters in opposing jets from the left and right hand sides and flows out of the top and bottom of the device. In this image, half the flow is dyed and the instability of the interface between the jets is visible. Reproduced with permission from [23].

be unstable.

### Parallel shear flows

Parallel shear flows have no streamline curvature in their laminar flows, meaning that the Pakdel-McKinley condition does not apply. So far, numerical and analytical studies have ruled out the low Reynolds number linear instability of plane Poiseuille flow [19] (the flow between parallel plates) and of plane Couette flow [20] (the same flow, but with the plates moving in opposite directions). However, there is some evidence to suggest that these flows may still be unstable, but this will be addressed in the following section on purely elastic turbulence. Oscillatory flows can also become unstable to a purely elastic instability. Experiments on worm-like micelles in a pipe flow driven by an oscillating end wall show a transition to a vortical flow [21, 22]. The mechanism responsible for the instability is explored numerically in this thesis in Chapters 3 and 5.

### Extensional flows

Another kind of instability is present in flows where the fluid is highly stretched, known as extensional flows. The two canonical flows for these instabilities are the cross slot and four-roll mill (described in detail in Keller and Odell [24]). The four roll mill contains

4 rotating upright cylinders. The fluid is drawn into the device between the cylinders along one axis and expelled along the other. This creates a highly stretched region along the outflow axis. The cross-slot device uses opposing jets to achieve a similar flow. The jets meet in the centre of the device and fluid flows out of outlets to either side, making a cross shaped device (Fig. 1.4). Again, there is a strongly extensional flow along a line between the two outlets. Both flows align the polymers and stretch them, creating very large normal stress. The orientation of the polymers is visible in experiments as a birefringent line. For long enough polymer chains in solution the line is unstable and forms a birefringent cylinder [25]. The interface between the jets can also become unstable [23, 26]. For very elastic solutions there are also flaring events, where the aligned region suddenly spreads throughout most of the device before dying back to the birefringent line.

#### Layered flows of different fluids

Purely elastic instability can also occur in multi-layered flows, where the interface between the fluids can become unstable. This flow is important for processing of multi-layered plastic products and for thin-film coating flows. Chen [27, 28] performed long wavelength stability analysis of UCM pipe and Couette flow demonstrating that these flows shows elastic instability. Su and Khomami look at the corresponding instability of two fluids under plane Poiseuille flow with the Oldroyd-B model [29], and converging channel flow with a power law shear thinning Oldroyd-B model [30]. Ganpule and Khomami [31] used four models, UCM, multimode Gisekus, Gisekus and modified PTT and repeated both the long and short wave linear stability analyses for a three layer channel flow. They also compare all their results to the experiments of [32]. Hinch et al. [33] provide a general understanding of the mechanism behind the pipe elastic stratification instability of [27, 34]. They look for an arbitrary constitutive model and show that jumps in the first normal stress difference can cause this instability.

### 1.1.4 Purely elastic turbulence

The presence of purely elastic instabilities at low $Re$ and high $Wi$ naturally leads us to ask whether, by analogy with Newtonian turbulence, there is a turbulent state at sufficiently high $Wi$. In fact there is now evidence of purely elastic turbulence in many different flows. It is believed that this turbulence is caused by and sustained by some of the effects identified above, particularly the normal stress effect. This is an entirely viscoelastic phenomenon, and does not show dependence on $Re$ provided it is low. The Weissenberg number $Wi$ is the relevant control parameter for the onset of purely elastic turbulence - at low $Wi$ the flow is laminar and as $Wi$ increases the flow becomes more

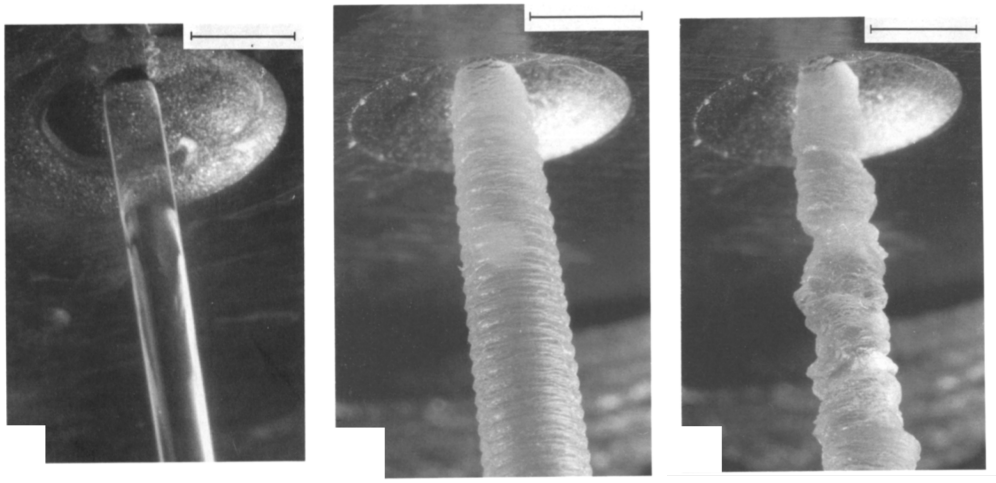

(a) (b) (c)

Figure 1.5: a) The laminar flow of a polymer extrudate. b) The sharkskin state. At high flow rates the surface of the extrudate becomes rough with regular grooves. c) Melt fracture. At very high flow rates the extrudate becomes very rough and the surface appears chaotic. The scale bars in the top right indicate $1mm$. These images are reproduced with permission from Piau et al. [36].

complex before entering a disordered state reminiscent of Newtonian turbulence. Larson has called this phenomenon turbulence without inertia [35] because the turbulence is brought about by elastic effects in the fluid when the inertial effects usually responsible for turbulence have been minimised.

It is difficult to perform experiments to explore purely elastic turbulence because both small channels and long chain polymers are needed to reach the correct $Re$ and $Wi$. This makes it very difficult to visualise the flow. However, one scenario where purely elastic turbulence may be of industrial relevance is in the extrusion of polymers through a narrow die (Fig. 1.5a). At high $Wi$ this experiment results in a surface roughness of the polymer extrudate known as sharkskin (see Fig. 1.5b). At even higher $Wi$ the extrudate surface becomes very irregular, known as gross fracture (Fig. 1.5c). Many mechanisms for these instabilities are suggested [37], including stick and slip of the polymeric fluid at the wall and shear banding instabilities. However, there is reason to believe that sharkskin is due to a flow instability and that gross fracture is due to purely elastic turbulence [8, 38].

Following the identification of the viscoelastic flow instabilities above, Groisman and Steinberg [39] found elastic turbulence in a plate-plate flow. They used a low Reynolds number ($Re \sim 1$) and a high Weissenberg number $Wi \sim 10$. At first they observed spiral flow patterns [16], but as they raised the rotation rate these structures disappeared and the flow became turbulent. The resulting flow is shown in Fig. 1.6. They took

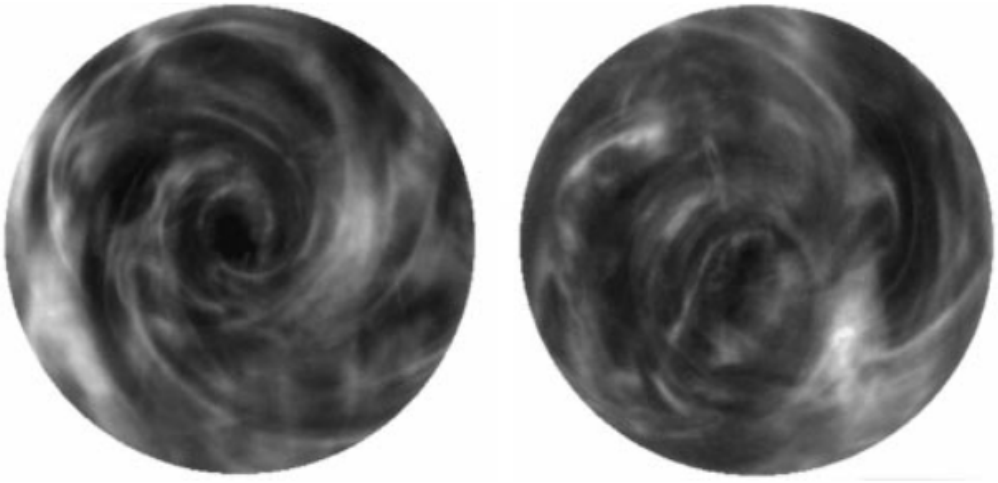

Figure 1.6: Images of light reflecting flakes in an elastically turbulent plate-plate flow at $Wi = 13, Re = 0.7$. Image reproduced with permission from [39].

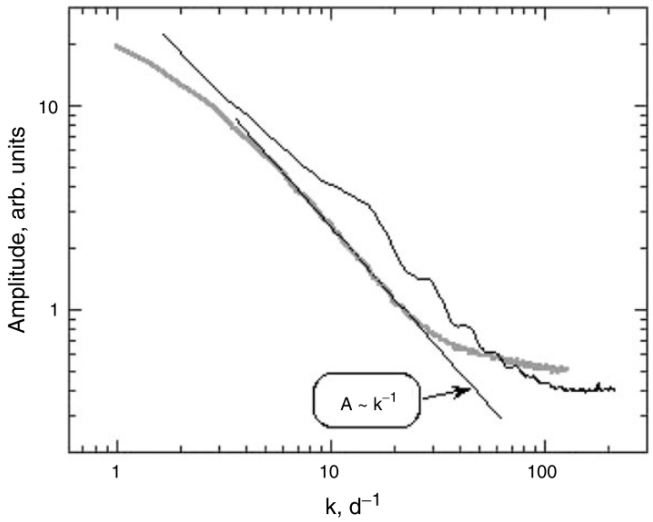


Figure 1.7: The Fourier transform of the brightness along the diameter (black line) and the circumference (grey line). The amplitude falls away $\sim k^{-1}$, which suggests that energy is dissipated at the small scales in purely elastic turbulence, similar to the cascade seen in Newtonian turbulence. Image reproduced with permission from [39].

the Fourier transform of the flow and identified a turbulent cascade of energy, just as in Newtonian flows, from the large structures to the small structures (Fig. 1.7). Since then purely elastic turbulence has been discovered in a few other flows. For example, experiments on purely elastic pipe Poiseuille flow show evidence of a turbulent state [40]. This state shows hysteresis, which suggests that this is the (previously predicted [41]) subcritical bifurcation from infinity scenario for the transition, discussed later in the introduction.

So far we have considered purely elastic turbulence as distinct from Newtonian turbulence. However, there is a third, intermediate state between these two when the Reynolds number is not negligible but $Wi$ is still very high, known as elasto-inertial turbulence (EIT). This state seems to have a different structure again to either purely elastic or Newtonian turbulence and has been observed in both pipe flows and numerical simulations [42, 43].

## 1.2 The transition to inertial turbulence

The transition to turbulence in Newtonian flows has been studied since the late $19^{th}$ century, beginning with Helmholtz, Kelvin and Rayleigh and linear stability analysis of the Navier-Stokes equations. Linear stability analysis starts from a laminar flow and adds an infinitesimal perturbation. The resulting equations can be linearised so that we can assume a Fourier form for the perturbation $\sim \mathrm{e}^{i\mathbf{k}\cdot\mathbf{x}+\lambda t}$. When this perturbation grows in time, the laminar flow is unstable, and must transition to a different state which may be turbulent. We label the Reynolds number at the onset of unconditional instability $Re_{ls}$. Near to $Re_{ls}$, the bifurcation due to the instability may be either subcritical or supercritical. If the flow is supercritical then the non-laminar state grows continuously after $Re_{ls}$, as shown in Fig. 1.8a. If the transition is subcritical then the flow jumps discontinuously at $Re_{ls}$ to the non-laminar state and this state is accessible from some lower Reynolds number $Re_{sn}$, as shown in Fig. 1.8b.

Unfortunately this approach using states local to the laminar flow state in phase space has been of limited use in understanding the transition to turbulence. Often the flow transitions by jumping to structures that differ greatly from the laminar flow: ones which are both not local to the laminar flow in phase space, and not connected by simple subcritical or supercritical bifurcations. For many flows there is no linear instability of the laminar flow and no finite $Re_{ls}$. Even flows where $Re_{ls}$ has been calculated, turbulence has been shown to set in at much lower $Re$. A recent review of the transition to turbulence can be found in Manneville [44].

In Figs 1.8a and 1.8b we characterised the transition using a single parameter $A$, the amplitude of some fairly simple wavy perturbation to the laminar flow. In general,

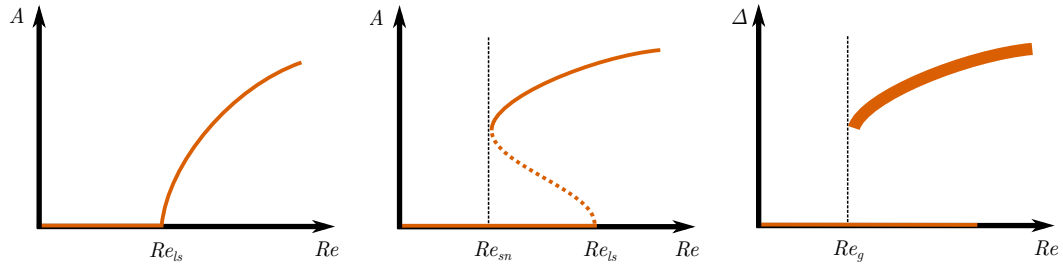


(a) (b) (c)

Figure 1.8: Kinds of bifurcation. a) A local super-critical transition. $A$ is the amplitude of a wavy perturbation to the laminar flow. At low $Re$ the flow is laminar, but at $Re_{ls}$ the flow begins a smooth transition to a non-laminar flow. b) A local sub-critical transition. At $Re_{ls}$ the flow suddenly jumps to a distant non-laminar flow state. This state is accessible via a finite-size perturbation for $Re > Re_{sn}$. c) A global bifurcation. $\Delta$ represents some measure of the velocity fluctuations not present in the laminar flow. At long times, the flow is always laminar below $Re_g$. Above $Re_g$ finite size perturbations will transition the flow to a non-laminar flow state which may be unstable and lead to turbulence. At sufficiently high $Re$ there may be a stable laminar solution or not depending on the particular flow. This figure is inspired by the illustrations in [44].

the transition may be more complex than this and we use the kinetic energy of the non-laminar flow, for example, to characterise the transition. There are three kinds of transition we consider in this thesis: the supercritical and subcritical bifurcations (Figs 1.8a and 1.8b), and the globally subcritical scenario of Fig. 1.8c. This scenario involves a sudden transition to turbulence without any connection to the linear stability of the laminar flow. Real flows can have any of these behaviours. The mixing layer, where a high speed flow meets a slower flow directly after a splitter plate, is an example of locally supercritical transition [45]. Other examples include the breakdown of a jet and the wake of a bluff body [44]. These flows all contain a Kelvin-Helmholtz like instability, the instability between two laminar regions of fluid with a sudden jump in velocity [45]. Examples of locally subcritical transition are given by the formation of Tollmien-Schlichting waves in plane Poiseuille flow (PPF, the pressure driven flow between parallel plates) [46, 47], Blasius Boundary layer flow (BBL, the flow over a flat plate) and the Asymptotic Suction Boundary Layer flow (ASBL, the flow over a flat plate with uniform suction to remove spatial dependence of the laminar flow) [48, 49]. A review of Tollmien-Schlichting waves (TS waves) can be found in Schmid and Henningson [50]. There are also flows where there is no linear stability of the base flow at all ($Re_{ls} = \infty$), for example, Plane Couette Flow (PCF, the flow between parallel plates moving in opposite directions) [51] and Hagen-Poiseuille flow (HPF, the pressure driven flow in a pipe) [52, 53].

As we shall see, even the flows with a linear instability can become turbulent for $Re << Re_{ls}$. In PPF, $Re_{ls} = 5772$ [46] and yet experiments reveal localised turbulent spots for $Re \simeq 1000$ and simulations can find weakly turbulent banded flows as low as $Re \simeq 500$ [54, 55]. To understand the transition to turbulence, we are interested in finding the lowest Reynolds number where turbulence is possible, $Re_g$. In the following sections we will look at the techniques used to identify $Re_g$ and perturbations to a flow which will make it turbulent. We will examine how this number relates to fixed points and periodic solutions to the Navier-Stokes equations, known as Exact Coherent Structures (ECS) and briefly review the state of the art in using these structures to model the onset of turbulence borrowing the concept of universality as used in statistical mechanics.

### 1.2.1 The transition to turbulence for a linearly unstable flow

The first attempts at characterising the transition to turbulence considered infinitesimal perturbations to the laminar flow. We ignore terms quadratic in the perturbation to obtain a linear set of equations and express the space and time dependence of a flow in terms of complex Fourier modes in the unbounded directions. For a flow in a channel this gives,

$$g(x, y, z) = \hat{g}(y)\mathrm{e}^{i(k_x x + k_z z) + \lambda t}\,, \tag{1.31}$$

where $g$ is any scalar flow variable, $v_i$ or $p$. We choose the coordinate system so that the no-slip boundary conditions are in the $y$ direction, with the other directions periodic. $\hat{g}(y)$ is the $y$-dependence of the eigenfunction. Substitution of (1.31) into the Navier-Stokes equations (1.15) and linearising gives a linear problem for $\hat{v}_i, \hat{p}$ and $\lambda$ given $k_x, k_z$ and $Re$. Unstable perturbations occur where $\mathrm{Re}(\lambda) > 0$ and the eigenfunctions are given by the real parts of the complex disturbances, $\mathrm{Re}(g(x, y, z))$.

If the instability leads smoothly into a new stable state after $Re_{ls}$, as in Fig. 1.8a, the flow is undergoing a supercritical bifurcation. An example of this kind of instability can be seen in the mixing layer, where the interface between the two initially laminar layers becomes wavy via a Kelvin-Helmholtz instability. As the Reynolds number increases the state rapidly gets more complicated, however, for $Re$ close to $Re_{ls}$ the bifurcation is supercritical.

#### 2D flows and Squire's theorem

Linear stability analysis becomes much more powerful when combined with Squire's theorem [56]. This mathematical theorem states that for a one dimensional, laminar

base flow which depends only on the wall-normal direction ($\big(U(y),0,0\big)^T$) there is a 2-dimensional instability (dependent on $x$ and $y$) that sets in at lower $Re$ than any 3-dimensional instability. The proof of Squire's theorem also identifies a transformation that relates the $Re$ of the three dimensional instability to that of the two dimensional one,

$$Re_{2D} = \frac{k_x}{\sqrt{k_x^2 + k_z^2}} Re_{3D}\,. \tag{1.32}$$

The theorem also holds for viscoelastic fluids including the UCM [57] and Oldroyd-B models [58]. The Squire transformation for the Weissenberg number is given by,

$$Wi_{2D} = \frac{k_x}{\sqrt{k_x^2 + k_z^2}} Wi_{3D}\,, \tag{1.33}$$

and the transformation for the Reynolds number is the same as for the Newtonian case.

This transformation ensures that to find $Re_{ls}$ and $Wi_{ls}$ for any parallel laminar flow it is enough to only consider two dimensional disturbances. In this thesis we use this result to consider only two dimensional disturbances where possible (Chapters 2, 3 and 5).

### 1.2.2 Subcritical instabilities

In the previous section we considered the critical Reynolds number, $Re_{ls}$, beyond which a laminar flow is unstable for infinitesimal perturbations. We discussed the case of a smooth transition from laminar to non-laminar flow in the mixing layer. In real linearly unstable flows, turbulence often sets in long before $Re_{ls}$. Under carefully controlled experimental conditions it is possible to obtain a laminar flow close to $Re_{ls}$. But Reynolds numbers beyond this point the steady state behaviour of the flow jumps to a new state, very different from the laminar flow. Transitions where there is a sudden change in the flow are subcritical and display hysteresis: on reducing the Reynolds number, the laminar flow only reappears at $Re < Re_{ls}$.

To investigate subcritical instabilities linear stability analysis is not enough. Instead, we try to identify the state that the laminar flow jumps to for $Re > Re_{sn}$, and the Reynolds number of its onset. For plane Poiseuille flow, the pressure driven flow between two infinite plates, there is a subcritical linear instability at $Re_{ls} = 5772$ [46]. It is possible to use the eigenfunctions for this linear instability as a guess to a non-laminar solution to the Navier-Stokes equations near to $Re_{ls}$. This guess is combined with a numerical nonlinear PDE solver method, such as the Newton-Raphson method of Appendix A.2.2, to find a solution. Using numerical methods, it is possible to track

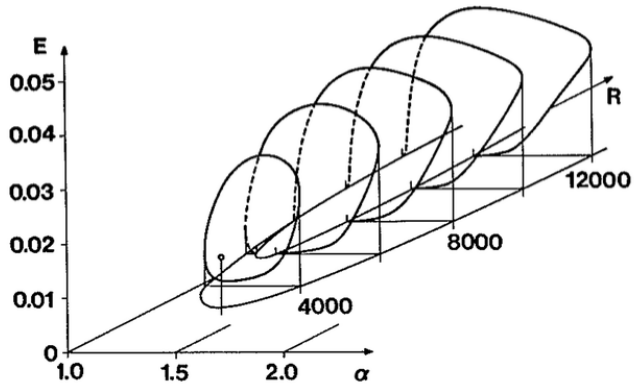


Figure 1.9: The bifurcation of TS waves from the laminar flow. The vertical, energy axis uses the energy of the first Fourier mode, the axis into the page is for $Re$, and the horizontal axis is the streamwise wavenumber, $k_x$. Reproduced with permission from [59].

this unstable solution back to a minimum Reynolds number, where it emerges in a saddle-node bifurcation at $Re_{sn} = 2935$ [47, 59] (Fig. 1.9). The upper branch of this bifurcation corresponds to a solution which is stable in 2D, consisting of travelling waves propagating down the channel known as Tollmein-Schlichting (TS) waves.

We would hope that the onset of Tollmein-Schlichting waves and similar states which bifurcate from the base flow would tell us the $Re$ for the transition to turbulence in Plane Poiseuille flow, however, experiments reveal 3-dimensional turbulent spots at much lower Reynolds number ($Re \simeq 1000$) [60]. This suggests that in plane Poiseuille flow a different, 3D state to the 2D TS waves is responsible for the transition to turbulence, one that is not connected to the laminar flow by linear stability at all. We consider situations like this one in the next section.

### 1.2.3 The bypass transition to turbulence

Sometimes the flow is linearly stable for all $Re$, and sometimes the linear instability is not connected to the transition to turbulence, as in plane Poiseuille flow. These flows still become turbulent, but the onset of turbulence depends on the amplitude of the perturbation to the flow. For example, the pressure driven flow in a pipe (Hagen-Poiseuille flow) is linearly stable at all $Re$, yet turbulence sets in by $Re \sim 2040$ [61] and

turbulent regions, known as puffs, are excitable at much lower Reynolds numbers. We want to predict the lowest $Re$ where turbulence is possible, $Re_g$, and the amplitude and form of the perturbations which lead to turbulence.

Numerical studies determined that Newtonian plane Couette flow was stable for all infinitesimal perturbations of the flow at all Reynolds numbers [62]. However, experimental observations show that plane Couette flow is turbulent from about $Re \sim 400$ [63]. To resolve this mismatch, we must go beyond linear stability and consider finite-size perturbations to the flow. A transition due to a finite-size perturbations is sometimes called a bypass transition, because it bypasses the linear instability. We do this by calculating new exact coherent structures which are not connected to the laminar flow by linear instability. These exact coherent structures are non-laminar solutions to the equations of motion (the Navier-Stokes equations).

## 1.3 Exact coherent structures and turbulence

Exact coherent structures (ECS) are recurring patterns in a flow. They are observed in simulations and experiments of flows near transition to turbulence and can be time dependent or stationary. We can view the equations of motion for a fluid flow, (1.15), as a dynamical system, $\dot{\mathbf{x}} = F(\mathbf{x})$, where $\mathbf{x}$ is a vector containing all the flow variables $(\mathbf{v}, p)$ and $F$ includes the boundary conditions. Exact coherent structures correspond to exact solutions of this system. Although we call them exact, these solutions must be obtained numerically and so the phase space $\{\mathbf{x}\}$ is of very large but finite dimension. If the pattern is time-dependent it might be a periodic orbit or a travelling wave solution, and if the pattern is time-independent then the solution is a very high dimensional fixed point. We think of turbulence as being constructed from these exact solutions. Some solutions mark the boundary between laminar and turbulent regions of phase space, known as edge states. As such they determine the minimal size and shape of a perturbation required to trigger the transition to turbulence. Other solutions exist inside the turbulent region and give good approximations to the statistics of a turbulent flow. By finding these solutions we can predict the onset of turbulence and possibly manipulate a flow to delay the transition [64].

For a linearly stable laminar flow, it is difficult to know where to start to look for exact solutions. There are three main options available: the homotopy, direct numerical simulation, and body forcing strategies. The homotopy strategy starts from a known exact coherent structure in a related flow to the flow of interest. This exact solution is then continued by smoothly altering parameters until it can be connected with an ECS in the flow of interest. This approach was used to connect wavy vortices in Taylor Couette flow to plane Couette flow exact coherent structures [65]. In the

direct numerical solution strategy, one identifies an initial guess for an exact solution by considering many simulation runs of a turbulent flow close to transition. Careful analysis of simulation trajectories with different sized domains can reveal recurring or time-independent structures. This strategy has been used in plane Couette flow to find periodic exact coherent structures [66]. For the body forcing strategy, one forces the equations so as to introduce a linear instability and a new, non-laminar, solution. The forcing is then carefully reduced to track this new solution to the original unforced flow. This strategy relies on choosing a forcing that generates a flow similar to an exact coherent structure. One of the ways of identifying this forcing is through transient growth analysis, which we discuss next.

Even for linearly stable flows, we can identify perturbations which grow transiently at short times before they exponentially decay. These perturbations are more likely to lead to turbulence. The transient growth of perturbations is due to the non-normality of the linear operator. This makes the eigenmodes far from orthogonal, even though they are linearly independent. The eigendecomposition for a perturbation can contain large contributions from multiple eigenmodes. This leads to a long initial transient while the perturbation rotates into a single eigenmode and begins to decay [67]. For high enough $Re$ initial transient growth of this kind can make the size of a perturbation large enough so that nonlinear effects come into play, and linear stability analysis is not sufficient. We can use the most non-normally amplified perturbations for the body forcing in the body forcing strategy, thereby using structures that we know are important to the stability of the flow to find exact coherent structures. In the next section, we will examine in more detail how this strategy was used to find exact coherent structures in plane Couette flow [68], but first we consider exact coherent structures more generally.

Initially, exact coherent structures were sought by employing the smallest number of degrees of freedom possible. This approach begins with the discovery of the minimal flow unit, the smallest periodic domain in a flow that can sustain a non-laminar solution to the equations of motion. For example, in plane Couette flow the minimal flow unit is approximately $1.75\pi L \times 2L \times 1.2\pi L$ in the streamwise, wall-normal and spanwise directions, where $L$ is half the distance between the plates. It turns out that restricting the domain using periodic boundary conditions makes it much easier to find an ECS. Early efforts to identify the minimal flow unit in plane Couette flow used simulations [69, 70] and lead to the ECS of Waleffe [71], as we shall see in section 1.3.2.

The minimal flow unit identifies the mechanisms which trigger the transition to turbulence. For Newtonian fluids, this is the presence of streamwise vortices in mean shear flow, which we discuss in more detail below. The full state space of minimal flow unit plane Couette solutions has now been explored [72]. For pressure driven pipe flow (Hagen-Poiseuille), experiments have managed to identify minimal flow unit ECS seen

in simulations [73]. Although the minimal flow unit solutions are qualitatively useful, they do not provide accurate predictions of $Re_g$, the lowest Reynolds number for the existence of turbulence. Turbulence tends to set in lower than that suggested by these solutions, with localised patches of turbulent flow coexisting with the laminar flow [44]. To predict the onset of patchy states like these we need to consider larger domains with exact coherent structures localised to small regions surrounded by laminar flow. Localised structures are often more complex than minimal flow unit structures and so more difficult to obtain. So far they have been identified for the asymptotic boundary layer [74], Hagen-Poiseuille flow [75], and plane Couette flow [76] and provide much better prediction of $Re_g$.

As well as knowing $Re_g$, we would like to know what is the form and strength of the perturbation that is required to trigger turbulence? The state that marks the boundary between the laminar and turbulent regimes is known as the edge state [77]. Knowing the edge state may provide a way to control the onset of turbulence. Forcing the flow so that the edge state is more difficult to reach may make the laminar flow more stable. This edge state gives the minimal perturbation to the laminar flow for a given Reynolds number required to trigger turbulence. These edge states have been discovered for the minimal flow unit solutions in Hagen-Poiseuille flow [78], Plane Couette flow [79] and the asymptotic suction boundary layer [80]. They have also been found in the same flows for localised structures [74–76].

The transition to turbulence usually begins with localised coherent structures, known as spots or puffs. These spots nucleate and merge until turbulence fills the entire flow. One objective in recent research has been to use the localised coherent structures we know about to obtain an analogue of thermodynamics for this process. Using small units (the size of the minimal flow unit) as the particles in this theory, the intention is to take the thermodynamic limit for many units and look at the spatio-temporal development of turbulence. Thermodynamic systems can show phase transitions where the order parameter jumps discontinuously at a critical point, known as a first order transition. Near criticality there is phase coexistence, similar to the coexistence of laminar and turbulent regions in a flow near the transition to turbulence. The correlations in the order parameter are scale-free and depend on a set of exponents. These exponents determine what is known as the universality class of the transition. All systems with the same symmetry of the order parameter and dimensions in physical space are in the same universality class and use the same exponents. One of the goals has been to identify the universality class of the transition to turbulence.

It has long been suggested that directed percolation would be a good fit for the universality class for turbulence [81, 82]. This possibility assumes that the important process is the spread of a turbulent region and that this process happens stochastically.

Turbulence spreads when the finite velocity disturbances in a turbulent spot are large enough to trigger turbulence in a neighbouring region. In this model, turbulence also has a probability to decay as well as spread. If all turbulence decays the flow reaches the absorbing state, the laminar flow. This problem belongs to the directed percolation universality class, which also includes epidemics and wildfires [83]. There are some recent experiments that support this view, for example, in Taylor Couette flow [84], and plane Poiseuille flow [85]. Similar to the directed percolation approach, cellular automata have been used to model the spread of turbulence. In pipe flow a deterministic model can reproduce some of the experimental behaviour near to transition [86]. A model of the asymptotic suction boundary layer inspired by directed percolation and including spot nucleation has been fitted using constants from a full numerical simulation [87].

### 1.3.1 Exact solutions in inertial plane Couette flow

Currently, there are no known coherent structures for purely elastic shear flows. To find them we will focus on the simple shear flows that were used to find some of the first inertial exact coherent structures, plane Poiseuille flow (PPF) and plane Couette flow (PCF). The latter is the flow between two parallel plates which are moving in opposite directions (shown later in the thesis in Fig. 6.1). In this section we will review the methods used to identify coherent structures in plane Couette flow with periodic boundary conditions. These methods serve as a guide in the search for purely elastic coherent structures where we will vary $Wi$ rather than $Re$.

The earliest approach to exact coherent structures in plane Couette flow started from structures obtained in Taylor Couette flow (flow between two counter-rotating cylinders as shown in Fig. 1.10a) and connected them to plane Couette flow [65]. The Taylor Couette flow is first considered in a rotating frame of reference. Taking the limit of large radius of curvature gives the Navier-Stokes equations with an additional Coriolis body force. When this force is large enough, the flow behaves like the Taylor-Couette flow and it is possible to recover the Taylor Vortex flow shown in Fig. 1.10a. These are vortices with their axes along the streamwise direction arranged spanwise across the channel. For large enough $Re$ these solutions become wavy in the azimuthal direction, a state known as wavy vortex flow [88]. Starting from wavy vortex flow Nagata steadily reduced the Coriolis force and solved for the flow using a Newton-Raphson method. When the Coriolis force is zero the problem corresponds to the plane Couette flow and the wavy, non-laminar solution is an exact coherent structure. This solution appear at about $Re \sim 450$ and is the same solution we discuss in the next section, where we explore the mechanism which sustains this ECS.

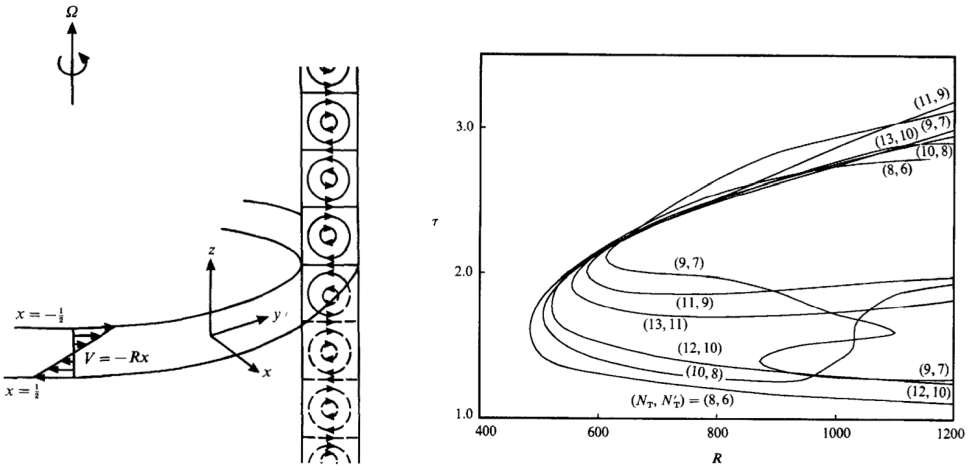


(a) (b)

Figure 1.10: a) Diagram of Taylor-Couette vortex flow in the system used by Nagata. Here $R$ is the Reynolds number. b) A bifurcation diagram which for the exact solutions at various numerical resolutions against the Reynolds number. $\tau$ is the momentum transport and $\tau = 1.0$ for the laminar flow solution. Images taken with permission from [65].

### 1.3.2 Waleffe's self sustaining process

The mechanism behind the minimal flow unit coherent structures has been explored in detail. This is sometimes called the vortex-wave interaction (after the analytical work of [89]), but here I refer to it as the self-sustaining process (SSP) after Waleffe [71]. The mechanism was identified by noticing a common structure in shear flows, known as streaks. Streaks are regions of slower or faster fluid than the mean flow, aligned parallel with the flow. They were discovered in the boundary layer flow over a surface [90]. These streaks were explained by streamwise oriented vortices that lift fluid up between them, creating spanwise fluctuations in the streamwise velocity [91, 92]. The vortices which produce the streaks are the most non-normally amplified structures in plane Couette flow. In plane Couette flow numerical simulations were used to identify the smallest possible periodic box that could contain coherent structures (the minimal flow unit) [70]. This minimal flow unit consists of a pair of streamwise vortices and a streak between them. Moffatt [93] provided a simple proof that streamwise vortices and streaks which depend only on the wall-normal ($y$) and spanwise ($z$) directions decay, leaving just the laminar flow. Waleffe [71] sought to identify the mechanism which sustains the vortices and streaks, and prevents them from decaying. He used a simpler plane Couette flow, with free-slip boundary conditions. He began by forcing the flow with streamwise vortices of the size suggested by the minimal flow unit of Hamilton

et al. [70]. Then he numerically calculated the streaks generated by the vortices, to give him all three components of the base flow, $U(y,z), V(y,z)$ and $W(y,z)$. He performed a linear stability analysis and found that the flow of streamwise vortices and streaks is mechanically unstable to a Kelvin-Helmholtz-like instability. Next he calculated the nonlinear terms in the Navier-Stokes equations due to the instability interacting with itself. These terms provide a forcing to the equations which regenerates the vortices. This is the self-sustaining process of Fig. 1.11: vortices generate streaks which are unstable and the instability regenerates the vortices. All these processes happen simultaneously so that the flow is self-sustaining. Waleffe [94] tracked this exact solution to unforced plane Couette flow by reducing the forcing and imposing no-slip boundary conditions. This solution is the same the solution found in [65].

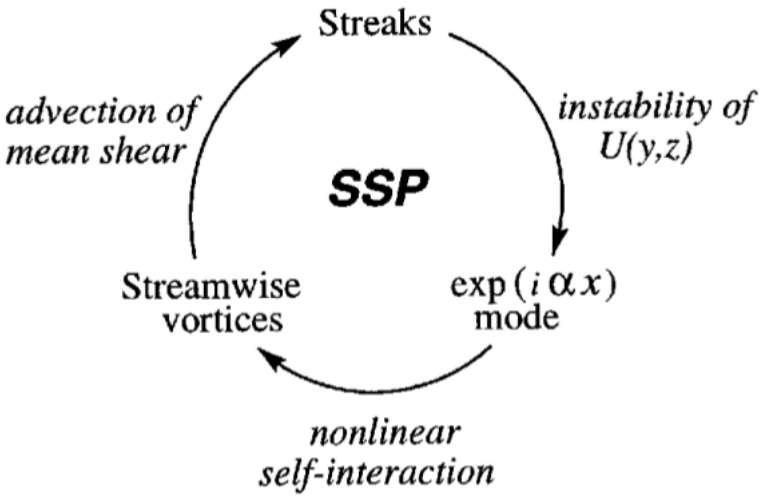


Figure 1.11: The self-sustaining cycle. Reproduced from Waleffe [95].

## 1.4 Outline of the research programme

During the introduction, we have seen that there exists a poorly understood state known as purely elastic turbulence. We have also seen that a nonlinear dynamics approach to turbulence — where we find numerically exact solutions to the equations of motion — is a fruitful way of understanding Newtonian turbulence. These solutions correspond to patterns in the flow called exact coherent structures (ECS), which are seen in flows near to transition, and which determine the onset of turbulence. It seems sensible then to investigate the extension of the Newtonian concepts and methods around exact coherent structures to see whether they also describe purely elastic turbulence. To do this, we start by replicating the first step on the road to Newtonian exact coherent

structures but for purely elastic flows: the calculation of an exact coherent state in a purely elastic turbulent flow. The research program of this thesis is primarily directed towards finding such an exact solution.

The exact coherent states found for Newtonian flows can be obtained in many ways (see, for example, Kawahara et al. [96] for a review). Here we consider two possible routes to exact coherent structures and attempt to replicate them for purely elastic fluids. The first route can work only if the exact solution connects to the laminar solution via a sequence of linear instabilities, however the second approach can be used when there is no linear instability of the base flow. Although there are no linear instabilities of either purely elastic plane Poiseuille or plane Couette flow, we will see that we can still make use of both the first and the second method to look for exact coherent structures.

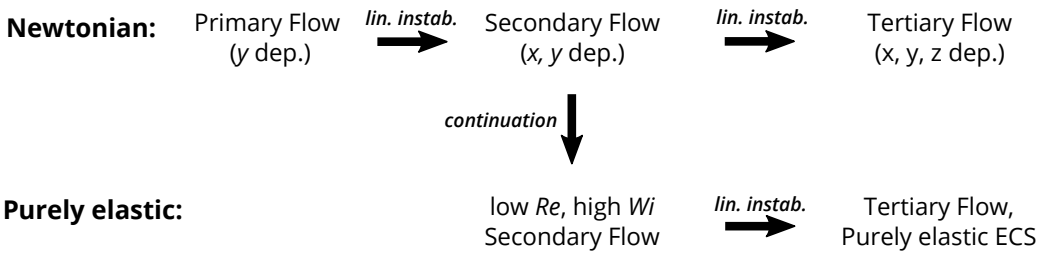


Figure 1.12: Diagram describing the research program for using a linear instability of the laminar flow of a Newtonian flow to find both Newtonian and purely elastic exact coherent structures (ECS). $x$, $y$ and $z$ are the streamwise, wall-normal and spanwise directions respectively.

The first approach we consider begins with a linear instability in a two-dimensional Poiseuille flow. As a consequence of Squire's theorem, this instability sets in at a lower Reynolds number than any linear instability of the three-dimensional flow. The aim is to find a connection between this linear instability and a 3D ECS via a series of bifurcations. For Newtonian flows, we begin with the linear instability of laminar plane Poiseuille flow at $Re = 5772$ [46]. This corresponds to the first linear instability in Fig. 1.12, where $x$, $y$ and $z$ are the streamwise, wall-normal and spanwise directions respectively. The Poiseuille flow instability connects to finite amplitude travelling waves [47] (the Newtonian secondary flow of Fig. 1.12). This secondary flow is dependent on the streamwise and wall-normal directions, but still not dependent on the spanwise direction, so it is not yet a full 3D exact solution. The next step for Newtonian fluids is to take these secondary solutions and examine their linear stability to perturbations in

$z$. This is the linear instability of the secondary flow in Fig. 1.12 carried out by Orszag and Patera [59]. In Newtonian fluids, the linear instability of the two-dimensional flow connects to a three-dimensional flow [97] (this is the Newtonian flow of Fig. 1.12) although it is presently unclear how this state connects to the ECS found via the self-sustaining process. Likely the connection between the two is indirect, possibly involving a region of state space at a much higher $Re$, where the flow is fully turbulent. In the Newtonian problem, the two-dimensional travelling wave flow is very different to the self-sustaining process ECS, however, this might not be true in the purely elastic case, where the mechanisms of instability are still not well understood.

We use this first approach to look for an ECS in purely elastic flows. There is a difficulty, since purely elastic plane Poiseuille flow is linearly stable for all Weissenberg numbers [19]. This means that there is no linear instability of the laminar flow for the first step in purely elastic fluids. Instead, we consider the secondary flow in the Newtonian problem and attempt to connect these solutions to low $Re$, high $Wi$ states by raising the Weissenberg number and then reducing the Reynolds number. The intention is to look at the linear instability of these two dimensional solutions to disturbances in the $z$ direction and see if we can obtain a purely elastic ECS. Our progress in this strategy is outlined in Chapter 2.

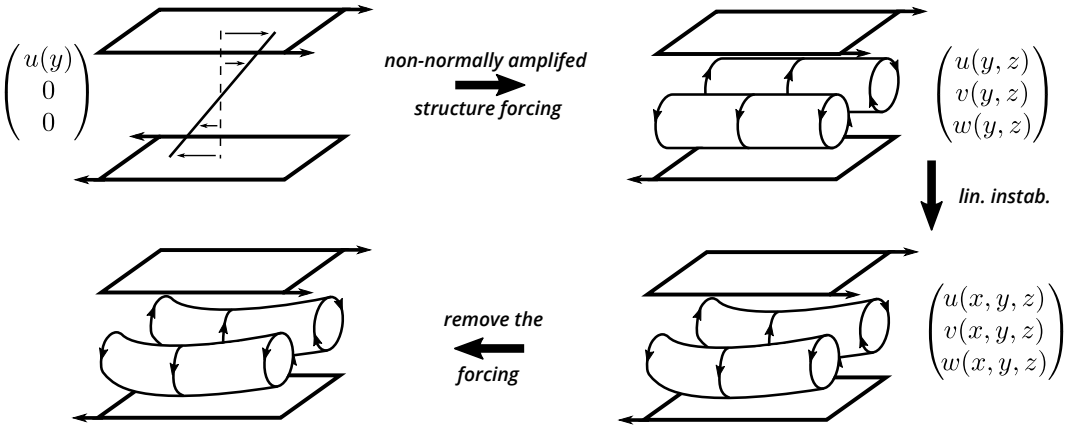


Figure 1.13: Diagram describing the research program for finding exact coherent structures when there is no laminar flow instability, by using a self-sustaining process. $x$, $y$ and $z$ are the streamwise, wall-normal and spanwise directions respectively.

The second method for finding an ECS we consider is outlined in Fig. 1.13 and follows the research programme in Waleffe [71, 94, 95]. This method gives an ECS for Newtonian plane Couette flow, even though the laminar flow is linearly stable for all Reynolds numbers [51]. This method begins by considering the most non-normally

amplified disturbances to the laminar flow. For plane Couette, this is an array of streamwise oriented counter-rotating rolls with the fluid moving in the $(y, z)$ plane, orthogonal to the direction of the laminar flow. Although these disturbances decay exponentially in time, they experience algebraic transient growth initially, allowing them survive long enough to lead the flow away from the laminar to finite amplitude steady states. The secondary flow (Fig. 1.13), where the laminar flow coexists with small amplitude rolls and a slightly modified streamwise velocity, is produced by forcing the Navier-Stokes equations. This flow is linearly unstable to disturbances in the streamwise direction, $x$, at a large enough Reynolds number. This instability connects to an exact solution of the equations — the forced tertiary flow of Fig. 1.13, known as a self-sustaining process (SSP) [95]. An exact solution to the unforced plane Couette flow problem was obtained by tracking the solution with the forcing as the forcing was reduced to zero [94].

This method gets around the lack of a linear instability of the base flow by considering a closely related problem where there is a linear instability, and then carefully tracking the solution back from this flow to the original problem. Similarly, laminar plane Couette flow of UCM fluids is linearly stable for all Weissenberg numbers [20]. This inspires our similar research programme for purely elastic flows: we copy the Newtonian approach and construct a purely elastic SSP, beginning with the first step of Fig. 1.13.

First, we identify a non-normally amplified structure for the flow forcing. For purely elastic plane Couette flow we already know that streamwise independent rolls fill this role [98]. Next we identify a mechanism responsible for the instability of the secondary flow. This mechanism drives the secondary flow unstable and leads to an exact solution with the forcing. With an instability mechanism in hand, we can explore the purely elastic self-sustaining process that leads this instability to take the role of our initial forcing. All that remains after this is to perform a numerical continuation by reducing the forcing and tracking the solution to purely elastic plane Couette flow.

Given that we already know the appropriate forcing for the first step of this approach, we move on to the next step and explore the mechanism for the instability of the forced secondary flow. In Newtonian fluids it is a Kelvin-Helmholtz mechanism: the instability of the interface between two parallel flow regions of fluid at differing velocity. For the SSP the two regions have different streamwise velocities, $u$, and are known as streaks. For purely elastic fluids, this secondary instability is driven by large changes in the first normal stress difference. In Chapter 3 we investigate the generic Kelvin-Helmholtz-like instability of a purely elastic shear layer that provides this mechanism. The instability of a purely elastic shear layer is an interesting problem in its own right, and in Chapter 4 we explore direct numerical simulations and exact solutions for the

nonlinear development of this flow.

The shear layer instability is generic enough to have wider applications than just for the SSP. In Chapter 5 we consider one of these complementary problems, the instability of the purely elastic oscillatory shear flow. Analysis shows that a purely elastic oscillatory shear flow can support resonant waves in the laminar flow velocity [99]. Experiments show that oscillatory pipe flow under these conditions is unstable, with a nonlinear evolution to a steady state of vortex rings [22, 100]. The laminar profile at these resonances produces regions of large shear between regions of fluid flowing at different velocities, similar to our purely elastic shear layer instability. In order to explain the experiments, I perform linear stability analysis and nonlinear direct numerical simulation to investigate the stability of oscillatory purely elastic plane Couette flow. The results of this investigation are in Chapter 5.

I return in Chapter 6 to the purely elastic self-sustaining process. Following the approach laid out in Fig. 1.13, I first produce a secondary flow using a forcing for streamwise independent rolls. Then I look at the instability of this flow to streamwise disturbances, looking for an instability similar to the purely elastic shear layer instability. Finally, I use this instability to show that there is likely an exact solution to the forced flow problem.

## 1.5 Variables and their meanings

Tensors are always in bold font, e.g $\mathbf{v}$ and $\boldsymbol{\tau}$. A velocity with a number for a subscript (e.g. $v_n$) implies that this is a variable in Fourier-space with wave-vector $nk$. For linear stability problems, upper case flow fields are base flows and lower case variables are infinitesimal perturbations to these flows, otherwise lower case is used.

| Category | Variable | Description | Defn. |
|---|---|---|---|
| Space and time | $t$ | time | Fig. 2.1 |
| | $x$ | streamwise distance | Fig. 2.1 |
| | $y$ | wall-normal distance | Fig. 2.1 |
| | $z$ | spanwise distance | Fig. 2.1 |
| Flow fields | $\mathbf{v}$ | velocity vector | (1.15) |
| | $U$ & $u$ | streamwise velocity | (1.15) |
| | $V$ & $v$ | wall-normal velocity | (1.15) |
| | $W$ & $w$ | spanwise velocity | (1.15) |
| | $\Psi$ & $\psi$ | streamfunction | (2.8) |
| | $\omega$, $\omega$ | vorticity or frequency | (4.36)/Fig. 5.1 |
| | $C_{ij}$ & $c_{ij}$ | polymeric conformation tensor | (1.24) |
| | $T_{ij}$ & $\tau_{ij}$ | polymeric stress tensor | (1.23) |
| Dimensionless numbers | $Re$ | Reynolds number | (1.16) |
| | $De$ | Deborah number | (5.9) |
| | $El$ | Elasticity number | (5.26) |
| | $Wi$ | Weissenberg number | (1.27) |
| Flow parameters | $\lambda$ | relaxation time or eigenvalue | (1.22)/(1.31) |
| | $\mu$ | dynamic viscosity | (1.16) |
| | $\nu$ | kinematic viscosity or wave speed | (1.16)/(2.6) |
| | $\ell$ | FENE polymer length scale | (1.26) |
| | $L$ | flow length scale | (1.16) |
| | $\beta$ | viscosity fraction | (1.28) |
| | $\mathbf{k}$ & $k_i$ | wave-vector & wavenumber in direction $i$ | (1.31) |
| Numerical variables | $n$ | Fourier mode | (A.2) |
| | $N$ | total Fourier modes | (A.2) |
| | $m$ | Chebyshev mode | (A.4) |
| | $M$ | total Chebyshev modes | (A.4) |

Table 1.1: A list of commonly used variables, a brief description, and a reference to the full definition.

# Chapter 2

# Travelling waves in viscoelastic Poiseuille channel flow

In this chapter, we begin work on the main aim of the thesis: finding a purely elastic exact coherent structure. We do this by starting from the Newtonian structures, as outlined in the first strategy of our research programme (section 1.4). First, we numerically solve for travelling wave solutions to the Oldroyd-B equations in Poiseuille channel flow. We then consider their stability to perturbations spanwise across the channel. In summary, we find travelling wave solutions at high Reynolds number ($Re$) in the viscoelastic regime; however, we do not find any connection between these solutions and purely elastic exact coherent structures.

The plane Poiseuille flow of Newtonian fluids is linearly unstable to perturbations in the streamwise direction at $Re = 5772$ [46]. This linear instability occurs earlier than any 3D instability, as a direct consequence of Squires theorem (as discussed in section 1.2.1). The instability of the laminar base profile leads to an exact solution for the 2D flow equations involving streamwise travelling waves [47]. Perturbations across the span of the channel trigger a secondary instability of the flow [59]. This instability then connects to a 3D exact solution to the equations of motion [97]. It is possible that this 3D solution can be connected to the exact coherent structures responsible for the transition to turbulence (although this route may be indirect).

In this chapter we explore the possibility of a similar route to a 3D coherent structure in purely elastic flows. Although at low Reynolds numbers a viscoelastic flow is linearly stable for all Weissenberg numbers ($Wi$), we investigate whether the Newtonian travelling wave solutions connect with similar structures in the high $Wi$, low $Re$ regime. We also examine the linear instability of high $Wi$ solutions to see if they lead to full 3D purely elastic coherent structures. Unfortunately, we were unable to find these structures, however, we can provide some evidence to rule out this route

as a viable route to exact coherent structures in the purely elastic regime.

A secondary motivation for the work in this chapter is the unanswered questions about moderate $Re$ viscoelastic channel flow. This research has revealed another turbulent state, intermediate between Newtonian and purely elastic turbulence (at moderate $Re$ and high $Wi$), known as elasto-inertial turbulence (EIT). Flow structures seen during EIT are markedly different than those seen in Newtonian turbulence, and this is thought to be due to the dominance of elastic instabilities in the flow [42]. To investigate EIT, we look for connections between the Elasto-inertial regime and Newtonian travelling waves. The flow structures seen in EIT are almost 2-dimensional, and resemble travelling waves. This study shows that these structures are not connected to Newtonian travelling wave solutions and are due to a completely separate purely elastic effect.

The third motivation for this chapter is to provide some additional evidence of turbulent drag reduction by polymers, a phenomenon where a turbulent dilute polymeric flow exerts less drag than a Newtonian one. This decreased drag has immediate practical application in Alaskan oil pipelines because it lowers the energy required to pump the fluid [4]. In order to explain drag reduction, previous work has investigated the effects of viscoelasticity on Newtonian exact coherent structures.

Direct numerical simulation of turbulent flow [101], and linear stability analysis of travelling wave solutions [102], both provide evidence that the presence of polymers suppress the travelling wave solutions. The Newtonian, 3D exact coherent structure formed of rolls and streaks, (discussed in section 1.3.2) has been examined for a weakly elastic flow. This exact coherent structure is suppressed with the addition of a small polymeric component to the fluid [103, 104]. This drag reduction effect has not been checked at low $\beta$, the ratio of polymeric viscosity to total viscosity, which is the regime where elastic effects become even more important. It is also not clear what effect the unusually high Schmidt number (the measure of the strength of stress diffusion) used by Stone et al. [103, 104] will have on the flow. We examine travelling wave solutions and show that they behave similarly to the exact coherent structures of Stone et al. [103, 104]. Just as for those structures, we find that as $Wi$ increases the onset of the travelling waves is delayed to higher $Re$.

In this chapter we attempt to find exact coherent structures in plane Poiseuille flow. We find that this is not possible using a connection from the Newtonian travelling wave state. We also address two subsidiary motivations, both showing that Newtonian 2D travelling waves are not connected to EIT and corroborating existing evidence that viscoelasticity weakens turbulence and reduces drag in high Reynolds number flows.

## 2.1 The 2D flow equations

We consider pressure driven Plane Poiseuille flow. This is the flow of a fluid between two infinite parallel plates driven by a constant pressure gradient. We choose a coordinate system such that the streamwise ($x$), wall-normal ($y$) and spanwise ($z$) directions are as shown in Fig. 2.1.

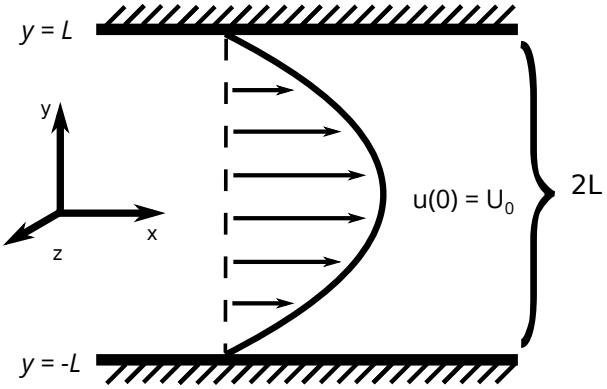


Figure 2.1: Diagram of plane Poiseuille flow.

### 2.1.1 The laminar flow

The laminar flow solution for this problem is similar in both Newtonian and Oldroyd-B fluids. Using the Navier-Stokes and Oldroyd-B equations (1.23) with all variables independent of $x$, $z$ and $t$, and a pressure gradient, $\delta = -\frac{\mathrm{dp}}{\mathrm{dx}}$ we obtain,

$$\begin{aligned} \delta + \eta_s \frac{\partial^2 u}{\partial y^2} + \frac{\mathrm{d}\tau_{xy}}{\mathrm{d}y} &= 0 \\ \tau_{xx} - 2\lambda\tau_{xy}\frac{\mathrm{d}u}{\mathrm{d}y} &= 0 \\ \tau_{yy} &= 0 \\ \tau_{xy} - \lambda\tau_{yy}\frac{\mathrm{d}u}{\mathrm{d}y} &= \eta_p \frac{\mathrm{d}u}{\mathrm{d}y}\,. \end{aligned} \tag{2.1}$$

After some algebra, we can solve this system of equations for $u$ subject to the no slip boundary conditions, $u(\pm L) = 0$. We find that

$$\tau_{xy} = \eta_p \frac{\mathrm{d}u}{\mathrm{d}y} \qquad \tau_{xx} = 2\lambda\eta_p \left(\frac{\mathrm{d}u}{\mathrm{d}y}\right)^2 \qquad \tau_{yy} = 0 \tag{2.2}$$

$$u(y) = \frac{\delta L^2}{2\eta_T}\left(1 - \frac{y^2}{L^2}\right)\,, \tag{2.3}$$

where we now set the centerline velocity as a velocity scale, $U_0 = \frac{\delta L^2}{2\eta_T}$ and make our equations dimensionless using the dimensionless variables:

$$\begin{aligned} \hat{\mathbf{v}} &= \frac{\mathbf{v}}{U_0} \qquad & \hat{\mathbf{x}} &= \frac{\mathbf{x}}{L} \qquad & \hat{t} &= \frac{U_0}{L}t \qquad & \hat{\boldsymbol{\tau}} &= \frac{L}{\eta_p U_0}\boldsymbol{\tau} \\ \hat{p} &= \frac{L}{\eta_T U_0}p \qquad & \beta &= \frac{\eta_s}{\eta_s+\eta_p} \qquad & Re &= \frac{\rho U_0 L}{\eta_T} \qquad & Wi &= \frac{\lambda U_0}{L}\,. \end{aligned} \tag{2.4}$$

From here on we drop the $\hat{}$ symbols on the dimensionless variables and work with the dimensionless Oldroyd-B equations in terms of the conformation tensor $\boldsymbol{\tau} = (\mathbf{C}-\mathbb{I})/Wi$:

$$\begin{aligned} Re\left[\frac{\partial \mathbf{v}}{\partial t} + \mathbf{v}\cdot\nabla\mathbf{v}\right] &= -\nabla p + \beta\nabla^2\mathbf{v} + \frac{1-\beta}{Wi}\nabla\cdot\mathbf{C} \\ \nabla\cdot\mathbf{v} &= 0 \\ \frac{1}{Wi}(\mathbf{C}-\mathbb{I}) + \frac{\partial\mathbf{C}}{\partial t} + \mathbf{v}\cdot\nabla\mathbf{C} &= (\nabla\mathbf{v})^T\mathbf{C} + \mathbf{C}(\nabla\mathbf{v})\,. \end{aligned} \tag{2.5}$$

### 2.1.2 The 2D Oldroyd-B travelling wave equations

We search for exact solutions to the above equations for flow fields which are periodic in time. We restrict ourselves to travelling wave solutions (solutions with a constant speed in the streamwise direction) and make a decomposition into Fourier modes in this direction such that

$$g(x,y) = \sum_{n=-N}^{N} \breve{g}_n(y)\mathrm{e}^{ink_x(x-st)}\,, \tag{2.6}$$

where $g$ can be any of the flow variables, $N$ gives the total number of Fourier modes and $s$ is the speed of the travelling wave. Then we make the Galilean transformation on the equations of motion,

$$\frac{\partial g}{\partial t} = -s\frac{\partial g}{\partial x}\,. \tag{2.7}$$

This gives us a system of equations to solve for a flow field that depends on $x$ and $y$ only. To reduce the number equations and absorb the incompressibility constraint, we introduce the streamfunction, $\psi$, defined by $u = \frac{\partial\psi}{\partial y}$ and $v = -\frac{\partial\psi}{\partial x}$. Upon substitution into (2.5) and assuming only $x$ and $y$ dependence, we obtain a system of equations for

the $x$ dependent flow

$$-Res\frac{\partial\nabla^2\psi}{\partial x} = -\left(\frac{\partial\psi}{\partial x}\frac{\partial}{\partial y} - \frac{\partial\psi}{\partial y}\frac{\partial}{\partial x}\right)\nabla^2\psi + \beta\nabla^4\psi + (1-\beta)\left(\frac{\partial^2\tau_{xy}}{\partial y^2} - \frac{\partial^2\tau_{xy}}{\partial x^2} + \frac{\partial^2\tau_{xx}}{\partial x\partial y} - \frac{\partial^2\tau_{yy}}{\partial x\partial y}\right) \tag{2.8}$$

$$-s\frac{\partial C_{xx}}{\partial x} = \left(\frac{\partial\psi}{\partial x}\frac{\partial}{\partial y} - \frac{\partial\psi}{\partial y}\frac{\partial}{\partial x}\right)C_{xx} + 2\frac{\partial^2\psi}{\partial x\partial y}C_{xx} + 2\frac{\partial^2\psi}{\partial y^2}C_{xy} - \tau_{xx} \tag{2.9}$$

$$-s\frac{\partial C_{yy}}{\partial x} = \left(\frac{\partial\psi}{\partial x}\frac{\partial}{\partial y} - \frac{\partial\psi}{\partial y}\frac{\partial}{\partial x}\right)C_{yy} - 2\frac{\partial^2\psi}{\partial x^2}C_{xy} - 2\frac{\partial^2\psi}{\partial x\partial y}C_{yy} - \tau_{yy} \tag{2.10}$$

$$-s\frac{\partial C_{xy}}{\partial x} = \left(\frac{\partial\psi}{\partial x}\frac{\partial}{\partial y} - \frac{\partial\psi}{\partial y}\frac{\partial}{\partial x}\right)C_{xy} - \frac{\partial^2\psi}{\partial x^2}C_{xx} + \frac{\partial^2\psi}{\partial y^2}C_{yy} - \tau_{xy}\,, \tag{2.11}$$

and for the mean flow,

$$Re\overline{\frac{\partial}{\partial t}\frac{\partial\psi}{\partial y}} = Re\overline{\frac{\partial\psi}{\partial x}\frac{\partial^2\psi}{\partial y^2}} + \beta\overline{\frac{\partial^3\psi}{\partial y^3}} + (1-\beta)\overline{\frac{\partial C_{xy}}{\partial y}} + 2\,. \tag{2.12}$$

The $\bar{\cdot}$ indicates the mean in the $x$ direction of the variables underneath. In addition to these equations, there are 6 more constraint equations to determine the problem. Five are boundary conditions, four of which ensure no slip at the walls ($u(y=\pm1)=0$, $v(y=\pm1)=0$), as well as a boundary condition to set the gauge of the streamfunction ($\psi(y=-1)=0$). The final constraint sets the phase of the wave, and allows us to calculate the wave speed, $s$. We set this condition such that $\mathrm{Im}(\check{\psi}_1(0.5))=0$, or equivalently, such that the first mode of the streamfunction is a pure cosine in $x$ at $y=0.5$.

In order to solve these equations numerically, we approximate the problem via a Fourier decomposition in the $x$ direction and Chebyshev decomposition in the $y$ direction, truncated at the $N^{\text{th}}$ Fourier and $M^{\text{th}}$ Chebyshev modes. This fully spectral representation provides much greater accuracy than any finite difference scheme (technical details are contained in appendix A.1). We solve the equations by discretising them onto this spectral grid and performing a Newton line search. This is a well known algorithm, briefly discussed in appendix section A.2.2. The partial differential equations above are dominated by their nonlinearities and as such, require an accurate approximate solution for a root finding algorithm to converge. In general, known solutions are used as initial conditions to find unknown ones at slightly different parameters — a process referred to as numerical continuation.

The measure used to decide if a solution is the laminar solution or a true travelling wave is the kinetic energy of the flow. We write the kinetic energy as a sum of contributions due to each Fourier component and normalise by the kinetic energy of

the laminar flow,

$$KE = \frac{1}{2KE_{lam}} \left[ \left( \frac{\partial \check{\psi}_0}{\partial y} \right)^2 + \sum_{n=1}^{N} \left( \frac{\partial \check{\psi}_n}{\partial y} \frac{\partial \check{\psi}_{-n}}{\partial y} + \frac{\partial \check{\psi}_n}{\partial x} \frac{\partial \check{\psi}_{-n}}{\partial x} \right) \right] , \tag{2.13}$$

where the subscripts indicate the Fourier component in question.

## 2.2 Newtonian travelling waves

Both to validate the method and to obtain a result for comparison with the viscoelastic case, we begin by re-examining travelling waves for a Newtonian flow. Starting from a simple wavy perturbation of plane Poiseuille flow at $Re = 5700$ at a low resolution, I obtained a set of travelling wave solutions. Fig. 2.2a shows an example solution, located at the critical Reynolds number for the existence of travelling waves, and represented by a colour map of the out-of-plane vorticity ($\omega = (\nabla \times \mathbf{v}) \cdot \mathbf{e}_z$) with arrows representing the orientation and strength of the velocity. The undulation in the velocity in the streamwise direction is weak for the travelling waves, but it is easier to see if we focus on the layer of arrows near the walls.

Numerical continuation in $Re$ and wavenumber yields a bifurcation surface in energy (Fig. 2.2b), where the solutions are plotted relative to laminar flow ($KE_0 = 1$) in the space of $k_x$, $Re$ and $KE$. Each point on this surface represents an exact solution to the equations. Fig. 2.3 is a 2D representation of the bifurcation surface where $Re$ is given by the colour. The green dot is the location of the saddle node solution at the critical Reynolds number.

We find that the critical wavenumber and Reynolds number of these solutions is $Re_{sn} = 2939$ and $k_{x,sn} = 1.319$ consistent with earlier work on the Newtonian travelling waves, which find that $Re_{sn} = 2934$ and $k_{x,sn} = 1.323$ [47]. The differences are likely due to the smaller number of Fourier and Chebyshev modes used (4 Fourier modes and 40 Chebyshev modes compared with 7 and 50 in this study). We can also compare the shape of the surface with the low $Re$ end of the surface of Orszag and Patera [59] (Fig. 1.9).

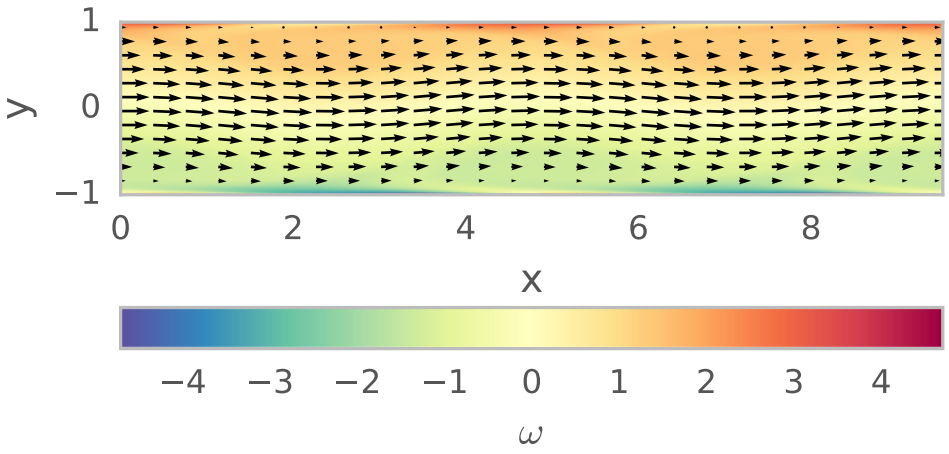


(a)

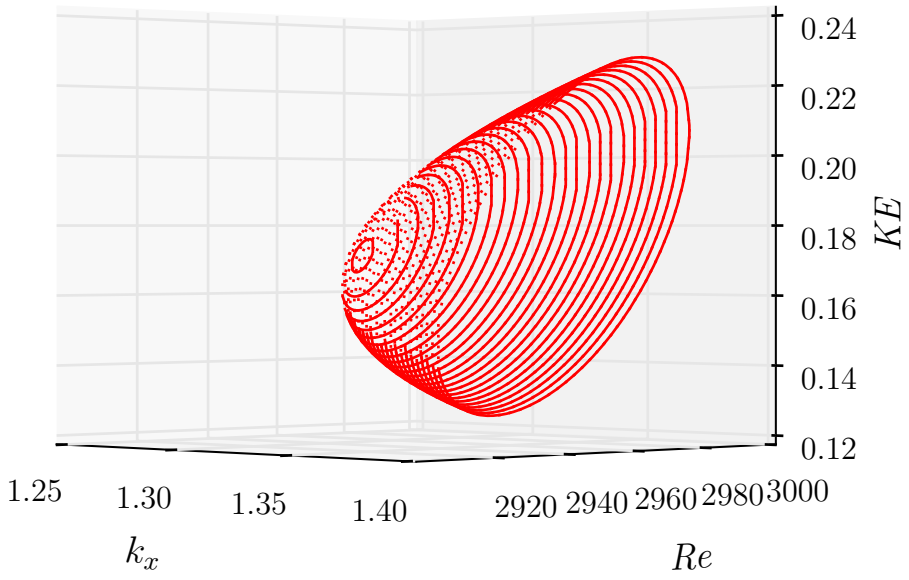


(b)

Figure 2.2: a) Plot of two wave lengths for an example travelling wave solution at the saddle node point (the green dot in Fig. 2.3) with $Re = 2939$ and $k_x = 1.319$. The colour gives the vorticity and the arrows give the velocity. b) A representation of the Newtonian travelling wave solutions using the kinetic energy of the first mode, the wavenumber, and the Reynolds number. The shape is shown at a resolution of 7 Fourier and 50 Chebyshev modes, sufficient for convergence. It is similar to a plot by Orszag and Patera [59], given in the introduction (Fig. 1.9), using the energy of the first Fourier mode.

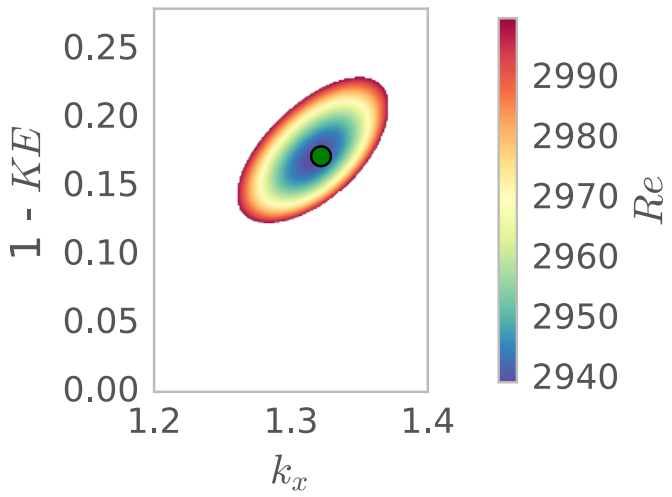


Figure 2.3: Another representation of the same data as Fig. 1.9 but where the Reynolds number is given by a colour map. The $x$-axis, where $KE = 1$, corresponds to laminar flow.

## 2.3 The effects of viscoelasticity on travelling waves

To begin to examine the effects of viscoelasticity, we first connect the Newtonian travelling wave solutions to viscoelastic ones. I used the Newtonian solution at $Re = 3000$ as the initial condition in a viscoelastic version of the code at high $\beta$ and low $Wi$. Further numerical continuation of this solution (using less elastic solutions as guesses for more elastic ones) yields small $\beta$ and high $Wi$ solutions. Some example solutions are shown for constant $Wi$ and $\beta = 0.9$ and $\beta = 0.1$ (Figs 2.4 and 2.5). We show one wavelength of the vorticity and the velocity (again, the colour gives the vorticity and arrows give the velocity) as well as the three stresses $\tau_{xx}$, $\tau_{yy}$ and $\tau_{xy}$.

We can also remove the mean flow in the streamwise direction from the solutions by setting the zeroth Fourier mode to zero. Without the mean flow, we can clearly see that travelling wave is really a vortical flow superposed on the laminar Poiseuille flow. This is visible at $\beta = 0.1$ in Fig. 2.6 at $Wi = 0.5$ and Fig. 2.7 at $Wi = 1.5$.

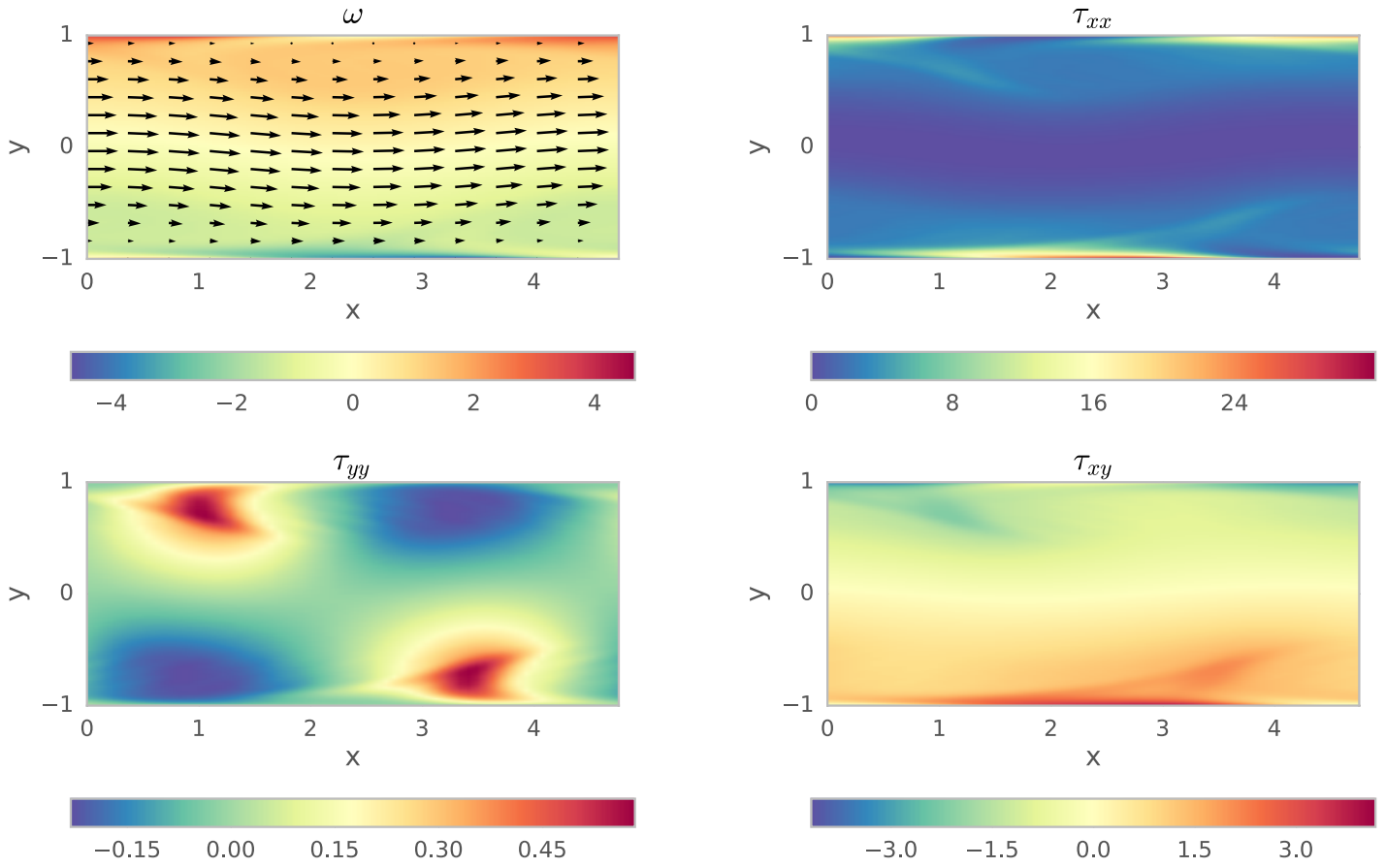


Figure 2.4: An example viscoelastic travelling wave solution at the saddle node point for $\beta = 0.9$ and $Wi = 1.0$ with a resolution of $(8, 50)$. At this saddle node $k_{x,sn} = 1.32$ and $Re = 2843.0$.

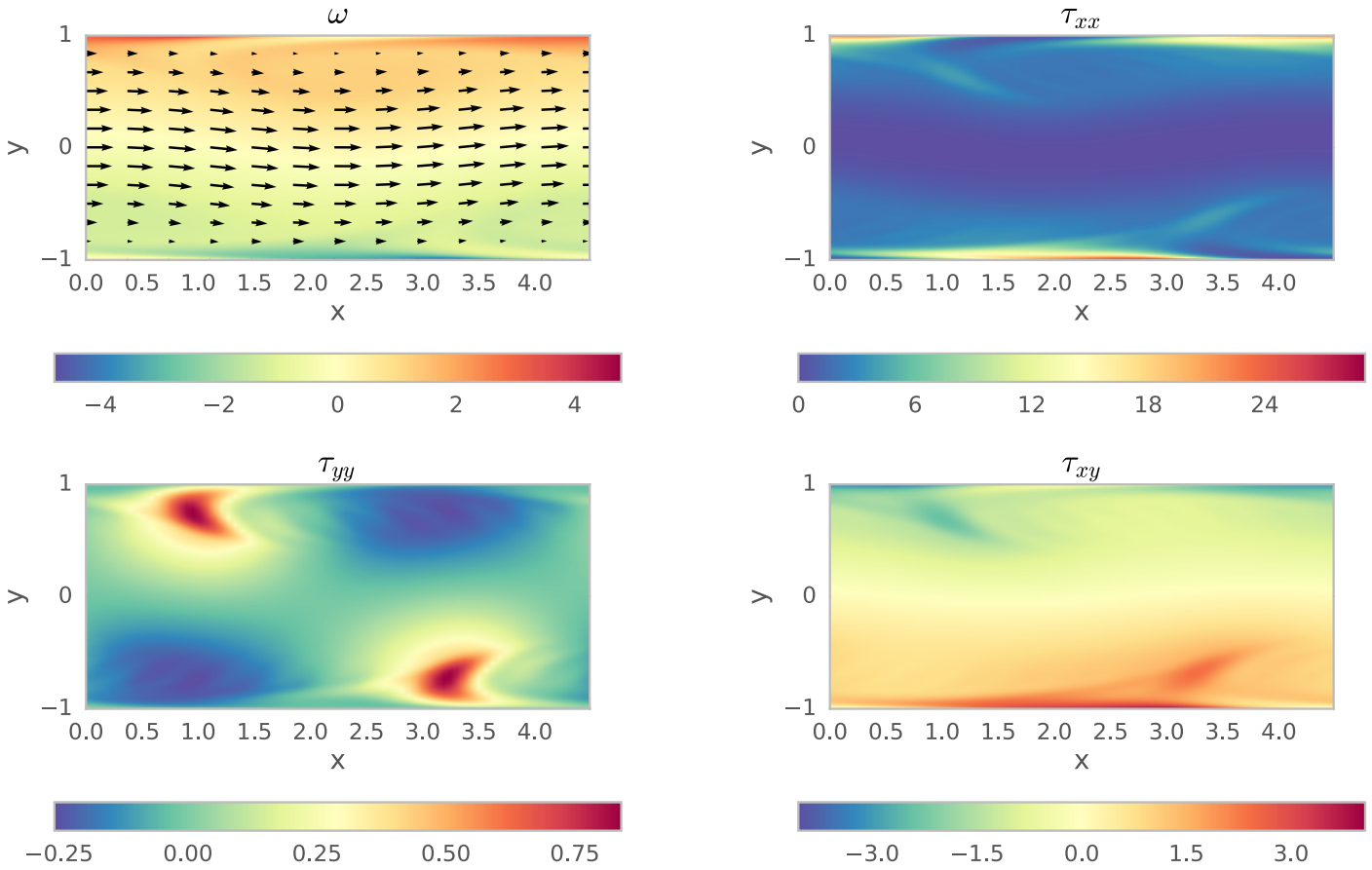


Figure 2.5: An example viscoelastic travelling wave solution at the saddle node point for $\beta = 0.1$ and $Wi = 1.0$ with a resolution of $(9, 60)$. At this saddle node $k_{x,sn} = 1.40$ and $Re = 2218.0$.

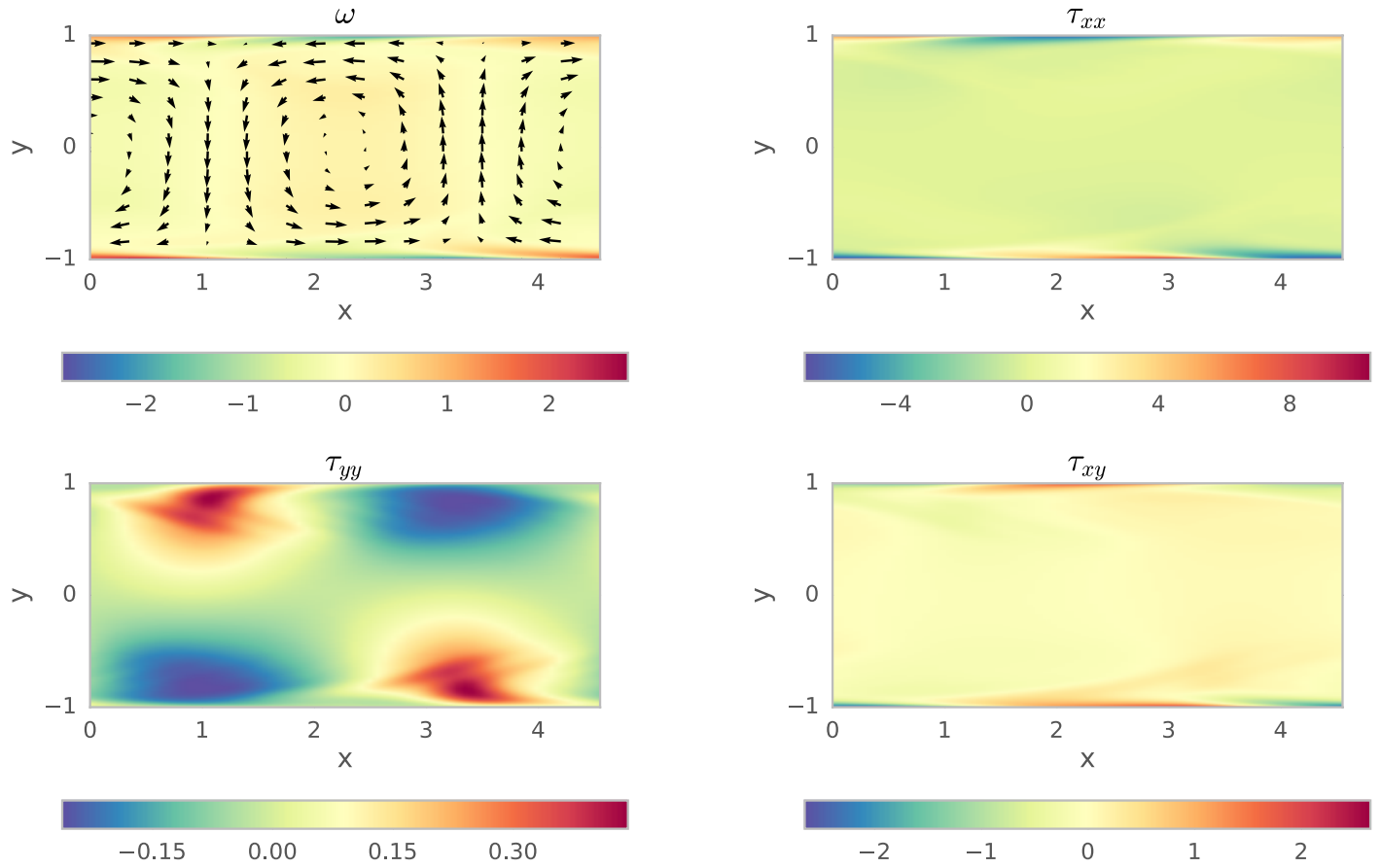


Figure 2.6: Mean flow subtracted viscoelastic travelling wave solution at the saddle node point for $\beta = 0.1$ and $Wi = 0.5$ with a resolution of $(8, 50)$. At this saddle node $k_{x,sn} = 1.38$ and $Re = 2397.0$.

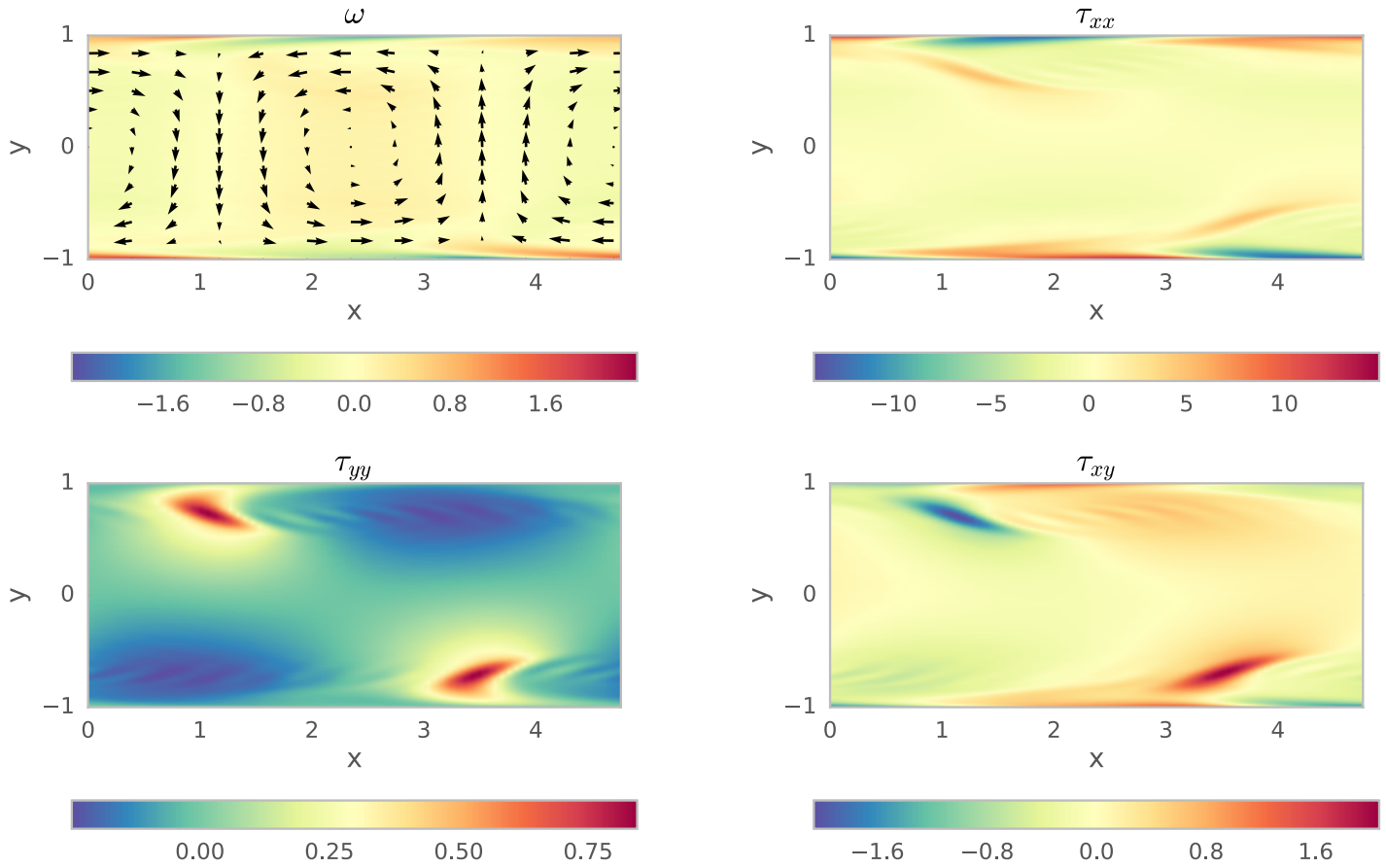


Figure 2.7: Mean flow subtracted viscoelastic travelling wave solution at the saddle node point for $\beta = 0.1$ and $Wi = 1.5$ with a resolution of $(9, 60)$. At this saddle node $k_{x,sn} = 1.32$ and $Re = 2265.0$.

### 2.3.1 The bifurcation surface

Just as for the Newtonian solutions, we do a numerical continuation, slowly varying $Re$ and $k_x$ and using previous solutions as an initial condition for new solutions. These solutions form bifurcation surfaces in $Re$ $k_x$ and $KE$ space at each choice for the viscoelastic parameters $\beta$ and $Wi$. For each of these surfaces, there is again a minimum $Re$ solution, the saddle node point, which we denote with the subscript $sn$.

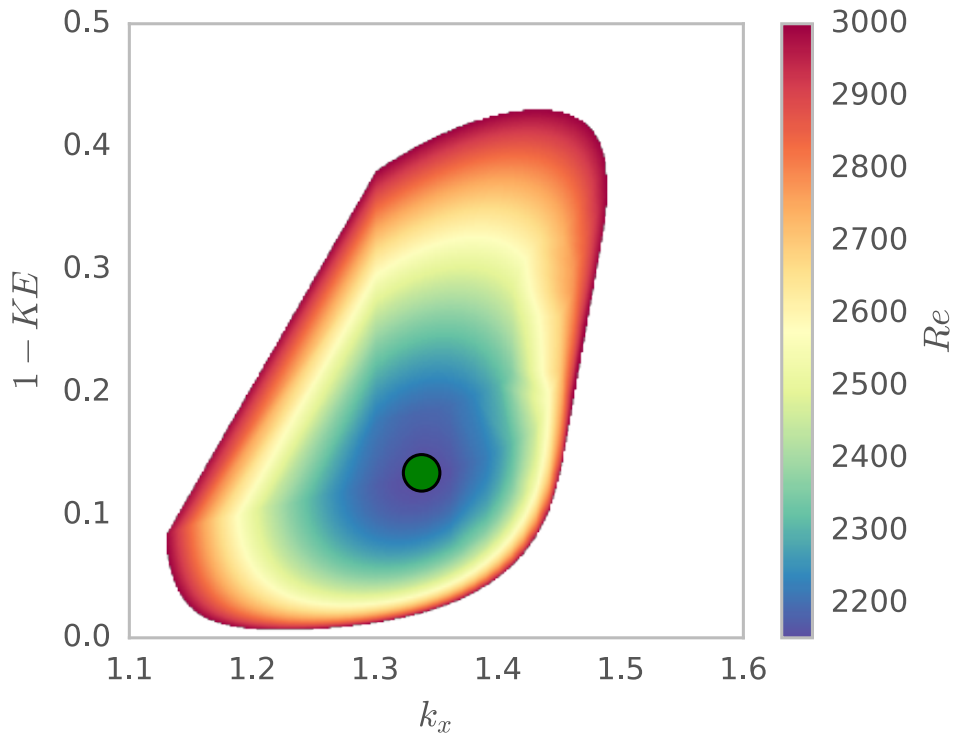


Figure 2.8: An example low resolution ($N = 3$, $M = 40$) bifurcation surface for $\beta = 0.1$ and $Wi = 1.5$ where $Re$ is given by the colour map. There is a large interpolation in the Reynold's number in the upper left corner of the colour map. This is because in this region I could not find solutions for wavenumbers lower than than about $k_x = 1.29$.

Figure 2.8 shows a low resolution bifurcation surface up to $Re = 3000$. The most important point on this surface, the saddle node point, marks the lowest possible $Re$ for the existence of these travelling wave solutions at this $Wi$ and $\beta$.

We examined how the properties of the saddle node points change as we vary the viscoelastic parameters. We compare some of the basic properties of the saddle node solutions: $Re_{sn}$, $k_{x,sn}$ and $s_{sn}$. $Re$ and $k_x$ are parameters that we control as part of

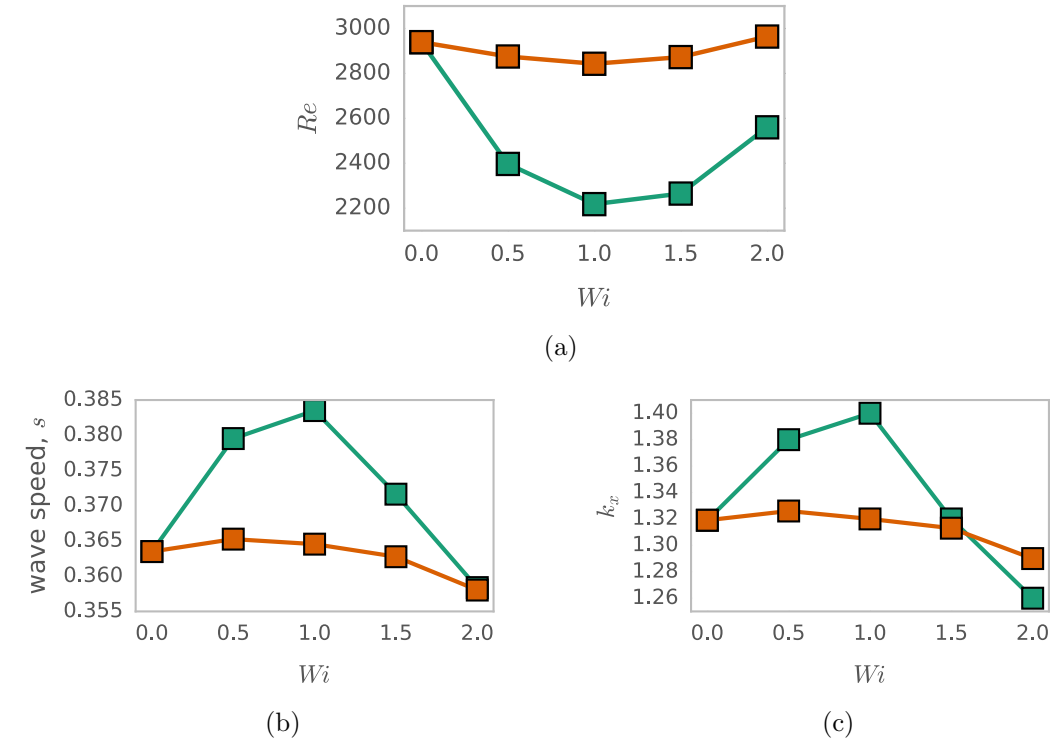


Figure 2.9: The dependence of (a) $Re$, (b) the wave speed $s$ and (c) the wavenumber $k_x$ of the saddle node solution on the viscoelastic parameters. The data in green is for $\beta = 0.1$ and in orange $\beta = 0.9$.

the numerical continuation and the wave speed $s$ is found as part of the solution. We plot Reynolds number of the saddle node solutions against $Wi$ for $\beta = 0.1, 0.9$. We find that the addition of viscoelasticity lowers the critical $Re$ for $Wi < 1$ before raising it again for $Wi > 1$ (Fig. 2.9a). The trend is reversed for the mean speed $s_{sn}$ and critical wavenumber $k_{x,sn}$, which both increase for $Wi < 1$ and decrease for $Wi > 1$ (Figs 2.9b and 2.9c).

To investigate the effects on the shape of the surfaces, we examine a fixed plane, where $Re = Re_{sn} + 100$. We track the solutions by numerical continuation for wave numbers in this plane at high $\beta$ (Fig. 2.10a) and low $\beta$ (Fig. 2.10b) and do this for a range of Weissenberg numbers. These plots are insensitive to changing resolution, except at high Weissenberg number, where slight differences can be seen.

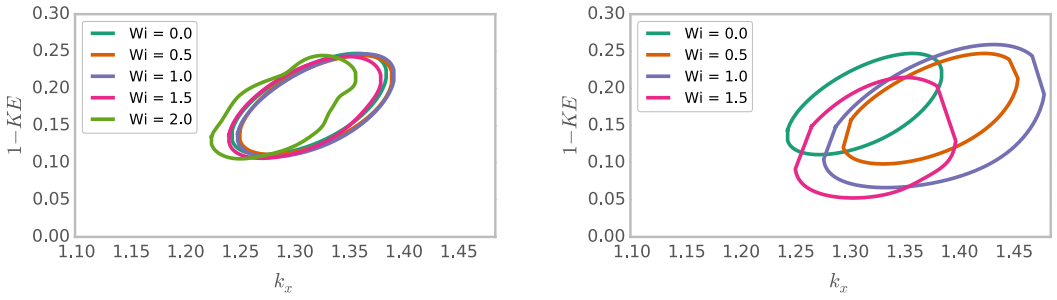


(a) (b)

Figure 2.10: Bifurcation surfaces at $Re = Re_{sn} + 100$ for $\beta = 0.9$ and $\beta = 0.1$ in a) and b) respectively. We can see that the surfaces follow a similar trend to in Figs 2.9a and 2.9c.

## 2.4 Linear stability of 2D travelling waves

Following Orszag and Patera [59] we examine the linear stability of the 2D solutions to perturbations along the span of the channel. The saddle node solutions are the solutions at the smallest possible $Re$. Seeing as we are interested in the low Reynolds number limit, we will just examine the linear stability of these points at various viscoelastic parameters. Taking the solutions obtained earlier, we relabel each 2D variable in upper case to represent that the 2D flow is now the base flow, and we add to it a spanwise disturbance,

$$g(x,y,z) = \sum_{m=0}^{M} \sum_{n=-N}^{N} \check{g}_{n,m} \mathrm{e}^{ink_x x + ik_z z + \lambda t} \cos(m \arccos(\pi y)) \,, \tag{2.14}$$

where $g$ may be $u, v, w, p$ or $c_{ij}$. This makes the total streamwise velocity, for example, $U_{3D} = U(x,y) + u(x,y,z)$. Substitution of these variables into the Oldroyd-B equations (2.5) gives an eigenvalue problem for $\lambda$, where the $\lambda$ with the largest real part of corresponds to the growth rate of the most unstable eigenmode at each spanwise perturbation wavenumber $k_z$. The set of linear stability equations are provided in the appendix, section B. We solve this eigenvalue problem numerically and obtain dispersion relations for the dependence of the growth rate on the wavenumber.

The eigenvalue spectra show that there are many unstable modes, both in the viscoelastic and Newtonian cases at high and low $\beta$ (Figs 2.11a and 2.11b). The spectra for the instability of the saddle node solution are converged, as is visible in the overlap of spectra in Fig. 2.11c. The spectra at some distance along the upper and lower branches is also shown in Fig. 2.11d, where it is clear that the branch furthest from the laminar flow, the upper branch, is more stable than the lower branch.

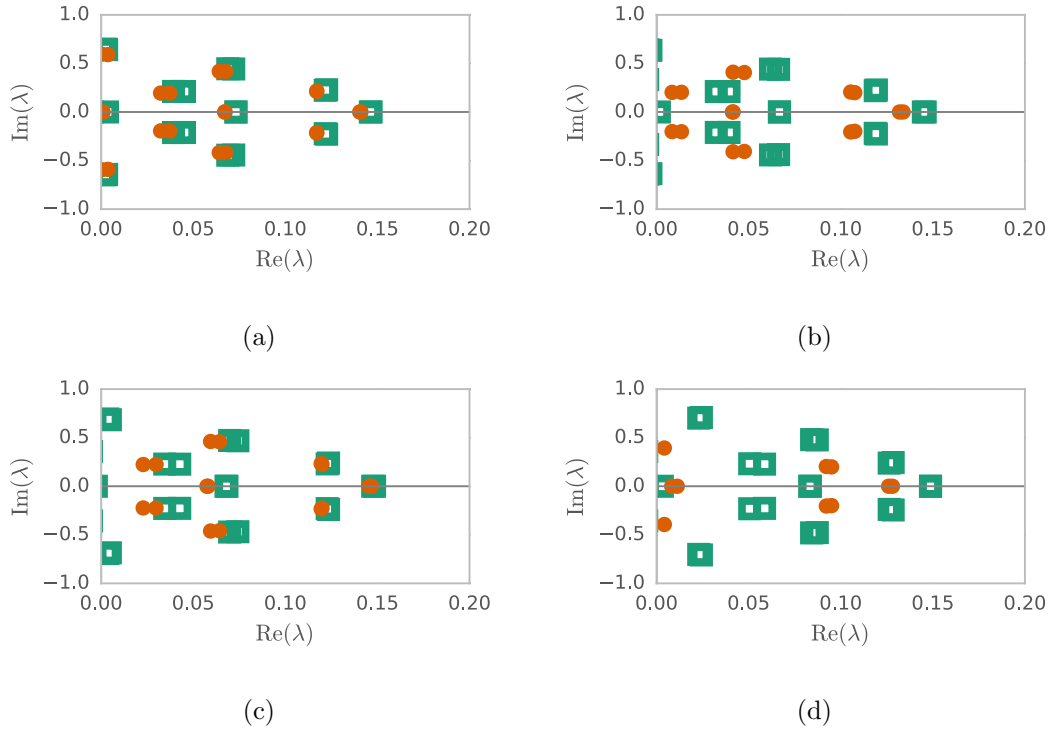


Figure 2.11: Eigenvalue spectra. a) for the Newtonian (turquoise squares) and $\beta = 0.9$, $k_z = 2.2$ and $Wi = 1.0$ (orange circles) saddle node solutions. b) for the Newtonian (turquoise squares) and $\beta = 0.1$, $k_z = 2.0$ and $Wi = 2.0$ (orange circles) saddle node solutions. c) $k_z = 2.0$, $\beta = 0.9$ at $Wi = 1.0$ for the saddle node solutions of at two resolutions, (9, 60) and (8, 50). d) The same parameters as c) but at $Re_{sn} + 100$. The turquoise squares give the spectrum on the lower branch, the orange circles give the upper branch spectrum.

There are both stationary and spanwise-travelling modes, the latter given by the eigenvalues with $\mathrm{Im}(\lambda) \neq 0$. The most unstable mode will grow exponentially faster than the next largest, and we can restrict the rest of our analysis to this eigenmode. We now calculate the most unstable mode as a function of the spanwise wavenumber $k_z$ to generate dispersion relations at the saddle node points.

At high spanwise wavenumber, the stationary instability appears to be superseded by a spanwise travelling one. This seems to be robust under increased resolution and true of all saddle node points. We can see this by examining the imaginary part of the eigenvalues, shown in Figs 2.12b and 2.13b.

We examine the eigenvectors of the instability for spanwise wavenumbers near the peak of the dispersion relations for different viscoelastic parameters. Velocity vector fields are plotted for the eigenfunctions in Figs 2.14a, 2.14b at $\beta = 0.9$ and $\beta = 0.1$ respectively.

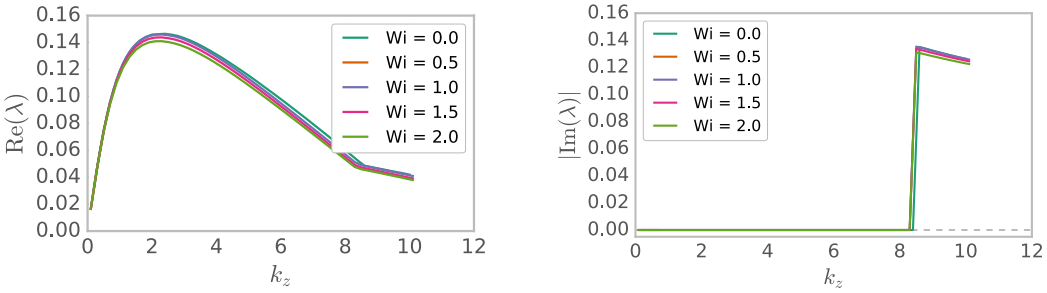


(a) (b)

Figure 2.12: a) Growth rate of the most unstable eigenmode from the linear stability analysis of the saddle node travelling wave solution at $\beta = 0.9$. b) Wave speed of this eigenmode in the $z$ direction.

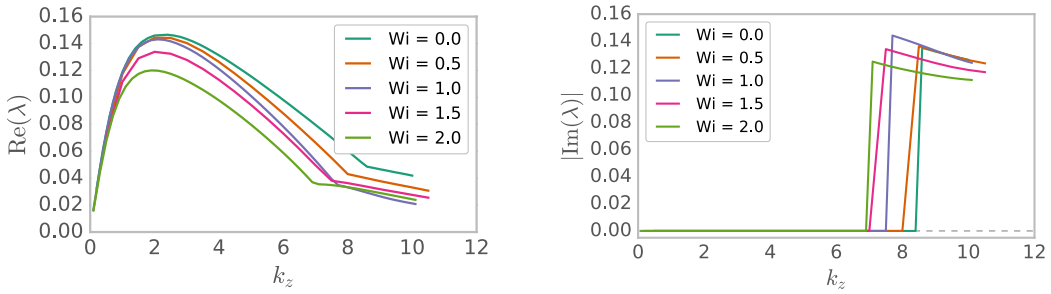


(a) (b)

Figure 2.13: a) Growth rate of the most unstable eigenmode from the linear stability analysis of the saddle node travelling wave solution at $\beta = 0.1$. b) Wave speed of this eigenmode in the $z$ direction.

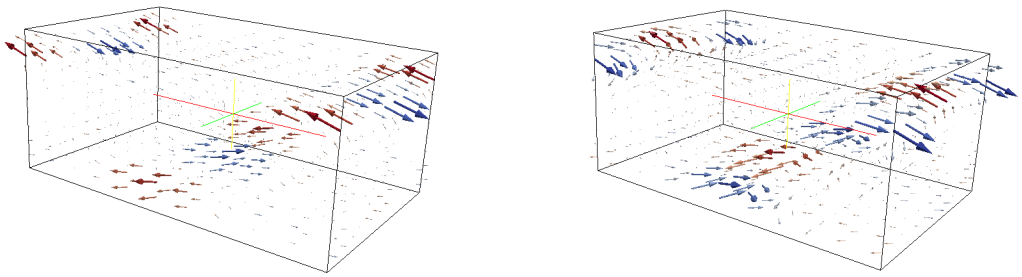

(a) (b)

Figure 2.14: Velocity vector fields of eigenvectors of the instability at the saddle node points. a) $k_z = 2.2$, $\beta = 0.9$, $Wi = 1.0$, b) $k_z = 2.2$, $\beta = 0.1$, $Wi = 1.0$. Both at a resolution of $N = 8$, $M = 50$

## 2.5 Discussion

First, we shall consider the shapes of the viscoelastic travelling wave solutions. Increasing $\beta$ moves the nonlinear interaction from the advective term in the Navier-Stokes to the nonlinear terms in the constitutive equation for the stresses. However, we found that the qualitative form of the stresses does not change much as we go from $\beta = 0.9$ to $\beta = 0.1$ (Figs 2.4 and 2.5), suggesting that the mechanism which sustains the viscoelastic travelling wave is still fundamentally the same as the mechanism that sustains the Newtonian one. As we change $Wi$ at low $\beta$ we find that the shape of solution stays broadly the same, albeit with greater stress localisation at higher $Wi$ (see the mean flow subtracted solutions in Fig. 2.6 and 2.7). Figure 2.6 appears to contain some aliasing errors, but the total kinetic energy does not vary much as the resolution changes, so this is unlikely to cause any problems in the rest of the analysis.

### 2.5.1 Viscoelastic bifurcation surface

As expected from considerations of the linear stability analysis of Sadanandan and Sureshkumar [102], we find that the addition of viscoelasticity lowers the critical $Re$ for $Wi < 1$ before raising it again for $Wi > 1$ (Fig. 2.9a). This trend may be connected to the fact that for laminar flow, the streamwise component of the conformation tensor is $\sim Wi^2$ whilst the shear component is $\sim Wi$. This suggests that for $Wi < 1$ shear stress effects will dominate, whilst for $Wi > 1$ normal stress effects will become more important. Since we expect that any purely elastic instability will be caused by large normal stress differences, the trend suggests that we will be unable to continue these solutions to low $Re$, even at very large $Wi$. It also suggests that the mechanism behind these solutions is unconnected to any purely elastic or elasto-inertial mechanism, since high $Wi$ delays the solution to higher $Re$.

For high $\beta$ we find very little changes in the shape of the bifurcation surface as we increase $Wi$ (Fig. 2.10a). It looks as though the travelling waves are shifting to a slightly smaller wavenumber and longer wavelength, consistent with the behaviour of the saddle points and the linear stability results of Sadanandan and Sureshkumar [102]. At low $\beta$, the results are very different (Fig. 2.10b). It appears that the surface is enlarged and moves to higher wavenumber. Unfortunately, adequately resolving the bifurcation surface at low $\beta$ and high $Wi$ is very computationally expensive, leading to results only up to $Wi = 1.5$ in this region. However, we do see a similar behaviour to that of the saddle node point, in that after an initial move to higher wavenumbers, the bifurcation surface for high $Wi$ rapidly moves to much lower wavenumbers. The width in wavenumber of the surface also seems to vary at low $\beta$.

These effects on the shape of the surface may be at least partly due to our choice to

compare the surface at this $Re$. It is possible that a $Re$ based on a fractional distance between the saddle node point and the point of linear stability would remove some or all of these trends in the shape of the surface. Recalculating the linear stability results of Sadanandan and Sureshkumar [102] and finding the bifurcation surfaces in such planes may be an interesting extension to this work.

### 2.5.2 3D linear stability

The spectra appear to be well converged even at the higher $Wi$ end of our calculations (Fig. 2.11c) and it appears that the most unstable eigenvalue remains the same as we increase $Wi$ (Fig. 2.11b). This suggests that the instability is of the same form and has the same origin as the Newtonian one.

At $\beta = 0.9$ the dispersion relations do not show much variation from the Newtonian case (Fig. 2.12a). This suggests that the spanwise Newtonian instability of [59] is largely unchanged by viscoelasticity at this $\beta$. However, at low $\beta$ it appears that the strength of the instability is damped by the presence of viscoelasticity (Fig. 2.13a). It would be interesting to examine how this shape changes as the Weissenberg number increases still further, unfortunately, linear stability in three dimensions at the required resolutions would have taken longer than the available time, using the current code.

The eigenvectors of the instability also look very similar at high and low $\beta$ (Figs 2.14a and 2.14b), again suggesting that the instability is still essentially the Newtonian instability of the travelling wave solutions. The instability mostly acts near the walls where the bend in the travelling wave comes closest to the channel wall. This is where the largest shear rates are and so it seems natural that there should be an instability here.

### 2.5.3 Conclusions

Given that we are unable to continue these solutions to sufficiently low Reynolds number, and the fact that there are no eigenvalues of a purely elastic origin, we cannot connect these Newtonian travelling waves to full purely elastic 3D exact coherent structures. Furthermore, the trend of increasing critical $Re$ in Fig. 2.9a lead us to conclude that there is unlikely to be a route to purely elastic coherent structures at higher $Wi$.

It is still possible that these solutions connect with the 3D exact coherent structures used in Stone et al. [103, 104]. In those studies they observe the same trend as Fig. 2.9a, small $Wi$ slightly lowers $Re_{sn}$ relative to the Newtonian structure, whilst large $Wi$ raises $Re_{sn}$. It is possible that the linear instability of our 2D travelling wave solutions connects indirectly to those 3D viscoelastic structures, perhaps passing through some

intermediate turbulent state.

The fact that we cannot find these viscoelastic travelling waves at low or moderate $Re$ strongly suggests that they cannot be connected to any structures observed in the experiments and simulations of EIT by Samanta et al. [42]. However, it is interesting to observe that the flow is much more strongly influenced by $\beta$ than $Wi$, and so lowering $\beta$ in other flow scenarios may lead to purely elastic effects previously unnoticed. We will explore an example of this in Chapter 3, where we examine a fairly generic low $\beta$ purely elastic instability.

# Chapter 3

# A viscoelastic shear layer instability

In the previous Chapter, we demonstrated the infeasibility of the first of our two approaches to purely elastic exact coherent structures. In this Chapter, we prepare the ground for the self-sustaining process (SSP) — our second approach to purely elastic exact coherent structures (discussed in the research programme section 1.4). This strategy has been used in Newtonian flows, where Waleffe [95] identified a Newtonian self sustaining process in plane Couette flow. First, the flow is forced with the most non-normally amplified structures: streamwise oriented rolls [70]. These rolls redistribute the velocity into a streaky flow, with low- and high-speed streaks in the streamwise velocity. The streaky profile is unstable to undulatory disturbances in the streamwise direction, through a Kelvin-Helmholtz instability. Finally, the nonlinear effects due to the instability re-energise the original streamwise rolls.

Just as for Newtonian flows, for purely elastic flows we know that streamwise vortices and streaks are the most non-normally amplified structures [98]. The second step of the Newtonian SSP is an instability of the flow generated by the vortices. In purely elastic fluid, there is no known instability of this flow. In fact, it was believed that a bulk purely elastic instability of this kind was ruled out by the study of Azaiez and Homsy [105] [4, 106].

Azaiez and Homsy [105] used multiple constitutive models (Oldroyd-B, Gisekus and the co-rotational Jeffrey's model) to perform a linear stability analysis of the free shear flow of a dilute polymer solution. They found that the addition of polymers suppresses the inertial instability. In the appendix to this study, E. J. Hinch shows that the instability they observe maps onto the Newtonian shear layer instability with surface tension. The inviscid flow of the polymeric fluid leads to an elastic membrane formed from streamwise aligned polymers. The large normal forces create tension in this sheet

that resists bending. The instability has been replicated in a spatially developing linear stability analysis [107], as well as in experiments on the flow after a backwards facing step [108], and in wakes [109, 110]. However, it is important to emphasise that the above studies considered a high Reynolds number ($Re$), high Weissenberg number ($Wi$), and low polymer fraction flow, a very different limit to the purely elastic limit examined in this chapter.

In this chapter we demonstrate the existence of a purely elastic analogue of the Newtonian shear layer instability, controlled by the Weissenberg number rather than the Reynolds number. This provides a potential mechanism for the instability of a purely elastic vortical flow (the second stage of the SSP). Using a linear stability analysis we examine a new Kelvin-Helmholtz like instability in both Oldroyd-B and FENE fluids. A purely elastic fluid is found to be unstable at sufficiently high Weissenberg number for both the Oldroyd-B and FENE constitutive models. In Chapter 6 we explore how this instability opens up a route to an exact coherent structure via a purely elastic self-sustaining process.

We are interested in a generic instability for flows with a sharp change in the streamwise velocity, and so large normal stresses in the fluid. Because we are searching for a generic mechanism, we assume that the instability will be somewhat insensitive to the particular laminar profile. For convenience, we select a hyperbolic tangent shear layer. We examine the dependence of the instability on flow properties ($\beta$, $Wi$ and $Re$) and the influence of boundaries. We consider both a nearly free shear layer in section 3.2.1 (with a finite, but large, region of constant velocity between the shear layer and the walls), and a free shear layer in section 3.2.2.

The flow we consider is a hyperbolic tangent shaped laminar profile for the streamwise velocity across a channel. This is given by

$$U(y) = \tanh\left(y/\Delta\right)\coth\left(L/\Delta\right) , \tag{3.1}$$

where $y = \pm\Delta$ is the region of shear. $y = 0$ is the centreline of the channel, so that as $\Delta$ tends to zero the flow tends to a free shear instability (see Fig. 3.1).

This geometry is usually overlooked for purely elastic flows because it cannot be realised in the classical shear layer experiment, the flow over a backwards facing step (see e.g Sato [111] for an example of this experiment). At high $Re$, the flow overshoots the step due to inertia and the flow immediately after the step is approximated by a hyperbolic tangent streamwise flow velocity. Purely elastic fluids have negligible inertia, and so there is no inertial overshoot, and the flow adopts the channel flow profile immediately after the step. Despite this, there are many flows with sharp changes in streamwise flow velocity. As we shall see in the self-sustaining process (Chapter

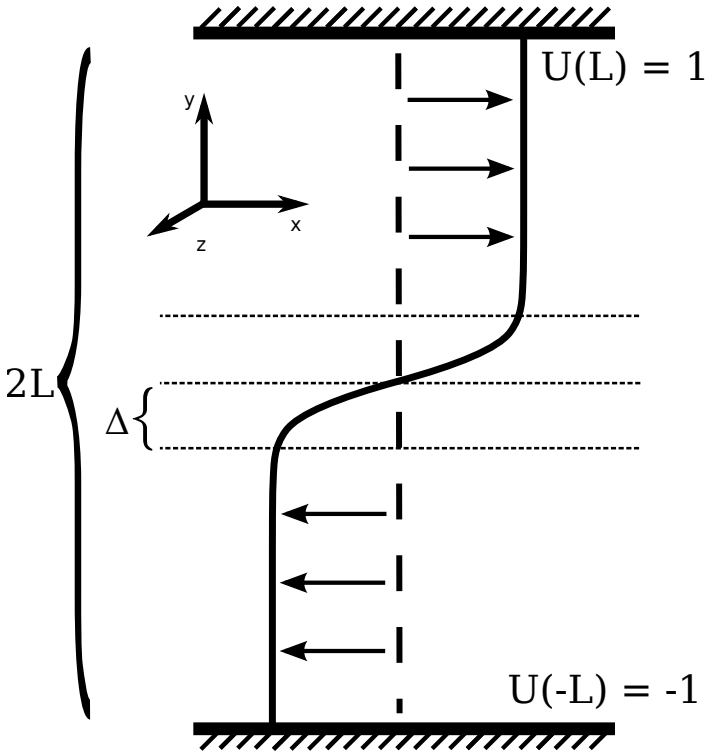


Figure 3.1: Diagram of a shear layer in a channel. $x, y$ and $z$ are the streamwise, wall-normal and spanwise directions respectively. The black line shows the hyperbolic tangent velocity profile. $L$ is half the width of the channel.

6), transitional plane Couette flow can also contain shear layers, but we expect the instability to have wider applications as well, such as oscillatory pipe flow (Chapter 5), purely elastic Kolmogorov flow [58, 112], purely elastic Taylor-Couette instabilities in shear-banded flows [113, 114] and turbulence in an elasto-inertial channel flow [42, 43].

An important class of unstable flows, closely related to the shear layer, are the co-flows. These multi-layer or co-extrusion instabilities occur when the interface between two immiscible fluids with differing properties becomes unstable. We believe that there is an analogy between the sharp jump in first normal stress in the shear layer and the jump in first normal stress across the interface in a co-flow. Thus we expect our instability to be localised in and near the region of high shear rate. Sharp changes in stress are responsible for instability in layered flows of different fluids, and so we expect the mechanisms involved to be similar.

Theoretical studies of layers of UCM and Oldroyd-B fluids flowing in pipe, channel or plane Couette geometries revealed that a contrast of the first normal stress difference

across a mathematically-sharp interface causes undulations of the interface along the flow direction [27–29, 34, 115–122], while a contrast of the second-normal stress difference results in undulations of the interface along the vorticity direction [123]. Studies employing more complex constitutive equations reach a similar conclusion (see [31], for example), and the existence of these instabilities is corroborated by experiments performed with polymer solutions and melts (see [32, 119, 122, 124–128], for example). Hinch et al. [33] discuss the general mechanism of this instability, an analysis that we explore further in the discussion section of this Chapter. Related instabilities have been predicted and observed in shear-banded flows of worm-like micellar solutions where the contrast of elastic properties between bands of the same fluid drives undulations of the interface [113, 114, 129–138]. Finally, Wilson and Rallison [139] demonstrated that channel flows of elastic fluids having continuously stratified elastic properties are also unstable.

We begin by describing the shear layer problem for purely elastic flows. We will examine the numerical linear stability analysis for a shear layer confined to a channel flow: looking at dispersion relations and the dependence on the viscosity ratio, Reynolds number, and Weissenberg number. We will explore how the eigenvector of the instability compares to the Newtonian instability, before examining the influence of the boundaries using an analysis of the free shear layer. Finally, we will consider the influence of finite-extensibility on the problem using the FENE-P model.

## 3.1 Problem formulation

Throughout this Chapter, dimensionless quantities are non-dimensionalised relative to the half width of the shear layer, $\Delta$, rather than the half-channel width, $L$. This allows us to examine how the shear layer instability depends on $L$ as we approach the free shear limit of $L = \infty$. The dimensionalisation we use is similar to the one given in (2.4), but we take $\Delta$ rather than $L$ as the length scale, and $U_0$ (the velocity at the walls) as the velocity scale. This allows us to define $Wi$ and $Re$ based on the characteristic shear rate, $U_0/\Delta$.

We used an Oldroyd-B fluid at low Reynolds number (typically $Re < 10$) and a small ratio between the solvent and total viscosities $\beta = \frac{\mu_s}{\mu_s+\mu_p}$. This approximates a purely elastic flow, where the polymer contribution to the stress on the fluid is much larger than the solvent contribution. The Oldroyd-B Navier-Stokes and constitutive

equations are then:

$$
\begin{aligned}
Re\left[\frac{\partial \mathbf{v}}{\partial t} + \mathbf{v}\cdot\nabla\mathbf{v}\right] &= -\nabla p + \beta\nabla^2\mathbf{v} + (1-\beta)\nabla\cdot\boldsymbol{\tau} + \mathbf{f} \\
\frac{\partial \mathbf{C}}{\partial t} + \mathbf{v}\cdot\nabla\mathbf{C} &= (\nabla\mathbf{v})^T\cdot\mathbf{C} + \mathbf{C}\cdot(\nabla\mathbf{v}) - \boldsymbol{\tau} \\
\boldsymbol{\tau} &= \frac{1}{Wi}\left(\mathbf{C} - \mathbb{I}\right) ,
\end{aligned} \tag{3.2}
$$

where $\mathbf{v}$ is the velocity, $\mathbf{f}$ is the forcing that maintains the shear layer, $\boldsymbol{\tau}$ is the polymeric stress tensor and $\mathbf{C}$ is the conformation tensor.

For the laminar flow with $\mathbf{v} = (U(y), 0, 0)^T$, the stresses are given by

$$
\begin{aligned}
T_{xx}(y) &= 2\,Wi\left(\frac{\partial U}{\partial y}\right)^2 \\
T_{xy}(y) &= \frac{\partial U}{\partial y} \\
T_{yy}(y) &= 0\,,
\end{aligned} \tag{3.3}
$$

and $T_{ij}$ is the stress tensor for the base flow. The numerical method, described in Appendix A.1, uses a collocation method in the $y$ direction and a Fourier decomposition,

$$
g(y) = \left(\widetilde{g}(y)e^{ikx} + \widetilde{g}^*(y)e^{-ikx}\right)e^{\lambda t}\,, \tag{3.4}
$$

for all disturbance variables $g = u, v, p, \tau_{i,j}$. Where $k$ is the streamwise wavenumber of the disturbance and $\mathrm{Re}(\lambda)$ is the growth rate of the mode.

## 3.2 Linear stability analysis

At low Reynolds number, low $\beta$ and sufficiently large Weissenberg number we observe an instability across a range of streamwise disturbance wavenumbers. This instability persists for small $L$ (albeit with a fairly complex dependence on the boundaries) and under the FENE-P model. Before we examine the free shear instability, we will focus on the instability when the flow is affected by the channel walls.

### 3.2.1 The bounded shear layer

Now we consider a two dimensional flow with boundaries, with the laminar flow given in (3.1) and (3.3). To validate our approach, we examine the high Reynolds number regime and recover a Newtonian Kelvin-Helmholtz instability. At high Reynolds number the

instability is insensitive to the distance to the walls when $L = 10$ (Fig. 3.2) and is consistent with the Kelvin-Helmholtz instability given in Criminale et al. [62].

We see the maximum growth rate of the instability decrease with increasing Weissenberg number, and this trend is stronger for smaller $\beta$ (Fig. 3.3). This is the same behaviour reported by Azaiez and Homsy [105] for the Kelvin-Helmholtz instability of a polymeric fluid. At low Reynolds number, we find that the width of the channel has a greater affect on the instability of the flow. However, the flow is still unstable at large $L$ (Fig. 3.5).

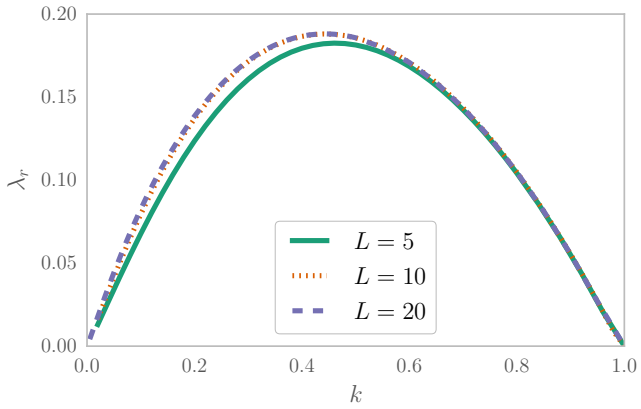


Figure 3.2: Dispersion relations for various values of $L$ and $Re = 1000$, $Wi = 0.01$. When results are rescaled, the instability is found to be insensitive for $L = 10$.

At $L = 10$ the flow is unstable for $Re < 0.01$ far lower than the usual linear stability threshold of $Re_{ls} \sim 1000$ for a Newtonian Kelvin-Helmholtz instability. This is shown in the dispersion relations of Fig. 3.4a and the maximum growth rate dependence on $Re$ in Fig. 3.4b. In the $Re = 0$ and low $\beta$ regime, we observe a maximum in the growth rate against Weissenberg number (Fig. 3.4c). The critical Weissenberg number is fairly constant up to $\beta = 0.5$. For larger $\beta$, the onset is delayed to very large $Wi$.

As the Reynolds number decreases the walls become more important to the instability (for example, see the dispersion relations in 3.5), this makes a true $Re = 0$ instability difficult for us to observe. In order to remove the dependence on the walls and recover a free shear instability it is necessary to move them further away. This problem gets worse at lower $Re$. By introducing just a very small contribution from inertia (results are taken for $Re \lesssim 0.1$ on the length scale of the instability), we can remove the dependence on the walls.

The streamfunction (where the instantaneous fluid velocity is tangent to the lines of constant colour, Fig. 3.6a), and the stresses (Figs 3.6b, 3.6c and 3.6d), show a complex

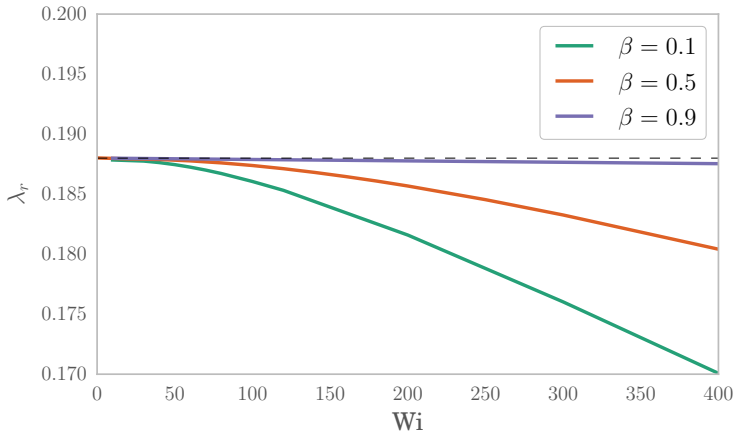


Figure 3.3: Maximum growth rate against Weissenberg number at $Re = 1000$, $L = 10$. The maximum of the dispersion relation decreases for the Kelvin-Helmholtz instability as the Weissenberg number is increased. The grey dashed line is the maximum of the dispersion relation for the Newtonian fluid. The decrease in $\lambda_r$ corresponds to increased stability of the base flow, this matches the observations made in Azaiez and Homsy [105].

flow. As well as vortices within the shear layer, there are large vortices arranged with opposite rotational directions above and below the shear region which extend almost to the walls (Figs 3.7a and 3.7b). The streamfunction (Fig. 3.8a) shows that the eigenvector extends far from the shear layer even when $L$ is very large. This is a very different situation from that observed for the Newtonian Kelvin-Helmholtz instability, where there is an exponential decay in the velocity outside the region of shear (Fig. 3.8b). The larger penetration depth out of the shear layer by the viscoelastic eigenvector is likely linked to the stronger dependence on $L$ relative to the Newtonian instability.

As $L$ increases for a particular purely elastic instability, the width of the instability increases slightly, however in the limit of very large $L$ the eigenvector appears independent of the walls (Figs 3.8a and 3.6a). The extended vortices in our purely elastic case seem to correspond to the eigenvectors in Azaiez and Homsy [105] at larger elasticity ($G \sim Wi/Re$). Their $G = 5$ case would correspond to only $Wi = 0.5$ for $Re = 0.1$ in our units, such that the instability they observe is still the inertial instability (see Azaiez and Homsy [105] Fig. 8). Nonetheless at least one of their observations does apply: the fact that the velocity disturbance is lower within the shear layer than outside it implies that the shear layer will be less likely to roll up. In the Newtonian instability, net velocities within the shear layer will distort its shape, however the purely elastic instability appears to have less of an effect on flow within the shear layer.

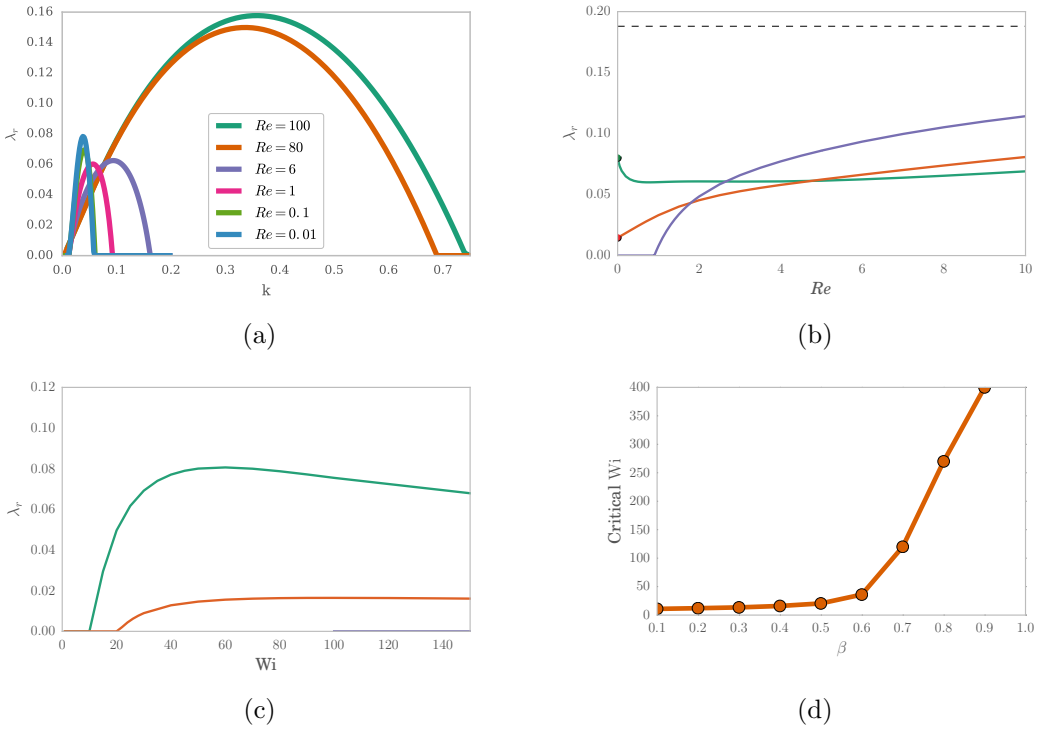


Figure 3.4: a) Dispersion relations at $Wi = 50$ for $L = 10$ with $Re = 0.01, 0.1, 1, 6, 80, 100$ and where $Re$ increases from left to right. b) The change in the maximum of the dispersion relation as the Reynolds number decreases at $Wi = 5.0$, for $\beta = 0.1$ (turquoise), $\beta = 0.5$ (orange), and $\beta = 0.9$ (purple). At low $Re$ the instability is clearly still present for large polymer concentrations with $L = 10$. For comparison, the grey line shows the maximum growth rate for the Newtonian instability at $Re = 1000$. c) The change in the maximum of the dispersion relation as $Wi$ is increased at $Re = 0$ with $L = 10$. The turquoise and orange lines gives the behaviour at $\beta = 0.1$, $\beta = 0.5$ respectively. d) The critical Weissenberg number against $\beta$ at $Re = 0$, $L = 10$. The onset of the purely elastic instability is strongly suppressed for $\beta$ larger than 0.5.

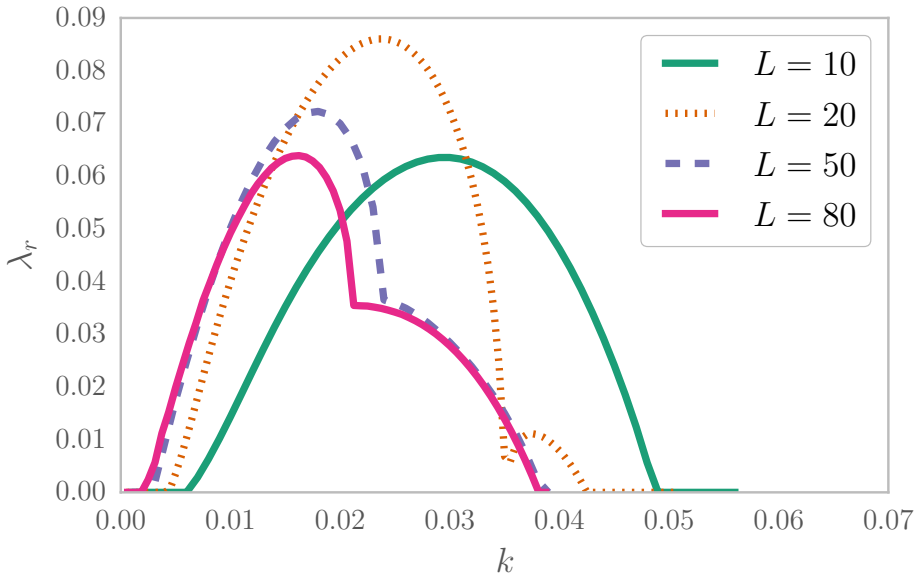


Figure 3.5: Dispersion relations for various values of $L$ at $Re = 0.1$, $Wi = 100$. Even when the system is insensitive to the walls (at $L = 80$ for this Reynolds number) there is still an instability present.

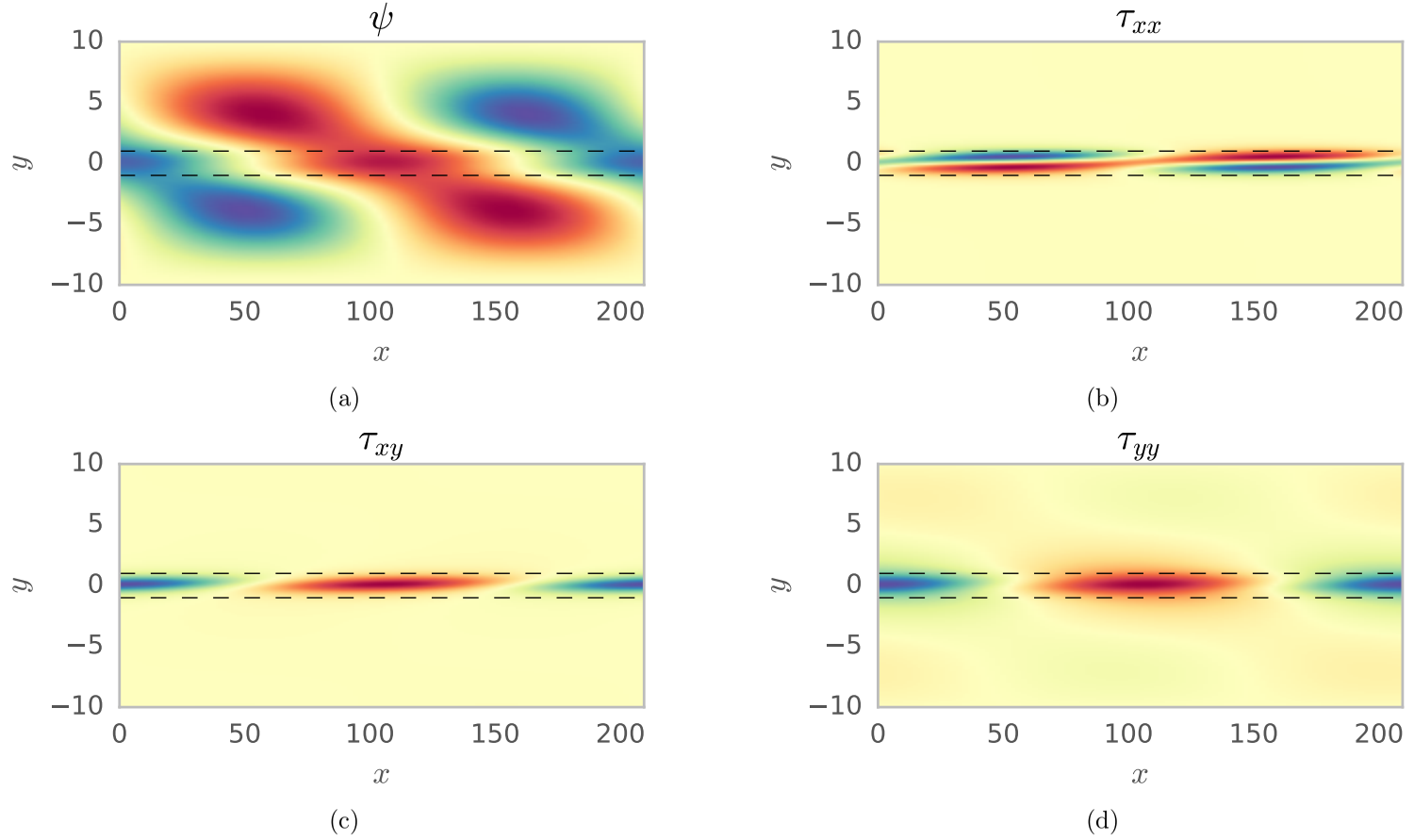


Figure 3.6: The instability at $L = 10$, $Wi = 100$, $Re = 0.1$ and $k = 0.03$ using 250 psuedospectral points. Panel a) shows streamfunction of the eigenfunction — lines of constant colour are streamlines in the flow. Panel b) shows $\tau_{xx}$, c) shows $\tau_{xy}$, and d) shows $\tau_{yy}$. The axes are in units of the half channel width.

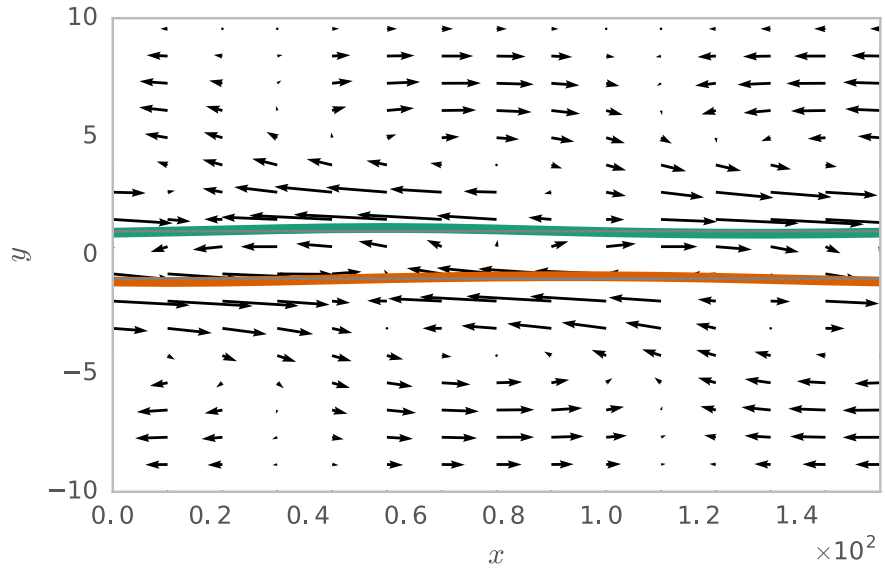


(a)

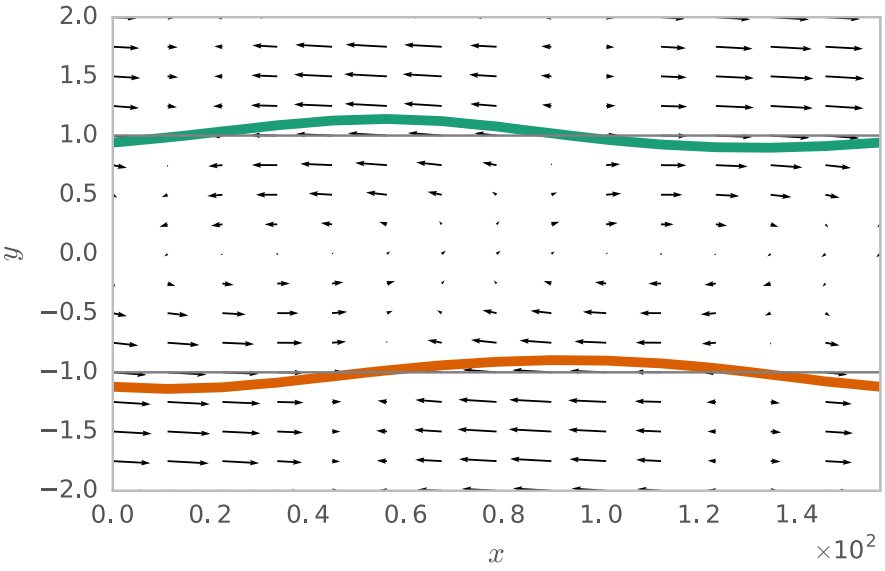


(b)

Figure 3.7: Vector plots of the eigenfunction of the instability when $Re = 0.1$, $Wi = 50$, $L = 10$, $\beta = 0.1$ and $k = 0.04$ using 200 psuedospectral points. The axes are in units of the half channel width. Turquoise is the isoline for $u = U(\Delta)$, orange is the isoline for $u = U(-\Delta)$. b) is a zoomed version of a).

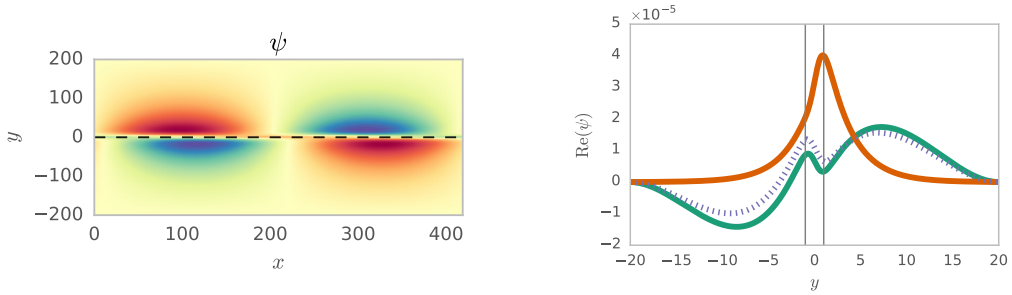


(a) (b)

Figure 3.8: Panel a) shows streamfunction of the largest eigenfunction of the instability when $Re = 0.1$, $Wi = 100$, $L = 200$, $\beta = 0.1$ and $k = 0.015$ using 250 psuedospectral points. Red is positive (streamlines of the flow point clockwise around the contours), Blue is negative (streamlines of the flow point anticlockwise around the contours). Panel b) shows real part of the streamfunction of the Newtonian Kelvin Helmholtz instability at $Re = 100$, $k = 0.722$ compared with the purely elastic Oldroyd-B and FENE-P instability for $\beta = 0.1$, $Re = 0.0$, $k = 0.02$, $Wi = 50.0$, both at $L = 20$. Newtonian eigenvector (orange), with the Oldroyd-B (turquoise) and the FENE model (dashed purple) at $\ell = 100$. The phases of the three eigenfunctions are such that the $y = 0.5$ point has zero imaginary part. The streamfunction of the Newtonian Kelvin Helmholtz instability decays exponentially towards the channel walls, whereas large vortices are present outside the shear layer in the purely elastic case.

### 3.2.2 The free shear layer

The analysis was repeated in the limit of no boundaries on the flow by performing a passive transform of the coordinate system from $y = [-1, 1]$ to a new variable,

$$z(y) = \begin{cases} \dfrac{y}{1-y}, & 0 \leq y \leq 1 \\ \dfrac{y}{1+y}, & -1 \leq y \leq 0 \end{cases} \tag{3.5}$$

$$U = \tanh z\,, \tag{3.6}$$

This system ought to be completely insensitive to the boundary conditions at the walls so we refer to it as 'free shear' throughout this chapter.

For a free shear layer we observe an instability grow from around $k \sim 0.06$ and move to lower wavenumber as the Weissenberg number increases. The dispersion relations shown in Fig. 3.9b show this dependence of the unstable eigenvalues on $Wi$. The dispersion relation for the instability remains broad in $k$ until $Wi \sim 100$ where a new eigenvector becomes dominant.

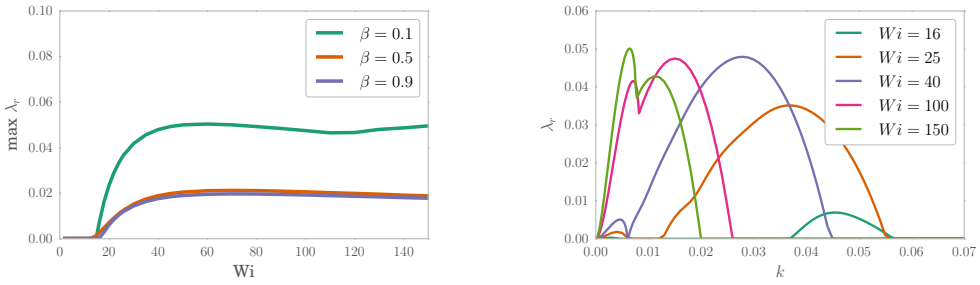


(a) (b)

Figure 3.9: a) Free shear version of the instability. Plot of the maximum growth rate against Weissenberg number at $Re = 0.01$. b) Dispersion relations at various Weissenberg numbers to accompany the trend in Fig. a).

The maximum of the instability also increases with increasing Weissenberg number. Extracting the maximum growth rate from the dispersion relations at a fixed $Re$ for various $Wi$ allows us to show how the instability depends on both $\beta$ and $Wi$ (Fig. 3.9a). The maximum growth rate saturates at $Wi \sim 50$ and remains approximately constant with increasing Weissenberg number. The slight non-monotonicity in the curve is the result of the switch-over in the dominant instability eigenmode.

As the Reynolds number is reduced the Newtonian Kelvin-Helmholtz instability disappears and an entirely separate, purely elastic instability arises. Although the

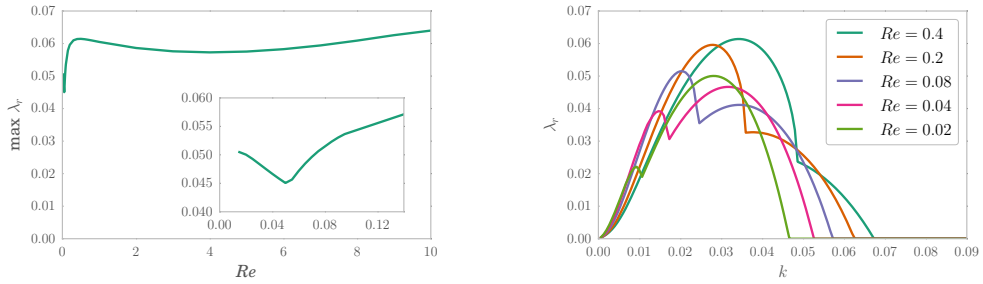


(a) (b)

Figure 3.10: a) Free shear version of the instability. Plot of the maximum growth rate against Reynolds number with $Wi = 50$. b) Dispersion relations at various Reynolds numbers to accompany the trend in Fig. a).

dominant eigenvalue changes often as $Re$ decreases, the flow is still unstable even down to $Re = 0.01$ (see Figs 3.10a and 3.10b). Again, the complicated dependence on $Re$ appears to be due to the appearance and disappearance of new dominant eigenmodes of the instability.

The free shear layer does show some differences from the shear layer with walls as the Reynolds number is reduced, however at high $Re$ they look very similar (Fig. 3.11).

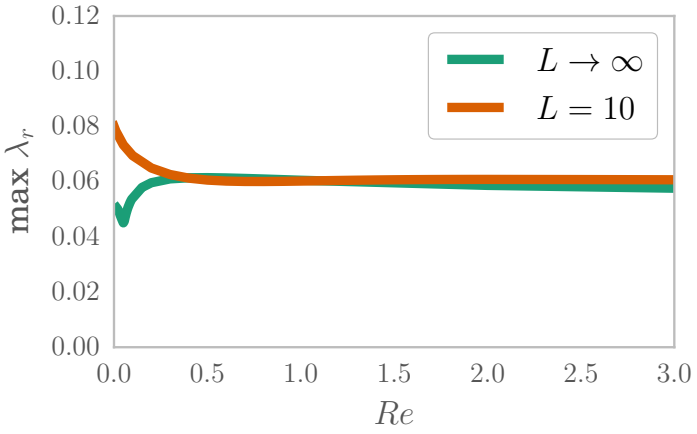


Figure 3.11: The maximum growth rate for the instability of the free shear layer (turquoise) and bounded shear layer (orange) at $L = 10$. By $Re = 1$ the bounded shear layer appears insensitive to $L$.

### 3.2.3 Consistency of results with the FENE model

The FENE-P viscoelastic fluid has the advantage of being similarly easy to analyse using our spectral method, but also including a finite extensibility for the polymers. This leads to a stress which depends on a conformation tensor ($\mathbf{C}$) for the polymer dumbbells via a non-linear spring force:

$$\boldsymbol{\tau}_p = \frac{1}{Wi}\frac{\mathbf{C}-\mathbb{I}}{1-\frac{Tr(\mathbf{C})}{\ell^2}}\,. \tag{3.7}$$

This is the dimensionless form of (1.26). As discussed in the introduction, this model adds shear thinning to the Oldroyd-B model, and prevents the stress diverging as tr($\mathbf{C}$) approaches $\ell^2$. $\ell$ is a measure of the maximum extension of the polymers — unrelated to the length scale of the flow $L$.

The finite extensibility version of the shear layer with walls gives good agreement with the Oldroyd-B version with a half-channel width of $L = 10$. The dispersion relations (not shown) have a similar shape to Fig. 3.4a. Shorter lengths bring about a stronger instability and do not delay it to higher Weissenberg number (Fig. 3.12). A shorter length scale for the polymers results in an amplification of the instability.

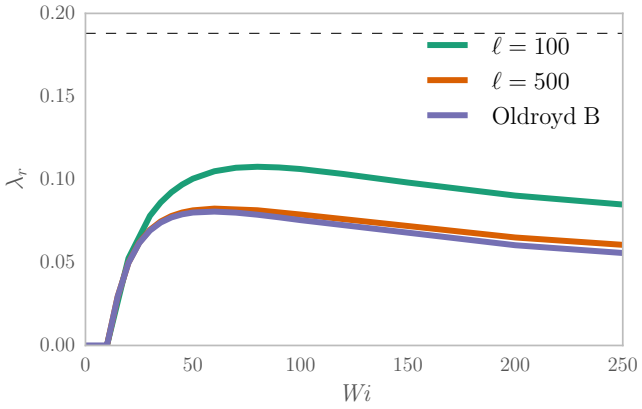


Figure 3.12: Plot of the maximum growth rate against Weissenberg number at $Re = 0$, $\beta = 0.1$ and $L = 10$ for the Oldroyd-B model and two values of $\ell$, the maximum polymer extension length. The Oldroyd-B model corresponds to $\ell \to \infty$. The grey line shows the maximum growth rate for the Newtonian instability at $Re = 1000$ for reference.

## 3.3 Discussion

In Fig. 3.3, we have reproduced the behaviour of the Kelvin-Helmholtz instability in a dilute polymer solution, given by Azaiez and Homsy [105]. We have also shown that there is a new, purely elastic shear layer instability at low $Re$ and high $Wi$ (Fig. 3.4a). The instability is both robust under altering the width of the channel containing the shear layer, and is present in flows with boundaries as well as in the unbounded flow (Figs 3.4a and 3.9b). However, when the shear layer is wide and the Reynolds number is small, the shape of the dispersion relation is affected by the presence of the walls (Fig. 3.5), and the maximum growth rate increases (Fig. 3.11). The linear instability consists of vortices above and below the shear layer (Fig. 3.7a) as well as within it (Fig. 3.7b). This is in contrast to the Newtonian Kelvin-Helmholtz instability, where there is an exponential decay in velocity outside the shear layer.

The analysis for the system in the channel has implications for the self-sustaining process. The Kelvin-Helmholtz instability in the Newtonian SSP takes place on a length scale of about 10% of the width of the channel, or $L = 10$. If this length scale is similar in the purely elastic case, we can say that the viscoelastic Kelvin-Helmholtz instability is sensitive to the walls at $L = 10$ and a $Re \lesssim 1$ (see Fig. 3.11). However, this uses the shear layer length scale $\Delta$ for $Re$: using the channel length scale $L$, the boundaries will affect the flow when $Re \lesssim 10$. Given that purely elastic flows typically occur with $Re < 1$, the purely elastic shear layer instability in the plane Couette self-sustaining process (Chapter 6) should be affected by the boundaries.

We have seen and characterised a generic instability of a shear layer in a purely elastic flow. In Chapter 5 we will investigate this instability as a mechanism for the instability of the oscillatory channel flow of an Oldroyd-B liquid. In Chapter 6, we expose the instability which drives streamwise vortices and streaks in plane Couette flow (the most non-normally amplified structures) unstable. We will see that the wavenumbers, Weissenberg and Reynolds numbers characteristic of the shear layer instability are consistent with an instability of purely elastic streaks. In the next chapter, we check the non-linear behaviour of this instability and show that the non-linear terms do not saturate until the instability has produced a secondary flow with kinetic energy of $\sim 1\%$ of the base flow.

# Chapter 4

# The nonlinear dynamics of a viscoelastic shear layer

In the previous chapter, we found an instability in a viscoelastic shear layer. In this Chapter we obtain 2D steady and travelling wave solutions from that instability. We use both an adapted form of the root finding algorithm of Chapter 2, and a 2D time iteration code for the Oldroyd-B model, which is introduced below.

The nonlinear dynamics of the Newtonian shear layer is an important flow, with relevance to a wide variety of experimental flows, from combustion devices to water waves. We know that the Kelvin-Helmholtz instability of a shear layer has an eigenvector known as Kelvins cat-eyes — a line of vortices within the shear layer [140]. From here the shear layer widens, and nonlinear effects become more and more important until eventually it rolls up and the vortices merge. Experiments show that this process repeats, with vortices pairing and merging as the shear layer develops (an example experiment is given by Winant and Browand [141]). Theoretical approaches to the problem include small amplitude nonlinear equations, such as the Stuart Landau equation as well as simulations of point vortices and full time dependent flow simulations [142]. The Stuart Landau equation accurately reproduces the roll-up of the vortices [143]. Direct numerical simulations of a spatially periodic flow show that all vortices eventually merge until there is one vortex in the domain [144].

In the introduction to the previous chapter we considered the interfacial instability between two fluids of different viscosity — a Newtonian problem which is quite close to our own. This problem has also been the subject of some nonlinear analysis: including terms of higher order in the perturbation, and in the long wavelength limit, weakly nonlinear analysis yields a Kurumoto-Sivashinsky equation with steady, quasi-periodic and travelling wave states [145]. To date, there is no evidence of roll-up of the interface for this instability.

There is little understanding of the nonlinear dynamics of viscoelastic flows. A weakly nonlinear analysis has demonstrated the nonlinear instability of viscoelastic plane Poiseuille flow [146], despite its linear stability [19]. The closest numerical study to our own is probably by Renardy [147], where they consider a Landau expansion for the plane Poiseuille flow of two layers of UCM fluid. This problem also involves a jump in viscosity to replicate the experiments of Khomami et al. [148], however, when the viscosity of the two fluids is the same they find an instability when the height of the lower fluid layer is 30% of that of the upper layer. Removing the effects of viscosity stratification and surface tension, they find that the instability caused by the jump in $Wi$ at the interface is supercritical.

In shear banded Plane Poiseuille flow of the Johnson-Segalman model there is numerical evidence for a nonlaminar steady state [135]. The flow shear bands such that there is a plug flow in the centre of the channel with zero shear rate. The shear banding interfaces at the top and bottom of this region are unstable to waves in the streamwise direction. In the final steady state, these interfaces are travelling waves that move in-phase.

In Chapter 3 we found an instability for the purely elastic shear layer flow. In this Chapter, we check that this instability does not saturate at very small amplitude, and that it has a significant effect on the flow. We also explore the whether the instability is subcritical or supercritical as we change the Weissenberg number. The problem we consider is the same laminar profile as (3.1). The set-up is identical to Fig. 3.1, but in order to maintain the laminar profile we must introduce a body forcing to the equation for the streamwise velocity. This forcing ensures that the hyperbolic tangent profile is the laminar flow, and that any deviation from this is due to instability.

As this is a 2D problem, the continuity equation reduces to $\frac{\partial u}{\partial x} = -\frac{\partial v}{\partial y}$. We eliminate this equation using the streamfunction formulation of (3.2) where $u = \frac{\partial \psi}{\partial y}$ and $v = -\frac{\partial \psi}{\partial x}$. This leaves us with 4 equations for the streamfunction and 3 components of $C$, the polymeric conformation tensor,

$$Re\left[\partial_t \nabla^2\psi + (\mathbf{v}\cdot\nabla)\,\nabla^2\psi\right] = \beta\nabla^4\psi - (1-\beta)\nabla\times\nabla\cdot\boldsymbol{\tau} \tag{4.1}$$

$$\nabla\cdot\mathbf{v} = 0 \tag{4.2}$$

$$\boldsymbol{\tau} = \frac{1}{Wi}(\mathbf{C}-\mathbb{I}) \tag{4.3}$$

$$\partial_t\mathbf{C} + (\mathbf{v}\cdot\nabla)\,\mathbf{C} = (\nabla\mathbf{v})^T\cdot\mathbf{C} + \mathbf{C}\cdot(\nabla\mathbf{v}) - \boldsymbol{\tau}\,. \tag{4.4}$$

We still require an additional equation for the mean velocity. For the $y$-component, the boundary conditions ensure that this is zero everywhere. However, for the $x$-component

mean velocity, $\overline{u} = \overline{\frac{\partial \psi}{\partial y}}$, we must solve

$$Re\overline{\frac{\partial}{\partial t}\frac{\partial \psi}{\partial y}} = Re\overline{\frac{\partial \psi}{\partial x}\frac{\partial^2 \psi}{\partial y^2}} + \beta\overline{\frac{\partial^3 \psi}{\partial y^3}} + \frac{1-\beta}{Wi}\overline{\frac{\partial C_{xy}}{\partial y}} + f(y)\,, \tag{4.5}$$

where $\overline{\cdot}$ is an average in the $x$ direction, corresponding to the zeroth Fourier mode, and $f(y)$ is the forcing. The laminar stresses given in (3.3) for a $x$ independent flow imply that the forcing is

$$f(y) = -\frac{\partial^3 \psi_{lam}}{\partial y^3} = \frac{\partial^2 U}{\partial y^2}\,. \tag{4.6}$$

In the case of the bounded shear layer flow, $U(y) = \tanh\left(y/\Delta\right)\coth\left(1/\Delta\right)$ just as in (3.1).

## 4.1 Time iteration numerical method

In order to simulate these equations we discretise them in both time and space. We developed a spectral method in space and a 4th order implicit-explicit hybrid method in time. For the spatial discretisation we transform the 4 variables to Fourier-Chebyshev space so that,

$$\begin{aligned} g(x,y) &= \sum_{n=-N}^{N}\sum_{m=0}^{M+1} \tilde{g}_{n,m} \mathrm{e}^{ink_x x} T_m(y) \\ T_m(y) &= \cos(m\,\arccos(x))\,, \end{aligned} \tag{4.7}$$

where $g$ is any flow variable, $T_m$ is the $m^{th}$ Chebyshev polynomial of the first kind, $N$ is the number of Fourier modes, $M$ is the number of Chebyshev modes and $k_x$ is the wavenumber of the discretisation. We use the pseudospectral method given in appendix A.1 to perform derivatives and products.

To discretise in time, we use a 2-stage, partially implicit method. First we calculate a prediction of the fields at the half step, then we use this prediction for the calculation of the nonlinear terms in the full step. For each of these stages the calculation is implicit in the linear terms and explicit in the nonlinear ones.

The equation for the streamfunction, given in (4.1), involves a time derivative of the Laplacian of $\psi$, therefore, in order to calculate $\psi$ we must invert a differential operator. Fortunately, this problem decouples in Fourier space, so we may treat each Fourier

mode separately. The equations for each time step have the structure,

$$
\begin{aligned}
c^* &= \left(1 + \frac{h}{4\,Wi}\right)^{-1} \left(c^s - \frac{h}{4\,Wi}c^s + h\Theta(\psi^s, c^s, t)\right) \\
c^{s+1} &= \left(1 + \frac{h}{2\,Wi}\right)^{-1} \left(c^s - \frac{h}{2\,Wi}c^s + h\Theta(\psi^*, c^*, t + \frac{h}{2})\right)
\end{aligned} \tag{4.8}
$$

$$
\begin{aligned}
\psi^* = \left[\nabla^2 - \frac{\beta h}{4Re}\nabla^4\right]^{-1} &\left(\nabla^2\psi^s + \frac{\beta h}{4Re}\nabla^4\psi^s \right. \\
&\left. + \frac{h}{4}\mathcal{D}(c^* + c^s) + h\Gamma(\psi^s, t)\right) \\
\psi^{s+1} = \left[\nabla^2 - \frac{\beta h}{2Re}\nabla^4\right]^{-1} &\left(\nabla^2\psi^s + \frac{\beta h}{2Re}\nabla^4\psi^s \right. \\
&\left. + \frac{h}{2}\mathcal{D}(c^{s+1} + c^s) + h\Gamma(\psi^*, t + \frac{h}{2})\right),
\end{aligned} \tag{4.9}
$$

where $s$ is the discrete index to the current time, $h$ is the size of the time step, $\Theta$ is a nonlinear function with terms in the products of $\psi$ and $c$, and $\Gamma$ is a nonlinear function with terms in the products of $\psi$ with $\psi$. $\mathcal{D}$ is an operator which acts on $c$ to give the polymeric stress terms in (4.1). $\Theta$, $\Gamma$ and $\mathcal{D}$ are given by,

$$
\Theta(\psi, c) = \frac{\partial\psi}{\partial x}\frac{\partial c}{\partial y} - \frac{\partial\psi}{\partial y}\frac{\partial c}{\partial x} + A^T c + cA \tag{4.10}
$$

$$
A(\psi) = \nabla\mathbf{v} = \begin{pmatrix} \frac{\partial^2\psi}{\partial x\partial y} & \frac{\partial^2\psi}{\partial x^2} \\ \frac{\partial^2\psi}{\partial y^2} & -\frac{\partial^2\psi}{\partial x\partial y} \end{pmatrix} \tag{4.11}
$$

$$
\Gamma(\psi) = \frac{\partial\psi}{\partial x}\frac{\partial\nabla^2\psi}{\partial y} - \frac{\partial\psi}{\partial y}\frac{\partial\nabla^2\psi}{\partial x} \tag{4.12}
$$

$$
\mathcal{D}c = \frac{(\beta - 1)}{Re}\nabla \times (\nabla \cdot c)\,. \tag{4.13}
$$

The inverse operators in square brackets are formed by inverting a matrix problem once for each Fourier mode at the beginning of the code with the no-slip boundary conditions on the streamfunction,

$$
\begin{aligned}
\frac{\partial\psi_n}{\partial x}(\pm 1) &= 0 \\
\frac{\partial\psi_n}{\partial y}(\pm 1) &= 0\,.
\end{aligned} \tag{4.14}
$$

For the zeroth Fourier mode of $\psi$, we use (4.5) the streamwise component of the

momentum equation,

$$\overline{\psi^*} = \left[\frac{\partial}{\partial y} - \frac{\beta h}{4Re}\frac{\partial^3}{\partial y^3}\right]^{-1}\left(\frac{\partial\overline{\psi^s}}{\partial y} + \frac{\beta h}{4Re}\frac{\partial^3\overline{\psi^s}}{\partial y^3} + \overline{\frac{\partial\psi^s}{\partial x}\frac{\partial^2\psi^s}{\partial y^2}} + \beta\overline{\frac{\partial^3\psi^s}{\partial y^3}} + \frac{(1-\beta)}{Wi}\overline{\frac{\partial c^s_{xy}}{\partial y}} + f\right)$$

$$\overline{\psi^{s+1}} = \left[\frac{\partial}{\partial y} - \frac{\beta h}{4Re}\frac{\partial^3}{\partial y^3}\right]^{-1}\left(\frac{\partial\overline{\psi^s}}{\partial y} + \frac{\beta h}{4Re}\frac{\partial^3\overline{\psi^s}}{\partial y^3} + \overline{\frac{\partial\psi^*}{\partial x}\frac{\partial^2\psi^*}{\partial y^2}} + \beta\overline{\frac{\partial^3\psi^s}{\partial y^3}} + \frac{(1-\beta)}{Wi}\overline{\frac{\partial c^s_{xy}}{\partial y}} + f\right). \tag{4.15}$$

For this equation, the differential operators are $\left[\frac{\partial}{\partial y} - \frac{\beta h}{4Re}\frac{\partial^3}{\partial y^3}\right]$ and $\left[\frac{\partial}{\partial y} - \frac{\beta h}{2Re}\frac{\partial^3}{\partial y^3}\right]$. The boundary conditions are,

$$\frac{\partial\psi_0}{\partial y}(\pm 1) = 0 \tag{4.16}$$

$$\psi_0(-1) = 0\,. \tag{4.17}$$

This final boundary condition sets the gauge of $\psi$. The program is written in the C programming language, and is given online [149].

## 4.2 Time iteration code validation

Considerable effort was spent validating the time iteration code to ensure that it is accurate and numerically stable. In this section we summarise this analysis. Firstly, each method in the code (including the derivatives in $x$ and $y$, and the method for calculating products) was tested against analytical solutions and an independent code written in the Python programming language. For a global test of the entire code we considered well known flow results for plane Poiseuille flow, which can be corroborated using numerical and analytical linear stability analyses from the literature and using our own 1D linear stability codes. We have also used the solutions obtained from Chapter 2 to ensure that the time iteration code can reproduce the travelling wave solutions.

### 4.2.1 Poiseuille flow linear stability

Viscoelastic plane Poiseuille flow is linearly stable at all Reynolds and Weissenberg numbers, as well as viscosity ratios [19]. Each mode of the streamfunction, $\psi$ ought to decay exponentially with the leading eigenvalue $\lambda$, from the corresponding linear stability problem. Eventually the flow should return to plane Poiseuille flow. This

provides a test of the validity of our time iteration code.

We perform runs at two settings and perturb the zeroth, first and second modes in turn. The decay rate of the L2 norm of $\psi$ is then compared with the leading eigenvalue from the linear stability analysis for that mode. For eigenvalues with an imaginary part it is necessary to examine a single mode and fit a decaying sinusoidal oscillation. The imaginary part can be obtained from the frequency of this oscillation.

In order to check that the decay of perturbations to the time iteration code is correct, we need to perform a linear stability analysis of the base flow. At low amplitudes of perturbation (we use amplitudes of $\sim 10^{-8}$), the nonlinear terms are too weak to affect the dynamics and so different Fourier modes should decouple and evolve independently. By considering a perturbation in a single mode in the $x$-direction we can do a linear stability analysis to obtain a decay rate and an oscillatory wavelength for the decay of perturbations to the base flow. The flow is decomposed as,

$$g(x,y) = \sum_{m=0}^{M+1} \left( \tilde{G}_m + \tilde{g}_m \mathrm{e}^{ik_x x + \lambda t} \right) T_m(y)\,, \tag{4.18}$$

where the base flow variable is given by $\tilde{G}$ and $\tilde{g}$ gives the strength of the perturbation. $k_x$ is the wavenumber of the perturbation and $\lambda$ is the decay rate.

Substituting the above expression for the flow variables, $\psi$, $C_{xx}$, $C_{yy}$ and $C_{xy}$ and linearising about the base flow, we obtain the linear stability analysis equations given in B. Solving these equations for the decay rate corresponds to finding the solution to the generalised eigenvalue problem,

$$L\mathbf{q} = \lambda B\mathbf{q}\,, \tag{4.19}$$

where $\mathbf{q}$ is a vector containing the elements of $\psi_m$, $c_{xx,m}$, $c_{yy,m}$, $c_{xy,m}$ and $L$ and $B$ are matrices for the equations in spectral space.

### 4.2.2 The zeroth mode

For a perturbation with zero streamwise wavenumber, the linear stability equations reduce to,

$$Re\,\lambda u = \beta\frac{\partial^2 u}{\partial y^2} + \frac{1-\beta}{Wi}\frac{\partial c_{xy}}{\partial y} \tag{4.20}$$

$$\frac{c_{xx}}{Wi} + \lambda c_{xx} = 2\frac{\partial U}{\partial y}c_{xy} + 2\frac{\partial u}{\partial y}C_{xy} \tag{4.21}$$

$$\frac{c_{yy}}{Wi} + \lambda c_{yy} = 0 \tag{4.22}$$

$$\frac{c_{xy}}{Wi} + \lambda c_{xy} = \frac{\partial U}{\partial y}c_{yy} + \frac{\partial u}{\partial y}C_{yy}\,, \tag{4.23}$$

where $v = 0$ by incompressibility and the boundary conditions. The base profile is given by the Oldroyd-B steady state solution for Poiseuille flow,

$$U(y) = U_0\left(1 - y^2\right) \tag{4.24}$$

$$C_{xx}(y) = 1 - 2\,Wi^2\left(\frac{\partial u}{\partial y}\right)^2 \tag{4.25}$$

$$C_{yy}(y) = 1 \tag{4.26}$$

$$C_{xy}(y) = Wi\frac{\partial U}{\partial y}\,. \tag{4.27}$$

Solving these equations for $\lambda$ yields the decay rates of the various eigenmodes of the linear stability problem. Equation 4.22 gives either $c_{yy} = 0$ or

$$\lambda = -\frac{1}{Wi}\,. \tag{4.28}$$

Assuming $c_{yy} = 0$, we get

$$\frac{\partial^2 u}{\partial y^2} = -\alpha_v u \tag{4.29}$$

$$u(\pm 1) = 0 \tag{4.30}$$

$$\alpha_v = -\left(\beta + \frac{1-\beta}{1+\lambda\,Wi}\right)^{-1} Re\lambda\,, \tag{4.31}$$

with solution,

$$u = A\sin\sqrt{\alpha_v}y + B\cos\sqrt{\alpha_v}y\,, \tag{4.32}$$

where A and B are constants. From the boundary conditions we know that,

$$\sin\sqrt{\alpha_v} = 0\,, \cos\sqrt{\alpha_v} = 0\,, \tag{4.33}$$

and so,

$$\lambda = \frac{-Re - b\beta \pm \sqrt{(Re + b\beta)^2 - 4bRe}}{2\,WiRe} \tag{4.34}$$

$$b = Wi\left(\frac{\pi n}{2}\right)^2\,, \tag{4.35}$$

where n is an integer. This gives us the complete eigenvalue spectrum for perturbations with zero streamwise wavenumber.

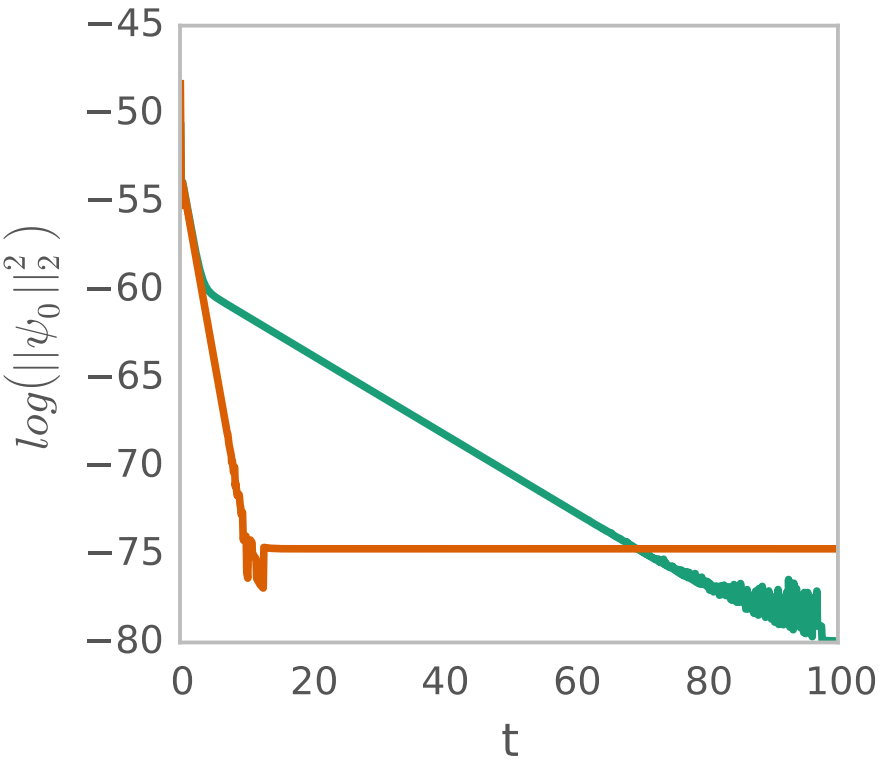


Figure 4.1: Norm of the streamfunction vector, M = 64, $Re = 0.1$, $Wi = 1.2$, $\beta = 0.8$, $k_x = 0.0$ for two different time steps, $10^{-3}$ (green) and $10^{-4}$ (red). The fit for the spectrum plots is found using the decay rate for the initial fast decay, approximately from $1 \sim 10$ time units.

To test the code we add the perturbation and record the norm of the streamfunction as it decays (Fig. 4.1). We then fit this plot to extract a decay rate and plot it on the

spectrum of eigenvalues (Fig. 4.2). As $\beta$ is reduced the decay rate of a perturbation becomes even more negative and it becomes increasingly difficult to measure. We believe the simulation requires a smaller time step in this regime because there is a large separation between the timescales of the Newtonian inertial motion of the fluid and the much longer elastic time scale of the polymeric fluid. For $\beta = 0.1$ we needed a time step of $10^{-4}$ to resolve the zeroth mode decay rate. However, as is evident from Fig. 4.2, the code is able to reproduce the linear stability analysis very accurately.

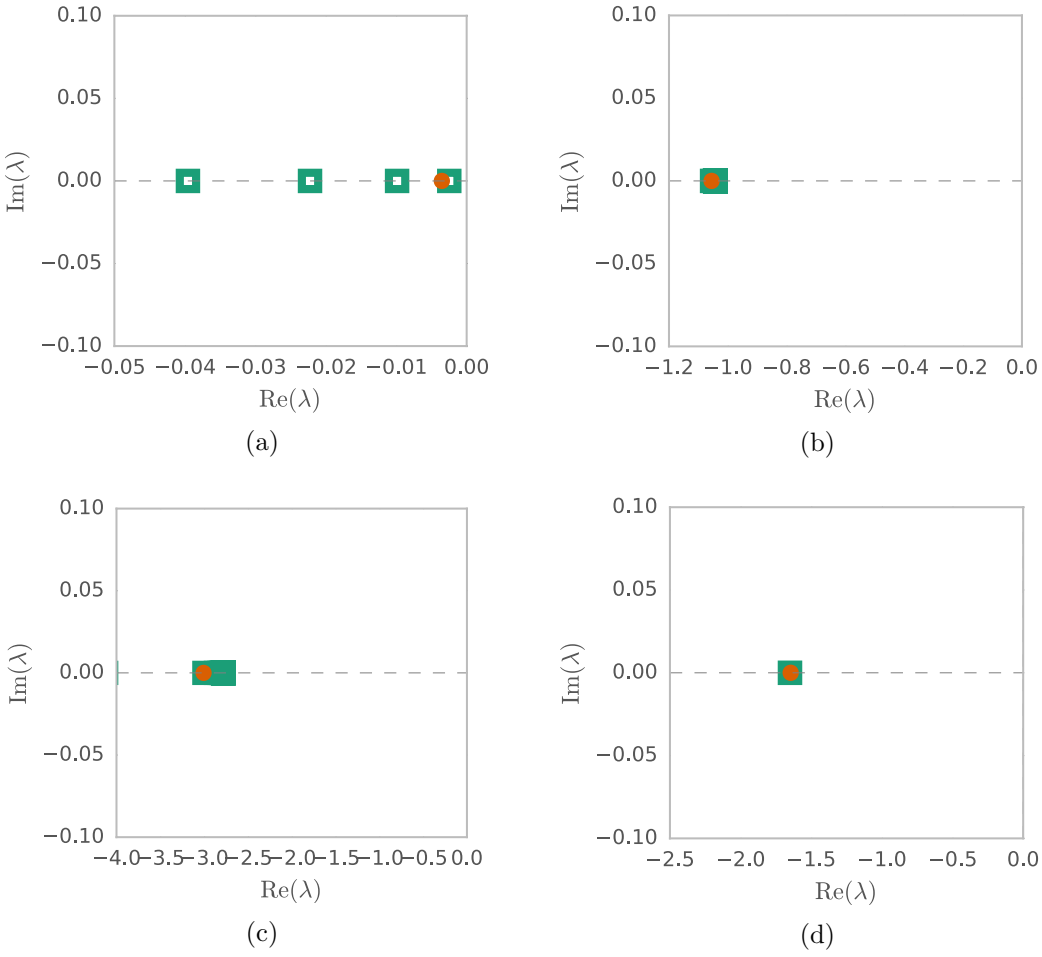


Figure 4.2: Eigenvalue spectra for the zeroth mode with M = 64 and a time step of $10^{-4}$. Square, turquoise symbols are the analytic solution, orange dots are the result from the fit of the time iteration code. a) $Re = 1000$, $Wi = 0.5$, $\beta = 0.9$, $k_x = 0.0$. b) c) and d) are the spectra for the viscoelastic case with $Re = 0.1$, $Wi = 1.2$ and $\beta = 0.8, 0.3, 0.1$ respectively.

### 4.2.3 The first and second modes

Rather than calculate the eigenvalue spectrum analytically when the streamwise wavenumber, $k_x$ is non-zero we use a 1D linear stability code to numerically calculate a spectrum of eigenvalues. The eigenvalues are now complex, but the calculation of the decay rate using the norm of the streamfunction can only provide the real part. To overcome this difficulty we also calculate the most unstable eigenvalue using a single Chebyshev mode (we arbitrarily choose the sixth mode in this analysis). The frequency of oscillation of this mode provides the imaginary part of the eigenvalue (Fig. 4.3).

Fig. 4.4 shows the results of a few of these fits on the first mode, and Fig. 4.5 shows the results for the second mode. Although the results do not match quite as well as the zeroth mode results, we believe this is due to the crowding of eigenvalues in the spectrum. It takes a long time for two states with nearly indistinguishable decay rates to separate completely. It seems likely that the flow is still made of a mix of eigenvectors, which makes it more difficult to accurately fit it to the eigenvalue spectrum.

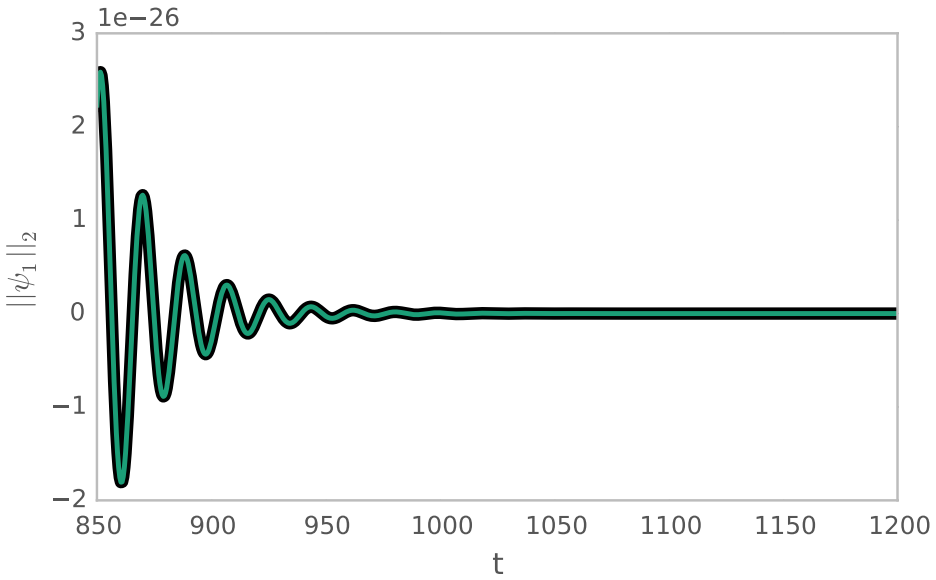


Figure 4.3: Example of a fit to a single Chebyshev mode of the 1st Fourier mode of $\psi$. M = 64, $Re = 1000$, $Wi = 0.5$, $\beta = 0.9$, $k_x = 1.0$.

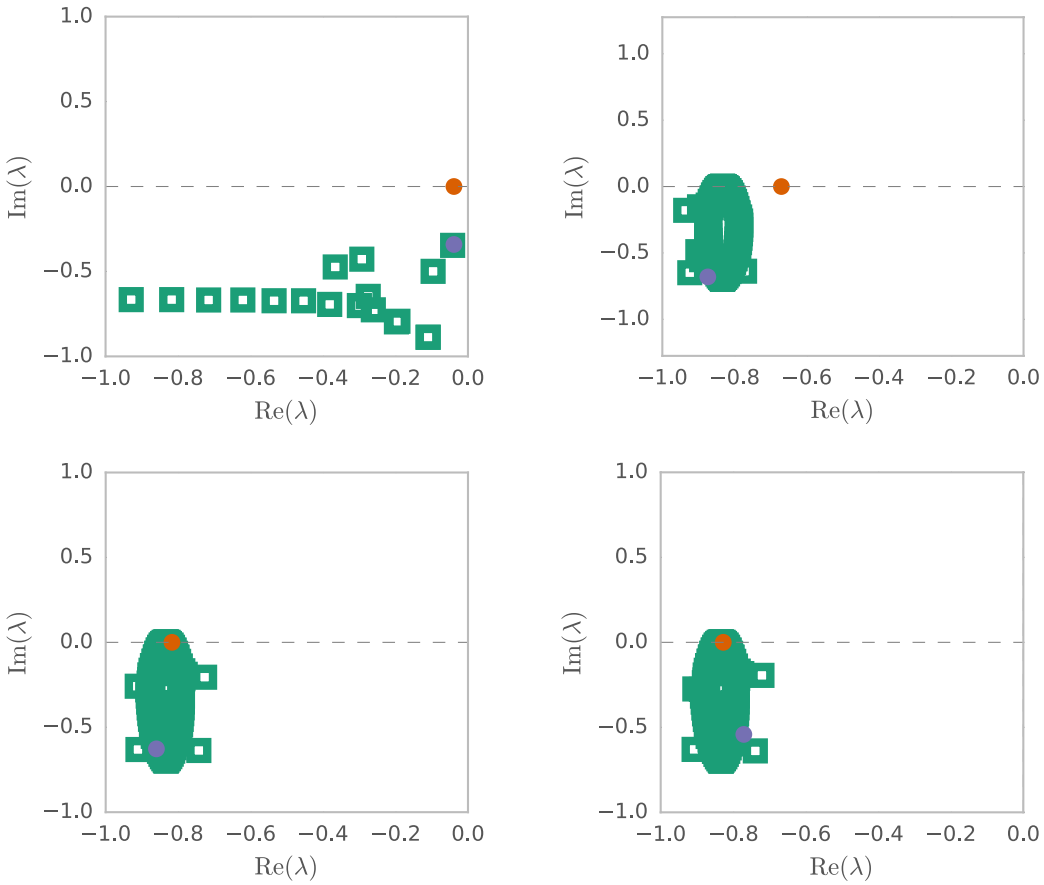


Figure 4.4: Eigenvalue spectra compared with the dynamics of the first Fourier mode with M = 64. The orange disc is the result from the fit of the time iteration code norm of the streamfunction, the purple disc is from the fit to the sixth Chebyshev mode. The turquoise squares are the linear stability analysis result. a) $Re = 1000$, $Wi = 0.5$, $\beta = 0.9$, $k_x = 1.0$. b) c) and d) are the spectra for the viscoelastic case with $Re = 0.1$, $Wi = 1.2$, $k_x = 0.7$ and $\beta = 0.8, 0.3, 0.1$ respectively.

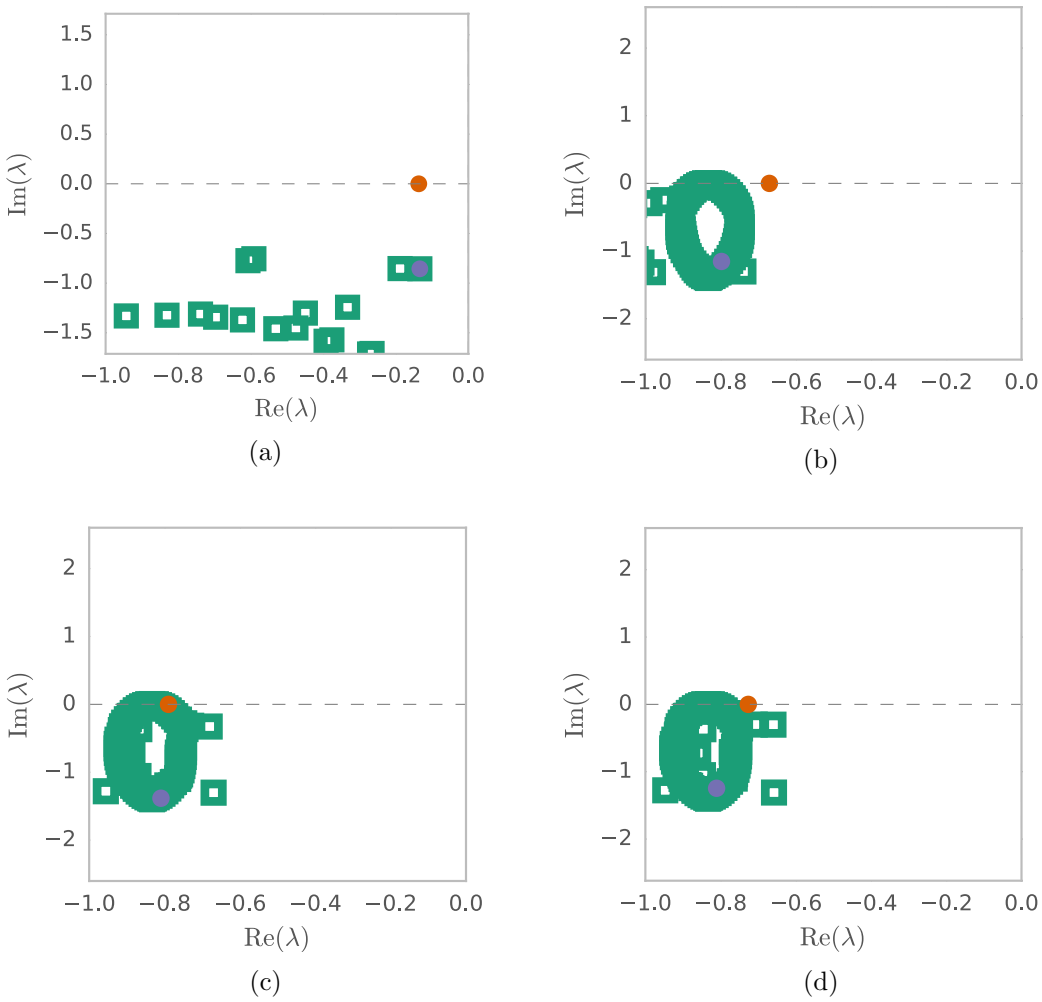


Figure 4.5: Eigenvalue spectrum compared to the fit of the second mode of the time iteration run at M = 64. The orange disc is the result from the fit of the time iteration code norm of the streamfunction, the purple disc is from the fit to the sixth Chebyshev mode. The turquoise squares are the linear stability analysis result. a) $Re = 1000$, $Wi = 0.5$, $\beta = 0.9$, $k_x = 2.0$. b), c) and d) with $Re = 0.1$, $Wi = 1.2$, $k_x = 0.7$ and $\beta = 0.8, 0.3, 0.1$ respectively.

### 4.2.4 Travelling wave solutions

We have also time iterated the viscoelastic travelling wave solutions of Chapter 2, to ensure that they correspond to a steady state (Fig. 4.6). If we compare the Fourier modes of the travelling wave solution and the steady state, the curves are coincident (these figures are not shown here). To measure the convergence, we measure the norm of the difference between the travelling wave solution and the time iterated steady state for each Fourier mode (shown in Figs 4.7).

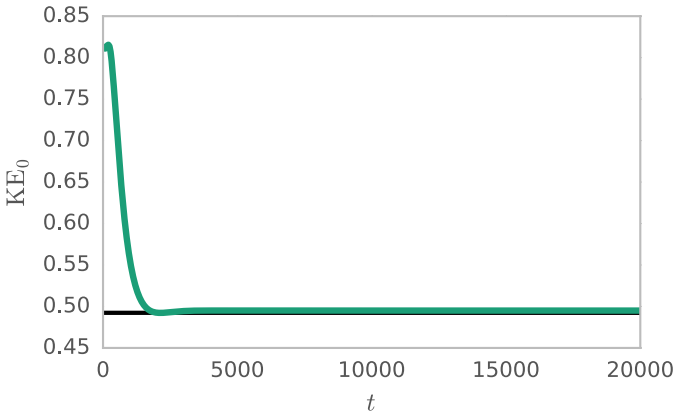


Figure 4.6: The kinetic energy with time of the travelling wave solution (horizontal line) and the time integration of a random initial perturbation to Poiseuille flow (turquoise). $N = 7$, $M = 40$, $Re = 4000$, $Wi = 1.0$, $\beta = 0.1$, $k_x = 1.38$, $h = 0.01$

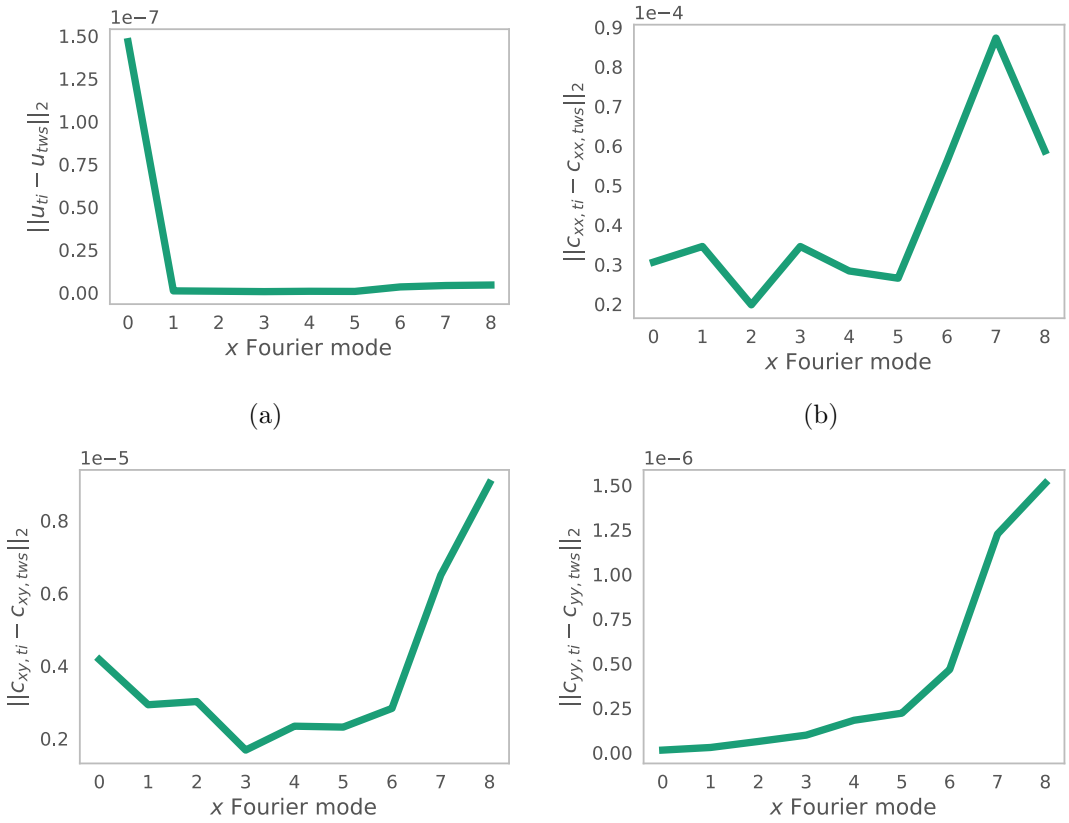


Figure 4.7: Comparison of the travelling wave solution and the time iteration solution after 2000 time units. The $x$-axis gives the Fourier mode and the $y$-axis shows the sum of squares of the difference between the travelling wave solution and the time iterated state, for $N = 8$, $M = 50$, $Re = 4000$, $Wi = 1.0$, $\beta = 0.1$, $k_x = 1.38$, $h = 0.001$. a) $u$, b) $C_{xx}$, c) $C_{xy}$ and d) $C_{yy}$.

## 4.3 Results of the 2D time iteration

Having validated the code, we look for nonlinear steady and time periodic solutions by time iteration of a purely elastic shear layer instability. We search for solutions at parameters on constant contours of elasticity ($El = Wi/Re$) and consistent with the linear stability analysis (Fig. 4.8). We time iterate the equations using a random initial condition which satisfies the boundary conditions.

After an initial transient (usually of around 100 time units), we obtain steady (Fig. 4.9a) or time periodic states (Fig. 4.9b). The nature of these states is evident from the behaviour of the kinetic energy which is either steady or oscillates with fixed period in time. The kinetic energy is scaled by Poiseuille flow, just as in (2.13), so that the kinetic energy of the laminar shear layer flow is $KE_{\text{lam}} = 1.6875$, and the nonlinear

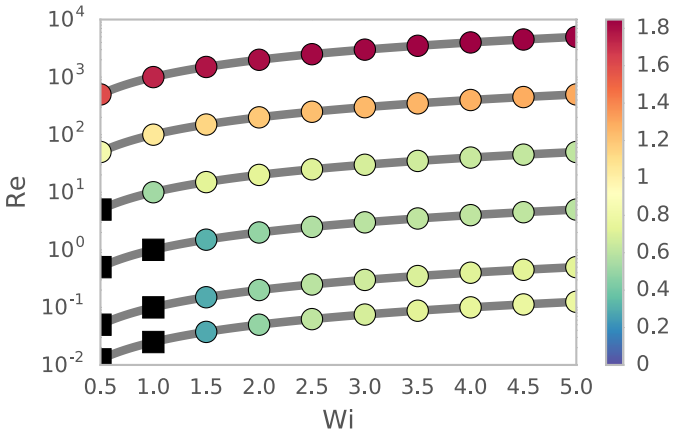


Figure 4.8: The linear stability analysis of Chapter 3. A phase diagram showing the growth rate for various Reynolds and Weissenberg numbers at $\beta = 0.1$. Grey lines are contours of constant elasticity. Black squares are data points for which the flow is linearly stable.

structures saturate with a kinetic energy of approximately $0.1 - 1\%$ of the laminar flow in the streamwise dependent modes.

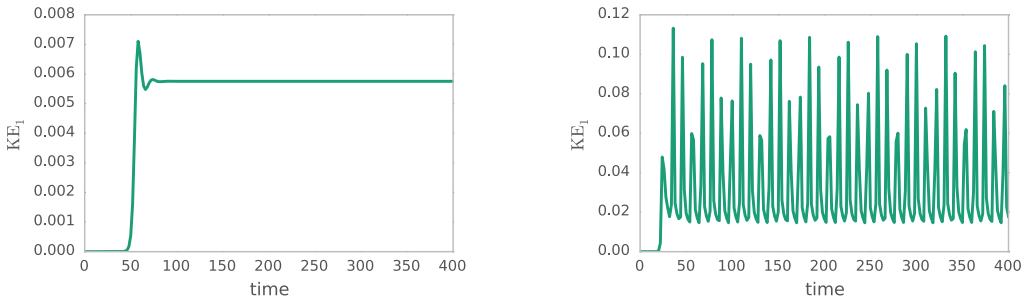


(a) (b)

Figure 4.9: Kinetic energy of the 1st mode from a viscoelastic run. 4 Fourier modes, 320 Chebyshevs, with a time step of $h = 0.01$. a) Steady state at Reynolds number of 0.15 and at Weissenberg 1.5. b) time periodic state $Re = 0.4$ and at $Wi = 4.0$. The large scale periodic pattern in the peaks is due to the low resolution sampling of the kinetic energy in time to make this plot.

We find that at low $Wi$ the flow transitions to a stationary wave at the interface, but at higher $Wi$ this wave begins to travel. The travelling wave state moves along the shear layer with a fixed velocity, otherwise, it looks very similar to the stationary state. Our simulations do not show roll-up of the interface for the purely elastic flow. An example travelling wave state with $Re = 0.1$, $Wi = 4.0$ and $\beta = 0.1$ is shown in Fig. 4.10. The orientation of the arrows gives the direction of the velocity, and the size

of the arrows gives its strength. The out-of-plane vorticity is a measure of the rotation of fluid parcels,

$$\omega = (\nabla \times \mathbf{v}) \cdot \mathbf{e}_z \tag{4.36}$$

A long wavelength dependence on the streamwise direction is visible in all the variables, $\mathbf{v}, \omega$ and the components of the stress.

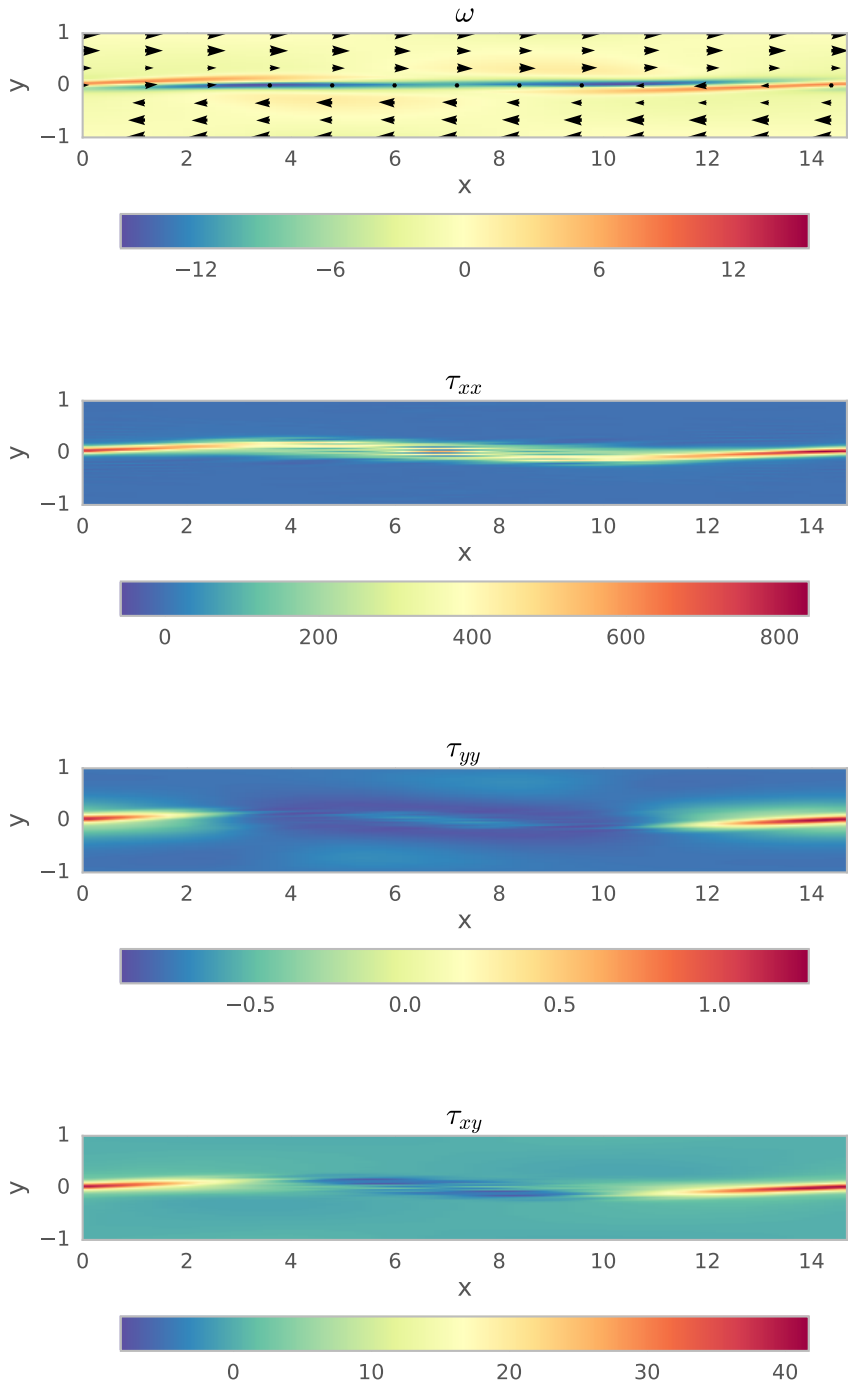


Figure 4.10: The vorticity (colour) and velocity (arrows) along with the three components of the stress. 6 Fourier modes, 320 Chebyshev polynomials, with a time step of $h = 0.01$ for $Re = 0.1$, $Wi = 4.0$, $\beta = 0.1$ and $k_x = 0.428$.

In Fig. 4.11 we explore the dependence of the average kinetic energy of the final state on $Re$ and $Wi$. Squares are stable points, circles are steady solutions, triangles are travelling wave solutions, and crosses mark simulations that became unphysical without reaching a steady state. The colour gives the time averaged kinetic energy, which we calculate by averaging over 200 time units of the simulation after it has reached its final state.

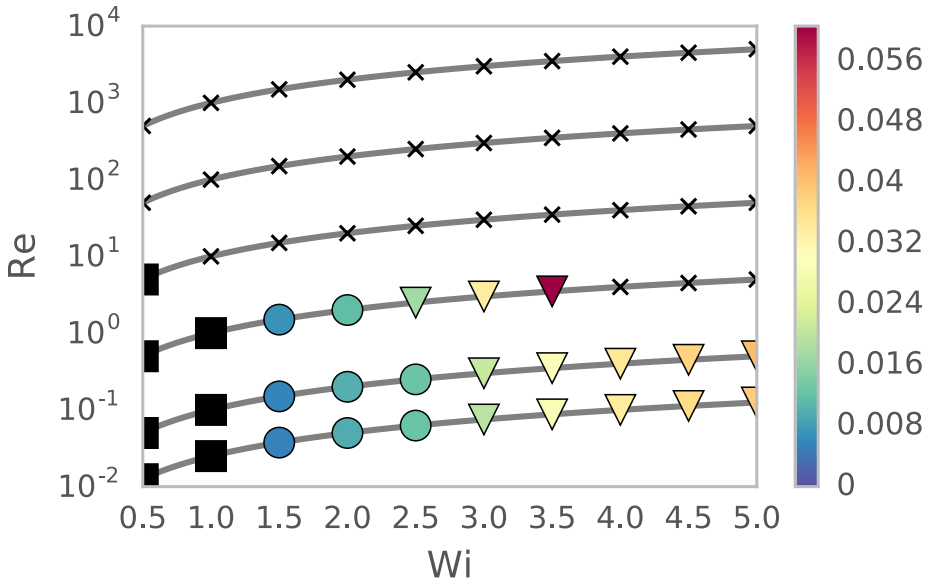


Figure 4.11: Kinetic energy of 1st mode of instability 4 Fourier modes, 320 Chebyshev polynomials, with a time step of $h = 0.01$, and wavenumber corresponding the most unstable mode from linear stability analysis. Squares are stable points, circles are steady solutions, triangles are travelling wave solutions, and crosses mark simulations that did not complete. Grey lines mark contours of constant elasticity.

We expect that the vorticity will increase in the nonlaminar flow, increasing energy dissipation. A global measure of the change in vorticity is given by the enstrophy,

$$\epsilon = \int \frac{1}{2}\omega^2 \, \mathrm{d}x\mathrm{d}y \tag{4.37}$$

where the integral is over the fluid area in one streamwise wavelength. We can plot the kinetic energy of the first Fourier mode and the enstrophy to produce bifurcation diagrams along lines of constant $El$ (Figs 4.12a and 4.12b). The transition appears to be supercritical, both from the laminar flow to the stationary waves, and from the stationary waves to travelling waves. The initial bifurcation to a stationary wave state bifurcates to travelling waves at $Wi \sim 2.5$.

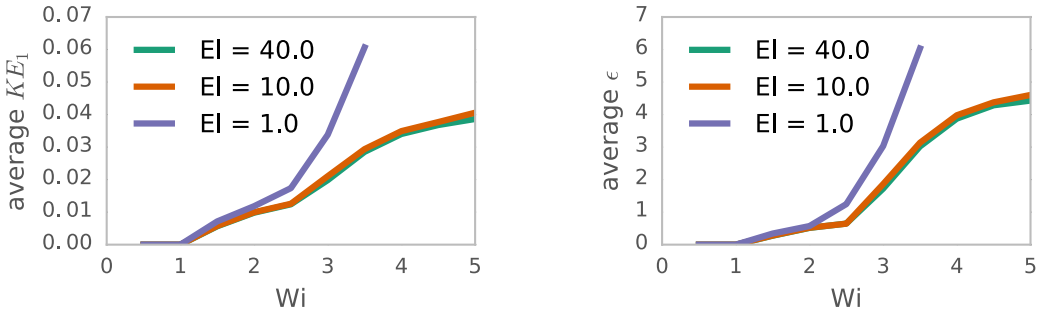


(a) (b)

Figure 4.12: Bifurcation plots for a) the kinetic energy of the first Fourier mode and b) the enstrophy of the instability subtracted from the background flow. The plots show the dependence of the solutions on Weissenberg number at constant elasticity. The results are converged, with 4 Fourier modes, 320 Chebyshev polynomials, and a time step of $h = 0.01$.

As $\beta$ increases it becomes increasingly difficult to time iterate the equations without the code becoming numerically unstable. However, just as we saw in the linear stability analysis, increasing $\beta$ stabilises the flow (Fig. 4.13a). We can also see from the phase diagram that both the stationary and travelling wave states persist for $\beta$ at least as large as 0.4. Although we could not obtain solutions above $\beta = 0.6$, the linear stability analysis (Fig. 3.4d) shows that the flow is quickly stabilised to the purely elastic shear layer instability at high $\beta$.

The instability is robust on changing the width of the shear layer, and persists up to $\Delta = 0.3$, $Wi = 5$ (Fig. 4.13b). It appears that the steady state solutions only exist for $\Delta \lesssim 0.1$, and that at higher $\Delta$ the flow transitions to the travelling wave solutions.

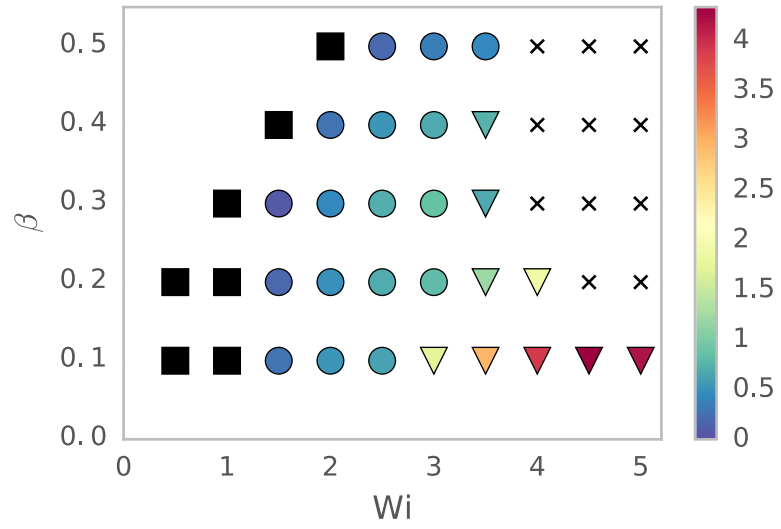


(a)

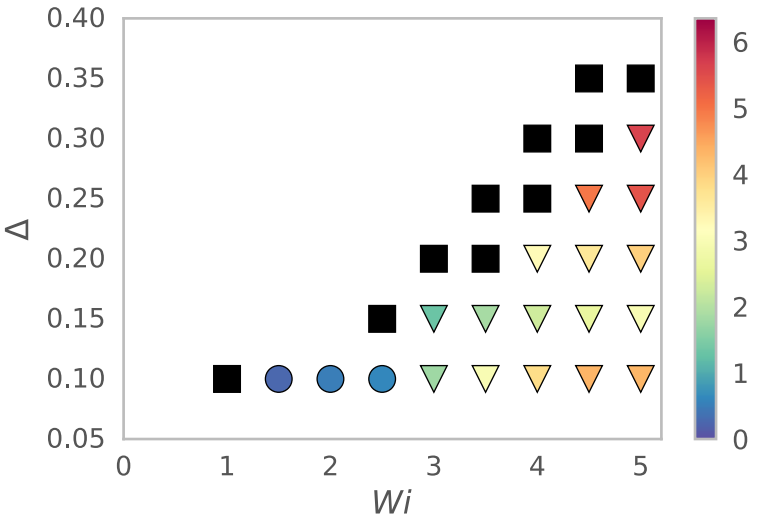


(b)

Figure 4.13: Phase diagrams for the enstrophy of the nonlaminar solutions in the at $Re = 0.1$: a) in the $\beta$, $Wi$ plane and b) in the $\Delta$, $Wi$ plane. All solutions have a resolution of 4 Fourier modes, 320 Chebyshev polynomials, and a time step of $h = 0.01$. The solution is calculated using the streamwise wavenumber corresponding the most unstable mode from linear stability analysis.

## 4.4 Exact solutions

Now that we have obtained a set of steady states, we can use these as approximate solutions for a Newton Raphson method, closely related to the method of Chapter 2. Using this method we were able to calculate a stationary solution at $Re = 0.1$ and $Wi = 1.2$. However, calculating shear layer exact solutions is difficult due to the high resolutions required to resolve these flows. At high $Wi$ the number of degrees of freedom needed to resolve the steady states becomes very high. This leads to very stiff numerical eigenvalue problems with high condition number, and makes Newton Raphson very difficult. However, the solution we find is very close to that found by time iteration, as shown in the mode by mode plots of the streamfunction and streamwise normal stress (Fig. 4.14 and 4.15).

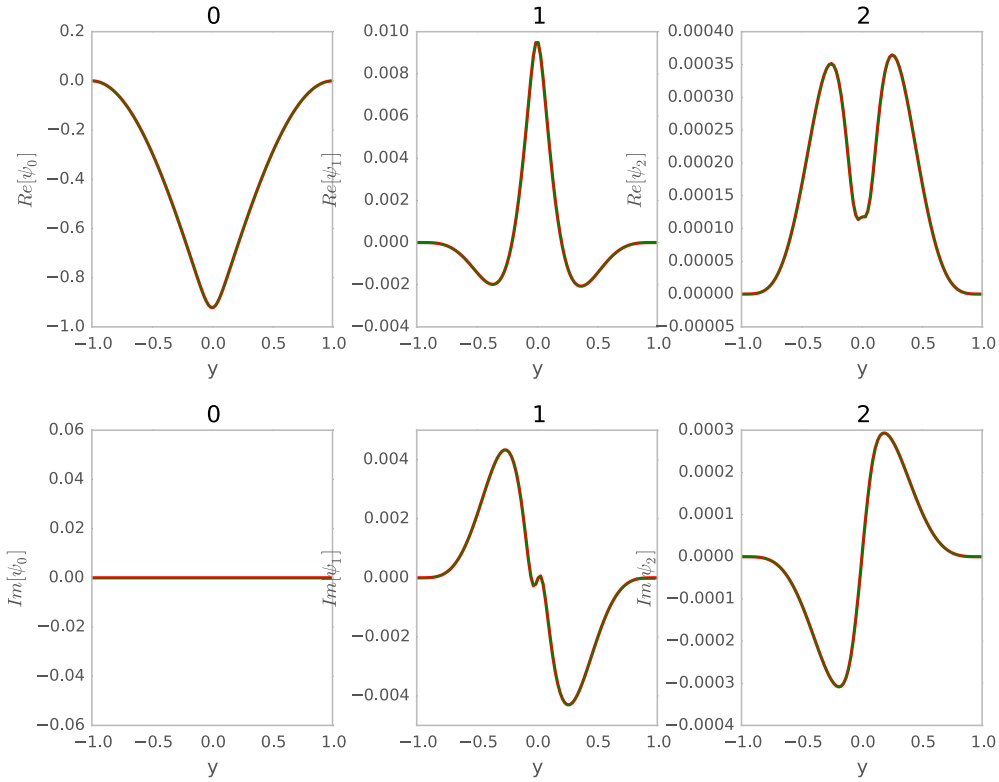


Figure 4.14: Mode by mode comparison of the streamfunction of a solution (green) with the corresponding steady state from time stepping the equations of motion. 4 Fourier modes, 256 Chebyshev polynomials, wavenumber of 0.7, at a Reynolds number of 0.1, $\beta = 0.1$ and Weissenberg of 1.2.

The laminar flow subtracted plots of the exact solutions show that the flow structure is very similar to the eigenvector of the linear instability (compare Figs 3.6a and

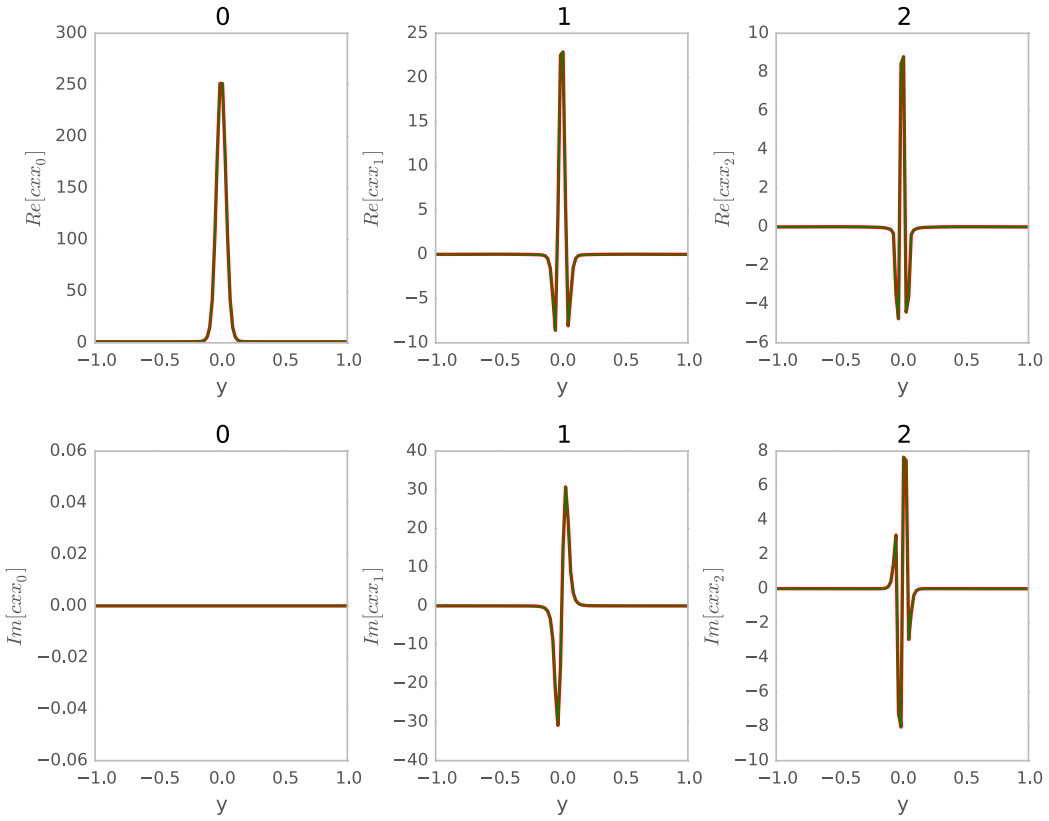


Figure 4.15: Mode by mode comparison of the $xx$ component of the conformation tensor of a solution (green) with the corresponding steady state from time stepping the equations of motion. 4 Fourier modes, 256 Chebyshev polynomials, wavenumber of 0.7, at a Reynolds number of 0.1, $\beta = 0.1$ and Weissenberg of 1.2.

4.16. It appears that the linear instability grows and then saturates without changing shape, giving a wave to the region of high shear. Focussing on a vector plot of the stationary state with the mean flow subtracted shows a similar structure to the linear stability eigenvector (compare Fig. 3.7a with 4.16 and 4.17). Contours show where the streamwise velocity is equal to its unperturbed value at the edge of the shear layer, $u = U(\pm\Delta)$.

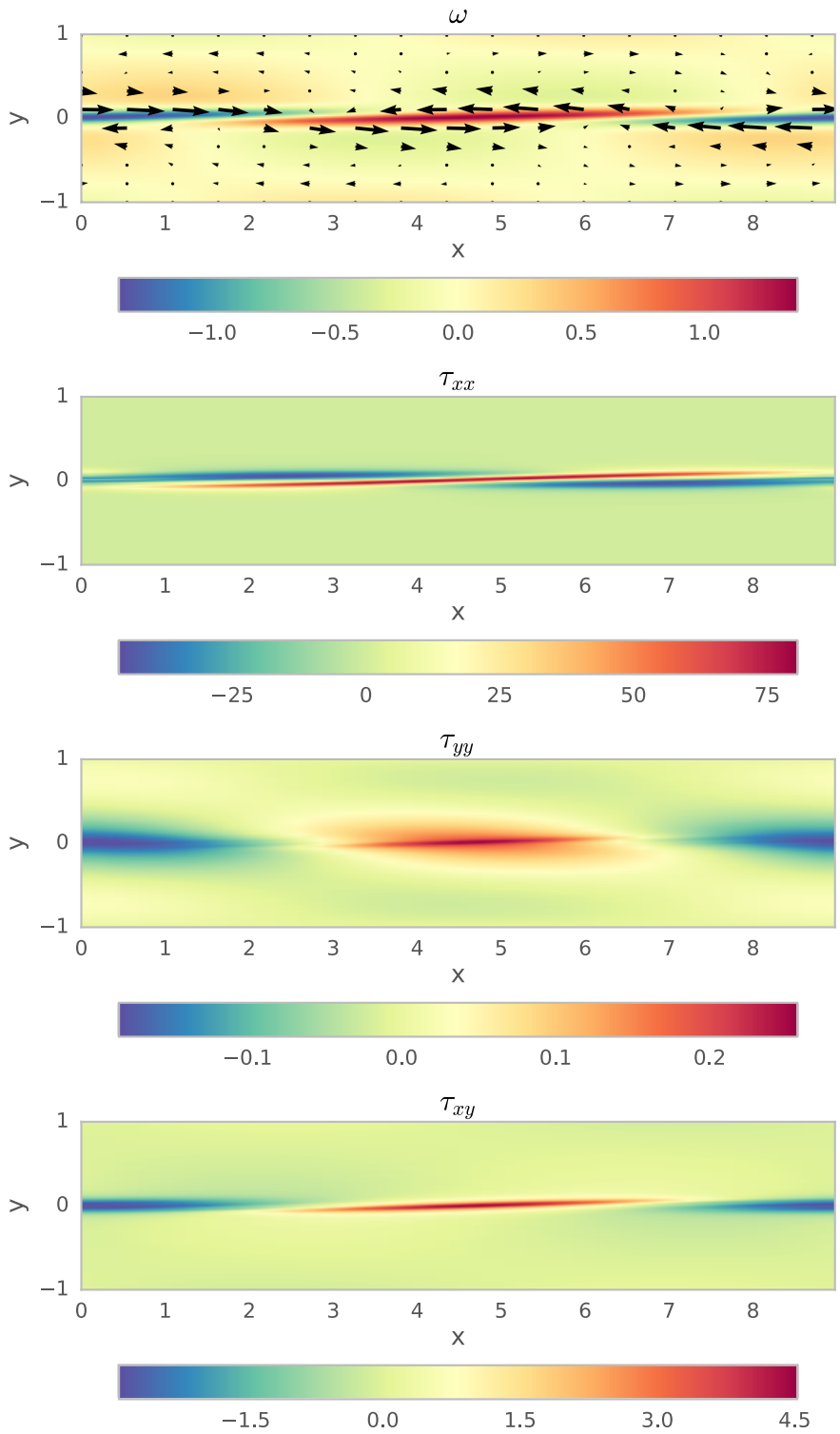


Figure 4.16: The mean flow subtracted velocity, vorticity and stresses of a stationary solution to the viscoelastic shear layer equations. 4 Fourier modes, 256 Chebyshev polynomials, wavenumber of 0.7, at a Reynolds number of 0.1, $\beta = 0.1$ and Weissenberg of 1.2.

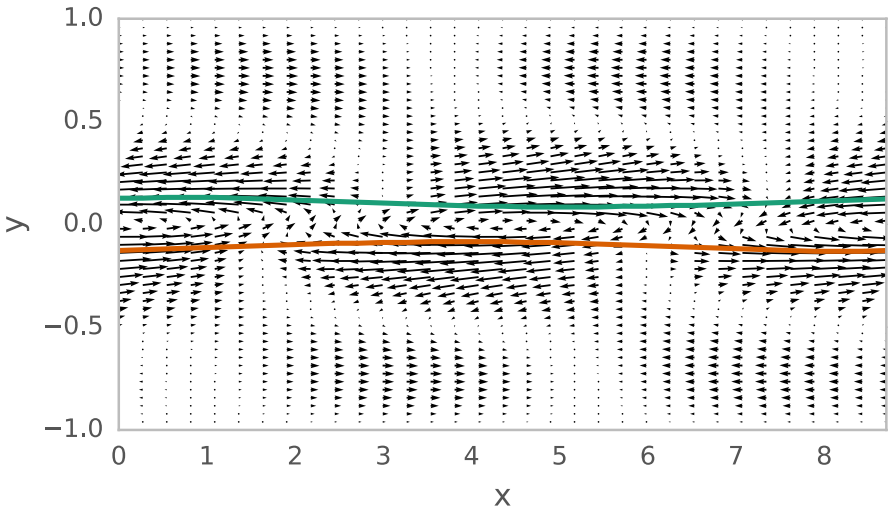


Figure 4.17: The mean flow subtracted velocity of a stationary solution to the viscoelastic shear layer equations. 4 Fourier modes, 256 Chebyshev polynomials, wavenumber of 0.7, at a Reynolds number of 0.1, $\beta = 0.1$ and Weissenberg of 1.2.

## 4.5 Discussion

In this chapter, we found that the purely elastic shear layer instability leads to non-laminar steady states in 2D. We have seen this using both a time dependent simulation and a Newton Raphson method on the Oldroyd-B equations. We found that beyond the onset Weissenberg number, the instability saturates to steady states with the same shape as the eigenvector and an amplitude relative to the mean flow of approximately 1%.

For low $Wi$ these steady states are stationary, but for $Wi \gtrsim 2.5$ they begin to travel in the streamwise direction. The bifurcation from the laminar flow to the stationary wave flow is supercritical as we increase $Wi$ at constant elasticity. This stationary wave flow bifurcates further at higher $Wi$ to the travelling wave flow, and this bifurcation is also supercritical.

In contrast to the Newtonian case, where the shear layer rolls up into vortices, a wavy shear layer in the purely elastic flow appears stable in 2D. It is possible that the purely elastic shear layer also rolls up for larger $Wi$. A possible next step would be to consider the stability of a single purely elastic vortex, as in Michalke and Timme [150]. This would allow us to say whether or not the shear layer can roll up as the Newtonian shear layer does. However, as we have discussed in the introduction to Chapter 3, the shear layer instability is of limited interest on its own. The importance of this instability is as a mechanism for the instability of more complex flows, where internal shear layers exist.

Now that we have validated the shear layer instability and the time iteration code that can reproduce it, we would like examine more complicated, real world flow scenarios to see if the shear layer instability can explain them. In the next chapter we use a slightly altered version of the time iteration code to we link the shear layer instability to the instability of purely elastic pressure driven oscillatory flow.

# Chapter 5

# Viscoelastic instabilities in oscillating channel flow

In this chapter, we consider a purely elastic instability related to the shear layer instability of Chapter 3. Although not directly related to the search for purely elastic exact coherent structures, we hope to relate the shear layer instability to a flow seen in experiments. We consider a channel flow driven by a sinusoidally oscillating piston (Fig. 5.1), ignore the end effects due to the piston, and consider only the flow due to an oscillating pressure gradient.

We shall see that, for a Newtonian fluid, the low Reynolds number laminar flow is very similar to the plane Poiseuille solution generated by the instantaneous pressure gradient. However, for some purely elastic flows, the laminar flow solution is more complex, leading to additional peaks in the streamwise velocity. These extra peaks can lead to large increases in the flow rate and a layered laminar profile with large shear rates between the layers. We will refer to purely elastic laminar solutions with this behaviour as laminar flow resonances.

These resonances have been thoroughly investigated, beginning with the analytical study on the flow between oscillating parallel plates [99]. The UCM model in pipe flow also shows these resonances [151, 152] and they persist when a spectrum of relaxation times are included [153].

Experiments on the flow of worm-like micelles under an oscillating pressure gradient in a pipe show a similar resonant behaviour due to the elasticity of the fluid [154]. The complexity of the laminar flow is understood in terms of the resonance of waves extending from the pipe walls [152, 155], and has been studied for our flow [99]. The resonant laminar flow leads to a linear instability and the formation of vortex rings [22]. The laminar flow at the instability consists of regions with large shear rate even at low $Re$, a similar flow scenario to that of the shear layer instability of Chapter 3.

This encourages us to investigate whether there is a connection between the instability of Chapter 3 and the instability of the worm-like micellar oscillatory flow.

However, worm-like micellar flows have a complex rheology, with the presence of both strong shear thinning as well as normal stress effects. In order to relate the instability of these experiments to the one of Chapter 3 we must separate out the shear thinning, normal stress and Newtonian mechanisms of instability. To eliminate the shear thinning effects we perform our analysis using the Oldroyd-B model. If our flow instability matches the experiments then we have reason to believe that shear thinning is not responsible.

To eliminate Newtonian effects, we must restrict ourselves to a range of parameters where the Newtonian oscillatory flow is stable. Experimental studies of Newtonian oscillatory flows have found critical Reynolds numbers in the range $Re = 100$–$1000$ [156–158]. In the transitional regime the flow contains bursts of turbulence during the cycle of the pressure gradient, followed by relaminarisation. Blennerhassett and Bassom [159] examined a Newtonian flow in a channel with oscillating walls. Although this flow is different, a mapping exists between the oscillation of the walls and the oscillation of end plates [154], which makes the laminar profiles similar. They perform a numerical linear stability analysis by decomposing disturbances into Fourier modes in time. Depending on the channel width, they found a critical $Re \simeq 640$ for the onset of instability. We will be operating where $Re < 1$, low enough that the Newtonian instability will not be relevant.

We examine the oscillating channel flow of an Oldroyd-B fluid within a channel, and find similar resonances to those found in the pipe case. We find a linear instability of the flow, dependent on the Weissenberg and Deborah numbers, and follow this instability to a nonlinear steady state. The neutral curve for the instability matches the resonance in the base flow and the eigenvectors are localised in regions of high shear, leading us to conclude that the enhanced shear rate of the resonant flow is responsible for the instability.

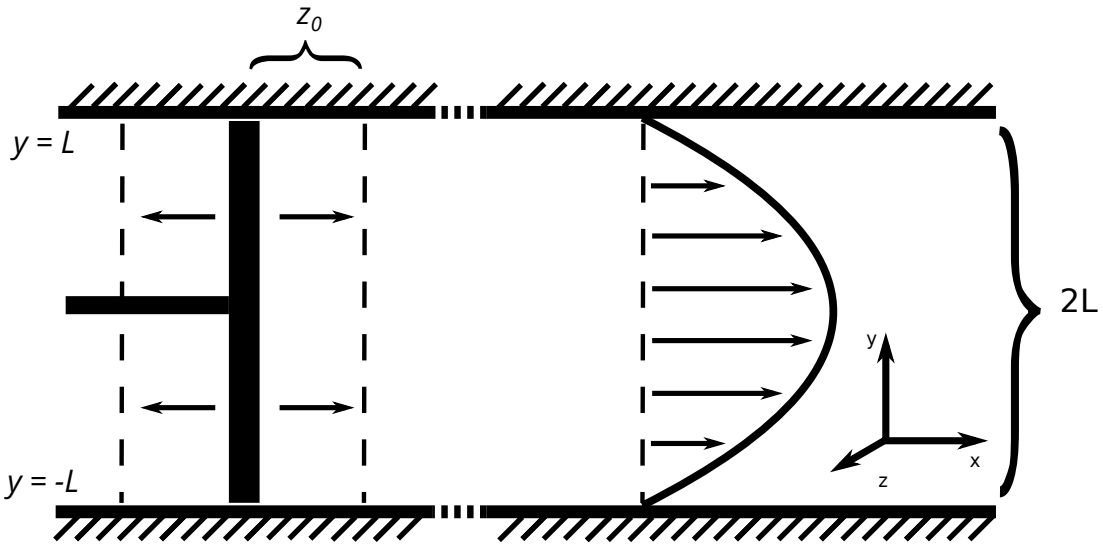


Figure 5.1: Diagram of a piston-driven plane Poiseuille flow. Far from the piston we can approximate the flow with an oscillatory pressure gradient.

## 5.1 Laminar flow solution

First we solve for the laminar flow of an Oldroyd-B fluid due to an oscillating applied pressure gradient, $\frac{\partial p}{\partial x} = \delta \cos(\omega t)$, in a channel. The pressure gradient forces a streamwise velocity profile, so that we can express each variable in terms of complex exponentials, for example, $u(y,t) = \mathrm{Re}\left(u(y)\mathrm{e}^{i\omega t}\right)$ for the streamwise velocity. From the Oldroyd-B equations for the stress (1.23) we obtain:

$$\begin{aligned}
\tau_{yy} &= 0 \\
\tau_{xy} &= \frac{1}{1+i\lambda\omega}\frac{\partial u}{\partial y} \\
\tau_{xx} &= \frac{2}{(1+\lambda i\omega)^2}\tau_{xy}\frac{\partial u}{\partial y}\,.
\end{aligned} \tag{5.1}$$

The equation of motion with an oscillatory applied pressure gradient is

$$\rho\frac{\partial \mathbf{v}}{\partial t} + \rho\mathbf{v}\cdot\nabla\mathbf{v} = \delta\cos(\omega t)\mathbf{e}_x + \eta_s\nabla^2\mathbf{v} + \nabla\cdot\boldsymbol{\tau}\,. \tag{5.2}$$

Substitution of the stresses gives a second order ordinary differential equation in $u$,

$$\left(\eta_s + \frac{\eta_p}{1+i\lambda\omega}\right)\frac{\partial^2 u}{\partial y^2} - i\rho\omega u = \delta\,, \tag{5.3}$$

with complementary solution,

$$u_c(y) = A\mathrm{e}^{\alpha y} + B\mathrm{e}^{-\alpha y}$$
$$\alpha^2 = \frac{i\rho\omega}{\eta_s + \frac{\eta_p}{1+i\omega\lambda}}\,, \tag{5.4}$$

where we choose the positive root of $\alpha^2$ throughout this chapter. The particular integral is given by

$$u_p = \frac{\delta}{i\rho\omega}\,. \tag{5.5}$$

Applying the boundary conditions for channel flow with half width $L$, $u(y = \pm L, t) = 0$, we find that

$$u(y,t) = \mathrm{Re}\left(\frac{\delta}{i\omega\rho}\left[1 - \frac{\cosh(\alpha y)}{\cosh(\alpha L)}\right]\mathrm{e}^{i\omega t}\right)\,, \tag{5.6}$$

where we have written the full time-dependent solution.

Later we will need the area of fluid swept out in a quarter cycle of the piston,

$$A = \int_{-L}^{L}\int_{0}^{\frac{\pi}{2\omega}} u(y,t)\,\mathrm{d}t\,\mathrm{d}y = \int_{-L}^{L}\int_{0}^{\frac{\pi}{2\omega}} \mathrm{Re}\left(\frac{\delta}{i\omega\rho}\left[1 - \frac{\cosh(\alpha y)}{\cosh(\alpha L)}\right]\mathrm{e}^{i\omega t}\right)\,\mathrm{d}t\,\mathrm{d}y$$
$$= \frac{2L\delta}{\omega^2\rho}C \tag{5.7}$$
$$C = \mathrm{Re}\left(\left[1 - \frac{\tanh(\alpha L)}{\alpha L}\right](1-i)\right)\,, \tag{5.8}$$

where C is a dimensionless constant of the flow.

### 5.1.1 Dimensionalisation

Following Casanellas and Ortín [152], we use both Deborah and Weissenberg numbers to characterise the flow. We also define the Reynolds number,

$$De = \lambda\omega \tag{5.9}$$
$$Wi = \frac{z_0}{L}De \tag{5.10}$$
$$Re = \frac{\rho U_0 L}{\eta_T}\,, \tag{5.11}$$

where $\eta_T$ is the total viscosity. A piston is situated far upstream of the simulation box to cause the oscillating pressure gradient. This piston enters the simulation only

through the parameter $z_0$, the amplitude of the piston oscillation. For the velocity scale of the dimensionalisation we choose the mean velocity of the laminar flow over a quarter cycle. This is just the area swept out by the piston in a quarter period divided by the width of the channel and the time interval,

$$U_0 = \frac{z_0}{\frac{\pi}{2\omega}} \equiv \frac{2L}{\pi\lambda}\,Wi\,. \tag{5.12}$$

We scale the time with $\omega$, the velocity with $1/U_0$, and the stress with $\frac{\eta_p U_0}{L}$.

We can rewrite the coefficient for the time derivative in terms of the dimensionless constants,

$$B = \frac{L^2\omega\rho}{\eta_T} = \frac{\pi}{2}\frac{ReDe}{Wi}\,. \tag{5.13}$$

To find the coefficient of the applied pressure gradient we need an expression for the amplitude, $\delta$ in terms of the other variables. We equate the area of fluid in a quarter cycle (5.7) to the area swept out by the piston, $2Lz_0$,

$$\begin{aligned} 2Lz_0 &= \frac{2L\delta}{\omega^2\rho}C \\ \delta &= \frac{z_0\omega^2\rho}{C}\,, \end{aligned} \tag{5.14}$$

using this expression for $\delta$ we can now write the coefficient of the pressure gradient term in terms of dimensionless numbers,

$$\frac{L^2\delta}{\eta_T U_0} = \left(\frac{\pi}{2}\right)^2 \frac{ReDe}{C\,Wi}\,. \tag{5.15}$$

Now the stress and momentum equations can be written in dimensionless form,

$$\frac{\pi}{2}\frac{ReDe}{Wi}\frac{\partial \mathbf{v}}{\partial t} + Re\,\mathbf{v}\cdot\nabla\mathbf{v} = \left(\frac{\pi}{2}\right)^2 \frac{ReDe}{C\,Wi}\cos(t)\mathbf{e}_x + \beta\nabla^2\mathbf{v} + (1-\beta)\nabla\cdot\boldsymbol{\tau} \tag{5.16}$$

$$\boldsymbol{\tau} + De\frac{\partial\boldsymbol{\tau}}{\partial t} + \frac{2}{\pi}Wi\Big[\mathbf{v}\cdot\nabla\boldsymbol{\tau} - (\nabla v)^T\cdot\boldsymbol{\tau} - \boldsymbol{\tau}\cdot(\nabla v)\Big] = (\nabla\mathbf{v})^T + \nabla\mathbf{v}\,. \tag{5.17}$$

### 5.1.2 Solving for the base profile

For the base profile, we divide (5.6) by $U_0$ and substitute in our expression for $\delta$,

$$u(y,t) = \mathrm{Re}\left(\frac{\pi}{2iC}\left[1 - \frac{\cosh(\tilde{\alpha}y)}{\cosh(\tilde{\alpha})}\right]\mathrm{e}^{it}\right)\,, \tag{5.18}$$

where $\tilde{\alpha} = \alpha L$ is the dimensionless wavenumber of the laminar flow. We can rewrite this in terms of the other dimensionless variables using (5.4) to give,

$$\tilde{\alpha}^2 = \frac{i\pi}{2}\frac{ReDe}{Wi}\left[\beta + \frac{1-\beta}{1+iDe}\right]^{-1} . \tag{5.19}$$

Now we calculate the components of the conformation tensor of the laminar flow using the equations above. We rescale the stress for this problem and define the dimensionless conformation tensor,

$$\boldsymbol{\tau} = \frac{\pi}{2\,Wi}\left(\boldsymbol{c} - \mathbb{I}\right) . \tag{5.20}$$

From (5.17) and (5.20) we find that $C_{yy} = 1$, as usual for laminar flow. The equation for $C_{xy}$ is,

$$C_{xy} + De\frac{\partial C_{xy}}{\partial t} = \frac{2\,Wi}{\pi}\frac{\partial U}{\partial y}C_{yy} . \tag{5.21}$$

To solve, we Fourier transform the variables in time, $g = \mathrm{Re}\left(\sum_{n=-\infty}^{\infty} g_n \mathrm{e}^{int}\right)$. After substituting in the value of $C_{yy}$ the equation is linear, and the Fourier modes decouple such that,

$$(1 + inDe)C_{xy,n} = \frac{2\,Wi}{\pi}U'_n , \tag{5.22}$$

for each Fourier mode $n$. Since only the first Fourier mode of the base flow is non-zero,

$$C_{xy} = \frac{2\,Wi}{\pi}\frac{1}{(1+iDe)}U'_1\mathrm{e}^{it} + c.c , \tag{5.23}$$

gives the $xy$ component. For the $xx$ component,

$$\begin{aligned} C_{xx} + De\frac{\partial C_{xx}}{\partial t} &= \frac{4\,Wi}{\pi}\frac{\partial U}{\partial y}C_{xy} + 1 \\ \sum_{n=-\infty}^{\infty}(1 + inDe)C_{xx,n} &= \frac{4\,Wi}{\pi}\left(\sum_{q=-1}^{1}U'_q\right)\left(\sum_{p=-1}^{1}C_{xy,p}\right) + 1 . \end{aligned} \tag{5.24}$$

So that,

$$\begin{aligned} C_{xx} = 1 &+ \frac{4\,Wi}{\pi}\left(U'_{-1}C_{xy,1} + U'_1 C_{xy,-1}\right) \\ &+ \frac{4\,Wi}{\pi(1+2iDe)}U'_1 C_{xy,1}\mathrm{e}^{2it} + \frac{4\,Wi}{\pi(1-2iDe)}U'_{-1}C_{xy,-1}\mathrm{e}^{-2it} . \end{aligned} \tag{5.25}$$

## 5.2 Resonance of the base flow

When we examine the laminar flow solution (5.18) we see that for most choices of the parameters the laminar profile match the Newtonian profile, consisting of an oscillating form of plane Poiseuille flow. However, at very low $\beta$ and depending on $De$, the laminar flow velocity can contain multiple peaks. These multiple peaked solutions are known as resonances in the laminar flow velocity. This effect has been observed before [99] and can be understood in terms of the constructive interference of waves in the streamwise velocity extending from the walls of the channel [152].

The experiments of Casanellas and Ortín [22] were performed with constant elasticity number,

$$El = \frac{Wi}{Re} = \frac{\pi}{2}\frac{\eta_T \lambda}{L^2 \rho} \tag{5.26}$$

To aid in comparison with the experiments, we choose the same constant value of the Elasticity number, $El = 1182.44$ and the same viscosity ratio, $\beta = 0.0016$. This means that $Re$ is determined by $Wi$ and we can characterise the flow using only $De$ and $Wi$.

We use (5.18) and look for parameters where there is a strong enhancement in the streamwise velocity. These resonances depend on $De$, and each resonance corresponds to a number of peaks. First there is one strong peak in the centre of the channel ($De \simeq 41$, Fig. 5.2a) then three ($De \simeq 120$, Fig. 5.2b), five ($De \simeq 220$, Fig. 5.2c), and so on. We also find that each successive resonance has a weaker maximum streamwise velocity.

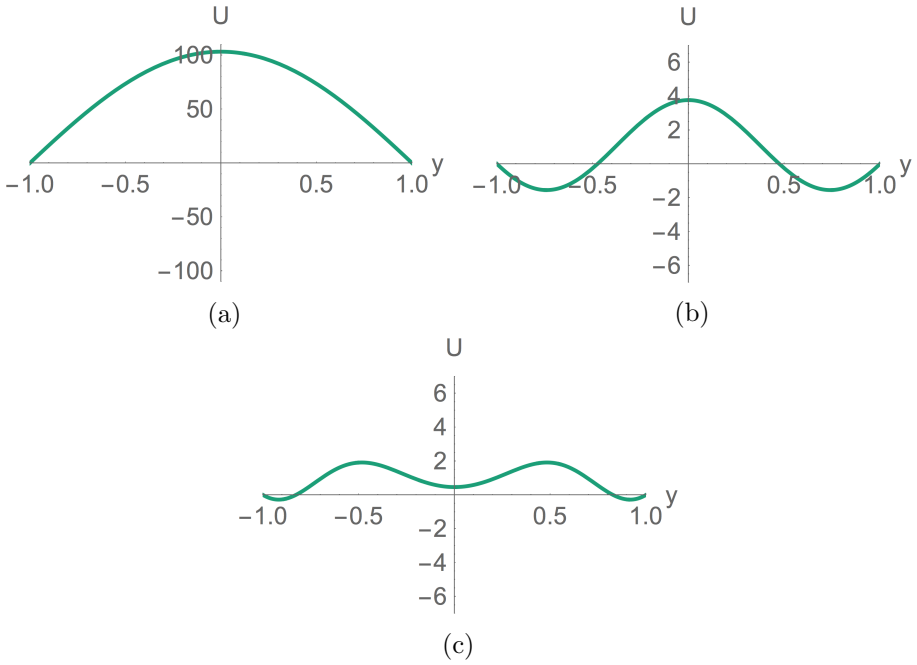


Figure 5.2: a) Shows the velocity profile at the time of the maximum velocity for $De = 41$. b) $De = 120$, c) $De = 220$.

At the resonances the flow is organised into layers or bands at different velocity with sharp changes in velocity between the layers. The strong layering in the resonant velocity profiles lead us to suspect that they may be vulnerable to a shear-layer instability. In Chapter 3 we showed that purely elastic shear layers are unstable. This implies that flows near a resonance should be unstable via a similar mechanism.

At a resonance, the shear waves extending from the walls interfere constructively and the maximum velocity increases. We can use this to quantify the locations of the resonances by optimising for the maximum velocity at $y = 0$ and over one piston oscillation ($T = 2\pi$). To do this we use a global method from the computer algebra software, *Mathematica* [160]. We find that the resonance is independent of our dimensionless $Wi$ (Fig. 5.3), and that there are peaks corresponding to the resonances (Fig. 5.4).

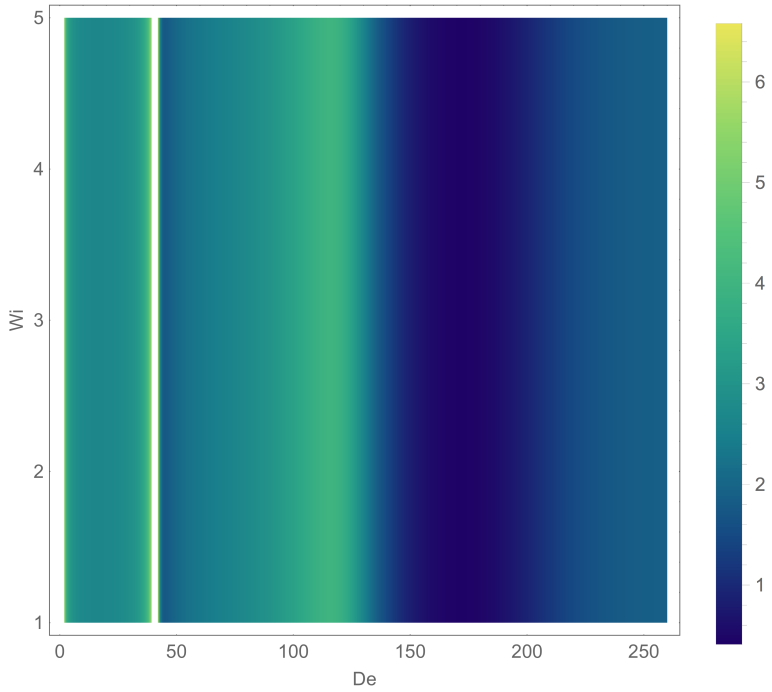


Figure 5.3: Density plot of the maximum velocity at $y = 0$ in a period of the base flow. It is independent of $Wi$ and there is a sharp peak around $De = 40$ and another at $De = 120$.

We know that the purely elastic shear layer instability depends on large changes in the first normal stress difference. For the laminar flow, $\tau_{yy} = 0$, therefore $\tau_{xx}$ is a measure of the first normal stress difference. If we plot the maximum of the first normal stress difference for the flow, optimised over $y$ and $t$, for all $De$ and $Wi$, we find that this does depend on $Wi$ (Fig. 5.6). We consider $\tau_{xx}$ over one period and average the stress at each location $y$, shown in Fig. 5.5. From this plot we can extract the points with the greatest stress, $y^*$, shown by the grey lines in the plot.

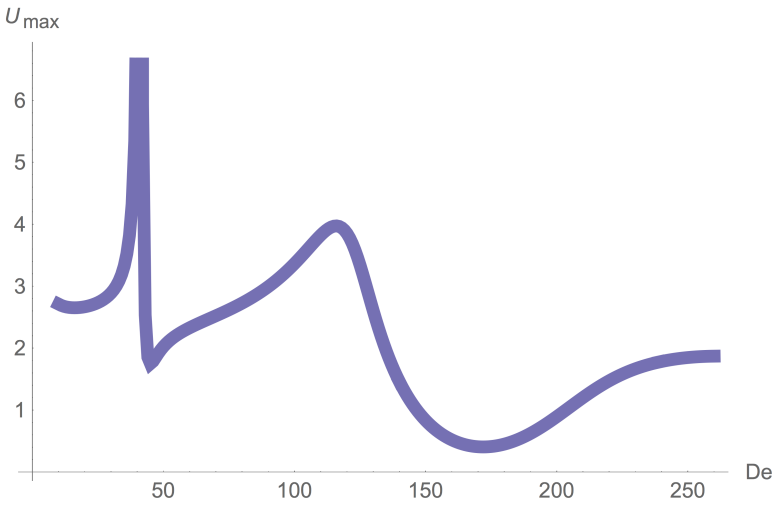


Figure 5.4: The maximum velocity for $y = 0$ in a period of the base flow. There is a sharp peak around $De \sim 40$, and a smaller peak around $De \sim 120$.

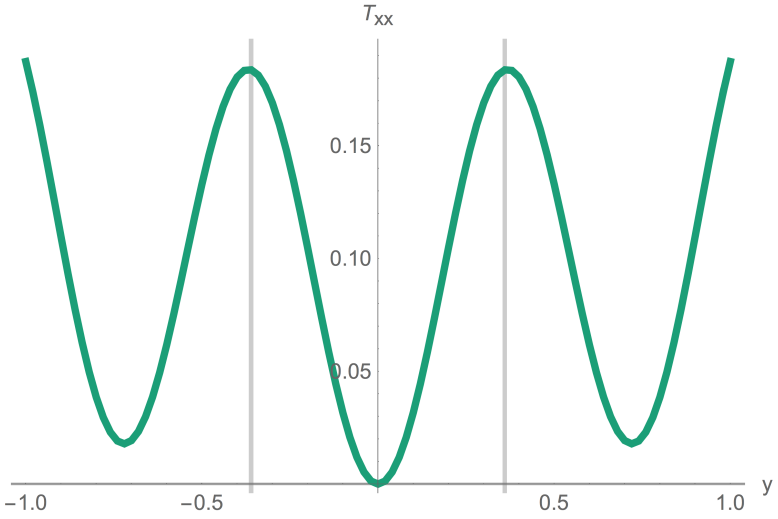


Figure 5.5: The average streamwise stress, $\tau_{xx}$, for $De = 120$, $Wi = 32$. The grey lines give the locations of the maxima at $y^* = \pm 0.36$.

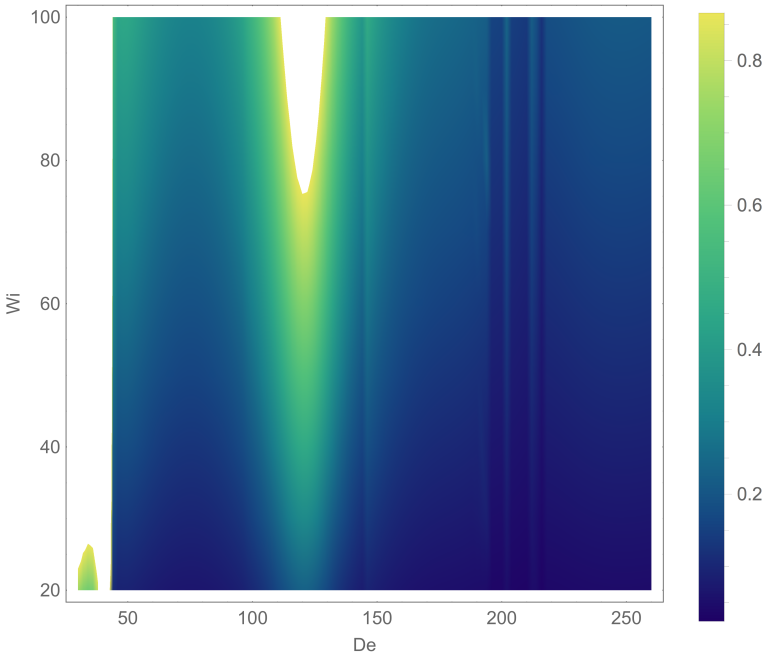


Figure 5.6: Density plot of the maximum streamwise stress, $\tau_{xx}$, over the domain in a period of the base flow.

## 5.3 Numerical method

We adjust the time iteration method outlined in Chapter 4, so that we can simulate the oscillatory flow equations. We use the same streamfunction ($u = \frac{\partial \psi}{\partial y}, v = -\frac{\partial \psi}{\partial x}$), but the system of equations (4.4) changes because of the new dimensionalisation and forcing,

$$B\frac{\partial \nabla^2}{\partial t}\psi + Re\,(\mathbf{v}\cdot\nabla)\,\nabla^2\psi = \beta\nabla^4\psi - (1-\beta)\nabla\times\nabla\cdot\boldsymbol{\tau} \tag{5.27}$$

$$B\frac{\partial}{\partial t}\overline{\frac{\partial \psi}{\partial y}} - Re\overline{\frac{\partial \psi}{\partial x}\frac{\partial^2\psi}{\partial y^2}} = \beta\overline{\frac{\partial^3\psi}{\partial y^3}} + (1-\beta)\overline{\frac{\partial \tau_{xy}}{\partial y}} + \left(\frac{\pi}{2}\right)^2\frac{ReDe}{CWi}\cos(t) \tag{5.28}$$

$$\nabla\cdot\mathbf{v} = 0 \tag{5.29}$$

$$\boldsymbol{\tau} = \frac{\pi}{2Wi}(\mathbf{c}-\mathbb{I}) \tag{5.30}$$

$$\frac{\pi De}{2Wi}\frac{\partial \mathbf{c}}{\partial t} + (\mathbf{v}\cdot\nabla)\,\mathbf{c} = (\nabla\mathbf{v})^T\cdot\mathbf{c} + \mathbf{c}\cdot(\nabla\mathbf{v}) - \boldsymbol{\tau}\,, \tag{5.31}$$

where the second equation is for the mean flow velocity. Where the bar symbol, $\overline{\phantom{x}}$, refers to the mean over the streamwise ($x$) direction of the variables underneath it. As well as the coefficients for the dimensionalisation, we also rescale the conformation tensor $c$ by $\pi/2$ in order to simplify the equations somewhat. When we take these equations and substitute them into the time iteration method of section 4.1 we obtain the time discretised equations,

$$\begin{aligned}
c^* &= \left[\frac{\pi}{2\,Wi}\left(De+\frac{h}{4}\right)\right]^{-1}\left(\frac{\pi}{2\,Wi}\left(De-\frac{h}{4}\right)c^s + \frac{h}{2}\Theta(\psi^s,c^s)\right)\\
c^{s+1} &= \left[\frac{\pi}{2\,Wi}\left(De+\frac{h}{2}\right)\right]^{-1}\left(\frac{\pi}{2\,Wi}\left(De-\frac{h}{2}\right)c^s + h\Theta(\psi^*,c^*)\right)\\
\psi^* &= \left[B\nabla^2 - \frac{\beta h}{4}\nabla^4\right]^{-1}\left(B\nabla^2\psi^s + \frac{\beta h}{4}\nabla^4\psi^s \right.\\
&\qquad\left. + \frac{h}{4}\hat{D}(c^*+c^s) + \frac{hRe}{2}\Gamma(\psi^s)\right)\\
\psi^{s+1} &= \left[B\nabla^2 - \frac{\beta h}{2}\nabla^4\right]^{-1}\left(B\nabla^2\psi^s + \frac{\beta h}{2}\nabla^4\psi^s \right.\\
&\qquad\left. + \frac{h}{2}\hat{D}(c^*+c^{s+1}) + hRe\Gamma(\psi^*)\right)\,,
\end{aligned} \tag{5.32, 5.33}$$

and for the mean flow equation,

$$\overline{\psi^*} = \left[B\frac{\partial}{\partial y} - \frac{\beta h}{4}\frac{\partial^3}{\partial y^3}\right]^{-1}\left(B\frac{\partial\overline{\psi^s}}{\partial y} + \frac{\beta h}{4}\frac{\partial^3\overline{\psi^s}}{\partial y^3} + Re\,\overline{\frac{\partial\psi^s}{\partial x}\frac{\partial^2\psi^s}{\partial y^2}} + \beta\overline{\frac{\partial^3\psi^s}{\partial y^3}} + \frac{(1-\beta)}{Wi}\overline{\frac{\partial c^s_{xy}}{\partial y}} + \left(\frac{\pi}{2}\right)^2\frac{ReDe}{C\,Wi}\cos\left(h\left(s+\frac{1}{2}\right)\right)\right)$$

$$\overline{\psi^{s+1}} = \left[B\frac{\partial}{\partial y} - \frac{\beta h}{4}\frac{\partial^3}{\partial y^3}\right]^{-1}\left(B\frac{\partial\overline{\psi^s}}{\partial y} + \frac{\beta h}{4}\frac{\partial^3\overline{\psi^s}}{\partial y^3} + Re\overline{\frac{\partial\psi^*}{\partial x}\frac{\partial^2\psi^*}{\partial y^2}} + \beta\frac{\partial^3\overline{\psi^s}}{\partial y^3} + \frac{(1-\beta)}{Wi}\overline{\frac{\partial c^s_{xy}}{\partial y}} + \left(\frac{\pi}{2}\right)^2\frac{ReDe}{C\,Wi}\cos(h(s+1))\right), \tag{5.34}$$

where just as in (4.11),

$$\Theta(\psi,c) = \frac{\partial\psi}{\partial x}\frac{\partial c}{\partial y} - \frac{\partial\psi}{\partial y}\frac{\partial c}{\partial x} + A^Tc + cA$$

$$A(\psi) = \nabla\mathbf{v} = \begin{pmatrix}\frac{\partial^2\psi}{\partial x\partial y} & \frac{\partial^2\psi}{\partial x^2}\\ \frac{\partial^2\psi}{\partial y^2} & -\frac{\partial^2\psi}{\partial x\partial y}\end{pmatrix} \tag{5.35}$$

$$\Gamma(\psi) = \left(\frac{\partial\psi}{\partial y}\frac{\partial}{\partial x} - \frac{\partial\psi}{\partial x}\frac{\partial}{\partial y}\right)\nabla^2\psi \tag{5.36}$$

$$\hat{D}(c) = (1-\beta)\frac{\pi}{2\,Wi}\left[\frac{\partial^2c_{xx}}{\partial x\partial y} - \frac{\partial^2c_{yy}}{\partial x\partial y} + \left(\frac{\partial^2}{\partial y^2} - \frac{\partial^2}{\partial x^2}\right)c_{xy}\right]. \tag{5.37}$$

The discrete index to the current time is $s$, $h$ is the size of the time step, $\Theta$ is a nonlinear differential operator with terms in the products of $\psi$ and $c$, and $\Gamma$ is a nonlinear differential operator with terms in the products of $\psi$ with $\psi$. $\hat{D}$ is an operator which acts on $c$ to give the polymeric stress terms in (5.27). The inverse operators (shown in square brackets in (5.33) and (5.34)) are formed by inverting a matrix problem for each Fourier mode at the beginning of the code with the no-slip boundary conditions on the streamfunction.

Again, we discretise the space in $y$ and $x$ using Chebyshev and Fourier series, following the fully spectral method outlined in Appendix A.1.

## 5.4 Linear stability

Blennerhassett and Bassom [159] performed a numerical Floquet analysis on the Newtonian oscillatory flow problem. They found that 200 to 300 modes in time were required to resolve the linear instability. Numerical analysis of viscoelastic flows typically requires much higher resolution than the corresponding Newtonian flows. Therefore, rather than attempt a similar analysis for viscoelastic flows, we have opted to time-iterate the linearised equations.

We use a linearised version of the time iteration code outlined in section 5.3 to simulate a small, initial perturbation to the flow with wavenumber $k_x$. After initial transients, this random perturbation will settle into the most unstable eigenmode of the linear stability problem. To measure the time dynamics in one simple parameter, we define a norm,

$$\|g_n\|_2^2 = \sum_m^M \check{g}_{n,m}\check{g}_{n,m}^* \tag{5.38}$$

where $\check{g}_{n,m}$ denotes the $n^{\text{th}}$ Fourier and $m^{\text{th}}$ Chebyshev element of the variable, $g$ in the simulation. Note, this quantity is not physical, and the absolute value depends on the Chebyshev resolution, $M$. Figs 5.7a and 5.7b show the log of the norm of the perturbation streamfunction, $\log\left(\|\psi_1\|_2^2\right)$ against simulation time for $De = 100$, $Wi = 55$. We can extract the growth rate of the instability from Fig. 5.7b by fitting a straight line over the last 100 cycles of the applied pressure gradient. For $De \sim 120$ (the second resonance) the norm of the streamfunction shows an additional frequency of oscillation to the piston frequency (Fig. 5.7d). We have ensured that we average out this oscillation when calculating the growth rate. After simulations at each $k_x$, we obtain a dispersion relation for the growth rate against wavenumber (Fig. 5.8).

As we discussed in section 5.2, varying the Deborah number controls the resonances in laminar flow velocity and the Weissenberg number controls the strength of the elastic stresses. At constant $De$ we find that the flow can become unstable for sufficiently high $Wi$ (Fig. 5.9). When we vary the Deborah number for constant Weissenberg number, we find that the flow becomes unstable before becoming stable again as we move across the resonance (Fig. 5.10).

To relate this region to the resonance map of Fig. 5.6 and the piston-driven pipe flow problem of Casanellas and Ortín [22] we draw stability diagrams in $De$, $Wi$ plane. We extract the maximum growth rates from dispersion relations at each $De$ and $Wi$ where black dots indicate stability (Fig. 5.11b). The wavenumber at this peak growth rate increases with increasing Deborah number (Fig. 5.11c).

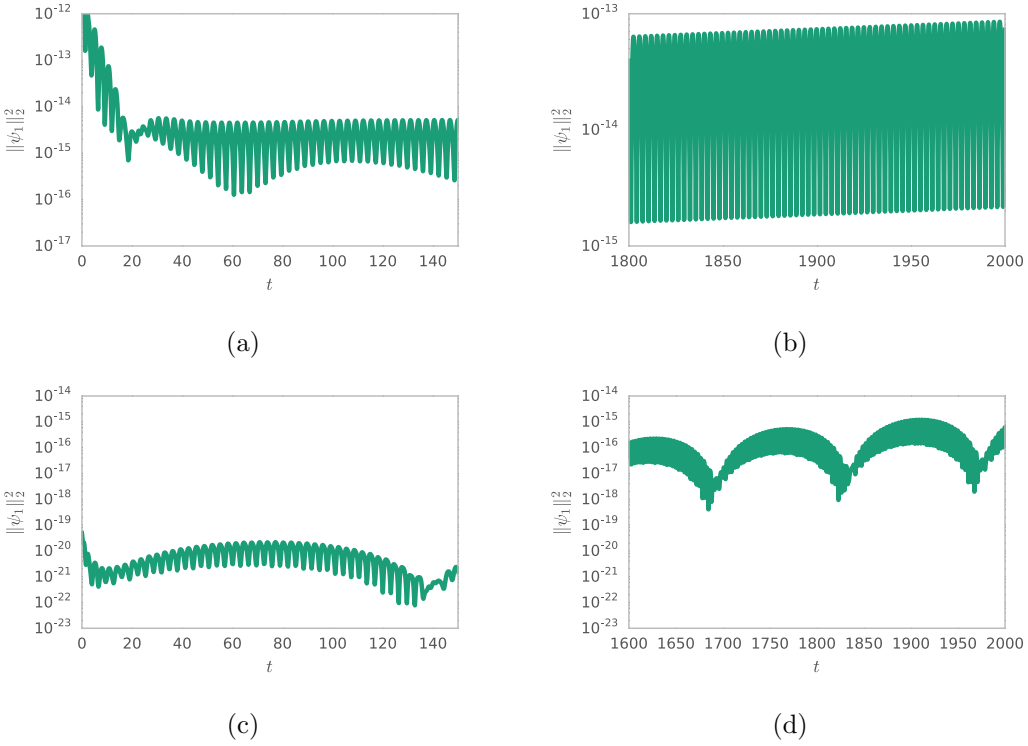


Figure 5.7: The time dynamics of the modulus of the streamfunction of the perturbation, $\|\psi_1\|_2^2$. Note the logarithmic $y$ axis. For panels a) and b), $De = 100$, $Wi = 55$, $k_x = 1.8$, and there are 192 Chebyshev modes. For panels b) and c) $De = 120$, $Wi = 32$, $k_x = 2.8$ and there are 320 Chebyshev modes. Panels a) and c) show the initial transient, and b) and d) show the behaviour after a long time.

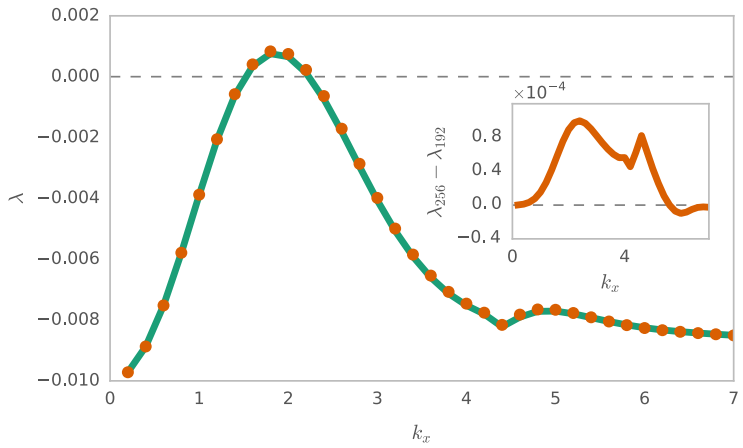


Figure 5.8: Convergence of a dispersion relation for $De = 100$, with $Wi = 55$. 192 Chebyshevs and a $h = 0.01$ in turquoise and 256 Chebyshevs and a time step $h = 0.001$ in orange. The inset plot shows the difference between the dispersion relations.

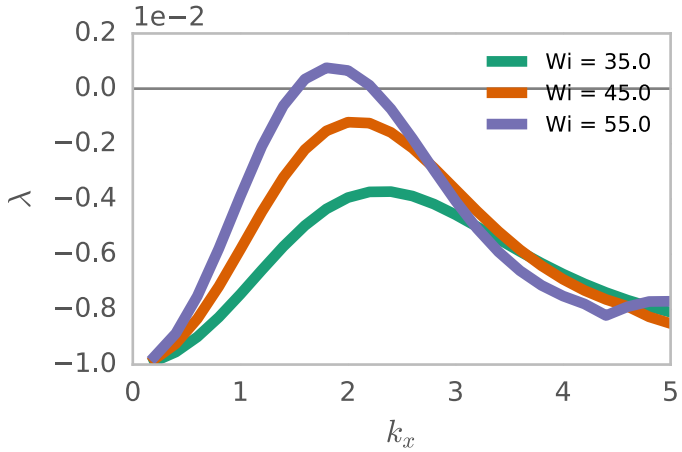


Figure 5.9: Dispersion relations for $De = 100$, with $Wi = 35, 45, 55$. The maximum of the curve increases as $Wi$ increases. Results are converged with 192 Chebyshevs and a $h = 0.01$.

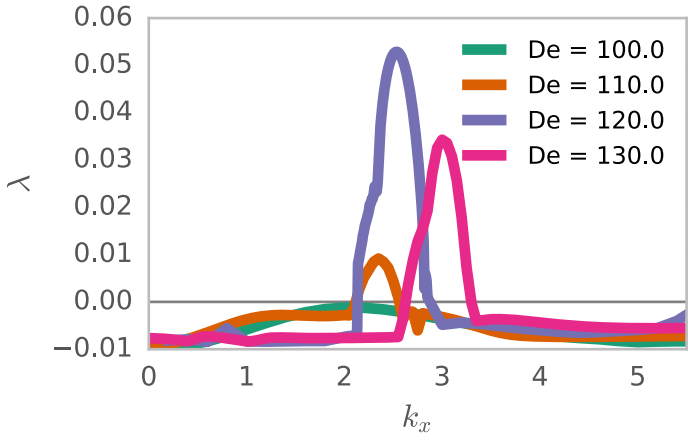


Figure 5.10: Dispersion relations for $Wi = 45$, for various $De$ spanning the region of instability. The width of the curve decreases as $De$ increases, and the most dangerous wavenumber moves to higher $k_x$. Results are converged for 256 Chebyshevs and a time step of $h = 0.01$.

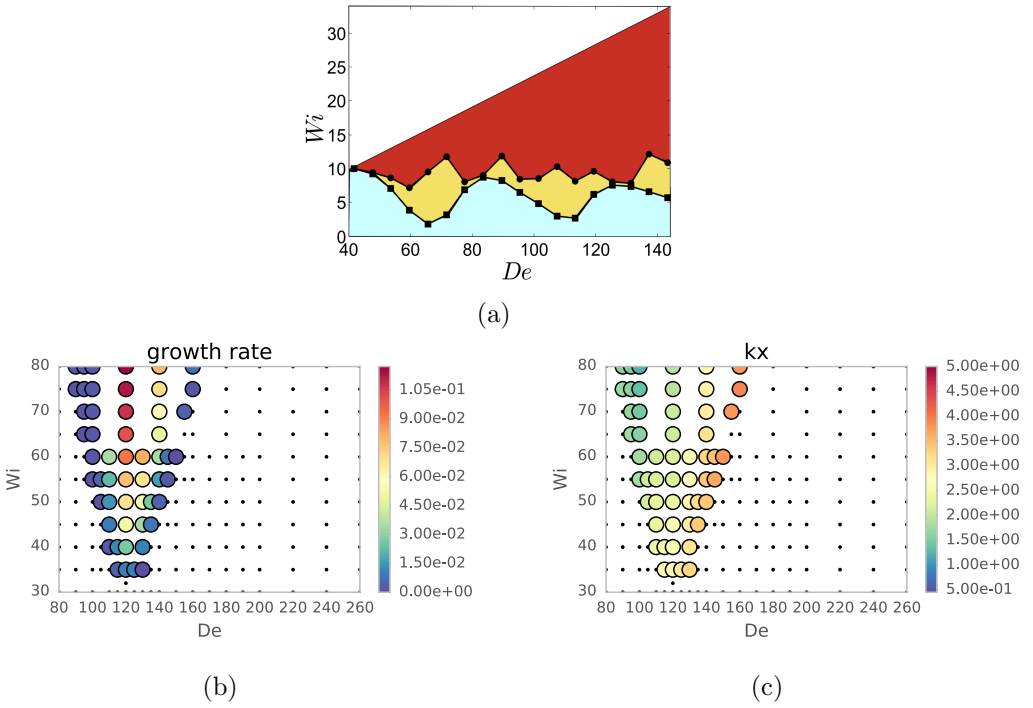


Figure 5.11: Phase diagram from the pipe flow experiments of Casanellas and Ortín [22]. The laminar base flow is represented in pale blue, the orange and red regions represent different kinds of non-laminar flow. In this chapter we have attempted to capture the boundary between the pale blue and orange regions but in a channel rather than a pipe. b) and c) show plots from our analysis of the critical growth rate and wavenumber for all dispersion relations in the $De$ and $Wi$ plane. Black squares correspond to points with no unstable wavenumbers below $k_x = 5$. (b) and (c) using $M = 256$ and $h = 0.01$.

In the pipe flow experiments of Casanellas and Ortín [22] (Fig. 5.11a) we see that the critical $Wi$ undulates with changing $De$. The values of $De$ where $Wi$ is lowest ($De \sim 65$, $De \sim 110$) correspond to resonances in the laminar pipe flow velocity [22]. The laminar profile for pipe flow is different to channel flow, and this explains the difference in $De$ for the locations of the resonances. We can see by comparing Figs 5.4 and 5.11b that the low critical $Wi$ points at $De \sim 120$ and $De \sim 220$ coincide with the resonances in our Oldroyd-B channel flow case. This suggests that the resonances may be responsible for the instability in our system, just as they appear to be in the pipe flow experiments.

We look at the most unstable eigenmodes of the instability. In Fig. 5.12 the laminar flow velocity, the streamfunction and $C_{xx}$ of the instability are shown for 4 separate times during a quarter cycle of the pressure gradient as the streamwise velocity increases. The streamwise velocity and stress at $y^*$ as defined earlier and $x^*$ a point with initially zero imaginary part, $u(x^*, y^*)$ and $\tau_{xx}(x^*, y^*)$, are shown against time in

Figs 5.14a and 5.14b.

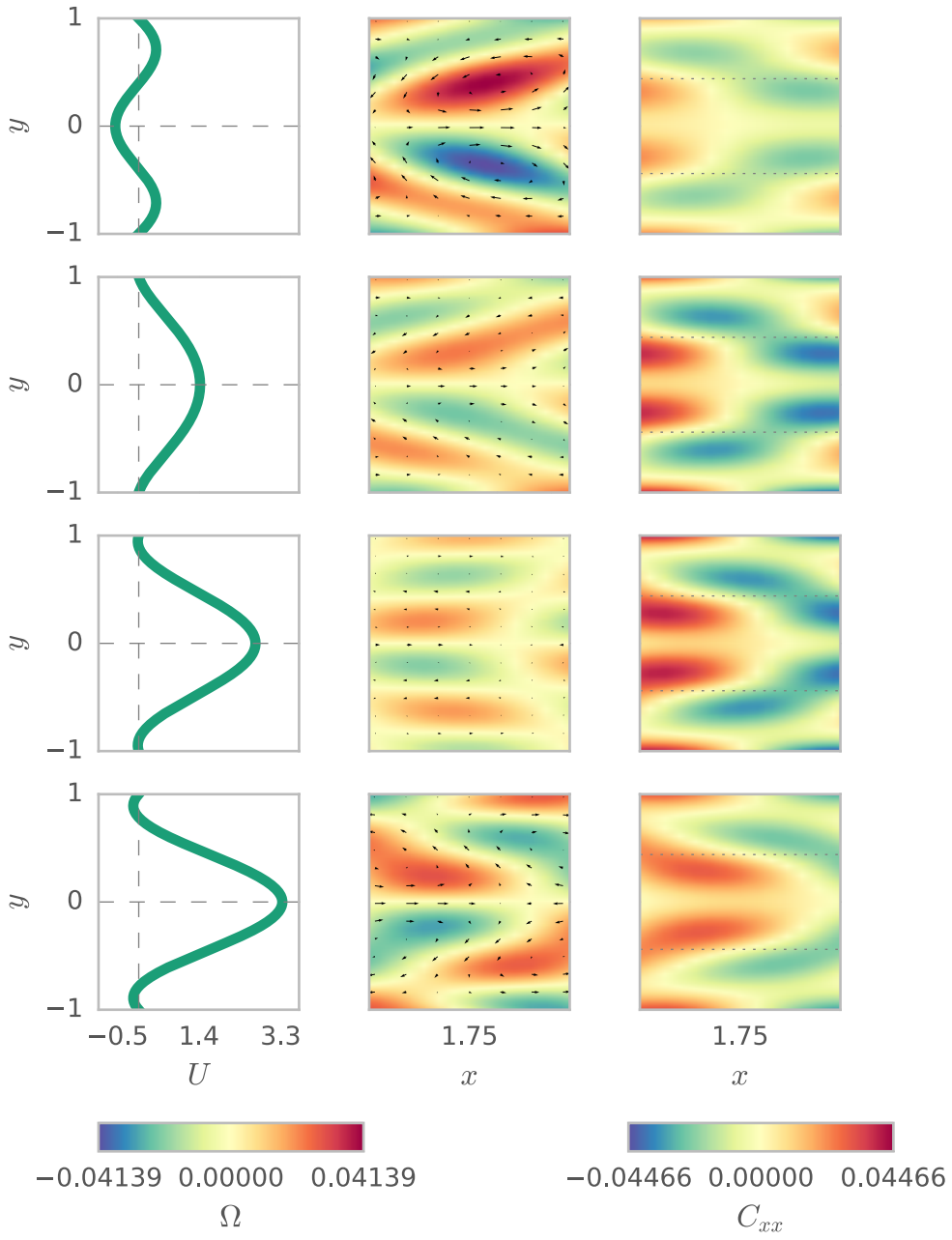


Figure 5.12: Snapshots taken at 4 equally spaced points in time over a quarter cycle of the pressure gradient. The three columns give: the base flow velocity (first column), vorticity and velocity vector field of the instability (second column), and $C_{xx}$ (third column) for $De = 100$, $Wi = 55$, $h = 0.01$ and 128 Chebyshev modes, after $\sim 1000$ time steps.

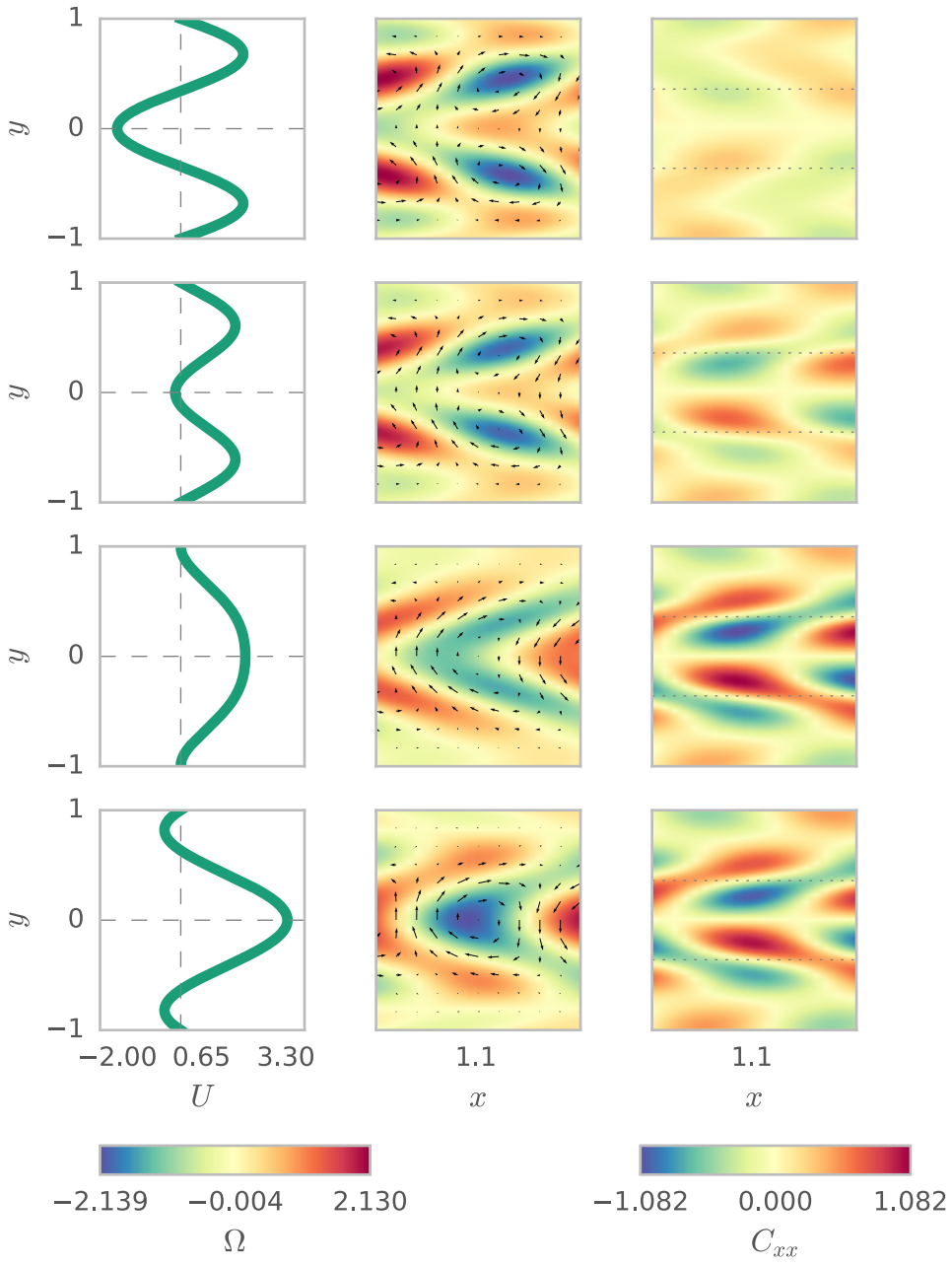


Figure 5.13: Snapshots taken at 4 equally spaced points in time over a quarter cycle of the pressure gradient. The three columns give: the base flow velocity (first column), vorticity and velocity vector field of the instability (second column), and $C_{xx}$ (third column) for $De = 120$, $Wi = 32$, $h = 0.01$ and 128 Chebyshev modes, after $\sim 1000$ time steps.

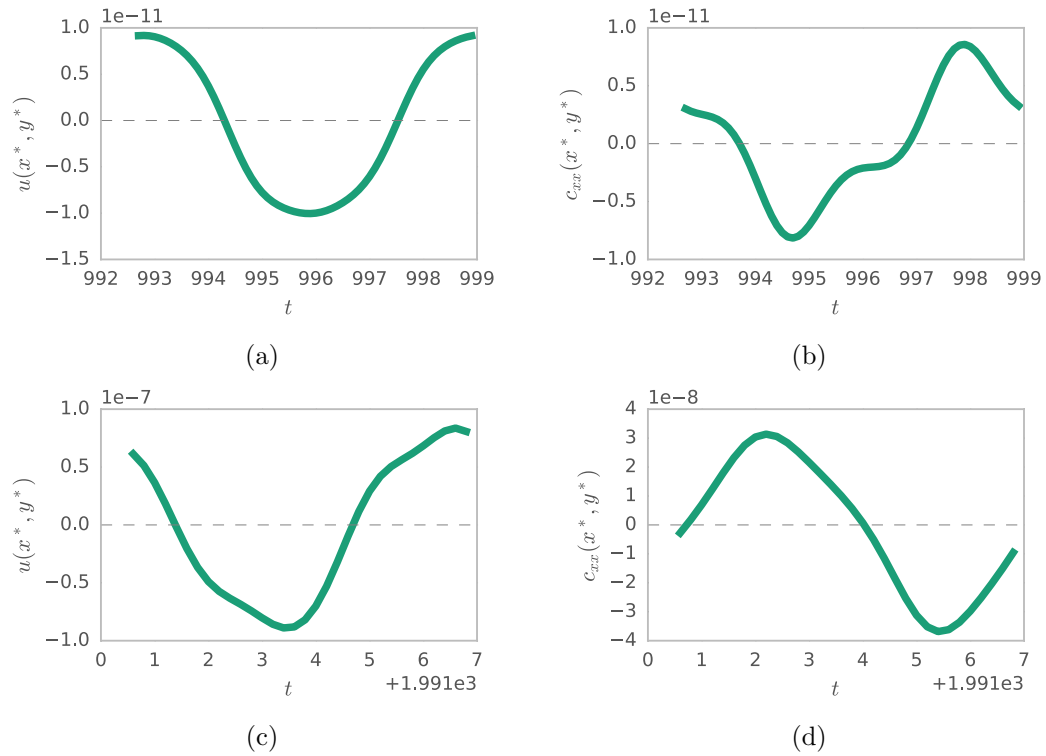


Figure 5.14: The streamwise velocity $u$, and $C_{xx}$ of the instability against time for one piston oscillation. The data is for the point $y^*$, a maximum in the average stress of the base flow, and $x^*$ such that the data at this point is at a maximum in $u$ at the initial time. For panels a) and b), $De = 100$, $Wi = 55$, $h = 0.01$ $M = 128$ and $y^* = 0.44$. The flow starts at the point in the cycle corresponding the first panel of Fig. 5.12. For panels c) and d) $De = 120$, $Wi = 32$, $h = 0.01$, $M = 320$ and $y^* = 0.44$. The flow starts at the point in the cycle corresponding the first panel of Fig. 5.13.

## 5.5 Nonlinear 2D time iteration

To confirm that our linear instability is not suppressed by nonlinearities, we look at the full nonlinear time evolution of the flow. This also allows us to investigate the secondary flow generated by the instability. We use the nonlinear time iteration code of section 5.3. Starting from a point where the base flow is linearly unstable and using the eigenmode of the instability as a perturbation, we time-iterate until we find a nonlinear steady state. Time iteration and convergence of steady states in this way is computationally expensive, so we only choose the most dangerous wavenumber at the lowest unstable $Wi$. This occurs where $De = 120$, $Wi = 32$. The price we pay for choosing this marginally unstable point is that the growth rate is very small. This means it takes a long time for the linear instability to saturate and for nonlinear effects to take hold. To check the convergence of the results we show here two resolutions: a low resolution run using 4 Fourier modes, 320 Chebyshev modes and a time step of $h = 0.01$, and a high resolution run using 6 Fourier modes, 448 Chebyshev modes and a time step of $h = 0.001$. Although we used other resolutions, we found that convergence depended on all three of these parameters. Other combinations of these resolutions either reproduce similar results or are numerically unstable. After a long time, we do observe nonlinear steady states. In Fig. 5.15a we show the behaviour of the norms of the first and second Fourier modes of the streamfunction as we approach a steady state.

The state at $De = 120$ and $Wi = 32$ has vortices located near the location of maximum stress, $y^*$ this is visible in the laminar-flow-subtracted streamfunction and in $c_{xx}$ (plotted over a quarter period in Fig. 5.20). The flow shown is at a resolution of $N = 4$, $M = 320$ with a time step of $h = 0.01$. Figs 5.16, 5.17, 5.18 and 5.19 show that this flow is not yet completely resolved for the first two Fourier modes, however, the disagreement is not large and flow is at least qualitatively similar. Movies of the data can be found in the *Edinburgh DataShare* online repository [161].

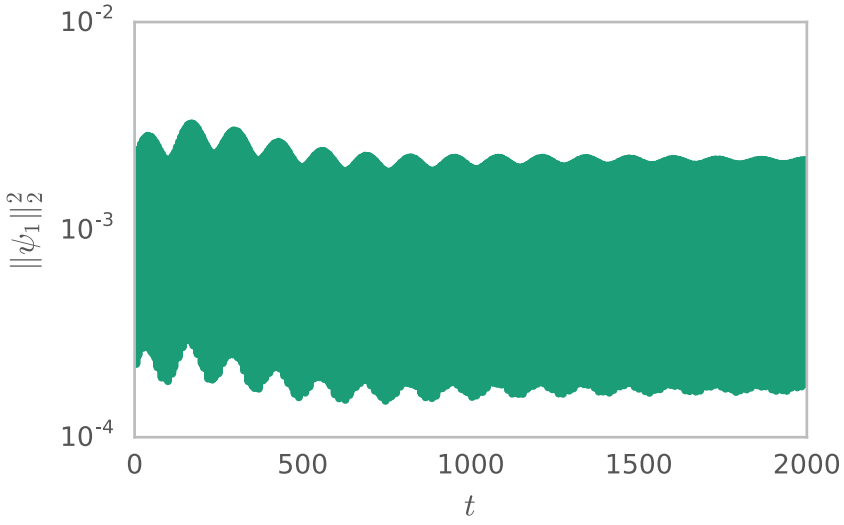


(a)

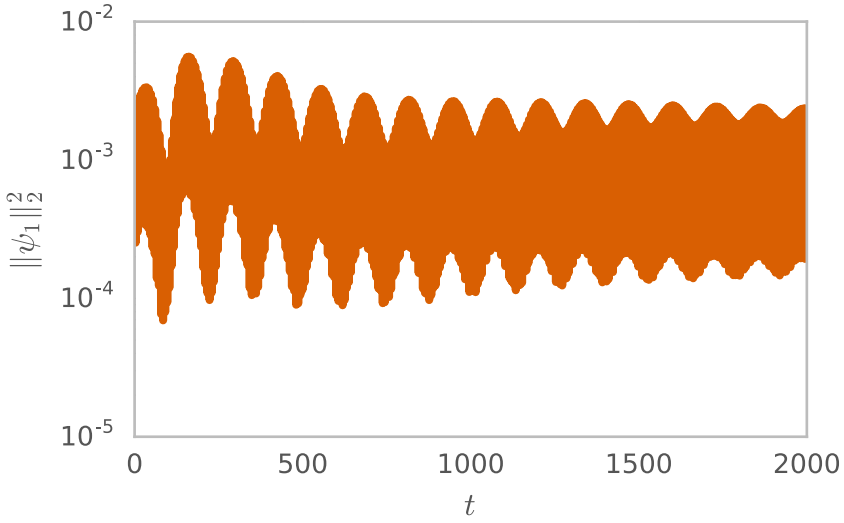


(b)

Figure 5.15: The time dynamics of the modulus of the streamfunction of the perturbation, $\|\psi_1\|_2^2$ when $De = 120$, $Wi = 32$ and $k_x = 2.8$. For panel a), $N = 4$, $M = 320$, and $h = 0.01$ Panel b) is at a higher resolution, $N = 6$, $M = 448$, and $h = 0.001$.

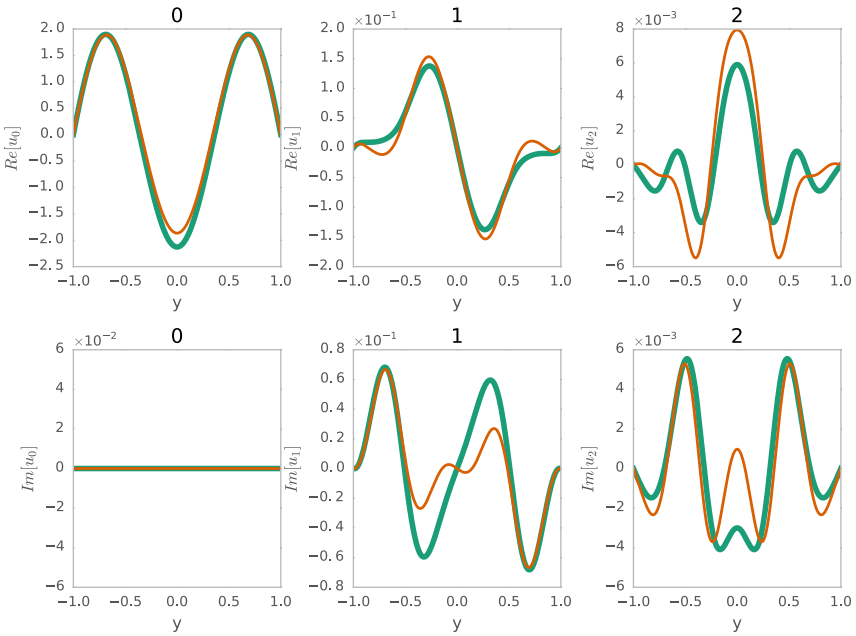


Figure 5.16: $u$ for $De = 120$, $Wi = 32$, at $k_x = 2.8$. Comparison of the zeroth, 1st and second modes for $N = 4$, $M = 320$, $h = 0.01$ (turquoise) and $N = 6$, $M = 448$, $h = 0.001$ (orange).

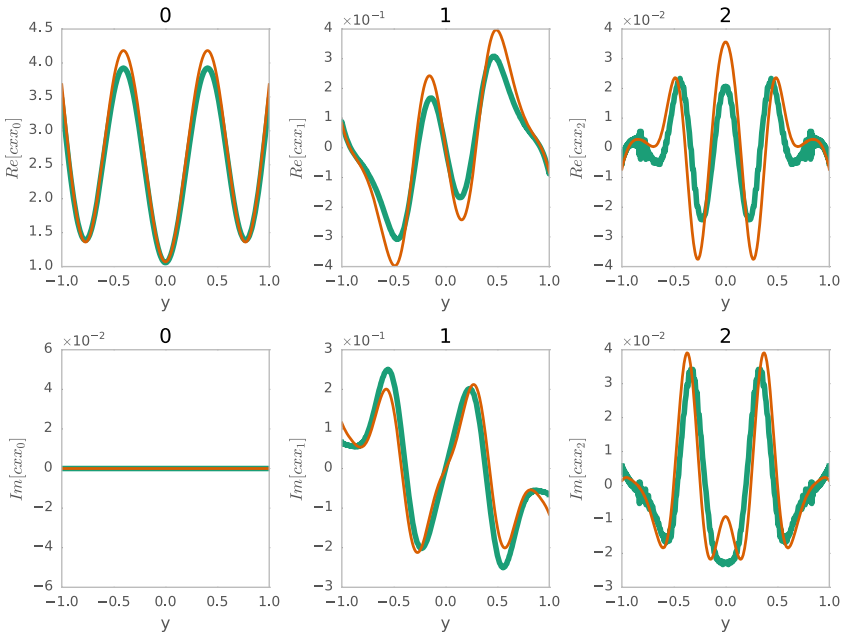


Figure 5.17: $C_{xx}$ for $De = 120$, $Wi = 32$, at $k_x = 2.8$. Comparison of the zeroth, 1st and second modes for $N = 4$, $M = 320$, $h = 0.01$ (turquoise) and $N = 6$, $M = 448$, $h = 0.001$ (orange).

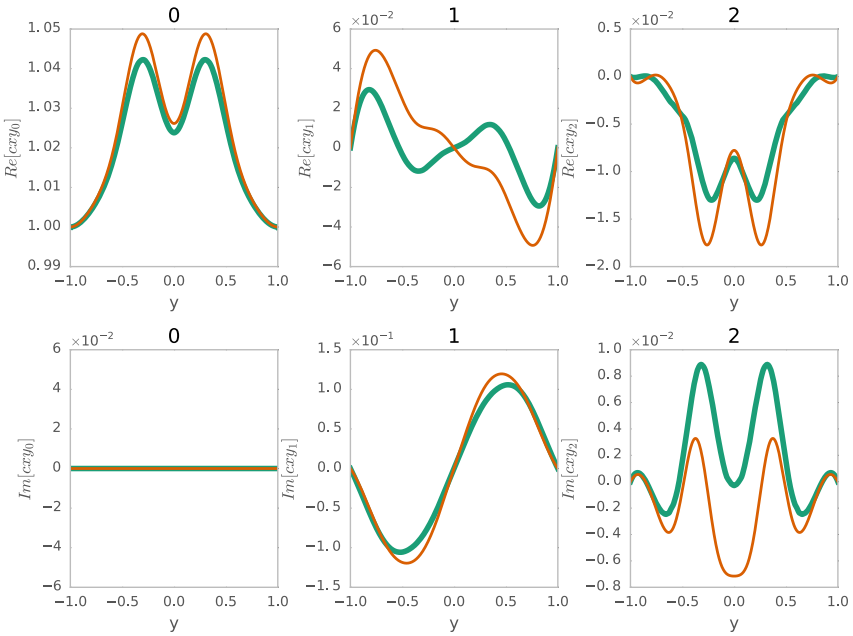


Figure 5.18: $C_{xy}$ for $De = 120$, $Wi = 32$, at $k_x = 2.8$. Comparison of the zeroth, 1st and second modes for $N = 4$, $M = 320$, $h = 0.01$ (turquoise) and $N = 6$, $M = 448$, $h = 0.001$ (orange).

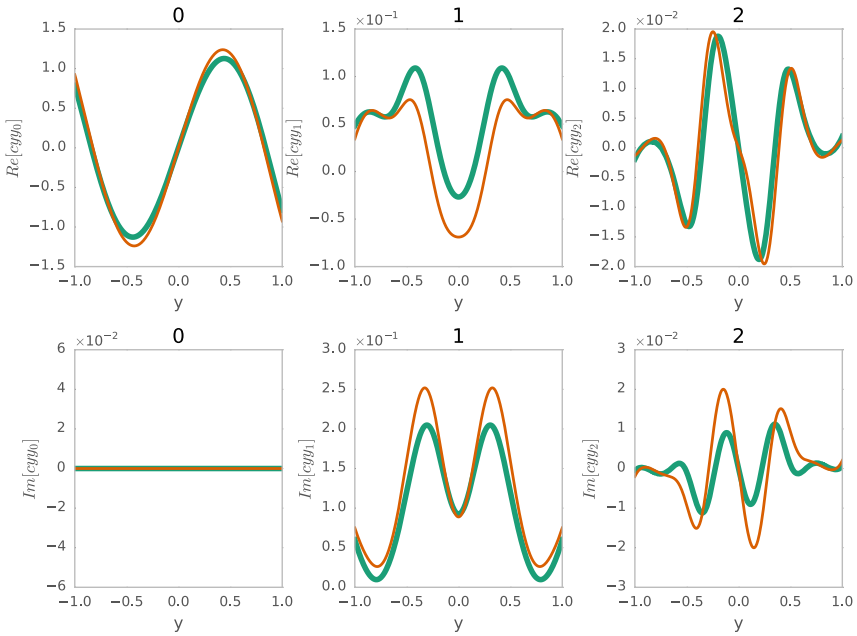


Figure 5.19: $C_{yy}$ for $De = 120$, $Wi = 32$, at $k_x = 2.8$. Comparison of the zeroth, 1st and second modes for $N = 4$, $M = 320$, $h = 0.01$ (turquoise) and $N = 6$, $M = 448$, $h = 0.001$ (orange).

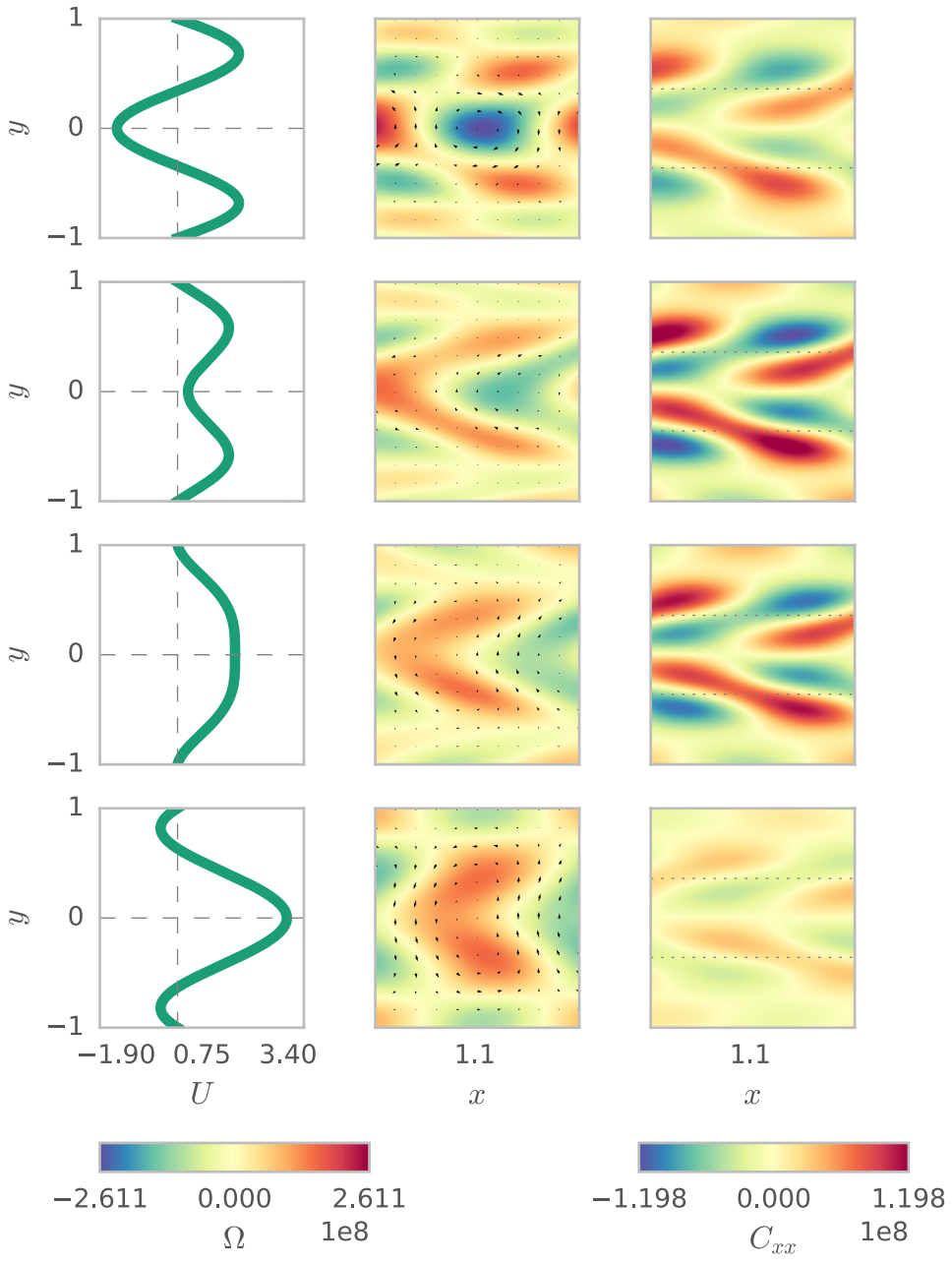


Figure 5.20: Snapshots taken at 4 equally spaced points in time over a quarter cycle of the pressure gradient. The three columns give: the base flow velocity (first column), vorticity and velocity vector field of the $x$-dependent part of the flow (second column), and $C_{xx}$ (third column) for $De = 120$, $Wi = 32$, $h = 0.01$ and 448 Chebyshev modes, after $\sim 1000$ time steps.

## 5.6 Discussion

We began examining this problem because of the similarities between the laminar flow of Thurston [99], Casanellas and Ortín [154] and the shear layer problem of Chapter 3. Just as in that problem, the oscillatory flow produces layers in the laminar flow with sharp gradients in velocity and corresponding sharp gradients in stress. These layers are caused by the viscoelasticity: the Reynolds number is always less than one for the flows we consider. In Chapter 3 we found that both free and confined shear layers like this are unstable. In this chapter we also found a linear instability, so long as the laminar flow is layered and $Wi$ is sufficiently high.

We find that the flow is unstable at low $Wi$ for $De \sim 100$–$130$. This corresponds to the second resonance at $De \sim 120$, where there are three peaks in the laminar flow velocity (Fig. 5.2b). The instability also shows dependence on $Wi$ (Fig. 5.11b), suggesting that the instability depends on the peak stresses in the laminar flow (Fig. 5.6). There is some evidence that there is an instability at the third resonance with $De \sim 240$ and at higher wavenumber, $k_x \sim 12$. However, we were unable to obtain converged results for this instability.

Unfortunately, we cannot make a direct comparison between this flow and the shear layer instability of Chapter 3. In that chapter we were free to prescribe the stress and the velocity of the base flow, however, in this problem the velocities and stresses of the laminar flow are determined by the applied pressure gradient and depend on time. Nonetheless, there are some encouraging signs that this instability and the shear layer instability may have the same mechanism. The dispersion relations are similar in shape to those of Chapter 3 (compare Figs 5.8 and 3.5). Additionally, the form of the eigenvectors seems similar to what we might expect from the shear layer instability. To explore this idea, we plot $y^*$, as the line of maximum average stress in the laminar profile defined in Fig. 5.5. Fig. 5.12 suggests that the eigenvector for the instability at $De = 100$, $Wi = 55$ consists of a pair of vortices with the centres near $y_*$ and large streamwise stresses above and below $y^*$. This leads us to suspect that the instability has a similar mechanism to the instability of Chapter 3.

There is a difference between the eigenvectors at $De = 100$ and $De = 120$. At $De = 100$ we see a double layer of vortices rotating in opposite directions, whereas at higher $De$ and lower $Wi$, there is only a single layer of vortices. This difference has not yet been explored fully, but would be an interesting subject for future work.

The nonlinear analysis of section 5.5 confirms that the instability does exist at $De = 120$ and $Wi = 32$, and does not saturate until it has approximately 1% of the energy of the base flow (Fig. 5.15a). In Figs 5.16–5.19 we show plots of the convergence of the first two modes of this nonlinear steady state. Imperfections in this convergence

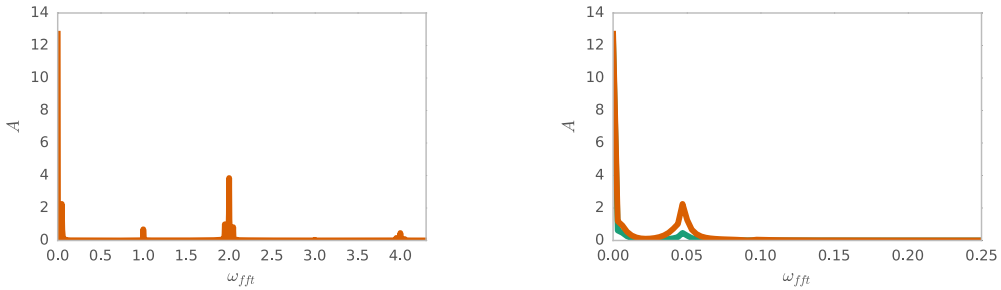


(a) (b)

Figure 5.21: The Fourier transform of Figs 5.15a (turquoise), and 5.15b (orange). Panel b) shows the low frequency region of a).

may be due to the difficulty in matching the phase of the two solutions caused by a large time scale oscillation in the solution.

Interestingly, both the linear and nonlinear analysis at these parameters shows the emergence of another frequency besides the frequency of the base flow. Fig. 5.21a shows a Fourier transform of Fig. 5.15a. The whole-number frequencies (at 1, 2, 3 and 4) correspond to the pressure gradient frequency and nonlinear interactions with it. The peak at much smaller frequency $\sim 0.05$, is not related to the pressure gradient frequency. Fig. 5.21b shows that it is also not related to the time step: decreasing the time step amplifies the signal, but keeps the frequency the same. A Fourier transform of the norm of the linear stability streamfunction, Fig. 5.7d leads to a plot almost identical to Fig. 5.21a. We have not had time to explore this oscillation in detail to see its effect on the dynamics.

# Chapter 6

# A viscoelastic self-sustaining process in plane Couette flow

In this chapter, we turn to the final stage of the research programme outlined in section 1.4. We explore a purely elastic analogue of the Newtonian self-sustaining process (the SSP) [95] as a basis for an exact coherent structure.

Exact coherent structures have been found in many numerical simulations and experiments [44]. The Newtonian turbulent attractor is thought to be constructed from a framework of exact solutions which increases in density in phase space as the Reynolds number ($Re$) increases. More recently, periodic orbit solutions have been discovered in plane Couette [66], pipe [162], boundary layer flows [80], and two dimensional Kolmogorov flow [163]. The flow statistics of these time- and space-dependent solutions match those of experimental turbulent flows remarkably well. According to the emerging picture, a turbulent fluid trajectory in phase space 'pinballs' between these states, spending most of its time very close to one of these solutions (see e.g. [44, 164–166] for an overview).

Here I briefly summarise the Newtonian self sustaining process of Waleffe [94, 95], a detailed discussion can be found in the introduction, section 1.3.2. The analysis begins by identifying long-lived structures in plane Couette flow (streamwise vortices [70]), which also correspond to the most non-normally amplified disturbances [167]. The SSP aims to explain why these vortices are present for such long times in plane Couette flow. It does this by forcing a flow with streamwise vortices to see if the three dimensional flow that results itself produces vortices. The effect of the vortices on the laminar flow is to lift up fluid, moving it between the plates. This creates high- and low-speed streaks in the spanwise velocity. These streaks alter the streamwise velocity to produce regions of large shear, which are vulnerable to a Kelvin-Helmholtz like instability. The surface of the streaks undulates in the streamwise direction, because of the instability.

Finally, the nonlinear self-interaction terms from the wavy disturbance regenerate the original streamwise rolls (see Fig. 1.11).

The effects of viscoelasticity on the Newtonian self-sustaining process has already been studied in the context of explaining the reduction in viscous drag due to the addition of a small concentration of polymeric fluid [101, 103, 104] (this effect is known as drag reduction, and is discussed in the introduction to Chapter 2 and in section 1.1.1 of the introduction). Elasticity delays the onset of the SSP solution until higher $Re$ because the polymeric stress opposes the nonlinearities that produce the vortices in the third phase of the process [103, 168, 169]. Below a minimum Reynolds number this SSP solution ceases to exist, regardless of the Weissenberg number. This suggests that Waleffe's SSP is not connected to exact coherent structures in the purely elastic regime.

In this chapter, we construct our own SSP for purely elastic flows. The presence of exact coherent structures is suggested by earlier experimental [40, 42] and numerical results [8] on transitional purely elastic flows. Given the previous results on viscoelastic coherent structures at high $Re$ [101, 103, 104, 169], it seems that purely elastic exact solutions cannot be found by homotopy from their Newtonian counterparts. Instead, we form a new SSP for the purely elastic case, using the fact that the nonlinearities in the Oldroyd-B equation can cause instability even at very low Reynolds number.

We investigate the three phases of the process numerically: the forcing of a streaky flow, the instability of the flow, and the feedback of this instability to reproduce the forcing. To begin, we look at the two candidates identified by Jovanović and Kumar [98] for the most non-normally amplified structures in the flow: a strong fluctuation in the $\tau_{yy}$ component of the stress in section 6.2, and a flow of streamwise oriented vortices in section 6.3. We find that the $\tau_{yy}$ forcing can not produce an SSP, however, we use a Newton-Raphson method to show that streamwise independent rolls force a streaky flow at low $Re$. Then, in section 6.4, we perform a linear stability analysis of this flow to show that it is unstable to perturbations both dependent and independent of the streamwise coordinate $x$. Finally in section 6.5 we investigate how the eigenvectors which correspond to these instabilities reinforce the base flow, completing the SSP.

## 6.1 Problem Formulation

We begin by examining the laminar flow of an Oldroyd-B fluid between two infinite parallel plates in relative motion, plane Couette flow (Fig. 6.1). Again, we choose a coordinate system such that $x$ is the streamwise direction (the direction of motion of the upper plate), $y$ is the wall-normal direction, and $z$ the spanwise direction. The dimensional Oldroyd-B equations (1.23), with functional dependence on $y$ only and no

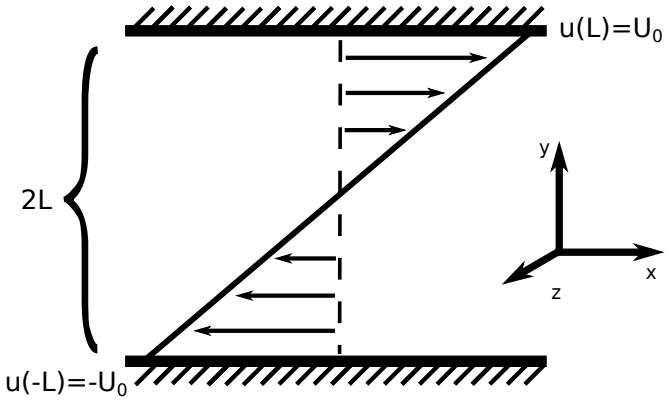


Figure 6.1: Couette flow diagram with the coordinate system.

forcing of the flow, simplify to give:

$$\tau_{xx} - 2\lambda\tau_{xy}\frac{\mathrm{d}u}{\mathrm{d}y} = 0 \tag{6.1}$$

$$\tau_{xy} - \lambda\tau_{yy}\frac{\mathrm{d}u}{\mathrm{d}y} = \eta_p\frac{\mathrm{d}u}{\mathrm{d}y} \tag{6.2}$$

$$\tau_{yy} = 0 \tag{6.3}$$

$$\eta_s\frac{\mathrm{d}^2u}{\mathrm{d}y^2} + \frac{\mathrm{d}}{\mathrm{d}y}\tau_{xy} = 0\,. \tag{6.4}$$

Rearranging and solving gives,

$$\tau_{xy} = \eta_p\frac{\mathrm{d}u}{\mathrm{d}y} \qquad \tau_{xx} = 2\lambda\eta_p\left(\frac{\mathrm{d}u}{\mathrm{d}y}\right)^2 \qquad \tau_{yy} = 0 \qquad u(y) = \frac{U_0}{L}y\,, \tag{6.5}$$

where we have used the boundary conditions, $u(\pm L) = \pm U_0$, to solve for $u$. Just as in (2.4) we use the wall speed, $U_0$, and the half distance $L$ to make the equations dimensionless. This gives us the dimensionless Oldroyd-B and Navier-Stokes equations:

$$\begin{aligned}
Re\left[\frac{\partial\mathbf{v}}{\partial t} + \mathbf{v}\cdot\nabla\mathbf{v}\right] &= -\nabla p + \beta\nabla^2\mathbf{v} + (1-\beta)\nabla\cdot\boldsymbol{\tau} \\
\nabla\cdot\mathbf{v} &= 0 \\
Wi\left[\frac{\partial\boldsymbol{\tau}}{\partial t} + \mathbf{v}\cdot\nabla\boldsymbol{\tau}\right] &= Wi\left[(\nabla\mathbf{v})^T\cdot\boldsymbol{\tau} + \boldsymbol{\tau}\cdot(\nabla\mathbf{v})\right] + (\nabla\mathbf{v})^T + \nabla\mathbf{v} - \boldsymbol{\tau} \\
\mathbf{v}(\pm 1) &= \pm\mathbf{e}_x\,,
\end{aligned} \tag{6.6}$$

where $Re$ is the Reynolds number, $Wi$ is the Weissenberg number, $\nabla$ is the gradient operator, $\nabla^2$ is the Laplacian.

For the first step of the self-sustaining process we need to calculate the flow due to the most non-normally amplified structures. In the Newtonian problem, these are streamwise vortices. The most non-normally amplified purely elastic structures have already been studied [98]. One of the these structures consists of a constant wall-normal stress, $\tau_{yy}$. This stress is advected by the mean shear to give fluctuations in the streamwise stress, $\tau_{xx}$. We shall see that this flow cannot lead to an SSP. The other purely elastic non-normally amplified structure is streamwise independent rolls. These vortices look much like the Newtonian ones, so our analysis of this problem will closely follow that of Waleffe [95].

## 6.2 $\tau_{yy}$ Forcing

First we consider the streaky flow due to the non-normally amplified forcing of $\tau_{yy}$. Jovanović and Kumar [98] found that this leads to the strongest transient growth when the forcing is independent of the spanwise direction $z$. Therefore, we consider a forcing which only depends on $y$ and a wavenumber $k_f$, such that

$$T_{yy} = \begin{cases} either & A\cos\left(k_f y\right) \\ or & A\sin\left(k_f y\right), \end{cases} \tag{6.7}$$

where $A$ is the amplitude of the forcing. The base flow, represented using upper-case letters $\mathbf{V} = (U, V, 0)^T$, is given by the solution to the system of differential equations:

$$\begin{aligned} Re\left[\frac{\partial U}{\partial t} + (\mathbf{V}\cdot\nabla)U\right] &= \beta\nabla^2 U + (1-\beta)\left(\frac{\partial T_{xx}}{\partial x} + \frac{\partial T_{xy}}{\partial y}\right) \\ Re\left[\frac{\partial U}{\partial t} + (\mathbf{V}\cdot\nabla)V\right] &= \beta\nabla^2 V + (1-\beta)\left(\frac{\partial T_{xy}}{\partial x} + \frac{\partial T_{yy}}{\partial y}\right) \\ T_{xx} + Wi\left[\frac{\partial T_{xx}}{\partial t} + (\mathbf{V}\cdot\nabla)T_{xx} - 2T_{xx}\frac{\partial U}{\partial x} - 2T_{xy}\frac{\partial U}{\partial y}\right] &= 2\frac{\partial U}{\partial x} \\ T_{xy} + Wi\left[\frac{\partial T_{xy}}{\partial t} + (\mathbf{V}\cdot\nabla)T_{xy} - T_{xx}\frac{\partial V}{\partial x} - T_{yy}\frac{\partial U}{\partial y}\right] &= \frac{\partial U}{\partial y} + \frac{\partial V}{\partial x}, \end{aligned} \tag{6.8}$$

where

$$(\mathbf{V}\cdot\nabla) = U\frac{\partial}{\partial x} + V\frac{\partial}{\partial y}. \tag{6.9}$$

Because the laminar flow depends only on $y$, we can simplify these equations to give:

$$\begin{aligned} T_{xx} &= 2\,Wi T_{xy}\frac{\partial U}{\partial y} \\ T_{xy} &= \left(1+\,Wi T_{yy}\right)\frac{\partial U}{\partial y} \\ \beta\frac{\partial^2 U}{\partial y^2} + (1-\beta)\frac{\partial T_{xy}}{\partial y} &= 0 \\ U(\pm 1) &= \pm 1\,. \end{aligned}$$

When $T_{yy} = A\cos\left(k_f y\right)$, solving this system of differential equations gives,

$$U(y) = \frac{\operatorname{atanh}\left(\left(1-\tilde{A}\right)\frac{\tan\left(\frac{k_f y}{2}\right)}{\sqrt{\tilde{A}^2-1}}\right)}{\operatorname{atanh}\left(\left(1-\tilde{A}\right)\frac{\tan\left(\frac{k_f}{2}\right)}{\sqrt{\tilde{A}^2-1}}\right)}, \tag{6.10}$$

where $\tilde{A} = A\,Wi(1-\beta)$. When $T_{yy} = A\sin\left(k_f y\right)$ the solution is,

$$\begin{aligned} U(y) &= \frac{2}{B_u - B_l}\arctan\left(\frac{\tilde{A}+\tan\left(\frac{k_f y}{2}\right)}{\sqrt{1-\tilde{A}^2}}\right) - \frac{B_u+B_l}{B_u-B_l} \\ B_l &= \arctan\left(\frac{\tilde{A}-\tan\left(\frac{k_f}{2}\right)}{\sqrt{1-\tilde{A}^2}}\right) \\ B_u &= \arctan\left(\frac{\tilde{A}+\tan\left(\frac{k_f}{2}\right)}{\sqrt{1-\tilde{A}^2}}\right). \end{aligned} \tag{6.11}$$

The cosinusoidal forcing produces laminar velocities which are anti-symmetric about $y = 0$ (Fig. 6.2a), and the sinusoidal forcing produces asymmetric flows about $y = 0$ (Fig. 6.2b). These solutions both have singularities in the domain for particular values of $A, k_f$, $Wi$ and $\beta$. We can avoid parameters where this occurs since we expect our hydrodynamic fields to be smooth, however, there is a more serious problem. We know from the discussion in the introduction that the Oldroyd-B model is only physical when the conformation tensor is positive definite (section 1.1.2) — only the cosinusoidal forcing with positive amplitude satisfy this condition.

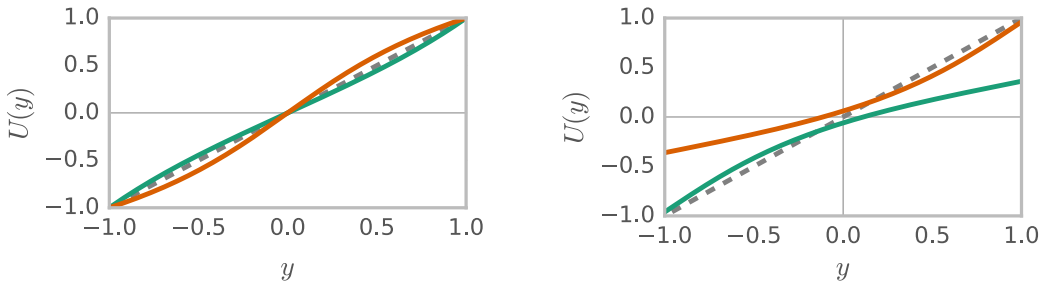


(a) (b)

Figure 6.2: The laminar velocity, $U(y)$, for plane Couette flow with a forcing to $T_{yy}$ at $k_f = \pi/2$, $\beta = 0.1$ and $Wi = 2.0$. a) The cosinusoidal forcing, $T_{yy} = A\cos(k_f y)$ with $A = 0.3$ in green and $A = -0.3$ in red. b) The sinusoidal forcing, $T_{yy} = A\sin(k_f y)$ with $A = 0.3$ in green and $A = -0.3$ in red.

### Linear stability

Having obtained solutions, we now examine their linear stability to perturbation in the streamwise direction. We use the pseudospectral method of Appendix A.1 and Chapter 3 to discretise the $y$ dependent variables onto a grid. For each linear perturbation field $(u, v, p, \tau_{ij})$ we consider the stability of this flow to perturbations in the $x$ direction, $g(x, y, t) = g(y)\mathrm{e}^{ik_x + \lambda t}$.

We find that forcing $\tau_{yy}$ with the cosinusoidal forcing is stable for all positive $A, 0 < k_f < \pi$ and $Wi < 10$ where the base flow is smooth. An example stable spectrum is shown in Fig. 6.3.

The $\tau_{yy}$ forcing does not appear to be unstable, and therefore is not a suitable basis for the SSP. In the rest of this Chapter, we shall instead force the flow using streamwise vortices, the alternative optimal structure for non-normal growth.

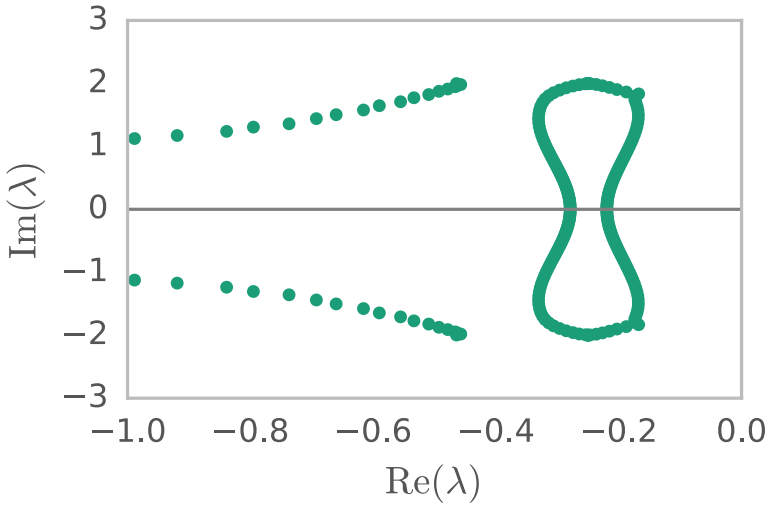


Figure 6.3: Spectrum for the instability of Couette flow forced with $T_{yy} = A\cos(k_f y)$, where $A = 0.24$, $k_f = 2.8$, $Re = 0.1$, $\beta = 0.1$ and $Wi = 4.0$. The plot is converged for this wavenumber, $k_x = 2$, with 100 Gauss-Lobatto pseudo-spectral points.

## 6.3 Streamwise oriented vortex forcing

The streamwise vortex problem is driven by fixing the wall-normal and spanwise base profile velocities,

$$\begin{aligned} V(y,z) &= \frac{A}{\hat{v}(0)}\hat{v}(y)\cos(\gamma z) \\ W(y,z) &= -\frac{A}{\hat{v}(0)\gamma}\frac{\partial \hat{v}}{\partial y}\sin(\gamma z)\,, \end{aligned} \tag{6.12}$$

where,

$$\hat{v}(y) = \frac{\cos(py)}{\cos(p)} - \frac{\cosh(\gamma y)}{\cosh(\gamma)}\,, \tag{6.13}$$

and the number of rolls in the wall-normal direction is set by $p$, a solution of $p\tan p + \gamma\tanh\gamma = 0$. We use an amplitude for the forcing, $A = 0.02$, unless otherwise stated.

Throughout the rest of this chapter we set $\gamma$, the spanwise wavenumber, to $\pi/2$ and use a $p$ such that there is a single layer of rolls. $\gamma = \frac{\pi}{2}$ approximately corresponds to the wavenumbers used by Jovanović and Kumar [98] and the velocity fields used above are an approximation for the non-normally amplified rolls. They are precisely the same rolls used in Waleffe [95] (shown by the arrows in Fig. 6.4a). These velocity fields are related to the lowest order eigenmode of the operator $\nabla^4$, a seemingly tangential remark which we will explore further in section 6.7.

Now we consider the plane Couette Oldroyd-B equations (6.6) for the flow $U(y,z)$, $\mathbf{T}(y,z)$ due to $V(y,z)$ and $W(y,z)$, given that the incompressibility condition is already satisfied. We find that the $(y,z)$ plane stresses decouple from the mean flow,

$$\begin{aligned}
\frac{\mathrm{D}T_{yy}}{\mathrm{D}t} &= 2T_{yy}\frac{\partial V}{\partial y} + 2T_{yz}\frac{\partial V}{\partial z} + \frac{2}{Wi}\frac{\partial V}{\partial y} - \frac{T_{yy}}{Wi} \\
\frac{\mathrm{D}T_{zz}}{\mathrm{D}t} &= 2T_{yz}\frac{\partial W}{\partial y} + 2T_{zz}\frac{\partial W}{\partial z} + \frac{2}{Wi}\frac{\partial W}{\partial z} - \frac{T_{zz}}{Wi} \\
\frac{\mathrm{D}T_{yz}}{\mathrm{D}t} &= T_{zz}\frac{\partial V}{\partial z} + T_{yy}\frac{\partial W}{\partial y} + \frac{1}{Wi}\left(\frac{\partial V}{\partial z} + \frac{\partial W}{\partial y}\right) - \frac{T_{yz}}{Wi}\,,
\end{aligned} \tag{6.14}$$

where,

$$\frac{\mathrm{D}}{\mathrm{D}t} = \left[\frac{\partial}{\partial t} + V(y,z)\frac{\partial}{\partial y} + W(y,z)\frac{\partial}{\partial z}\right]\,, \tag{6.15}$$

and capital letters indicate the streaky flow variables, which depend on $y$ and $z$ only. We calculate these stresses directly from $V$ and $W$. The fact that these stresses decouple from the mean flow means that viscoelastic flows that depend only on $y$ and $z$, such as streamwise vortices, decay exponentially unless they are forced. There are no terms to draw energy from the mean flow in these equations and force the stresses. Briefly returning to the unforced flow we can see that there are no terms in the equations for $V$ or $W$ which depend on the mean flow,

$$\begin{aligned}
Re\frac{\mathrm{D}V}{\mathrm{D}t} &= \beta\nabla^2 V + (1-\beta)\left(\frac{\partial T_{yy}}{\partial y} + \frac{\partial T_{yz}}{\partial z}\right) \\
Re\frac{\mathrm{D}W}{\mathrm{D}t} &= \beta\nabla^2 W + (1-\beta)\left(\frac{\partial T_{yz}}{\partial y} + \frac{\partial T_{zz}}{\partial z}\right)\,.
\end{aligned} \tag{6.16}$$

just as in the Newtonian case [93]. This means that a 2D exact coherent structure cannot only depend on $y$ and $z$, it must have dependence on some other combination or on all three coordinates.

The nonlinear problem for the flow in the streamwise direction is given by

$$\begin{aligned}
\frac{\mathrm{D}T_{xx}}{\mathrm{D}t} &= 2T_{xy}\frac{\partial U}{\partial y} + 2T_{xz}\frac{\partial U}{\partial z} - \frac{T_{xx}}{Wi} \\
\frac{\mathrm{D}T_{xy}}{\mathrm{D}t} &= T_{yy}\frac{\partial U}{\partial y} + T_{yz}\frac{\partial U}{\partial z} + T_{xy}\frac{\partial V}{\partial y} + T_{xz}\frac{\partial V}{\partial z} + \frac{\partial U}{\partial y} - \frac{T_{xy}}{Wi} \\
\frac{\mathrm{D}T_{xz}}{\mathrm{D}t} &= T_{yz}\frac{\partial U}{\partial y} + T_{zz}\frac{\partial U}{\partial z} + T_{xy}\frac{\partial W}{\partial y} + T_{xz}\frac{\partial W}{\partial z} + \frac{\partial U}{\partial z} - \frac{T_{xz}}{Wi} \\
Re\frac{\mathrm{D}U}{\mathrm{D}t} &= \beta\nabla^2 U + (1-\beta)\left(\frac{\partial T_{xy}}{\partial y} + \frac{\partial T_{xz}}{\partial z}\right) \\
U(\pm 1) &= \pm 1\,.
\end{aligned} \tag{6.17}$$

We use a Chebyshev-Fourier decomposition, with Chebyshev polynomials in the wall-normal ($y$) direction and Fourier modes in the spanwise ($z$) direction (the spectral method of the Appendix, section A.1). First we solve the linear problem for $T_{yy}$, $T_{zz}$, $T_{yz}$ using (6.14), then we solve for the streamwise velocity and stresses using (6.17). The second problem is nonlinear, and so we use a Newton Raphson method, as outlined in section A.2.2. The Fourier and Chebyshev transform of the variables gives,

$$G(y,z) = \sum_{n=-N}^{N}\sum_{m=0}^{M-1} G_{m,n}\mathrm{e}^{in\gamma z}T_m(y) + c.c, \tag{6.18}$$

where $G$ stands for any of the base profile variables $(U, V, W, T_{ij})$ in the problem and $T_m(y)$ is the $m^{\text{th}}$ Chebyshev polynomial of the first kind.

### The resulting flow

After using our Newton Raphson method, we obtain the flow consisting of $U$ and $\mathbf{T}$. To analyse this flow, we look at the streamwise velocity $U$ in the $(y,z)$ plane and compare it for the Newtonian and viscoelastic cases (Figs 6.4a and 6.4b). We also consider an average over the $z$ direction and compare this with the laminar flow in Fig. 6.4c. There are no polymeric stresses in the Newtonian case, but for the purely elastic case Fig. 6.6c shows a colour map of the first normal stress difference in the $(y,z)$ plane, $N_1 = T_{xx} - T_{yy}$.

At high $Re$ we find streaks in the streamwise velocity similar to those in [95] (Fig. 6.4a), however, as we decrease the Reynolds number with a fixed Weissenberg number, we find that these velocity streaks become less pronounced. This is clear by looking at both the streamwise velocity (Fig. 6.4b) and its average over $z$ (Fig. 6.4c and Fig. 6.4d), and corresponds to a decrease in the effectiveness of the Newtonian lift-up effect for lower $Re$.

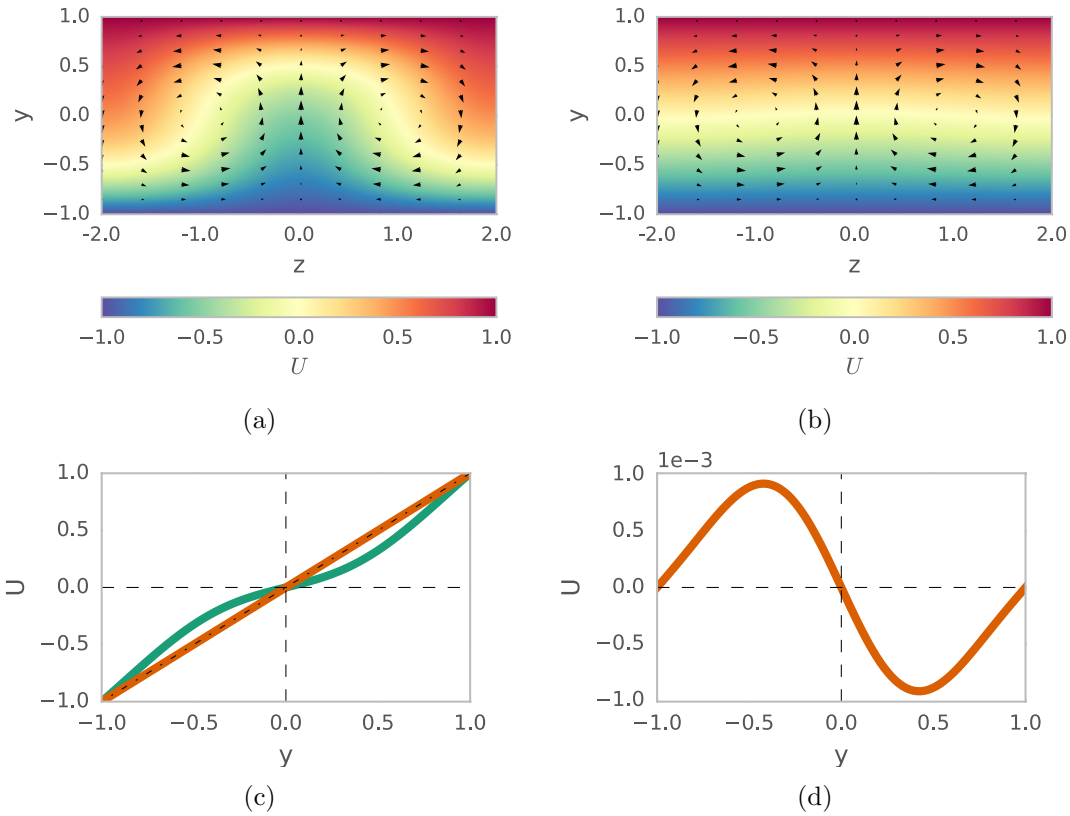


Figure 6.4: a) The magnitude of the streamwise velocity of the fluid at $Re = 200$, $\beta = 1.0$, $A = 0.02$, $N = 6$, $M = 40$. The arrows show the in plane velocity. Panel b) is the same as a) but for the purely elastic regime, $Re = 0.01$, $Wi = 2.0$, $N = 12$, $M = 40$. c) The mean streamwise velocity of the Newtonian (green) and purely elastic (orange) streaky flows. d) The same as c) but showing only the purely elastic case, and subtracting laminar Couette flow.

As noted earlier, instabilities in viscoelastic fluids are brought about by large changes in the first normal stress difference, since this brings about polymer stretching of the kind seen in the Weissenberg effect. Although we do not see streaks in the streamwise velocity for the purely elastic case, we do see them in the first normal stress difference, (Fig. 6.6c). These streaks appear in a similar pattern as the streamwise velocity streaks appear in the Newtonian self-sustaining process and are caused by the stretching and compression of the polymers by the vortical flow.

The purely elastic stresses show very large gradients near the walls (Figs 6.5 and 6.6). This suggests that a higher numerical resolution will be required to resolve the instability of the streaky flow in the purely elastic case than the Newtonian case, an issue we will return to in section 6.6.

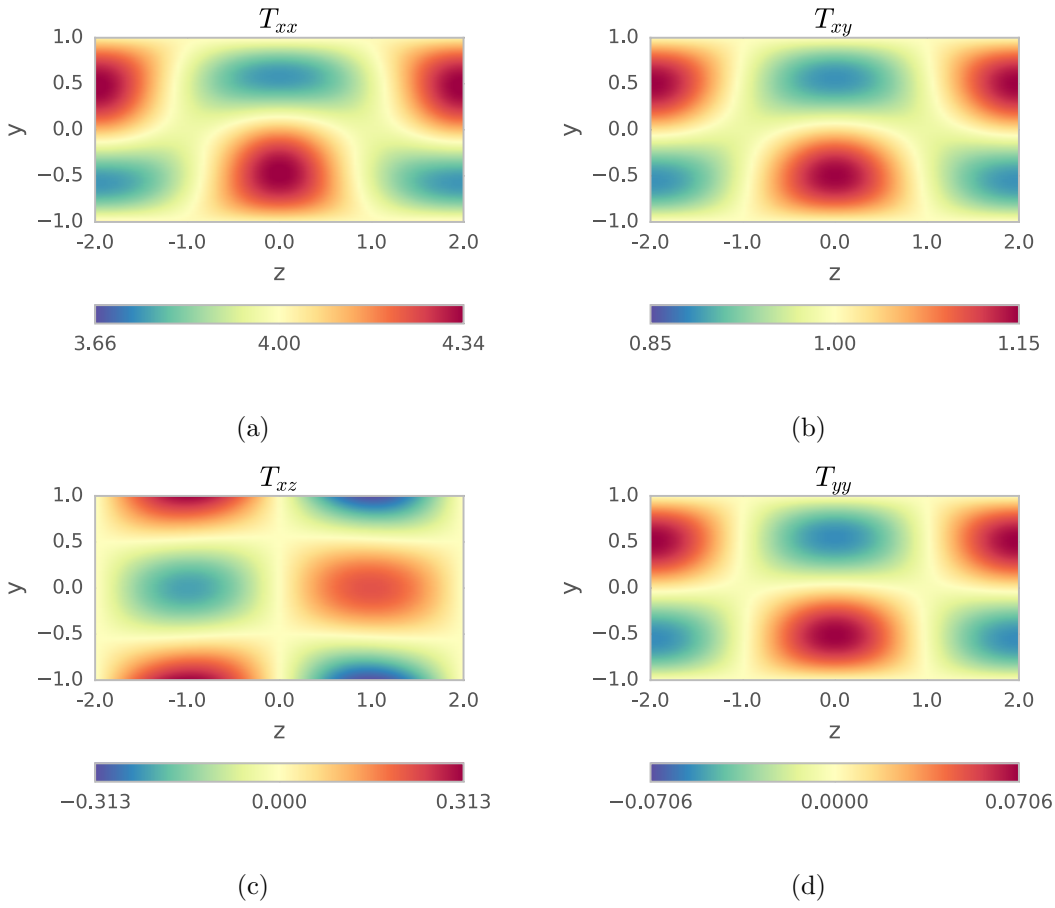


Figure 6.5: Colour maps of the stress components at $Re = 0.01$, $Wi = 2.0$, $N = 12$, $M = 40$. The white region corresponds to the value of the stress throughout the domain for the laminar flow. The panels show: a) $T_{xx}$, b) $T_{xy}$ c) $T_{xz}$ and d) $T_{yy}$.

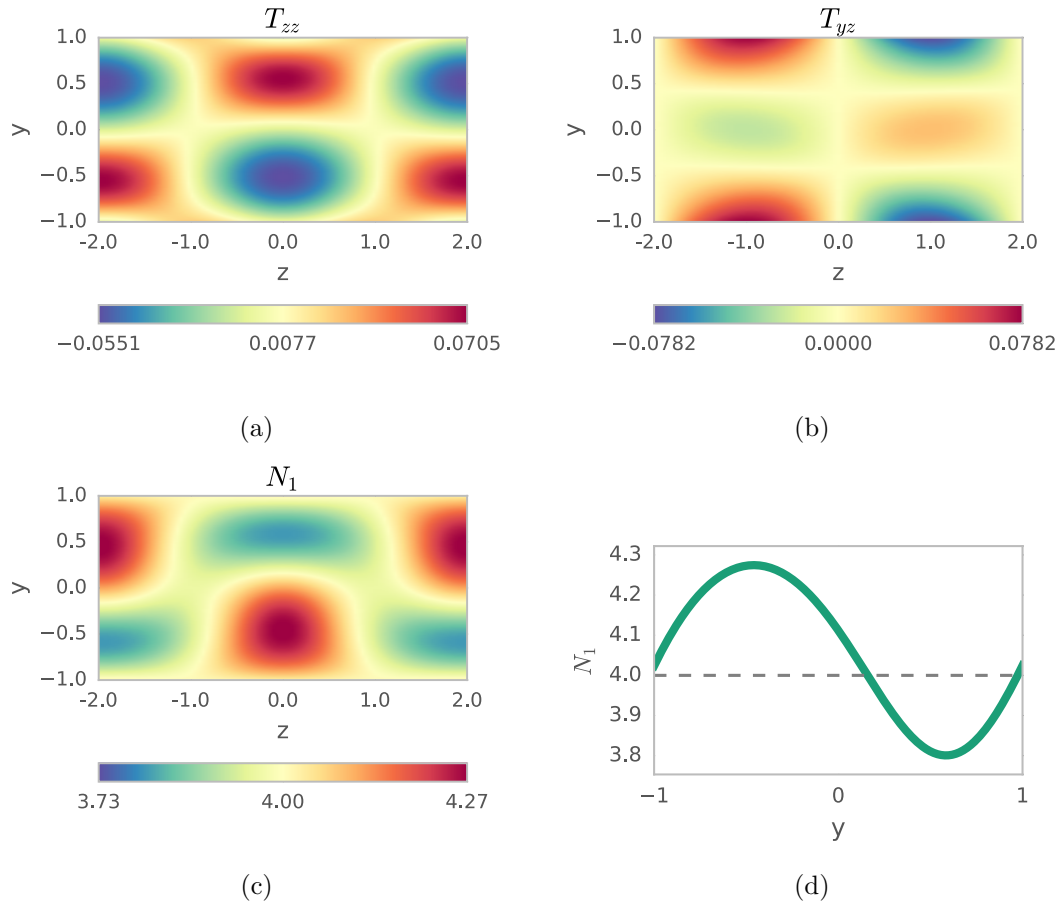


Figure 6.6: Colour maps of the stress components at $Re = 0.01$, $Wi = 2.0$, $N = 12$, $M = 40$. The panels show: a) $T_{zz}$, b) $T_{yz}$, c) the first normal stress difference, $N_1$, and d) the first normal stress difference dependence on $y$ at $z = 0$. The dashed line at $N_1 = 4$ shows the first normal stress difference for the laminar Couette flow.

## 6.4 Linear Stability Analysis

Having obtained the full base profile of the problem, we perform linear stability analysis to look for streamwise variation in the streaky flow. Just as in the Newtonian version of the process wavy instabilities are responsible for sustaining the exact coherent state. We begin this stage of the analysis by forming the linear stability equations,

$$\begin{aligned} Re\left[\frac{\partial \mathbf{v}}{\partial t} + \mathbf{v}\cdot\nabla\mathbf{v}\right] &= -\nabla p + \beta\nabla^2\mathbf{v} + (1-\beta)\nabla\cdot\boldsymbol{\tau} \\ \nabla\cdot\mathbf{v} &= 0 \\ \boldsymbol{\tau} + Wi\frac{\partial \boldsymbol{\tau}}{\partial t} &= (\nabla\mathbf{v})^T + (\nabla\mathbf{v}) - Wi\big[(\mathbf{V}\cdot\nabla)\boldsymbol{\tau} + (\mathbf{v}\cdot\nabla)\boldsymbol{T} \\ &\qquad - (\nabla\mathbf{V})^T\cdot\boldsymbol{\tau} - (\nabla\mathbf{v})^T\cdot\boldsymbol{T} - \boldsymbol{\tau}\cdot(\nabla\mathbf{V}) - \boldsymbol{T}\cdot(\nabla\mathbf{v})\Big]\,, \end{aligned} \tag{6.19}$$

where $\mathbf{v}$, $p$ and $\boldsymbol{\tau}$ are the linear disturbance quantities, and $\mathbf{V}$ and $\boldsymbol{T}$ are the base flow quantities.

We decompose the disturbance velocities in the same basis as above (6.18), but include streamwise dependence

$$g(x,y,z) = \mathrm{e}^{ik_x x}\sum_{n=-N}^{N}\sum_{m=0}^{M+1}\check{g}_{m,n}T_m(y)\mathrm{e}^{in\gamma z}\,, \tag{6.20}$$

where $g$ can be any of the disturbance variables $(u, v, w, p, \tau_{ij})$ and $k_x$ is the streamwise wavenumber.

Assuming an exponential dependence on time, $g(x,y,z,t) = \mathrm{e}^{\lambda t}g(x,y,z)$, we obtain the linearised system of equations for the eigenvalues $\lambda$. Unstable modes are those with a positive growth rate, given by the real part of the eigenvalue $\mathrm{Re}(\lambda) = \lambda_r$. We find the maximum $\lambda_r$ at each wavenumber, $k_x$, and obtain dispersion relations.

We performed this linear stability analysis for the flows found in section 6.3, however, the results did not converge over the range of resolutions we used (with maximum resolution $N = 10$ and $M = 80$). The large gradients in the boundary layers at $y = \pm 1$ are likely responsible for this difficulty, however, we expect the instability to take place in the centre of the channel, due to the large jump in $N_1$ (see Fig. 6.4b), and therefore to be insensitive to the boundary conditions. We use free slip boundary conditions on the disturbance velocities, $\frac{\partial u}{\partial y}(\pm 1) = v(\pm 1) = \frac{\partial w}{\partial y}(\pm 1) = 0$ to increase the numerical stability of the problem, just as was used for the Newtonian SSP [95]. The effects of this choice will be discussed further in section 6.6.

Dispersion relations are shown in Figs 6.7 and 6.8. The data shows that as the Reynolds number is decreased, the dispersion relation maximum decreases and moves

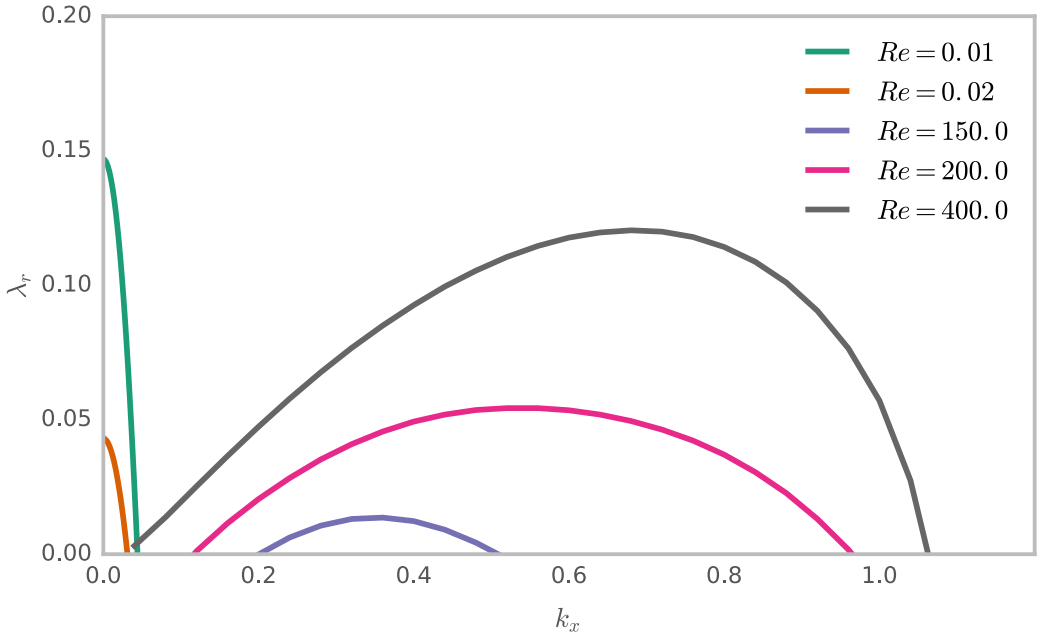


Figure 6.7: Dispersion relations as the Reynolds number is decreased at $Wi = 2$, $\beta = 0.1$ and $A = 0.02$.

to lower streamwise wavenumbers (Fig. 6.7). All of the dispersion relations we show are converged: an example of dispersion relations with two different resolutions is shown in Fig. 6.9. By about $Re = 100$ the base profile has become completely stable. The Newtonian instability is no longer present at this Reynolds number. However, once the Reynolds number becomes negligible in comparison to the Weissenberg number, we begin to see a purely elastic instability arise at very low streamwise wavenumber (Fig. 6.7). This purely elastic instability is amplified by further reductions in the Reynolds number.

The dispersion relation for the purely elastic instability grows as the Weissenberg number increases, and saturates by around $Wi \sim 20$ (Fig. 6.8). The kink in the dispersion relations arises because the dominant eigenvalue changes at around $k_x = 0.02$. This changeover in eigenvalue is slightly dependent on $Wi$.

We examine some of the eigenvectors for the purely elastic instability. We look at the Fourier components of $N_1$ and the velocities in Figs 6.10 and 6.11. These Fourier components are dominated by either the real or the imaginary part (for example, the imaginary part is nearly zero in 6.11b). To understand this, we recall the definition of the eigenvector fields (6.20) and see by substitution that requiring

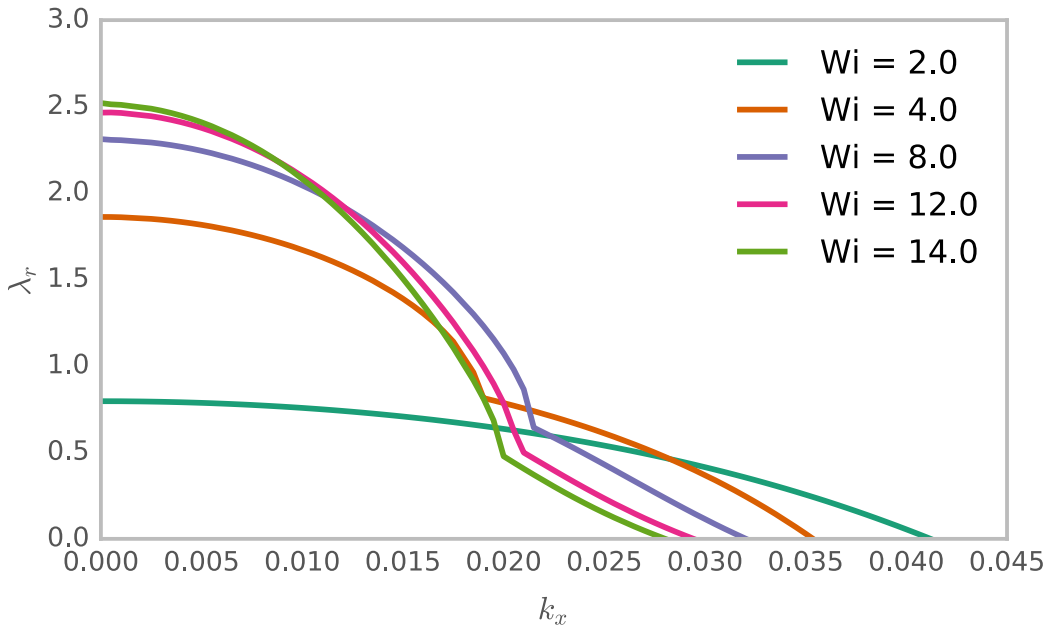


Figure 6.8: Dispersion relations for various $Wi$ at $Re = 0.001$, $\beta = 0.1$ and $A = 0.02$. The instability grows and then saturates for each successive curve with $Wi = 2, 4, 8, 12, 14$.

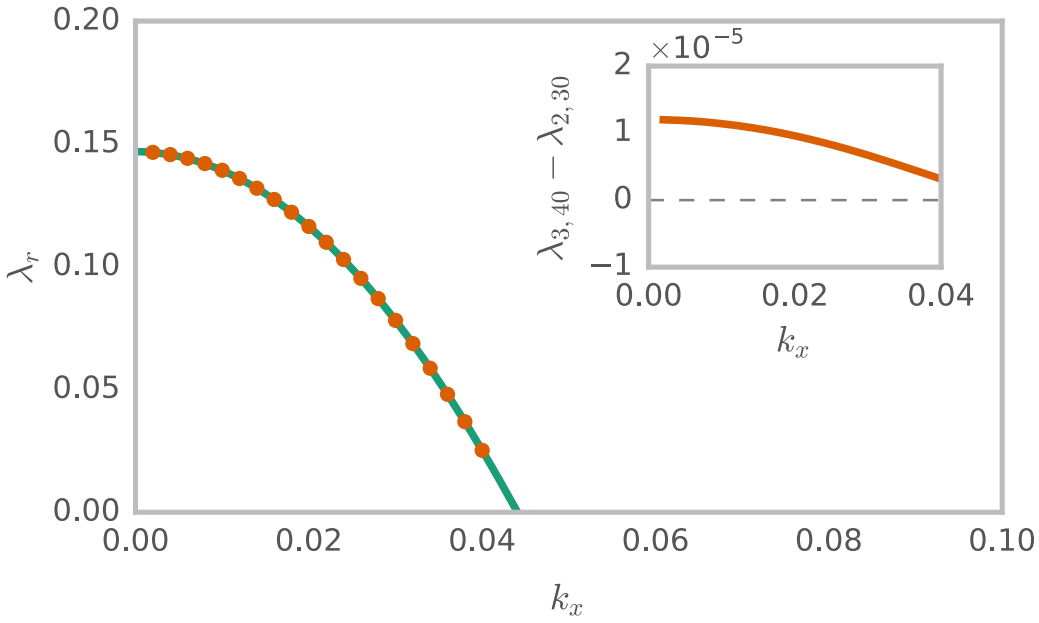


Figure 6.9: Dispersion relation for $Re = 0.01$, $Wi = 2.0$, $\beta = 0.1$. The green line shows the $N = 2$, $M = 30$ resolution and the red markers show the $N = 3$, $M = 40$ resolution. The inset plot shows the difference the two dispersion relations.

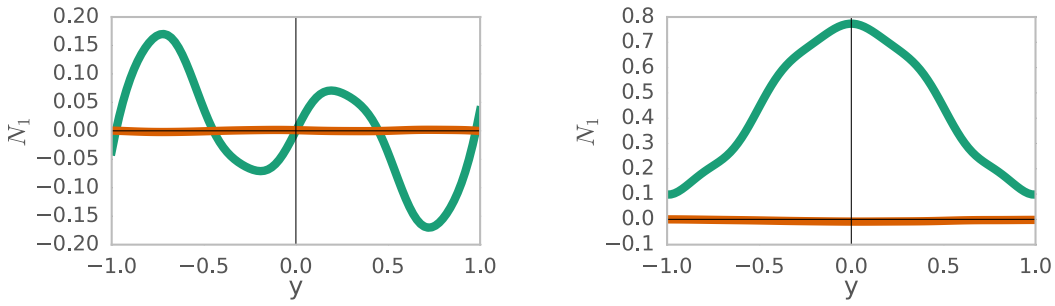


(a) (b)

Figure 6.10: a) 1st and b) 2nd $z$ Fourier modes of the first normal stress difference of the viscoelastic instability at $Wi = 10.0$, $Re = 0.01$, $\beta = 0.1$, $A = 0.02$ and $k_x = 0.01$ for $N = 7$, $M = 60$. Both the real part (Turquoise), and the imaginary part (red) are shown.

$v(x, y, z) = v(-x, y, -z)$ is equivalent to requiring,

$$v_{m,n} = v_{m,-n} = v^*_{m,n} \tag{6.21}$$

for all $m$ and $n$, where in the last expression we have used $^*$ to represent the complex conjugate. This implies that each Fourier component is real after performing the Chebyshev transform. Therefore, when each Fourier component is real the flow field has the symmetry, $v(x, y, z) = v(-x, y, -z)$. Similarly, when each Fourier component is pure imaginary, the flow field satisfies $w(x, y, z) = -w(-x, y, -z)$. Figs 6.10 and 6.11 imply that these symmetries are present here, and that it may be possible to obtain the same eigenvector using a numerical scheme that takes advantage of the symmetries to reduce the size of the problem.

We can visualise the effect of the eigenmode on the base vortical flow by examining the vorticity, $\mathbf{\Omega} = \nabla \times \mathbf{v}$. Figs 6.12b and 6.12d show colour maps of the $x$-component of the vorticity, $\Omega_{x,3D}$, and $N_{1,3D}$ for an eigenvector with the base flow, $G_{3D} = G(y, z) + g(x, y, z) + g^*(x, y, z)$. The 3D data is shown via cuts at $x = 0$, $y = 0$ and $z = 0$.

Both the Fourier components of the instability (Figs 6.10 and 6.11) and the 3D plots (Figs 6.12) show that the gradients in velocity, and the magnitude of the normal stress occur away from the channel walls. This supports our assumption that the boundary conditions make little difference to this instability.

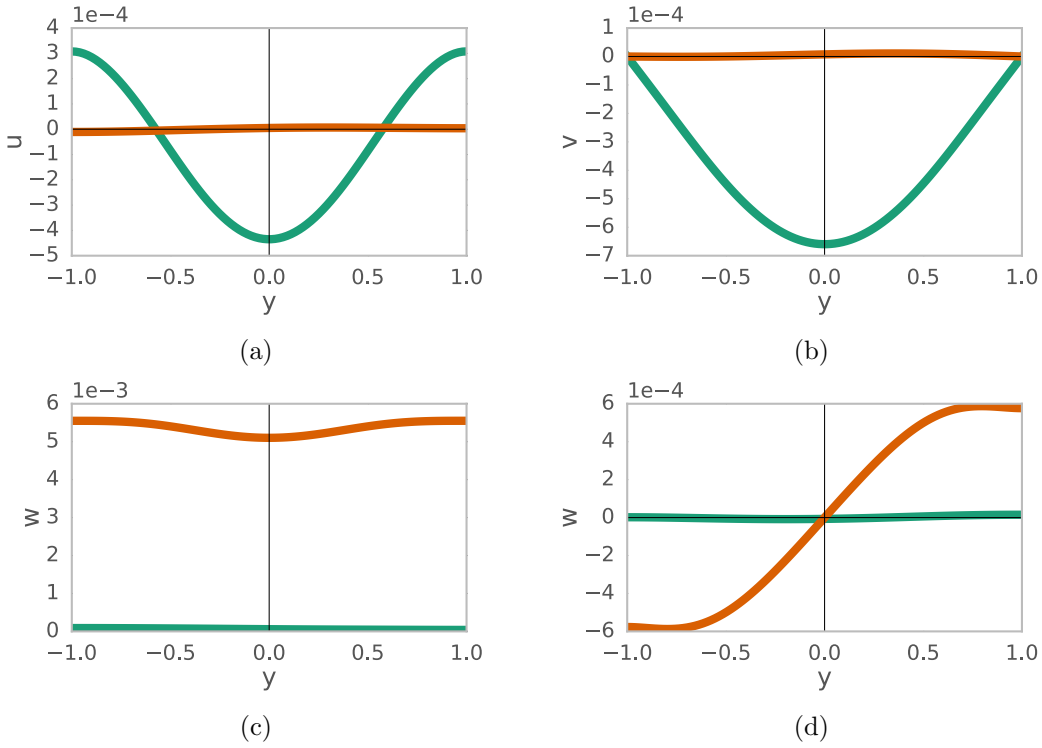


Figure 6.11: $z$ Fourier modes of the velocity components of the viscoelastic instability at $Wi = 10.0$, $Re = 0.01$, $\beta = 0.1$, $A = 0.02$ and $k_x = 0.01$ for $N = 7$, $M = 60$. Panels a) and b) give the 1st $z$ Fourier modes of $u$ and $v$, whilst c) and d) give the zeroth and 1st modes of $w$. Both the real part (Turquoise), and the imaginary part (red) are shown.

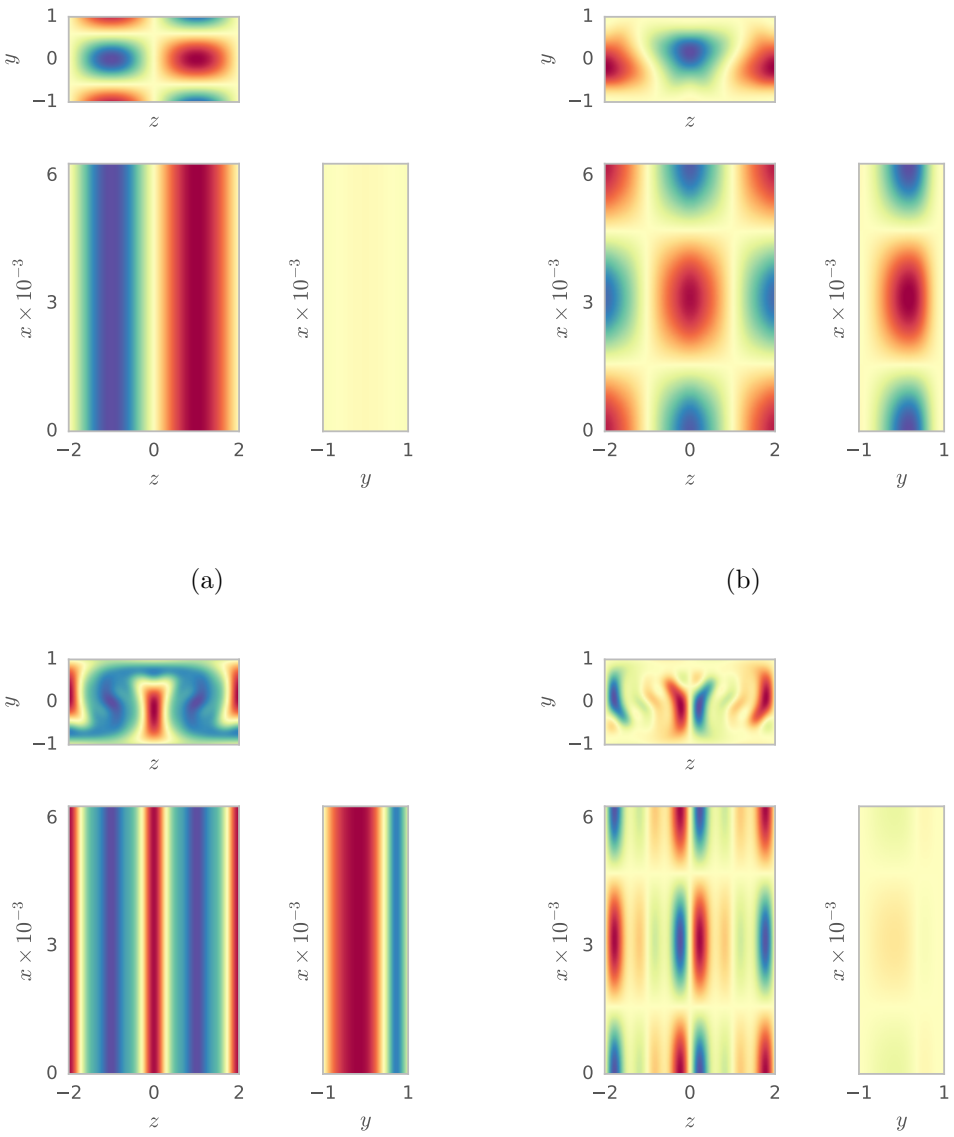


Figure 6.12: The streamwise vorticity and the first normal stress difference, $N_1$, of the base flow and the eigenmode of the instability. a) and b) give the streamwise vorticity. c) and d) show the first normal stress difference. a) and c) show the base flow and b) and d) show the eigenmode of the viscoelastic instability. All results are for a flow with $Wi = 10.0$, $Re = 0.01$, $\beta = 0.1$, $A = 0.02$ and $k_x = 0.01$ for $N = 7$, $M = 60$.

## 6.5 Nonlinear feedback on the rolls

In the Newtonian version of this self-sustaining process [95], the self-interaction terms due to the eigenvector of the instability feedback to produce the original rolls. Although not conclusive, this is evidence that the cycle is self-sustaining, and corresponds to an exact solution of the equations. A schematic analysis for the nonlinear feedback requires solving for $V'$ and $W'$ due to forcing from the nonlinear terms in the Oldroyd-B equation as well as the nonlinear terms from the velocities. First we eliminate the continuity equation for the mean flow in $x$ by using the $(y,z)$ plane streamfunction for the rolls, $\Psi'$, defined by $V' = \frac{\partial \Psi'}{\partial z}$ and $W' = -\frac{\partial \Psi'}{\partial y}$. Substituting this into the flow equations and taking the mean over $x$ gives a set of equations for the rolls induced by the instability,

$$
\begin{aligned}
\nabla^4 \Psi' =& Re\left(u^*\frac{\partial^2 v}{\partial x \partial z} - u^*\frac{\partial^2 w}{\partial x \partial y} + v^*\frac{\partial^2 v}{\partial y \partial z} - v^*\frac{\partial^2 w}{\partial y^2} + w^*\frac{\partial^2 v}{\partial z^2} - w^*\frac{\partial^2 w}{\partial y \partial z}\right) \\
&- (1-\beta)\left(\frac{\partial^2}{\partial y \partial z}T'_{yy} - \frac{\partial^2}{\partial y \partial z}T'_{zz} + \frac{\partial^2}{\partial z^2}T'_{yz} - \frac{\partial^2}{\partial y^2}T'_{yz}\right) + c.c \\
\Psi'(\pm 1) =& \frac{\partial \Psi'}{\partial y}(\pm 1) = 0
\end{aligned}
$$

$$
\begin{aligned}
T'_{yz} =& - Wi(u^*\frac{\partial}{\partial x} + v^*\frac{\partial}{\partial y} + w^*\frac{\partial}{\partial z})\tau_{yz} \\
&+ Wi\left[\frac{\partial v^*}{\partial x}\tau_{xy} - \frac{\partial u^*}{\partial x}\tau_{yz} + \frac{\partial v^*}{\partial z}\tau_{zz} + \frac{\partial w^*}{\partial x}\tau_{xy} + \frac{\partial w^*}{\partial y}\tau_{yy}\right] + c.c \\
T'_{yy} =& - Wi(u^*\frac{\partial}{\partial x} + v^*\frac{\partial}{\partial y} + w^*\frac{\partial}{\partial z})\tau_{yy} \\
&+ 2\,Wi\left[\frac{\partial v^*}{\partial x}\tau_{xy} + \frac{\partial v^*}{\partial y}\tau_{yy} + \frac{\partial v^*}{\partial z}\tau_{yz}\right] + c.c \\
T'_{zz} =& - Wi(u^*\frac{\partial}{\partial x} + v^*\frac{\partial}{\partial y} + w^*\frac{\partial}{\partial z})\tau_{zz} \\
&+ 2\,Wi\left[\frac{\partial w^*}{\partial x}\tau_{xz} + \frac{\partial w^*}{\partial y}\tau_{yz} + \frac{\partial w^*}{\partial z}\tau_{zz}\right] + c.c\,,
\end{aligned}
\tag{6.22}
$$

where $u, v, w$ and $\tau_{ij}$ are the velocities and stresses from the eigenvector of the instability and $c.c$ is the complex conjugate. Using the Fourier-Chebyshev decomposition described earlier and the methods described in the appendix, we discretise these equations and calculate $\Psi'$ and the stresses.

From $\Psi'$ and the boundary conditions, we calculate the wall-normal velocity, $V'$, due to the eigenvector. The linear analysis does not provide us with a scale for the velocity, therefore we can only compare the shape of the feedback mean-flow velocity with the

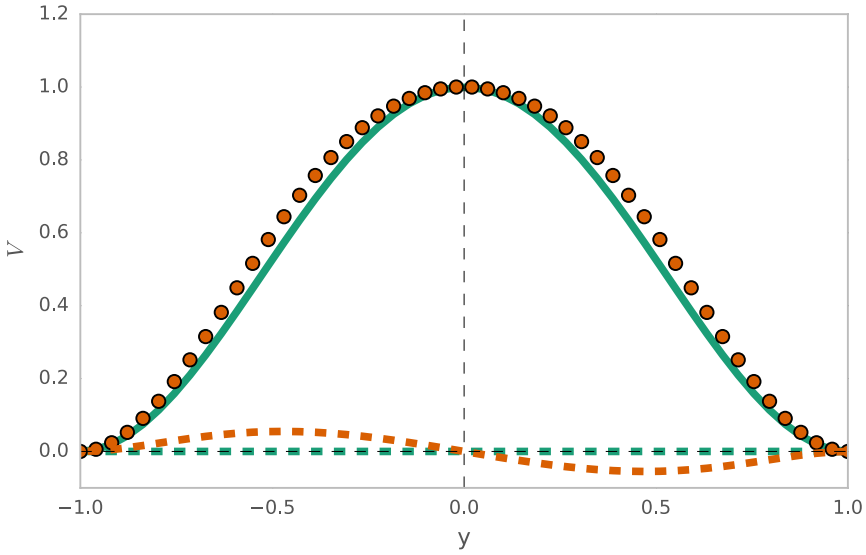


Figure 6.13: Comparison of the vortical flow and the mean flow induced by the nonlinear terms of the instability. The original amplitude of the rolls in the wall normal direction is shown in Turquoise. The solid line gives the amplitude of the $\cos(\gamma z)$ component of $V'$, and the dashed line gives the amplitude of the $\sin(\gamma z)$ component. The rolls obtained via nonlinear feedback from the viscoelastic instability at $Wi = 10.0$, $Re = 0.01$, $\beta = 0.1$, $A = 0.02$ and $k_x = 0.01$ is shown in orange. The dots are for the $\cos(\gamma z)$ component, and the dashed line is for $\sin(\gamma z)$ component. To aid comparison, the amplitude of the viscoelastic instability has been adjusted by a scaling factor according to a least squares fit with the amplitude of the original rolls using (6.22).

velocity we used to force the equations. To compare the two, we perform a least squares fit on the scale of the eigenvector using (6.22) to recalculate the feedback flow at each iteration of the least squares algorithm. Using this scaling of the eigenvector Fig. 6.13 shows that the sign and symmetry of the induced velocity matches the forcing velocity, suggesting that there is feedback to complete the self-sustaining process.

## 6.6 Cauchy boundary conditions

To investigate the effect of free slip boundary conditions, we re-examine the linear stability analysis with Cauchy boundary conditions,

$$\begin{aligned} \alpha \left.\frac{\partial u}{\partial y}\right|_{y=\pm 1} + (1-\alpha)u(y=\pm 1) &= 0 \\ v(y=\pm 1) &= 0 \\ \alpha \left.\frac{\partial w}{\partial y}\right|_{y=\pm 1} + (1-\alpha)w(y=\pm 1) &= 0 \end{aligned} \tag{6.23}$$

Where $\alpha$ is a control parameter for homotopy from free slip to no-slip boundary conditions. The linear stability analysis remains exactly as in section 6.4, apart from the changes to the constraint equations for the velocities.

We find that on decreasing $\alpha$ the dispersion relation grows in strength and broadens (Fig. 6.14), and that this problem is converged at low resolution (Fig. 6.15). We plot the full eigenvalue spectrum to examine the dependence of the instability on $\alpha$ at one wavenumber, $k_x = 0.01$. A complex conjugate pair of eigenvalues split, one with decreasing real and imaginary parts and the other with increasing real part (Fig. 6.16a). It appears that the real part of the larger of these eigenvalues tends to infinity as $\alpha \to 0$, whilst the smaller eigenvalue quickly crosses the imaginary axis (Fig. 6.16b). As $\alpha$ decreases the quality of the convergence of the eigenvalues and eigenvectors decreases, however, different resolutions show the same trend with $\alpha$.

When we completely remove slip at the walls the instability appears infinitely amplified (Fig. 6.16b). A possible explanation for this is that the instability moves into a region very close to the boundaries as we introduce free slip and can no longer be resolved. Fig. 6.17 seems to show that the first normal stress difference of the instability becomes more asymmetric as $\alpha$ tends to zero.

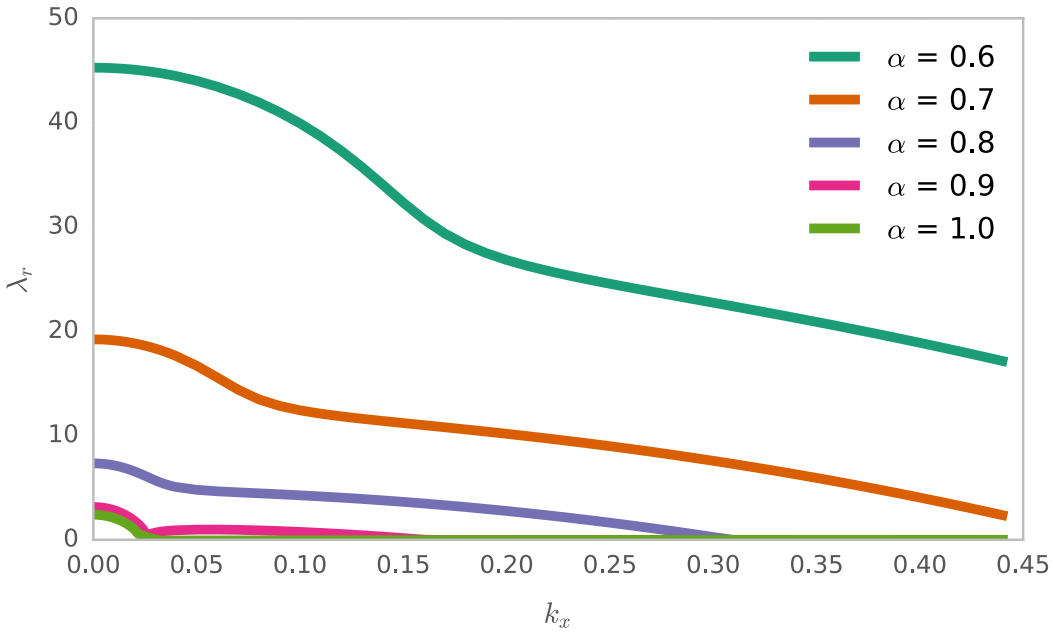


Figure 6.14: Dispersion relations as $\alpha$ the slip parameter, is reduced. As the system becomes closer to no-slip at the walls the instability grows for $Re = 0.001, \beta = 0.1$, $Wi = 10.0$.

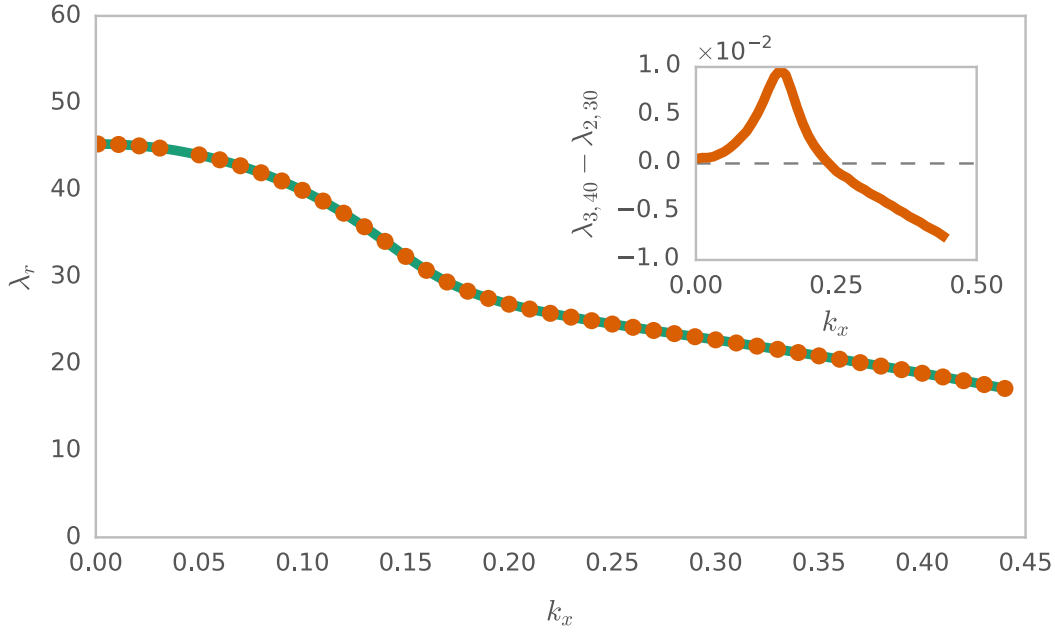


Figure 6.15: Convergence of the dispersion relations at $\alpha = 0.6$. The green line shows the $N = 2, M = 30$ resolution and the orange markers show the $N = 3, M = 40$ resolution for $Re = 0.001, \beta = 0.1, Wi = 10.0$. The inset plot shows the difference between the two dispersion relations.

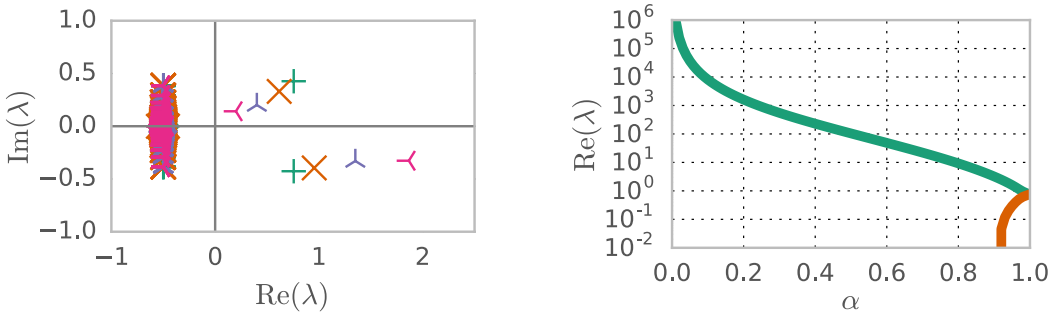


Figure 6.16: a) Example spectra as the slip parameter is varied. Green crosses represent the eigenvalues in the no-slip case, with successive symbols representing $\alpha = 0.98, 0.96, 0.94$ as the complex conjugate pair split. b) Growth rate of an eigenvalue at $k_x = 0.01$ as $\alpha$ the slip parameter, is reduced for $N = 2$, $M = 30$. The growth rate (turquoise) tends to infinity faster than exponentially as we approach the no slip condition for the largest eigenvalue. The second largest (orange, equal at $\alpha = 1.0$) is exponentially damped. The results are the same at increased resolution.

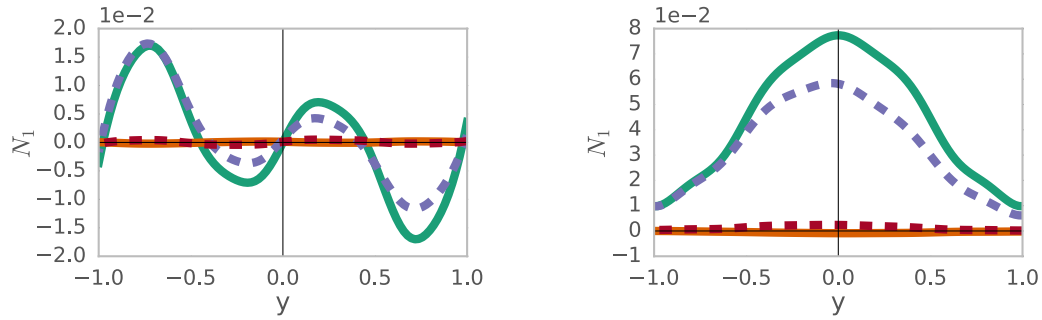


(a) (b)

Figure 6.17: a) 1st and b) 2nd $z$ Fourier modes of the first normal stress difference of the viscoelastic instability at $Wi = 10.0$, $Re = 0.01$, $\beta = 0.1$, $A = 0.02$ and $k_x = 0.01$. Turquoise/purple is the real part, orange/red is the imaginary part. Solid lines are for $\alpha = 1.0$, and dashed lines are for $\alpha = 0.8$. Results are rescaled so that $v_1(0.5)$ has no imaginary part and such that $\mathrm{Re}(v_1(0)) = \mathrm{Re}(v_1'(0))$ so that the eigenvectors have the same scale.

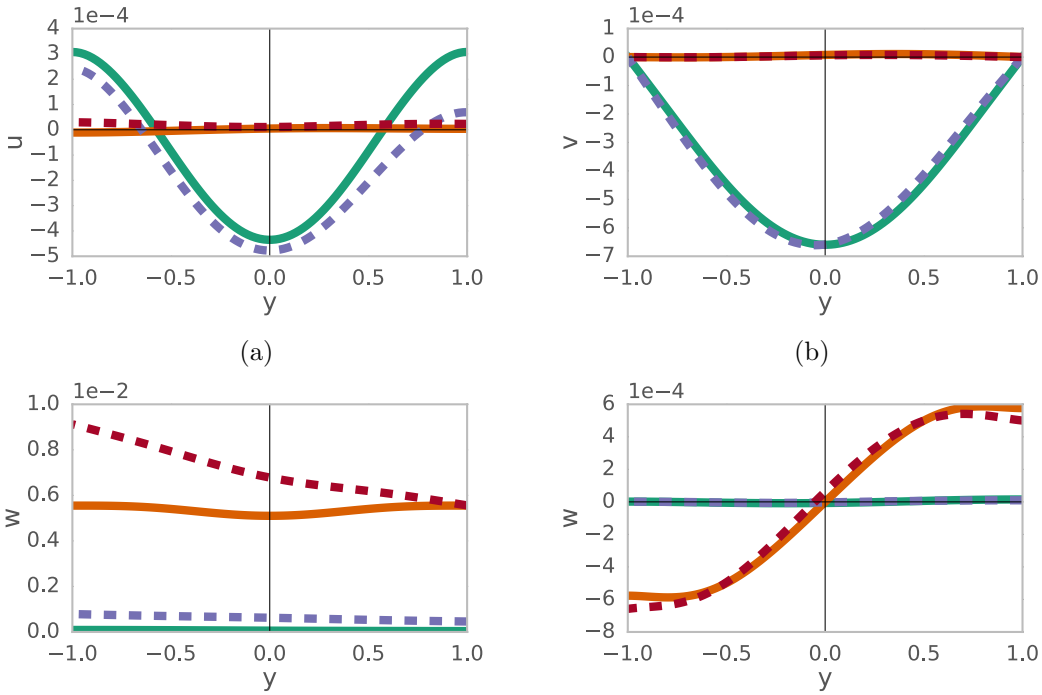


(a) (b)

(c) (d)

Figure 6.18: $z$ Fourier modes of the velocity components of the viscoelastic instability at $Wi = 10.0$, $Re = 0.01$, $\beta = 0.1$, $A = 0.02$ and $k_x = 0.01$. a) and b) give the 1st $z$ Fourier modes of $u$ and $v$, whilst c) and d) give the zeroth and 1st modes of $w$. Solid lines are for $\alpha = 1.0$, and dashed lines are for $\alpha = 0.8$.

## 6.7 Discussion

We have constructed a self-sustaining process following the same approach as used by Waleffe [95], but in the purely elastic regime. We have seen how the most non-normally amplified structures in purely elastic plane Couette flow sustain themselves via a linear instability. For high $Re$ we find an SSP consistent with Waleffe [95] and Stone et al. [103], however, we find a new flow with a new instability at much lower Reynolds numbers, once we enter the purely elastic regime.

We considered two of the most non-normally amplified structures in purely elastic plane Couette flow, a constant forcing to $\tau_{yy}$ and a streamwise roll forcing to the $y, z$ plane velocities $V$ and $W$ [98]. We then saw that streamwise rolls generate a flow which may be self-sustaining. The first step was to calculate the $x$ independent flow due to the forcing.

We first considered the case of a constant forcing to $\tau_{yy}$, but we found that the resulting flow contained no significant gradients in the velocities or stresses that would lead to a purely elastic instability of the type uncovered in Chapter 3. However, forcing streamwise rolls leads to significant gradients in the first normal stress difference between the rolls (Fig. 6.6d).

The flow due to the $\tau_{yy}$ forcing does not have an instability which feeds back to reinforce the original forcing. However, for free slip boundary conditions, there is an instability of the flow induced by streamwise rolls. For Waleffe, the forced flow is unstable to a Kelvin-Helmholtz like instability of the interface between the streaks and the rest of the fluid (see section 1.3.2). In the purely elastic case the instability we see resembles the shear layer instability of Chapter 3: the range of wave numbers (between about $k_x = 0$ and $k_x = 0.04$) matches up with the shear layer instability, as well as the onset Weissenberg number of $Wi = 2$ for $Re = 0.01$ in the bulk units (compare Figs 6.8 and 3.4c).

In the final step of the Newtonian SSP, the instability interacts with itself to reproduce the streamwise rolls. We found that our instability also interacts with itself to force the flow in the same way as the original forcing. The magnitude of the nonlinear forcing is unknown from our analysis, since it derives from the unknown magnitude of a linear instability. However, this is a test that the forcing has the correct sign and symmetry to produce rolls. The fact that the fit is so good in Fig. 6.13 is no coincidence, and is largely due to an important property of the bi-Laplacian, $\nabla^4$.

We were almost guaranteed to end up reproducing the shape, if not the sign of the rolls in Fig. 6.13. We can begin to see why by considering a general form of the nonlinear feedback problem. We were looking for our nonlinear feedback, $f$, to be such that $\Psi$ was the streamfunction of the original forcing given that $\nabla^4\Psi = F$. Assuming that the

forcing and streamfunction are cosinusoidal, $\Psi = \phi(y)\cos(\gamma z)$ and $F = f(y)\cos(\gamma z)$, we obtain,

$$\frac{\partial^4\phi}{\partial y^4} - 2\gamma^2\frac{\partial^2\phi}{\partial y^2} + \gamma^4\phi = \hat{B}\phi = f \tag{6.24}$$

$$\phi(\pm 1) = \left.\frac{\partial\phi}{\partial y}\right|_{\pm 1} = 0\,, \tag{6.25}$$

where $\hat{B}$ is a self-adjoint linear operator so that for some inner product, $\langle g(y), h(y)\rangle = \int_{-1}^{1} g(y)h(y)\,\mathrm{d}y$, we have that $\langle g, \hat{B}h\rangle = \langle \hat{B}g, h\rangle$. This implies that each eigenvalue is different and that their eigenfunctions form a complete orthogonal basis set. We label the $n^{th}$ eigenvalue $\lambda_n$ and eigenvector $\xi_n$ such that $\hat{B}\xi_n = \lambda_n\xi_n$ and the eigenvalues are in order of increasing magnitude. Returning to the nonlinear feedback problem, we express $\phi$ and $f$ in terms of the basis set, $\{\xi_n\}$,

$$\phi = \sum_n^\infty \phi_n\xi_n(y) \tag{6.26}$$

$$f = \sum_n^\infty f_n\xi_n(y)\,. \tag{6.27}$$

This allows us to take the inner product of the original problem with $\xi_m$ in the new basis to obtain,

$$\sum_n^\infty \langle \hat{B}\phi_n\xi_n, \xi_m\rangle = \sum_n^\infty \langle \phi_n\xi_n, \lambda_m\xi_m\rangle = \sum_n^\infty \langle f_n\xi_n, \xi_m\rangle\,, \tag{6.28}$$

where we have used the self-adjoint property of $\hat{B}$, and the fact that $\xi_n$ is an eigenvector. Given that $\xi_n$ are orthogonal, the above sum reduces to

$$\phi_m\lambda_m\langle\xi_m, \xi_m\rangle = f_n\langle\xi_m, \xi_m\rangle$$

$$\phi_m = \frac{f_m}{\lambda_m}\,. \tag{6.29}$$

The $f_m$ are either all of the same scale, or decreasing with increasing $m$, since we expect our fields to be smooth. By construction, as $m$ increases $\lambda_m$ increases. Therefore $\phi_m$ rapidly decreases for large $m$. Further, if the spectrum of the operator has a large gap between the first and second eigenvalue, then $\phi_1$ and so $\xi_1(y)$ will dominate the solution.

The spectrum of the bi-Laplacian ($\hat{B}$) has exactly this property. Fig. 6.19a shows the spectrum for the first ten eigenvalues, calculated using our collocation method. Our forcing is symmetric, and so we only consider the symmetric, odd numbered eigenmodes.

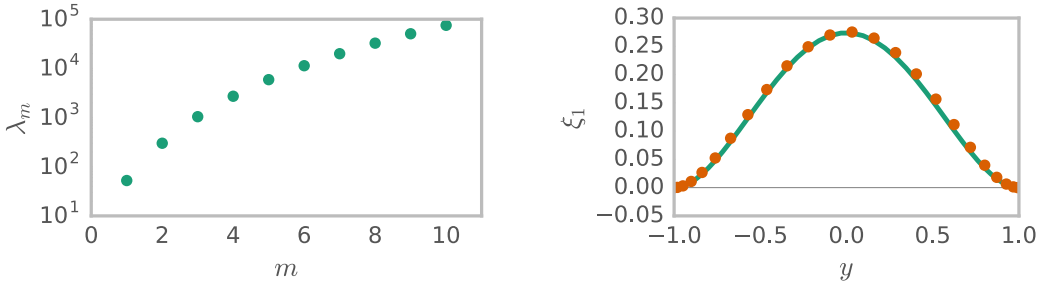


(a) (b)

Figure 6.19: a) The first ten eigenvalues of the bi-Laplacian with plane Couette boundary conditions, in ascending order, using the psuedospectral method with 50 points. b) The eigenvector, $\xi_1$, in green, compared with the solution to $\hat{B}\phi = f$ for a randomly chosen forcing $f$.

The difference between $\lambda_1$ and $\lambda_3$ is approximately an order of magnitude, making the coefficient of $\xi_3$ around 10 times smaller than that of $\xi_1$. This large gap in the spectrum of the bi-Laplacian means that for nearly any forcing, $f$, the solution will be dominated by $\xi_1$. Fig. 6.19b shows an example using a randomly chosen forcing $f$, solving for $\phi$, and comparing the solution with $\xi_1$. Clearly, the roll forcing used in our problem has a functional form similar to $\xi_1$ (compare Figs 6.13 and 6.19b). Therefore the above discussion implies that any forcing $f$ with the right sign and a projection onto $\xi_1$ will likely reproduce the rolls.

Although our analysis is mostly restricted to free slip boundary conditions, we find that the shear and the stress in the eigenmodes of this instability are localised far from the walls of the channel (Figs 6.11 and 6.10). We believe that this means that the free slip approximation is not responsible for the instability, and that the move to no slip boundary conditions ought to support a similar instability. Our efforts to find a connection between the eigenvalue of our instability and of a no slip instability have so far failed. It appears that the two unstable eigenvalues with degenerate real parts split, the larger one exponentially approaches infinity and the smaller one becomes so mixed up with spurious eigenvalues that it is impossible to track (Fig. 6.16b).

There are many possible reasons for the difficulty in finding a no-slip instability. It maybe that our numerical techniques are not of high enough resolution, and the lower of the two eigenvalues above is in fact unstable at zero slip. It is also possible that a different eigenvalue is responsible for the no-slip instability but with a similar mechanism. Indeed, we expect the no-slip eigenvector to look very different, with large gradients in velocity and stress near the walls. It is also possible that only the $x$-independent, $k_x = 0$ instability is present for no-slip boundary conditions. Although

we did not check this, if it is true it cannot be part of an SSP, since there is no way for an $x$ independent flow to generate an exact coherent structure (recall the discussion in section 6.3).

Compared to the free slip instability, the no slip instability will have large gradients in the velocities and stresses at the walls as well as those in the bulk. However, as we have seen, the shape of the rolls is largely independent of the shape of the eigenvector, and so we don't expect any change to the nonlinear feedback.

We find that the purely elastic instability, just as the Newtonian instability, forces the mean flow into streamwise rolls (Fig. 6.13) via nonlinear feedback. This implies that, provided $Re$ and $Wi$ are tuned properly, it ought to be possible to form a flow which is self-sustaining — the rolls produce streaks which are unstable and reproduce the rolls. In an ECS derived from this SSP these three processes happen simultaneously, producing a steady state solution.

The simulations of Sureshkumar et al. [101] and Stone et al. [104] consider the Newtonian SSP, where $Re >> 1$. A sensible next step might be to perform similar simulations at low $Re$, with our purely elastic SSP. However, they introduce an unphysical large stress diffusion term to aid numerical stability, which may remove sharp gradients in the stress. To rule out this possibility, we performed the analysis without any stress diffusion. It seems that this stress diffusion did not have a large impact on the high $Re$ flow, but it is not clear what impact it would have on a purely elastic exact coherent structure.

# Chapter 7

# Conclusions

Viscoelastic fluids, such as plastic, blood or the cell cytoplasm, can become turbulent provided the elastic forces in the flow are sufficiently strong. In the absence of an understanding of this purely elastic turbulence, we have pursued a research programme based on the study of Newtonian turbulence. This approach views the turbulent attractor as constructed from a skeleton of fixed point and periodic orbit solutions to the equations of motion, known as exact coherent structures (ECS). Our goal has been to find an ECS for purely elastic turbulence.

We began by attempting the easiest route to an ECS: a simple homotopy from a known Newtonian ECS. In Chapter 2 we explored travelling wave solutions of viscoelastic plane Poiseuille flow and sought a connection between Newtonian, high $Re$, exact coherent structures and the purely elastic regime. However, we could not find any such connection. Instead, we found that the behaviour of the weakly elastic exact coherent state matches the linear stability analysis of viscoelastic plane Poiseuille flow. As $Wi$ increases the critical Reynolds number follows a parabola, it decreases for $Wi < 1$ and then increases again for $Wi > 1$. Additionally, we investigated 3 dimensional disturbances to the weakly elastic ECS, and found the same form of instability as in the Newtonian case. Given these two findings, we concluded that the ECS is not related to the high $Wi$ low $Re$ purely elastic instabilities seen in experiments. However, it is still possible that these results are connected to elasto-inertial turbulence at moderate Reynolds number, and future studies may be able to use a similar analysis for elasto-inertial turbulence.

This work on plane Poiseuille flow exact coherent structures did not help with our hunt for an ECS. Our second strategy was to construct an ECS from scratch, using a method from the Newtonian turbulence literature. This method starts by identifying a self-sustaining process (SSP) in the flow — a sequence of flows that reinforce one another and lead to a non-laminar exact solution. In the purely elastic case, we immediately

ran into a problem. A key component of the Newtonian SSP is a shear layer instability, but it is believed that the purely elastic shear layer is stable. Our task in Chapter 3 was to show that in fact, the purely elastic shear layer is unstable.

We found that at high $Wi$, low $\beta$ and low $Re$ there is a previously unknown purely elastic version of the shear layer instability. We found that this new instability is robust on changing the width of the shear layer with respect to a confining channel and we found that the fluid model, either Oldroyd-B or FENE-P, did not affect the existence of the instability. We simulated this instability in a channel (Chapter 4) and found both steady and travelling wave states. However, the state quickly became too complex to resolve as the Weissenberg number increased. Nonetheless we did verify that nonlinear terms do not saturate out this instability, and that it leads to an appreciable affect on the flow.

We were unable to identify a mechanism behind the shear layer instability. Similar to instabilities in flows of co-extruded viscoelastic fluids, we believe that the large jump in normal stress difference across the shear layer is responsible for driving the flow unstable. However, we found that we cannot follow their analysis with our flow. It is evident from the eigenvector that simple varicose or sinuous disturbances are not adequate to describe the shape of the unstable shear layer. Future research will hopefully provide an analytical description and the mechanism, however, the discovery of the instability is far more interesting than identifying the mechanism, since its importance is as a means to drive instability in other, more complex flows.

The purely elastic shear layer instability lead us to investigate another previously unexplained experimental result. The oscillatory pipe flow of worm-like micelles consists of a layered laminar flow, with bands of fluid at different velocity. This flow shows an instability to axisymmetric vortices when the driving amplitude is large. In Chapter 5 we applied our code for the simulation of a 2D Oldroyd-B flow to a channel with an oscillating pressure gradient. Our aim was to link the instability of Chapter 3 to this experimental flow. We found a purely elastic linear instability for parameters consistent with the experiment, and with Chapter 3. Given the presence of the layered laminar flow, and the use of only the Oldroyd-B model, we are led to conclude that the experimental instability is a consequence of the elasticity of worm-like micellar flows and the purely elastic shear layer instability.

Finally, we returned to the main aim of the research programme, the discovery of purely elastic exact coherent structures using a self-sustaining process. The SSP will provide an accurate guess for a 3D solution forced by streamwise vortices, and lead to a purely elastic exact coherent state. We found that streamwise vortices produce streaks in the stress in purely elastic plane Couette flow. These streaks are unstable via the same purely elastic instability as the shear layer. The interaction of the linear

instability with itself forces the equations of motion resulting in the vortical flow. This completes the SSP, providing both the mechanism to sustain an ECS, as well as an accurate guess for the functional form of that state even at low $Re$ so long as $Wi$ is large.

The research programme we outlined in section 1.4 still contains much work to be done. The eigenfunctions for the SSP with no-slip boundary conditions look relatively simple. This suggests that the SSP could be reproduced using a simpler, low order model. Work has already begun on this problem, unfortunately not enough progress has been made to include results in this thesis. Eventually future work would involve a full 3D exact solver for purely elastic plane Couette flow with a forcing of streamwise rolls. Beginning from the SSP, this code could be used to find an exact solution. Hopefully, this state could be connected through a homotopy to a purely elastic ECS. This code would need to be very accurate and most probably parallel, a serious undertaking for future researchers.

This thesis opens the door to using exact coherent structures to address purely elastic turbulence. We have provided two mechanisms that are important to purely elastic turbulence: the shear layer instability and the purely elastic self-sustaining process. Perhaps one of these will form part of an accurate prediction of the onset of purely elastic turbulence, to improve the production of polymers and the understanding of biological flows.

# Appendix A

# Numerical methods

This appendix contains a brief description of the numerical methods used, with references to more detailed information and derivations. We will first briefly outline spectral methods as used in fluid dynamics. Then we will discuss performing linear stability analysis by solving an eigenvalue problem. Finally we will summarise the Newton-Raphson technique for finding numerical solutions of the Navier-Stokes equations.

## A.1 Spectral Methods

Spectral methods are a family of methods for numerical approximation of continuous functions, often used to solve differential equations. Each function and variable is expressed in terms of a series expansion in a set of basis functions. Provided the series expansion converges, a truncation at a finite number of basis functions can produce an accurate approximation to the original function,

$$f_{exact}(x) \simeq f(x) = \sum_{n=0}^{N} \check{f}_n \phi_n(x) \tag{A.1}$$

where $\phi_n(x)$ are the basis functions, $\check{f}_n$ are the coefficients of these basis functions and the series is truncated at the $N^{\text{th}}$ basis function.

This allows us to write an approximation to the function as a list of numbers, one for each basis function coefficient $\check{f}_n$. We refer to this list of numbers as the spectral space representation of $f$. By comparison, the physical space representation, as used in finite difference methods, represents a function $f$ by using its values at a finite number of points on a grid, $f_j(x_j)$. Provided the function is smooth, the spectral space representation is much more accurate for a given truncation level than the physical space

representation. Derivatives are more accurate, and the convergence of the numerical approximation to the exact function is exponential ($\check{f}_n \sim \mathcal{O}\left(\mathrm{e}^{-n}\right)$) [170].

The choice of basis functions depends on the problem. For the problems in this thesis, only two sets of basis functions have been used: Fourier polynomials for periodic coodinates and Chebyshev polynomials otherwise. The Fourier series expansion is given by,

$$f(x) = \sum_{n=-N}^{n=N} \check{f}_n \mathrm{e}^{ink_x x} \tag{A.2}$$

The Chebyshev polynomials of the first kind are given by,

$$T_m(x) = \cos\left(m \arccos\left(x\right)\right) \tag{A.3}$$

where $x \in [-1, 1]$. And the Chebyshev series expansion is,

$$f(x) = \sum_{m=0}^{M} \check{f}_m T_m(x) \tag{A.4}$$

where the series is truncated after $M + 1$ Chebyshev polynomials.

### Derivatives

For spectral methods using the Fourier representation, differention is easy. Using the expression for the derivative of a Fourier mode, $\frac{\partial}{\partial x}\mathrm{e}^{ink_x x} = ink_x \mathrm{e}^{ink_x x}$, the derivative for each coefficient is simply,

$$\check{f}'_n = ink_x \check{f}_n \tag{A.5}$$

For the Chebyshev representation, we can use the following expression for the derivative of a Chebyshev polynomial,

$$2T_m(x) = \frac{1}{m+1} T'_{m+1}(x) - \frac{1}{m-1} T'_{m-1}(x), \qquad m \geq 1 \tag{A.6}$$

Combined with (A.3) this provides a recurrance relation for the derivative of a Chebyshev coefficient,

$$\begin{aligned} &\check{f}'_0 = 0 \\ &2k\check{f}'_m = c_{m-1}\check{f}'_{m-1} - \check{f}'_{m+1}, \qquad m \geq 1 \end{aligned} \tag{A.7}$$

where

$$c_i = \begin{cases} 2, \ i = 0 \\ 1, otherwise \end{cases} \tag{A.8}$$

Both of these expressions can be expressed as matrices. The matrix form allows us to easily write algorithms for finding exact solutions and solving eigenvalue problems.

### Products

Products of functions in spectral methods can be computed in two ways. One way, used in pseudospectral methods, involves transforming the functions to physical space, performing the multiplication, and then transforming them back again. For fully spectral methods the multiplication is performed directly in spectral space. The time iteration codes used in Chapters 4 and 5 are pseudospectral. They use a Fast Fourier Transform (a version of the FFT for Chebyshev methods is given in the appendix of Canuto et al. [170]) to perform a transformation to real space. The values of the functions on the grid points are then multiplied together $f_i = g_i h_i$, and another transformation returns the function to spectral space.

The programs in Chapters 2 and 6 use a fully spectral method for multiplying spectral representations of functions. In these programs, the spectral coefficients are combined to calculate the product such that there is no need to transform to real space. This scheme tends to be more computationally demanding, but has the advantage of greater accuracy. A code is only fully spectral when all calculations are performed in spectral space (sums, products and derivatives).

For a function represented by Fourier coefficients, we can write down the product by considering all the contributions to a given Fourier coefficient,

$$\check{f}_n = \sum_{k=-N}^{N} \sum_{l=-N}^{N} \check{g}_k \check{h}_l \delta_{|k-l|,n} \tag{A.9}$$

where the sum is over all $k$ and $l$ and $\delta_{i,j}$ is the Kronecker delta function. This sum can also be expressed in matrix form, where the elements of $\check{g}_k$ are placed in a matrix $P(\check{g})$ such that $\check{f}_n = P_{n,l}(\check{g})\check{h}_l$. This proves useful when solving eigenvalue problems, as discussed in section A.2.1.

There is an analogous formula for a function represented by Chebyshev coefficients. To derive it, we first note a relationship between Chebyshev polynomials and their

products,

$$2T_k(x)T_l(x) = T_{k+l}(x) + T_{|k-l|}(x) \tag{A.10}$$

This relationship is a consequence of the trigonometric identities. Starting from this relation, one can derive an equation for the Chebyshev product [46]. The resulting expression is,

$$\check{f}_m = \frac{1}{8c_m} \sum_{k=-M}^{M} c_{|m-k|} g_{|m-k|} c_{|k|} h_{|k|} \tag{A.11}$$

Where $g_i, h_i = 0$ if $i > M$. Again, this equation can be written in terms of a matrix just as the Fourier product above.

Finally, it is important to note that the Fourier and Chebyshev representations can be combined, such that different coordinates can be represented using different systems. For example, the program of Chapter 2 uses a Fourier representation for the $x$ direction and a Chebyshev representation for the $y$ direction.

### A.1.1 Collocation methods

Unlike finite-difference methods where a few nearby grid points are used to perform derivatives, collocation methods use an interpolation across the entire domain. Unlike spectral methods, the function is satisfied at collocation points in the domain rather than for coefficients of the basis functions. This means that the calculation can take place entirely in the physical space without transforming to spectral space. The discussion in this section is based on [170–172].

We make use of a Chebyshev collocation method and use the Gauss-Lobatto collocation points given by,

$$x_j = \cos\left(\frac{\pi j}{M}\right) \tag{A.12}$$

where $x$ is the position in the domain and $j \in [0, M]$ denotes the grid point. One of the advantages of this set of points is that $x$ lies in the bounded domain between $-1$ and 1. This allows us to use Chebyshev points for the direction normal to the boundary in the flow. We approximate the function on the grid points as $f_j(x_j)$.

An expression for the derivative of a function defined on these points contains

contributions from all the points. This leads to a differentiation matrix

$$
\begin{aligned}
D_{00} &= \frac{2M^2+1}{6}, \qquad & D_{MM} &= -\frac{2M^2+1}{6} \\
D_{jj} &= \frac{-x_j}{2(1-x_j^2)}, \qquad & j &= 1,\ldots,M-1 \\
D_{ij} &= \frac{\overline{c}_i}{\overline{c}_j}\frac{(-1)^{i+j}}{x_i - x_j}, \qquad & i \neq j, \qquad & i,j = 0,\ldots,M
\end{aligned}
\tag{A.13}
$$

where,

$$
\overline{c}_i = \begin{cases} 2, \ i = 0, M \\ 1, otherwise \end{cases}
\tag{A.14}
$$

[171]. To calculate the derivative of a function defined on the Gauss-Lobatto grid we multiply the function by the differentiation matrix, $f_i' = \sum_{j=0}^{M} D_{ij} f_j$.

Products of collocation functions are easier to calculate than their spectral method counterparts since the values of the functions are defined on a grid in physical space. They can be calculated by multiplying together the values at each point, just as with finite difference methods, $f_i = g_i h_i$.

## A.2 Numerical Linear Algebra

There are two kinds of problem we deal with in this thesis, eigenvalue problems and boundary value problems. Eigenvalue value problems are linear, and so I will describe how we solve these first. Exact solutions to boundary value problems are harder to obtain because the problem is nonlinear. I will describe the simplest possible strategy we use to deal with these problems, known as the Newton-Raphson method.

### A.2.1 Eigenvalue problems

In general, linear stability analysis consists of solving a generalised eigenvalue problem — a system of equations for all solutions $\lambda$ where,

$$
\mathcal{L}(\mathbf{x}) = \lambda \mathcal{B}(\mathbf{x})
\tag{A.15}
$$

Here $\mathcal{L}(\mathbf{x})$ and $\mathcal{B}(\mathbf{x})$ are linear operators acting on some vector $\mathbf{x}$, a vector containing the state of the system. For a computational fluid mechanics problem the linear operator contains the equations of motion and the boundary conditions. To solve this problem numerically we rewrite the linear operator as matrix in either a spectral or collocation

representation. The problem is now one of finding the eigenvalues, $\lambda_i$ and eigenvectors $\mathbf{x}$ (which contain all the spectral coefficients for the variables $\{\check{\mathbf{u}}, \check{\mathbf{v}}, \check{p}, \check{\tau}_{ij}\}$ ) of the matrix. For all of the programs used in this thesis we use the eigenvalue solver from the scipy numerical linear algebra package for python [173], which in turn calls the LAPACK fortran library [174]. Both exact and iterative methods have been used for problems in this thesis. Iterative methods for calculating eigenvalues use the GMRES algorithm. A detailed description of the GMRES algorithm can be found in [175].

### A.2.2 Newton Raphson method

Finding the exact solution to a system of nonlinear partial differential equations is difficult. In general, an accurate guess of the solution is required in order to calculate the exact solution. The simplest method for refining a solution to the exact solution is the Newton Raphson method. This is the method we have used for the calculation of exact solutions in Chapter 6. We have used a slightly more sophisticated technique to calculate exact solutions in Chapter 2, known as a line search algorithm, which we discuss below.

Exactly solving a system of equations can be expressed in general as looking for the solution, $\mathbf{x}^*$ to

$$\mathbf{f}(\mathbf{x}^*) = 0 \tag{A.16}$$

where $\mathbf{f}$ is a nonlinear function of $\mathbf{x}$. Numerically, $\mathbf{x}^*$ is a vector containing the values of the spectral coefficients of all the variables. For example, in a 2D viscoelastic fluid mechanics problem $\mathbf{x}^* = \{\check{\mathbf{u}}, \check{\mathbf{v}}, \check{p}, \check{\tau}_{ij}\}$. For the Newton Raphson method, we must start with an accurate guess of the solution $\mathbf{x}$. Taylor expanding the problem and keeping only the linear terms we find that,

$$\mathbf{f}(\mathbf{x}) = -\mathrm{J}(\mathbf{x})\mathrm{d}\mathbf{x} \tag{A.17}$$

where $\mathrm{d}\mathbf{x}$ is the small step required to update $\mathbf{x}$ to $\mathbf{x}^*$. J is the Jacobian matrix, $\mathrm{J} = \frac{\partial \mathrm{f}}{\partial \mathrm{x}}$.

This calculation keeps only the terms to first order in $\mathrm{d}\mathbf{x}$. To calculate an accurate solution it is important to perform the process iteratively. First $\mathrm{d}\mathbf{x}$ is calculated for the initial guess. This generates a new guess for the solution, which is hopefully closer to the exact solution $\mathbf{x}_{new} = \mathbf{x}_{old} + \mathrm{d}\mathbf{x}$. For each iteration we must recalculate the function $\mathbf{f}(\mathbf{x})$, known as the residual. When the norm of the residual is below a threshold value ($\|\mathbf{f}\|_2 < \epsilon$, where in our code $\epsilon = 10^{-6}$) the algorithm halts and $\mathbf{x} = \mathbf{x}^*$ within numerical error. The nonlinear terms in the equations are such that the Jacobian must be recalculated at every Newton step. These terms require $\sim N^2M^2$ computations,

where $N$ and $M$ are the number of Fourier and Chebyshev coefficients, making this the most computationally demanding stage of the calculation.

### Line search algorithm

The line search algorithm is a variant on the standard Newton method but with more favourable convergence properties when the approximate solution is further from the true solution [176]. The length of the Newton step, $\mathrm{d}\mathbf{x} = -J(\mathbf{x}_{old})^{-1}\mathbf{f}(\mathbf{x}_{old})$ is adjusted $\mathbf{x}_{new} = \mathbf{x}_{old} + l\mathrm{d}\mathbf{x}$ so that the residual always decreases. The value of $l$ is calculated using a (up to) third order polynomial fit of the residual. This prevents overshoot of the solution, whilst still retaining the exponential convergence of the Newton method at short distances.

# Appendix B

# Oldroyd-B linear stability equations

$$
\begin{aligned}
Re\lambda u = -Re\left[ikWu + V\frac{\partial u}{\partial y} + U\frac{\partial u}{\partial x} + v\frac{\partial U}{\partial y} + u\frac{\partial U}{\partial x}\right] \\
-\frac{\partial p}{\partial x} + \beta\left[\frac{\partial^2}{\partial x^2} + \frac{\partial^2}{\partial y^2} - k^2\right]u \\
+\frac{(1-\beta)}{Wi}\left[ikc_{xz} + \frac{\partial c_{xy}}{\partial y} + \frac{\partial c_{xx}}{\partial x}\right]
\end{aligned} \tag{B.1}
$$

$$
\begin{aligned}
Re\lambda v = -Re\left[ikWv + V\frac{\partial v}{\partial y} + U\frac{\partial v}{\partial x} + v\frac{\partial V}{\partial y} + u\frac{\partial V}{\partial x}\right] \\
-\frac{\partial p}{\partial y} + \beta\left[\frac{\partial^2}{\partial x^2} + \frac{\partial^2}{\partial y^2} - k^2\right]v \\
+\frac{(1-\beta)}{Wi}\left[ikc_{yz} + \frac{\partial c_{yy}}{\partial y} + \frac{\partial c_{xy}}{\partial x}\right]
\end{aligned} \tag{B.2}
$$

$$
\begin{aligned}
Re\lambda w = -Re\left[ikWw + V\frac{\partial w}{\partial y} + U\frac{\partial w}{\partial x} + v\frac{\partial W}{\partial y} + u\frac{\partial W}{\partial x}\right] \\
-ikp + \beta\left[\frac{\partial^2}{\partial x^2} + \frac{\partial^2}{\partial y^2} - k^2\right]w \\
+\frac{(1-\beta)}{Wi}\left[ikc_{zz} + \frac{\partial c_{yz}}{\partial y} + \frac{\partial c_{xz}}{\partial x}\right]
\end{aligned} \tag{B.3}
$$

$$0 = ikw + \frac{\partial v}{\partial y} + \frac{\partial u}{\partial x} \tag{B.4}$$

$$\begin{aligned}\lambda\delta c_{xx} = &- Wi\, c_{xx} - \left[ik\frac{\partial}{\partial x} + V\frac{\partial}{\partial y} + ikW\right] c_{xx} - \left[u\frac{\partial}{\partial x} + v\frac{\partial}{\partial y}\right] C_{xx} \\ &+2ikuC_{xz} + 2C_{xy}\frac{\partial u}{\partial y} + 2C_{xx}\frac{\partial u}{\partial x} + 2c_{xy}\frac{\partial U}{\partial y} + 2c_{xx}\frac{\partial U}{\partial x}\end{aligned} \tag{B.5}$$

$$\begin{aligned}\lambda\delta c_{yy} = &- Wi\, c_{yy} - \left[ik\frac{\partial}{\partial x} + V\frac{\partial}{\partial y} + ikW\right] c_{yy} - \left[u\frac{\partial}{\partial x} + v\frac{\partial}{\partial y}\right] C_{yy} \\ &+2ikvC_{yz} + 2C_{yy}\frac{\partial v}{\partial y} + 2C_{xy}\frac{\partial v}{\partial x} + 2c_{yy}\frac{\partial V}{\partial y} + 2c_{xy}\frac{\partial V}{\partial x}\end{aligned} \tag{B.6}$$

$$\begin{aligned}\lambda\delta c_{zz} = &- Wi\, c_{zz} - \left[ik\frac{\partial}{\partial x} + V\frac{\partial}{\partial y} + ikW\right] c_{zz} - \left[u\frac{\partial}{\partial x} + v\frac{\partial}{\partial y}\right] C_{zz} \\ &+2ikwC_{zz} + 2C_{yz}\frac{\partial w}{\partial y} + 2C_{xz}\frac{\partial w}{\partial x} + 2c_{yz}\frac{\partial W}{\partial y} + 2c_{xz}\frac{\partial W}{\partial x}\end{aligned} \tag{B.7}$$

$$\begin{aligned}\lambda\delta c_{xy} = &- Wi\, c_{xy} - \left[ik\frac{\partial}{\partial x} + V\frac{\partial}{\partial y} + ikW\right] c_{xy} - \left[u\frac{\partial}{\partial x} + v\frac{\partial}{\partial y}\right] C_{xy} \\ &+ikvC_{xz} + C_{xx}\frac{\partial v}{\partial x} + c_{xx}\frac{\partial V}{\partial x} \\ &+ikuC_{yz} + C_{yy}\frac{\partial u}{\partial y} + c_{yy}\frac{\partial U}{\partial y} - ikwC_{xy}\end{aligned} \tag{B.8}$$

$$\begin{aligned}\lambda\delta c_{xz} = &- Wi\, c_{xz} - \left[ik\frac{\partial}{\partial x} + V\frac{\partial}{\partial y} + ikW\right] c_{xz} - \left[u\frac{\partial}{\partial x} + v\frac{\partial}{\partial y}\right] C_{xz} \\ &+C_{xy}\frac{\partial w}{\partial y} + C_{xx}\frac{\partial w}{\partial x} + c_{xy}\frac{\partial W}{\partial y} + c_{xx}\frac{\partial W}{\partial x} \\ &+ikuC_{zz} + C_{yz}\frac{\partial u}{\partial y} + c_{yz}\frac{\partial U}{\partial y} + c_{xz}\frac{\partial U}{\partial x} - C_{xz}\frac{\partial v}{\partial y}\end{aligned} \tag{B.9}$$

$$\begin{aligned}\lambda\delta c_{yz} = &- Wi\, c_{yz} - \left[ik\frac{\partial}{\partial x} + V\frac{\partial}{\partial y} + ikW\right] c_{yz} - \left[u\frac{\partial}{\partial x} + v\frac{\partial}{\partial y}\right] C_{yz} \\ &+ C_{yy}\frac{\partial w}{\partial y} + C_{xy}\frac{\partial w}{\partial x} + c_{yy}\frac{\partial W}{\partial y} + c_{xy}\frac{\partial W}{\partial x} \\ &+ ikvC_{zz} + C_{xz}\frac{\partial v}{\partial x} + c_{yz}\frac{\partial V}{\partial y} + c_{xz}\frac{\partial V}{\partial x} - C_{yz}\frac{\partial u}{\partial x}\end{aligned} \tag{B.10}$$

# Bibliography


[1] R. G. Larson, E. S. G. Shaqfeh, and S. J. Muller. A purely elastic instability in Taylor Couette flow. *Journal of Fluid Mechanics*, 218:573, 1990. doi: 10.1017/S0022112090001124.

[2] K. Weissenberg. A continuum theory of rheological phenomena. *Nature*, 159:310–311, 1947.

[3] the McKinley group website. MIT Non-Newtonian Fluid Dynamics Research Group, 2013. `http://web.mit.edu/nnf/` [Accessed: 22/08/16].

[4] M. D. Graham. Drag reduction in turbulent flow of polymer solutions. *Rheology Reviews*, 2004:143–170, 2004.

[5] A. N. Morozov and S. E. Spagnolie. Introduction to complex fluids. In S. E. Spagnolie, editor, *Complex Fluids in Biological Systems*, chapter 1, pages 3–52. Springer, New York, 2015. doi: 10.1007/978-1-4939-2065-5_1.

[6] L. D. Landau and E. M. Lifshitz. *Fluid Mechanics*. Pergamon Press, Oxford, 1959. ISBN 0080091040.

[7] R. Bird, R. Armstrong, C. Curtiss, and O. Hassager. *Dynamics of Polymeric Liquids*. John Wiley and Sons Inc., New York, 1977. ISBN 0-471-01596-X.

[8] A. N. Morozov and W. van Saarloos. An introductory essay on subcritical instabilities and the transition to turbulence in visco-elastic parallel shear flows. *Physics Reports*, 447 (3-6):112–143, 2007.

[9] S. J. Muller, R. G. Larson, and E. S. G. Shaqfeh. A purely elastic transition in Taylor-Couette flow. *Rheologica Acta*, 28(6):499–503, 1989. doi: 10.1007/BF01332920.

[10] A. Groisman and V. Steinberg. Elastic turbulence in curvilinear flows of polymer solutions. *New Journal of Physics*, 6(29), 2004. doi: 10.1088/1367-2630/6/1/029.

[11] Y. L. Joo and E. S. G. Shaqfeh. The effects of inertia on the viscoelastic Dean and Taylor-Couette flow instabilities with application to coating flows. *Physics of Fluids A*, 4(11):2415–2431, 1992. doi: 10.1063/1.858483.

[12] P. J. Northey, R. C. Armstrong, and R. A. Brown. Finite-amplitude time-periodic states in viscoelastic Taylor-Couette flow described by the UCM model. *Journal of Non-Newtonian Fluid Mechanics*, 42(1-2):117–139, 1992. doi: 10.1016/0377-0257(92)80007-K.

[13] M. Avgousti and A. N. Beris. Non-axisymmetric modes in viscoelastic Taylor-Couette flow. *Journal of Non-Newtonian Fluid Mechanics*, 50(2-3):225–251, 1993. doi: 10.1016/0377-0257(93)80033-8.

[14] J. J. Magda, J. Lou, S. G. Baek, and K. L. Devries. 2nd normal stress difference of a Boger fluid. *Polymer*, 32(11):2000–2009, 1991. doi: 10.1016/0032-3861(91)90165-F.

[15] G. H. McKinley, J. A. Byars, R. A. Brown, and R. C. Armstrong. Observations on the elastic instability in cone-and-plate and parallel-plate flows of a polyisobutylene Boger fluid. *Journal of Non-Newtonian Fluid Mechanics*, 40(2):201–229, 1991. doi: 10.1016/0377-0257(91)85013-9.

[16] J. A. Byars, A. Öztekin, R. A. Brown, and G. H. Mckinley. Spiral instabilities in the flow of highly elastic fluids between rotating parallel disks. *Journal of Fluid Mechanics*, 271: 173, 1994. doi: 10.1017/S0022112094001734.

[17] A. Öztekin and R. A. Brown. Instability of a viscoelastic fluid between rotating parallel disks: analysis for the Oldroyd-B fluid. *Journal of Fluid Mechanics*, 255(1):473, 1993. doi: 10.1017/S0022112093002563.

[18] P. Pakdel and G. McKinley. Elastic instability and curved streamlines. *Physical Review Letters*, 77(12):2459–2462, 1996. doi: 10.1103/PhysRevLett.77.2459.

[19] T. C. Ho and M. M. Denn. Stability of plane Poiseuille flow of a highly elastic liquid. *Journal of Non-Newtonian Fluid Mechanics*, 3:179–195, 1977.

[20] V. A. Gorodtsov and A. I. Leonov. On a linear instability of a plane parallel Couette flow of viscoelastic fluid. *Journal of Applied Mathematics and Mechanics*, 31(2):310–319, 1967. doi: 10.1016/0021-8928(67)90156-6.

[21] M. Torralba, A. A. Castrejón-Pita, G. Hernández, G. Huelsz, J. A. Del Río, and J. Ortín. Instabilities in the oscillatory flow of a complex fluid. *Physical Review E*, 75(5):1–9, 2007. doi: 10.1103/PhysRevE.75.056307.

[22] L. V. Casanellas and J. Ortín. Vortex ring formation in oscillatory pipe flow of wormlike micellar solutions. *Journal of Rheology*, 58(51):149–181, 2014. doi: 10.1007/s00397-012-0620-3.

[23] P. E. Arratia, C. C. Thomas, J. Diorio, and J. P. Gollub. Elastic instabilities of polymer solutions in cross-channel flow. *Physical Review Letters*, 96(14):12–15, 2006. doi: 10.1103/PhysRevLett.96.144502.

[24] A. Keller and J. A. Odell. The extensibility of macromolecules in solution; a new focus for macromolecular science. *Colloid and Polymer Science*, 263(3):181–201, 1985. doi: 10.1007/BF01415506.

[25] J. A. Odell, A. J. Muller, and A. Keller. Non-Newtonian behavior of hydrolyzed polyacrylamide in strong elongational flows - a transient network approach. *Polymer*, 29(7):1179–1190, 1988. doi: 10.1016/0032-3861(88)90042-0.

[26] R. J. Poole, M. A. Alves, and P. J. Oliveira. Purely elastic flow asymmetries. *Physical Review Letters*, 99(16):1–4, 2007. doi: 10.1103/PhysRevLett.99.164503.

[27] K. P. Chen. Interfacial instability due to elastic stratification in concentric coextrusion of two viscoelastic fluids. *Journal of Non-Newtonian Fluid Mechanics*, 40(2):155–175, 1991. doi: 10.1016/0377-0257(91)85011-7.

[28] K. P. Chen. Elastic instability of the interface in Couette flow of viscoelastic liquids. *Journal of Non-Newtonian Fluid Mechanics*, 40(2):261–267, 1991. doi: 10.1016/0377-0257(91)85015-B.

[29] Y. Y. Su and B. Khomami. Purely elastic interfacial instabilities in superposed flow of polymeric fluids. *Rheologica Acta*, 31(5):413–420, 1992. doi: 10.1007/BF00701121.

[30] Y. Y. Su and B. Khomami. Interfacial stability of multilayer viscoelastic fluids in slit and converging channel die geometries. *Journal of Rheology*, 36(2):357, 1992. doi: 10.1122/1.550349.

[31] H. K. Ganpule and B. Khomami. A theoretical investigation of interfacial instabilities in the three layer superposed channel flow of viscoelastic fluids. *Journal of Non-Newtonian Fluid Mechanics*, 79(2-3):315–360, 1998. doi: 10.1016/S0377-0257(98)00114-1.

[32] B. Khomami and M. M. Ranjbaran. Experimental studies of interfacial instabilities in multilayer pressure-driven flow of polymeric melts. *Rheologica Acta*, 36(4):345–366, 1997. doi: 10.1007/BF00396323.

[33] E. J. Hinch, O. J. Harris, and J. M. Rallison. The instability mechanism for two elastic liquids being co-extruded. *Journal of Non-Newtonian Fluid Mechanics*, 43:311–324, 1992.

[34] K. P. Chen and Y. Zhang. Stability of the interface in co-extrusion flow of two viscoelastic fluids through a pipe. *Journal of Fluid Mechanics*, 247:489, 1993. doi: 10.1017/S0022112093000539.

[35] R. G. Larson. Turbulence without inertia. *Nature*, 405:27–28, 2000.

[36] J. M. Piau, N. El Kissi, and B. Tremblay. Influence of upstream instabilities and wall slip on melt fracture and sharkskin phenomena during silicones extrusion through orifice dies. *Journal of Non-Newtonian Fluid Mechanics*, 34(2):145–180, 1990. doi: 10.1016/0377-0257(90)80016-S.

[37] M. M. Denn. Issues in viscoelastic fluid mechanics. *Annual Review of Fluid Mechanics*, 22:13–34, 1990.

[38] V. Bertola, B. Meulenbroek, C. Wagner, C. Storm, A. N. Morozov, W. van Saarloos, and D. Bonn. Experimental evidence for an intrinsic route to polymer melt fracture phenomena: A nonlinear instability of viscoelastic Poiseuille flow. *Physical Review Letters*, 90(11):114502, 2003. doi: 10.1103/PhysRevLett.90.114502.

[39] A. Groisman and V. Steinberg. Elastic turbulence in a polymer solution flow. *Nature*, 405(6782):53–5, 2000. doi: 10.1038/35011019.

[40] L. Pan, A. N. Morozov, C. Wagner, and P. E. Arratia. Nonlinear elastic instability in channel flows at low Reynolds numbers. *Physical Review Letters*, 110(17):174502, 2013. doi: 10.1103/PhysRevLett.110.174502.

[41] A. N. Morozov and W. van Saarloos. Subcritical finite-amplitude solutions for plane Couette flow of viscoelastic fluids. *Physical Review Letters*, 95(2):1–4, 2005. doi: 10.1103/PhysRevLett.95.024501.

[42] D. Samanta, Y. Dubief, M. Holzner, C. Schäfer, A. N. Morozov, C. Wagner, and B. Hof. Elasto-inertial turbulence. *Proceedings of the National Academy of Sciences of the United States of America*, 110(26):10557–62, 2013. doi: 10.1073/pnas.1219666110.

[43] Y. Dubief, V. E. Terrapon, and J. Soria. On the mechanism of elasto-inertial turbulence. *Physics of Fluids*, 25(64), 2013.

[44] P. Manneville. Transition to turbulence in wall-bounded flows: Where do we stand? *Mechanical Engineering Reviews*, pages 1–25, 2016. doi: 10.1299/mer.15-00684.

[45] P. Huerre and M. Rossi. Hydrodynamic instabilities in open flows. In C. Godrèche and P. Manneville, editors, *Hydrodynamics and Nonlinear instabilities*, chapter 2, pages 81–294. Cambridge University Press, 1998. ISBN 9780511524608.

[46] S. A. Orszag. Accurate solution of the OrrSommerfeld stability equation. *Journal of Fluid Mechanics*, 50(04):689, 1971. doi: 10.1017/S0022112071002842.

[47] T. Herbert. Periodic secondary motions in a plane channel. *Proceedings of the Fifth International Conference on Numerical Methods in Fluid Dynamics June 28-July 2*, 1976.

[48] L. M. Hocking. Non-linear instability of the asymptotic suction velocity profile. *Quarterly Journal of Mechanics and Applied Mathematics*, 28(3):341–353, 1975. doi: 10.1093/qjmam/28.3.341.

[49] J. M. Rotenberry. Finite amplitude steady waves in the Blasius boundary layer. *Physics of Fluids A: Fluid Dynamics*, 5(7):1840–1842, 1993. doi: 10.1063/1.858805.

[50] P. J. Schmid and D. S. Henningson. *Stability and Transition in Shear Flows*. Applied Mathematical Sciences. Springer New York, 2001. ISBN 9781461301851.

[51] V. A. Romanov. Stability of plane-parallel Couette flow. *Functional Analysis and its Applications*, 7:137, 1973.

[52] H. Salwen. Linear stability of Poiseuille flow in a circular pipe. *Journal of Fluid Mechanics*, 98:273–284, 1980. doi: 10.1017/S0022112080000146.

[53] Á Meseguer and L. N. Trefethen. Linearized pipe flow to Reynolds number $10^7$. *Journal of Computational Physics*, 186(1):178–197, 2003. doi: 10.1016/S0021-9991(03)00029-9.

[54] L. S. Tuckerman, T. Kreilos, H. Schrobsdorff, T. M. Schneider, and J. F. Gibson. Turbulent-laminar patterns in plane Poiseuille flow. *Physics of Fluids*, 26(11), 2014. doi: 10.1063/1.4900874.

[55] T. Tsukahara and T. Ishida. The lower bound of subcritical transition in plane Poiseuille flow, 2014.

[56] H. B. Squire. On the stability for three-dimensional disturbances of viscous fluid flow between parallel walls. *Proceedings of the Royal Society A*, 142(847):621–628, 1933. doi: 10.1098/rspa.1933.0193.

[57] G. Tlapa and B. Bernstein. Stability of a relaxation-type viscoelastic fluid with slight elasticity. *Physics of Fluids*, 13(3):565, 1970. doi: 10.1063/1.1692961.

[58] A. Bistagnino, G. Boffetta, A. Celani, A. Mazzino, A. Puliafito, and M. Vergassola. Nonlinear dynamics of the viscoelastic Kolmogorov flow. *Journal of Fluid Mechanics*, 590:61–80, 2007. doi: 10.1017/S0022112007007859.

[59] S. A. Orszag and A. T. Patera. Subcritical transition to turbulence in planar shear flows. In *Transition and turbulence; Proceedings of the Symposium on Transition and Turbulence in Fluids*, pages 127–146, 1981.

[60] D. R. Carlson, S. E. Widnall, and M. F. Peeters. A flow-visualization study of transition in plane Poiseuille flow. *Journal of Fluid Mechanics*, 121:487–505, 1982. doi: 10.1017/S0022112082002006.

[61] K. Avila, D. Moxey, A. de Lozar, M. Avila, D. Barkley, and B. Hof. The onset of turbulence in pipe flow. *Science*, 333(6039):192–196, 2011. doi: 10.1126/science.1203223.

[62] W. O. Criminale, T. L. Jackson, and R. D. Joslin. *Theory and Computation in Hydrodynamic Stability*. Cambridge University Press, Cambridge, 2003.

[63] N. Tillmark and P. H. Alfredsson. Experiments on transition in plane Couette flow. *Journal of Fluid Mechanics*, 235:89–102, 1992.

[64] B. Eckhardt and T. M. Schneider. How does flow in a pipe become turbulent? *European Physical Journal B*, 64(3-4):457–462, 2008. doi: 10.1140/epjb/e2008-00140-y.

[65] M. Nagata. Three-dimensional finite-amplitude solutions in plane Couette flow: bifurcation from infinity. *Journal of Fluid Mechanics*, 1990.

[66] G. Kawahara and S. Kida. Periodic motion embedded in plane Couette turbulence: regeneration cycle and burst. *Journal of Fluid Mechanics*, 449:291, 2001. doi: 10.1017/S0022112001006243.

[67] S. Grossmann. The onset of shear flow turbulence. *Reviews of Modern Physics*, 72(2): 603–618, 2000. doi: 10.1103/RevModPhys.72.603.

[68] F. Waleffe. Homotopy of exact coherent structures in plane shear flows. *Physics of Fluids*, 15(6):1517, 2003. doi: 10.1063/1.1566753.

[69] J. Jimenez and P. Moin. The minimal flow unit in near-wall turbulence. *Journal of Fluid Mechanics*, 225:231–240, 1991. doi: 10.1017/S0022112091002033.

[70] J. M. Hamilton, J. Kim, and F. Waleffe. Regeneration mechanisms of near-wall turbulence structures. *Journal of Fluid Mechanics*, 287:317, 1995. doi: 10.1017/S0022112095000978.

[71] F. Waleffe. Hydrodynamic stability and turbulence: beyond transients to a self-sustaining process. *Studies in Applied Mathematics*, 95(3):319–343, 1995.

[72] J. F. Gibson, J. Halcrow, and P. Cvitanovic. Visualizing the geometry of state space in plane Couette flow. *Journal Of Fluid Mechanics*, 611:107–130, 2008. doi: 10.1017/S002211200800267X.

[73] B. Hof, C. W. H. van Doorne, J. Westerweel, F. T. M. Nieuwstadt, H. Faisst, B. Eckhardt, H. Wedin, R. R. Kerswell, and F. Waleffe. Experimental observation of nonlinear traveling waves in turbulent pipe flow. *Science*, 305(5690):1594–8, 2004. doi: 10.1126/science.1100393.

[74] T. Khapko, T. Kreilos, P. Schlatter, Y. Duguet, B. Eckhardt, and D. S. Henningson. Localized edge states in the asymptotic suction boundary layer. *Journal of Fluid Mechanics*, 717:R6, 2013. doi: 10.1017/jfm.2013.20.

[75] F. Mellibovsky, A. Meseguer, T. M. Schneider, and B. Eckhardt. Transition in localized pipe flow turbulence. *Physical Review Letters*, 103(5):1–4, 2009. doi: 10.1103/PhysRevLett.103.054502.

[76] Y. Duguet, P. Schlatter, and D. S. Henningson. Localized edge states in plane Couette flow. *Physics of Fluids*, 21(11):111701, 2009. doi: 10.1063/1.3265962.

[77] J. Skufca, J. Yorke, and B. Eckhardt. Edge of chaos in a parallel shear flow. *Physical Review Letters*, 96(17):174101, 2006. doi: 10.1103/PhysRevLett.96.174101.

[78] T. M. Schneider, B. Eckhardt, and J. A. Yorke. Turbulence transition and the edge of chaos in pipe flow. *Physical Review Letters*, 99:2–5, 2007.

[79] T. M. Schneider, J. F. Gibson, M. Lagha, F. de Lillo, and B. Eckhardt. Laminar-turbulent boundary in plane Couette flow. *Physical Review E*, 78(3):3–6, 2008. doi: 10.1103/PhysRevE.78.037301.

[80] T. Kreilos, G. Veble, T. M. Schneider, and B. Eckhardt. Edge states for the turbulence transition in the asymptotic suction boundary layer. *Journal of Fluid Mechanics*, 726: 100–122, 2013. doi: 10.1017/jfm.2013.212.

[81] Y. Pomeau. Front motion, metastability and subcritical bifurcations in hydrodynamics. *Physica D*, 23(1-3):3–11, 1986. doi: 10.1016/0167-2789(86)90104-1.

[82] Y. Pomeau. The transition to turbulence in parallel flows: A personal view. *Comptes Rendus - Mecanique*, 343(3):210–218, 2015. doi: 10.1016/j.crme.2014.10.002.

[83] M. D. Graham. Turbulence spreads like wildfire. *Nature*, 526:508–509, 2015. doi: 10.1038/526508a.

[84] G. Lemoult, L. Shi, K. Avila, S. V. Jalikop, M. Avila, and B. Hof. Directed percolation phase transition to sustained turbulence in Couette flow. *Nature Physics*, 12:254–258, 2016. doi: 10.1038/nphys3675.

[85] M. Sano and K. Tamai. A universal transition to turbulence in channel flow. *Nature Physics*, 12(March):249–254, 2016. doi: 10.1038/NPHYS3659.

[86] Dwight Barkley. Simplifying the complexity of pipe flow. *Physical Review E*, 84(1):1–8, 2011. doi: 10.1103/PhysRevE.84.016309.

[87] T. Kreilos. *Turbulence Transition in Shear Flows and Dynamical Systems Theory*. PhD thesis, University of Marburg, 2014.

[88] D. Coles. Transition in circular Couette flow. *Journal of Fluid Mechanics*, 21(03):385, 1965. doi: 10.1017/S0022112065000241.

[89] P. Hall and F. T. Smith. On strongly nonlinear vortex/wave interactions in boundary-layer transition. *Journal of Fluid Mechanics*, 227:641, 1991. doi: 10.1017/S0022112091000289.

[90] H. T. Kim, S. J. Kline, and D. W. C. Reynolds. The production of turbulence near a smooth wall in a turbulent boundary layer. *Journal of Fluid Mechanics*, 50(1):133–160, 1971. doi: 10.1017/S0022112071002490.

[91] T. Ellingsen and E. Palm. Stability of linear flow. *Physics of Fluids*, 18(4):487, 1975. doi: 10.1063/1.861156.

[92] M. T. Landahl. A note on an algebraic instability of inviscid parallel shear flows. *Journal of Fluid Mechanics*, 98:243–251, 1980.

[93] H. K. Moffatt. Fixed points of turbulent dynamical systems and suppression of nonlinearity. In J Lumley, editor, *Whither Turbulence? Turbulence at the Crossroads*, pages 250–257, 1990. ISBN 978-3-540-47032-8. doi: 10.1007/3-540-52535-1_47.

[94] F. Waleffe. Three-dimensional coherent states in plane shear flows. *Physical Review Letters*, 81(19):4140–4143, 1998. doi: 10.1103/PhysRevLett.81.4140.

[95] F. Waleffe. On a self-sustaining process in shear flows. *Physics of Fluids*, 9(4):883, 1997. doi: 10.1063/1.869185.

[96] G. Kawahara, M. Uhlmann, and L. van Veen. The significance of simple invariant solutions in turbulent flows. *Annual Review of Fluid Mechanics*, 44(1):203–225, 2012. doi: 10.1146/annurev-fluid-120710-101228.

[97] U. Ehrenstein and W. Koch. Three-dimensional wavelike equilibrium states in plane Poiseuille flow. *Journal of Fluid Mechanics*, 228:111, 1991. doi: 10.1017/S0022112091002653.

[98] M. R. Jovanović and S. Kumar. Transient growth without inertia. *Physics of Fluids*, 22 (2):023101, 2010. doi: 10.1063/1.3299324.

[99] G. B. Thurston. Theory of oscillation of a viscoelastic medium between parallel planes. *Journal of Applied Physics*, 30(12):1855, 1959. doi: 10.1063/1.1735080.

[100] L. V. Casanellas. *Oscillatory pipe flow of wormlike micellar solutions*. PhD thesis, University of Barcelona, 2013.

[101] R. Sureshkumar, A. N. Beris, and R. A. Handler. Direct numerical simulation of the turbulent channel flow of a polymer solution. *Physics of Fluids*, 9(3):743, 1997. doi: 10.1063/1.869229.

[102] B. Sadanandan and R. Sureshkumar. Viscoelastic effects on the stability of wall-bounded shear flows. *Physics of Fluids*, 14(1):41, 2002. doi: 10.1063/1.1425847.

[103] P. Stone, F. Waleffe, and M. Graham. Toward a structural understanding of turbulent drag reduction: Nonlinear coherent states in viscoelastic shear flows. *Physical Review Letters*, 89(20):208301, 2002. doi: 10.1103/PhysRevLett.89.208301.

[104] Philip A. Stone, A. Roy, R. G. Larson, F. Waleffe, and M. D. Graham. Polymer drag reduction in exact coherent structures of plane shear flow. *Physics of Fluids*, 16(9):3470, 2004. doi: 10.1063/1.1775192.

[105] J. Azaiez and G. M. Homsy. Linear stability of free shear flow of viscoelastic liquids. *Journal of Fluid Mechanics*, 1994.

[106] M. Renardy. Current issues in non-Newtonian flows: a mathematical perspective. *Journal of Non-Newtonian Fluid Mechanics*, 90(2-3):243–259, 2000. doi: 10.1016/S0377-0257(99)00081-6.

[107] P. K. Ray and T. A. Zaki. Absolute instability in viscoelastic mixing layers. *Physics of Fluids*, 26(1), 2014. doi: 10.1063/1.4851295.

[108] F. Sausset, O. Cadot, and S. Kumar. Experimental observation of frequency doubling in a viscoelastic mixing layer. *Comptes Rendus Mecanique*, 332:1001–1006, 2004. doi: 10.1016/j.crme.2004.10.001.

[109] O. Cadot and S. Kumar. Experimental characterization of viscoelastic effects on two- and three-dimensional shear instabilities. *Journal of Fluid Mechanics*, 416:151–172, 2000. doi: 10.1017/S0022112000008818.

[110] O. Cadot. Partial roll-up of a viscoelastic Karman street. *European Journal of Mechanics, B*, 20(1):145–153, 2001. doi: 10.1016/S0997-7546(00)01100-6.

[111] H. Sato. Experimental investigation on the transition of laminar separated layer. *Journal of the Physical Society of Japan*, 11(6):702–709, 1956. doi: 10.1143/JPSJ.11.702.

[112] G. Boffetta, A. Celani, A. Mazzino, A. Puliafito, and M. Vergassola. The viscoelastic Kolmogorov flow: eddy viscosity and linear stability. *Journal of Fluid Mechanics*, 523: 161–170, 2005. doi: 10.1017/S0022112004002423.

[113] J. Beaumont, N. Louvet, T. Divoux, M. Fardin, H. Bodiguel, S. Lerouge, S. Manneville, and A. Colin. Turbulent flows in highly elastic wormlike micelles. *Soft Matter*, 9(3): 735–749, 2013. doi: 10.1039/C2SM26760H.

[114] M. A. Fardin, C. Perge, and N. Taberlet. "The hydrogen atom of fluid dynamics" introduction to the Taylor Couette flow for soft matter scientists. *Soft Matter*, 10(20): 3523, 2014. doi: 10.1039/c3sm52828f.

[115] Y. Y. Renardy. Stability of the interface in two-layer Couette flow of upper convected Maxwell liquids. *Journal of Non-Newtonian Fluid Mechanics*, 28:99–115, 1988.

[116] K. P. Chen and D. D. Joseph. Elastic short-wave instability in extrusion flows of viscoelastic liquids. *Journal of Non-Newtonian Fluid Mechanics*, 42(1-2):189–211, 1992. doi: 10.1016/0377-0257(92)80009-M.

[117] H. J. Wilson and J. M. Rallison. Short wave instability of co-extruded elastic liquids with matched viscosities. *Journal of Non-Newtonian Fluid Mechanics*, 72(2-3):237–251, 1997. doi: 10.1016/S0377-0257(97)00025-6.

[118] H. K. Ganpule and B. Khomami. An investigation of interfacial instabilities in the superposed channel flow of viscoelastic fluids. *Journal of Non-Newtonian Fluid Mechanics*, 81(1-2):27–69, 1999. doi: 10.1016/S0377-0257(98)00088-3.

[119] B. Khomami and K. C. Su. An experimental/theoretical investigation of interfacial instabilities in superposed pressure-driven channel flow of newtonian and well characterized viscoelastic fluids part I: linear stability and encapsulation effects. *Journal of Non-Newtonian Fluid Mechanics*, 91(1):59–84, 2000. doi: 10.1016/S0377-0257(99)00086-5.

[120] J. C. Miller and J. M. Rallison. Interfacial instability between sheared elastic liquids in a channel. *Journal of Non-Newtonian Fluid Mechanics*, 143(2-3):71–87, 2007. doi: 10.1016/j.jnnfm.2007.01.009.

[121] J. C. Miller and J. M. Rallison. Instability of coextruded elastic liquids at high weissenberg number. *Journal of Non-Newtonian Fluid Mechanics*, 143(2-3):88–106, 2007. doi: 10.1016/j.jnnfm.2007.01.008.

[122] O. Bonhomme, A. N. Morozov, J. Leng, and A. Colin. Elastic instability in stratified core annular flow. *Physical Review E*, 83(6, 2), 2011. doi: 10.1103/PhysRevE.83.065301.

[123] Y. Y. Renardy and M Renardy. Instability due to second normal stress jump in two-layer shear flow of the Giesekus fluid. *Journal of Non-Newtonian Fluid Mechanics*, 81(3): 215–234, 1999.

[124] A. A. Khan. On the interface deformation in the stratified two-phase flow of viscoelastic fluids. *Journal of Rheology*, 20(4):595, 1976. doi: 10.1122/1.549426.

[125] C. Han. A study of coextrusion in a circular die. *Journal of Applied Polymer Science*, 19:1875–1883, 1985.

[126] G. M. Wilson and B. Khomami. An experimental investigation of interfacial instabilities in multilayer flow of viscoelastic fluids. i. incompatible polymer systems. *Journal of Non-Newtonian Fluid Mechanics*, 45:355, 1992. doi: 10.1122/1.550446.

[127] G. M. Wilson and B. Khomami. An experimental investigation of interfacial instabilities in multilayer flow of viscoelastic fluids. ii. elastic and nonlinear effects in incompatible polymer systems. *Journal of Rheology*, 37(2):341, 1993. doi: 10.1122/1.550446.

[128] G. M. Wilson and B. Khomami. An experimental investigation of interfacial instabilities in multilayer flow of viscoelastic fluids. iii. compatible polymer systems. *Journal of Rheology*, 37(2):341, 1993. doi: 10.1122/1.550446.

[129] T. C. B. Mcleish and M. Road. Stability of the interface between two dynamic phases in capillary flow of linear polymer melts. *Journal of Polymer Science Part B: Polymer Physics*, 25:2253–2264, 1987.

[130] H. J. Wilson and S. M. Fielding. Linear instability of planar shear banded flow of both diffusive and non-diffusive Johnson-Segalman fluids. *Journal of Non-Newtonian Fluid Mechanics*, 138:181–196, 2006.

[131] S. Lerouge et al. Interface instability in shear-banding flow. *Physical Review Letters*, 96: 088301, 2006.

[132] S. M. Fielding. Complex dynamics of shear banded flows. *Soft Matter*, 3:1262–1279, 2007.

[133] S. Lerouge et al. Interface dynamics in shear-banding flow of giant micelles. *Soft Matter*, 4:1808–1819, 2008.

[134] Sandra Lerouge and Jean-Francois Berret. Shear-induced transitions and instabilities in surfactant wormlike micelles. *Advances in Polymer Science*, 230:1–71, 2010.

[135] S. M. Fielding and H. J. Wilson. Shear banding and interfacial instability in planar Poiseuille flow. *Journal of Non-Newtonian Fluid Mechanics*, 165(5-6):196–202, 2010. doi: 10.1016/j.jnnfm.2009.12.001.

[136] P. Nghe, S. M. Fielding, P. Tabeling, and A. Ajdari. Interfacially driven instability in the microchannel flow of a shear-banding fluid. *Physical Review Letters*, 104:248303, 2010.

[137] J. P. Decruppe et al. Azimuthal instability of the interface in a shear banded flow by direct visual observation. *Phys. Rev. Lett.*, 105:258301, 2010.

[138] A. Nicolas and A. N. Morozov. Non-axisymmetric instability of shear-banded Taylor-Couette flow. *Physical Review Letters*, 108(8):088302, 2012. doi: 10.1103/PhysRevLett.108.088302.

[139] H. J. Wilson and J. M. Rallison. Instability of channel flows of elastic liquids having continuously stratified properties. *Journal of Non-Newtonian Fluid Mechanics*, 85(2-3): 273–298, 1999. doi: 10.1016/S0377-0257(98)00186-4.

[140] P. G. Drazin and W. H. Reid. *Hydrodynamic Stability*. Cambridge University Press, Cambridge, 2 edition, 1981. ISBN 0521525411.

[141] C. D. Winant and F. K. Browand. Vortex pairing: the mechanism of turbulent mixing-layer growth at moderate Reynolds number. *Journal of Fluid Mechanics*, 63(02):237–255, 1974. doi: 10.1017/S0022112074001121.

[142] C. M. Ho and P. Huerre. Perturbed free shear layers. *Annual review of fluid mechanics*, 16:365, 1984. doi: 10.1146/annurev.fl.16.010184.002053.

[143] A. Michalke. Vortex formation in a free boundary layer according to stability theory. *Journal of Fluid Mechanics*, 22(02):371–383, 1965. doi: 10.1017/S0022112065000812.

[144] A. A. Amsden and F. H. Harlow. Slip instability. *Physics of Fluids*, 7(3):327, 1964. doi: 10.1063/1.1711202.

[145] A. P. Hooper. Long-wave instability at the interface between two viscous fluids: Thin layer effects. *Physics of Fluids*, 28(6):1613, 1985. doi: 10.1063/1.864952.

[146] B. Meulenbroek, C. Storm, A. N. Morozov, and W. van Saarloos. Weakly nonlinear subcritical instability of visco-elastic Poiseuille flow. *Journal of Non-Newtonian Fluid Mechanics*, 116(2-3):235–268, 2004. doi: 10.1016/j.jnnfm.2003.09.003.

[147] Y. Y. Renardy. Weakly nonlinear behavior of periodic disturbances in two-layer plane channel flow of upper-convected Maxwell liquids. *Journal of Non-Newtonian Fluid Mechanics*, 56(2):101–126, 1995. doi: 10.1016/0377-0257(94)01278-P.

[148] B. Khomami, Y. Renardy, K. C. Su, and M. A. Clarke. An experimental/theoretical investigation of interfacial instabilities in superposed pressure-driven channel flow of newtonian and well characterized viscoelastic fluids part II: Nonlinear stability. *Journal of Non-Newtonian Fluid Mechanics*, 91(1):85–104, 2000. doi: 10.1016/S0377-0257(99)00087-7.

[149] T. W. Searle. Github, . `https://github.com/twsearle`.

[150] A. Michalke and A. Timme. On the inviscid instability of certain two-dimensional vortex-type flows. *Journal of Fluid Mechanics*, 29:647, 1967. doi: 10.1017/S0022112067001090.

[151] J. del Río, M. López de Haro, and S. Whitaker. Enhancement in the dynamic response of a viscoelastic fluid flowing in a tube. *Physical Review E*, 58(5):6323–6327, 1998. doi: 10.1103/PhysRevE.58.6323.

[152] L. V. Casanellas and J. Ortín. Laminar oscillatory flow of Maxwell and Oldroyd-B fluids: Theoretical analysis. *Journal of Non-Newtonian Fluid Mechanics*, 166(23-24):1315–1326, 2011. doi: 10.1016/j.jnnfm.2011.08.010.

[153] Y. A. Andrienko, D. A. Siginer, and Y. G. Yanovsky. Resonance behavior of viscoelastic fluids in Poiseuille flow and application to flow enhancement. *International Journal of Non-Linear Mechanics*, 35:95–102, 2000.

[154] L. V. Casanellas and J. Ortín. Experiments on the laminar oscillatory flow of wormlike micellar solutions. *Rheologica Acta*, 51(6):545–557, 2012. doi: 10.1007/s00397-012-0620-3.

[155] J. D. Ferry. Studies of the mechanical properties of substances of high molecular weight i. a photoelastic method for study of transverse vibrations in gels. *Review of Scientific Instruments*, 12(2):79–82, 1941. doi: 10.1063/1.1769831.

[156] M. Clamen and P. Minton. An experimental investigation of flow in an oscillating pipe. *Journal of Fluid Mechanics*, 81(03):421, 1977. doi: 10.1017/S0022112077002146.

[157] D. M. Eckmann and J. B. Grotberg. Experiments on transition to turbulence in oscillatory pipe flow. *Journal of Fluid Mechanics*, 222:329–350, 1991. doi: 10.1017/S002211209100112X.

[158] P. Merkli and H. Thomann. Transition to turbulence in oscillating pipe flow. *Journal of Fluid Mechanics*, 68(03):567, 1975. doi: 10.1017/S0022112075001826.

[159] P. J. Blennerhassett and A. P. Bassom. On the linear stability of stokes layers. *Philosophical Transactions of the Royal Society A*, 366(1876):2685–2697, 2008. doi: 10.1098/rsta.2008.0055.

[160] Inc. Wolfram Research. Mathematica version 10.4, 2016.

[161] T. W. Searle. Edinburgh datashare, . `http://datashare.is.ed.ac.uk/`.

[162] T. Kreilos and B. Eckhardt. Periodic orbits near onset of chaos in plane Couette flow. *Chaos*, 22(4):047505, 2012. doi: 10.1063/1.4757227.

[163] G. J. Chandler and R. R. Kerswell. Invariant recurrent solutions embedded in a turbulent two-dimensional Kolmogorov flow. *Journal of Fluid Mechanics*, 722:554–595, 2013. doi: 10.1017/jfm.2013.122.

[164] B. Eckhardt, K. Marzinzik, and A. Schmiegel. Transition to turbulence in shear flows. In *A perspective look at nonlinear media*, pages 327–338. Springer Berlin Heidelberg, 1998. ISBN 3-540-63995-0.

[165] B. Eckhardt, T. M. Schneider, B. Hof, and J. Westerweel. Turbulence transition in pipe flow. *Annual Review of Fluid Mechanics*, 39(1):447–468, 2007. doi: 10.1146/annurev.fluid.39.050905.110308.

[166] P. Cvitanović. Recurrent flows: the clockwork behind turbulence. *Journal of Fluid Mechanics*, 726(1990):1–4, 2013. doi: 10.1017/jfm.2013.198.

[167] L. N. Trefethen, A. E. Trefethen, S. C. Reddy, and T. A. Driscoll. Hydrodynamic stability without eigenvalues. *Science*, 261(5121):578–584, 1993. doi: 10.1126/science.261.5121.578.

[168] A. Roy, A. N. Morozov, W. van Saarloos, and R. G. Larson. Mechanism of polymer drag reduction using a low-dimensional model. *Physical Review Letters*, 97(23):1–4, 2006. doi: 10.1103/PhysRevLett.97.234501.

[169] Y. Dubief, C. M. White, V. E. Terrapon, E. S. G. Shaqfeh, P. Moin, and S. K. Lele. On the coherent drag-reducing and turbulence-enhancing behaviour of polymers in wall flows. *Journal of Fluid Mechanics*, 514:271–280, 2004. doi: 10.1017/S0022112004000291.

[170] C. Canuto, M. Y. Hussaini, A. Quarteroni, and T. A. Zang. *Spectral Methods in Fluid Dynamics*. Springer Berlin, Heidelberg, 1988. ISBN 978-3-540-52205-8.

[171] L. N. Trefethen. *Spectral Methods in Matlab*. SIAM, Oxford, 2000. ISBN 978-0-898714-65-4.

[172] J. P. Boyd. *Chebyshev and Fourier Spectral Methods*. Dover Publications Inc., Dover, 2001. ISBN 0486411834.

[173] The Scipy Community. Scipy. `https://www.scipy.org/` [Accessed: 22/08/16].

[174] NAG Ltd., Univ. of Colorado Denver, Univ. of California Berkeley, and Univ. of Tennessee. Lapack. `http://www.netlib.org/lapack/` [Accessed: 22/08/16].

[175] L. N. Trefethen and D. Bau. *Numerical Linear Algebra*. SIAM, Oxford, 1997. ISBN 978-0-898713-61-9.

[176] J. E. Dennis and R. B. Schnabel. *Numerical Methods for Unconstrained Optimization and Nonlinear Equations*. SIAM, Philidelphia, 1996. ISBN 978-0-898713-64-0.